UNIVERSIDAD NACIONAL AUTÓNOMA DE MÉXICO

PROGRAMA DE MAESTRÍA Y DOCTORADO EN INGENIERÍA
ENERGÍA – FUENTES RENOVABLES

DESARROLLO DE SIMULADOR NUMÉRICO PARA DETERMINAR CONDICIONES TÉRMICAS DE TRABAJO INTERCAMBIADORES DE CALOR AIRE – TIERRA.

TESIS
QUE PARA OPTAR POR EL GRADO DE:
DOCTOR EN INGENIERÍA

PRESENTA:
M. en I. RICARDO MOLINA RODEA

TUTOR PRINCIPAL
Dr. JORGE ALEJANDRO WONG LOYA, IER – UNAM.
COMITÉ TUTOR
Dr. JORGE ALBERTO ANDAVERDE ARREDONDO, UV.
Dr. PATRICIO VALADÉS PELAYO, IER – UNAM.
Dr. OCTAVIO GARCÍA VALLADARES, IER – UNAM.
Dr. JESÚS ANTONIO DEL RÍO PORTILLA, IER – UNAM.

MÉXICO, TEMIXCO. JUNIO 2023

JURADO ASIGNADO:

Presidente:	Dr. Jesús Antonio del Río Portilla
Secretario:	Dr. Octavio García Valladares
1 er. Vocal:	Dr. Jorge Alejandro Wong Loya
2 do. Vocal:	Dr. Patricio Valadés Pelayo
3 er. Vocal:	Dr. Jorge Alberto Andaverde Arredondo

Lugar donde se realizó la tesis: Instituto de Energías Renovables, Temixco, Morelos, México.

TUTOR DE TESIS:

Dr. Jorge Alejandro Wong Loya

FIRMA

Resumen.

La humanidad ha aprovechado la energía geotérmica de manera directa desde hace 12 000 años utilizando las cavernas y manantiales termales. En la actualidad, la capacidad térmica instalada alrededor del mundo es seis veces superior que la capacidad de generación eléctrica a partir de recursos geotérmicos. Más de la mitad de esta capacidad térmica corresponden al uso de intercambiadores de calor enterrados, ya sea con bombas de calor o intercambiadores de calor aire tierra. Para poder aprovechar los recursos geotérmicos de baja entalpía utilizando intercambiadores de calor enterrados, es necesario conocer el comportamiento de distintos parámetros de funcionamiento de estos sistemas, que se pueden agrupar en propiedades del suelo y del intercambiador de calor. Esto se puede hacer de manera analítica, experimental, o numérica. Debido a la dificultad del estudio, las soluciones analíticas son poco utilizadas. El método experimental es muy preciso, pero el tiempo invertido en la metodología muchas veces representa más una desventaja. Obtener resultados de manera numérica se ha convertido en la herramienta más ampliamente utilizada alrededor del mundo debido al poco tiempo invertido y a la capacidad de resolver problemas de gran complejidad. Con el fin de aprovechar los recursos geotérmicos de baja entalpía, en este trabajo presenta el desarrollo de un simulador numérico capaz de determinar las condiciones térmicas de trabajo de intercambiadores de calor aire-tierra. El simulador numérico está compuesto por tres módulos que determinan de manera independiente distintos parámetros de funcionamiento de los intercambiadores de calor enterrados. El primer módulo consiste en conocer y modelar el perfil de temperatura del suelo en función de las condiciones meteorológicas, las propiedades físicas y termo físicas del suelo, y la temperatura ambiental. Con la ayuda de una sonda de medición se obtienen datos *in-situ* que son utilizados para validar experimentalmente el modelo numérico. Como resultado, se logra ajustar los datos numéricos y experimentales hasta un 80% mejor en comparación con una solución analítica utilizada ampliamente en diversos trabajos publicados. Con estos resultados es posible conocer la temperatura del suelo, que representa el dominio de estudio de los intercambiadores de calor enterrados. En el segundo módulo se reproduce la temperatura del fluido a lo largo del intercambiador de calor. Para ello, se analizaron variables del intercambiador de calor, del fluido, y del suelo. La validación experimental de este módulo se realizó instalando intercambiadores de calor verticales en las instalaciones del Instituto de Energías Renovables. Además, también se utilizaron datos numéricos encontrados en la literatura sobre el uso de pozos profundos abandonados para la validación del segundo módulo. El resultado de la comparación arroja que el modelo numérico es capaz de reproducir adecuadamente la temperatura del fluido a lo largo del intercambiador de calor con un coeficiente de determinación promedio de 0.8. Por último, el tercer módulo se utiliza para conocer y simular la afectación térmica del suelo como respuesta al flujo del aire por el interior de los tubos enterrados. La validación se realizó con datos experimentales de modelos a escala. El resultado muestra un ajuste del coeficiente de determinación superior a 0.9. La validación de los tres módulos del simulador numérico se realiza utilizando los datos experimentales de la sonda de medición y de los intercambiadores de calor que fueron recabados durante el doctorado. Para ello se modifica la velocidad al interior de los tubos enterrados y se compara la temperatura del fluido a lo largo del intercambiador de calor y la temperatura del suelo posterior a la afectación térmica. De este modo, se logra desarrollar un simulador numérico que reproduce las condiciones de trabajo de intercambiadores de calor enterrados durante la operación de estos.

Dedicatoria.

Dedico la realización de este trabajo a mi familia. A mis padres **Ricardo Molina J.** y **Ma. Guadalupe Rodea V.** ya que sin su sabiduría y consejo seguramente no estaría en este punto de mi vida. A mi papá, gracias por ser el mejor padre, amigo y consejero que la vida me pudo haber dado, estoy seguro de que nos volveremos a encontrar en este u otro plano. Los amo.

A mis hermanos **Rodrigo, Alitzel y Maricela**. Hermano, tus pláticas lejos del mundo académico me han complementado para ser quien soy ahora. Hermanas, su independencia y determinación son una muestra de lo que podemos llegar a hacer cuando confiamos en nosotros mismos. Maricela, te extraño y te honro. Los amo.

A mis amigos de cuatro patas **Loki, Akira y Babo**. Estoy seguro de que mi vida es más placentera cada que llego a casa y los veo a ustedes felices de verme. Loki, a lo largo de los últimos siete años has sido mi familia en Morelos y siempre tienes una mirada que me da paz. Los amo.

A **mis amigos** que conocí durante mis estudios de posgrado. Toda y cada una de las aventuras que viví con ustedes me han llenado la memoria de momentos irrepetibles que llevaré toda mi vida.

La vida es tan compleja y perfecta a la vez, como para querer imitarla con una serie de ecuaciones.

R. Molina-Rodea. 2023.

Agradecimientos.

Quiero agradecer al Dr. Jorge Alejandro Wong Loya por su valiosa tutoría durante el tiempo que he realizado mis estudios de posgrado en el IER – UNAM. Por la confianza de dejarme realizar este trabajo con ideas propias, pero sin dejar de lado su consejo y tutela. Por el conocimiento transmitido mediante charlas, reuniones y presentaciones. Por acercarme a la investigación, colaboración y publicación científica.

Al comité de tutores de este trabajo: Dr. Jorge Alberto Andaverde Arredondo, Dr. Patricio Valadés Pelayo, Dr. Octavio García Valladares, y Dr. Jesús Antonio del Río Portilla. Por todas las ideas y aportaciones que realizaron durante el desarrollo de este trabajo. Por los consejos recibidos durante las evaluaciones semestrales que, sin lugar a duda, me permitieron tener una perspectiva más amplia y completa durante los estudios de doctorado. Por las recomendaciones de la parte experimental y la parte computacional - numérica del trabajo con lo que pude obtener resultados satisfactorios. Por la tutela durante la redacción y publicación de los resultados de la investigación.

A mi comité de tutores en general, por impulsarme a ser mejor persona de lo que era cuando comencé esta tarea.

A demás investigadores y colaboradores que aportaron ideas para la realización de este trabajo. Al grupo de diseño bioclimático del IER encabezado por la Dra. Guadalupe Huelsz Lesbros y el Dr. Jorge Rojas Menéndez por la colaboración en el diseño del edificio anexo del IER. Al grupo de refrigeración del IER del Dr. Wilfrido Rivera Gómez Franco por la colaboración durante la publicación de trabajos en conjunto. Al Ing. Kevin Alquicira Hernández por su ayuda con el software de programación.

Al IER por ser mi segundo hogar durante los últimos 7 años, a toda su comunidad que te brinda una mano cuando más lo necesitas.

A la UNAM, por recibirme en sus instalaciones a lo largo de mis estudios superiores y de posgrado. Espero poder devolver de alguna manera u otra a esta casa de estudios todo el conocimiento que me ha brindado.

Al CONACYT por la beca recibida durante los cuatro años que dediqué a mis estudios de doctorado.

A los programas UNAM-DGAPA-PAPIME PE108721, PE108917, y PE110319 por el apoyo brindado para la realización de este trabajo.

Contenido.

Tabla de contenido

Resumen..... II

Dedicatoria..... III

Agradecimientos..... IV

Contenido..... V

Lista de figuras..... VII

Lista de tablas..... IX

Nomenclatura..... X

Capítulo I. "Introducción"..... 1

Introducción..... 1

Planteamiento del problema..... 4

Justificación..... 5

Objetivos..... 6

General..... 6

Específicos..... 6

Metodología..... 7

Estructura de la tesis..... 7

Capítulo II. "Perfil de temperatura del suelo"..... 10

Resumen..... 10

Publicación..... 11

Capítulo III. "Dispositivo experimental EAHE"..... 23

Resumen..... 23

Publicación..... 24

Capítulo IV. "Evaluación experimental del EAHE"..... 37

Resumen..... 37

Publicación..... 38

Capítulo V. "Modelo de comportamiento térmico de EAHE"..... 64

Resumen..... 64

Publicación..... 65

Capítulo VI. "Aplicación del modelo numérico"..... 88

Resumen..... 88

Publicación. 89
Capítulo VII. “Afectación térmica del suelo” 109
Resumen. 109
Publicación. 110
Capítulo VIII. “Validación experimental” 119
Validación del modelo 1. 120
Validación del modelo 2. 121
Validación del modelo 3. 123
Capítulo IX. “Conclusiones” 127
Conclusiones 127
Trabajo a futuro 128
Bibliografía 129
Fin 132

Lista de figuras.

1.1	Esquema de GSHP durante su operación como calefacción y acondicionamiento. ……..	2
1.2	EAHE de configuración horizontal conectado en serie y paralelo. ……..	3
1.3	EAHE de configuración vertical conectado en serie y paralelo. ……..	3
2.1	Esquema de la sonda de medición, vista longitudinal y transversal. ……..	13
2.2	Dispositivo experimental para la prueba de carga constante. ……..	14
2.3	Esquema del dominio considerado para la simulación térmica. ……..	15
2.4	Comparación entre datos experimentales y analíticos a 0.6 m, 1.2 m, y 1.8 m de profundidad. ……..	17
2.5	Comparación entre datos experimentales y modelo parcial a 0.6 m, 1.2 m, y 1.8 m de profundidad. ……..	18
2.6	Comparación entre datos experimentales y modelo completo a 0.6 m, 1.2 m, y 1.8 m de profundidad. ……..	19
2.7	Valores de la función de mérito para el modelo parcial, completo y analítico. ……..	20
2.8	Comparación entre datos experimentales, analíticos, modelo parcial y modelo completo a 0.6 m, 1.2 m, y 1.8 m de profundidad. ……..	20
3.1	Fotos de la instalación del dispositivo experimental de EAHE. ……..	25
3.2	Aislante térmico en la sección horizontal del EAHE. ……..	26
3.3	Dimensiones de los intercambiadores de calor enterrados. ……..	26
3.4	Localización de los termopares en el intercambiador de calor. ……..	27
3.5	Vista del fondo y de la parte superior de los intercambiadores de calor. ……..	27
3.6	Registro de temperatura a la entrada y salida del intercambiador de calor. Test 1. ……..	28
3.7	Registro de temperatura del suelo alrededor de los tubos enterrados. Test 1. ……..	29
3.8	Registro de temperatura a la entrada y salida del intercambiador de calor. Test 2. ……..	29
3.9	Registro de temperatura del suelo alrededor de los tubos enterrados. Test 2. ……..	30
3.10	Registro de temperatura a la entrada y salida del intercambiador de calor. Test 3. ……..	30
3.11	Registro de temperatura del suelo alrededor de los tubos enterrados. Test 3. ……..	31
3.12	Registro de temperatura a la entrada y salida del intercambiador de calor. Test 4. ……..	31
3.13	Registro de temperatura del suelo alrededor de los tubos enterrados. Test 4. ……..	32
3.14	Registro de temperatura a la entrada y salida del intercambiador de calor. Test 5. ……..	32
3.15	Registro de temperatura del suelo alrededor de los tubos enterrados. Test 5. ……..	33
3.16	Registro de temperatura a la entrada y salida del intercambiador de calor. Test 6. ……..	33
3.17	Registro de temperatura del suelo alrededor de los tubos enterrados. Test 6. ……..	34
4.1	Temperatura ambiental y precipitación mensual promedio en Temixco. ……..	43
4.2	Ubicación y configuración de los pozos. ……..	43
4.3	Esquema del UEHE conectado en serie y corte transversal del pozo. ……..	44
4.4	Ubicación de los termopares en el UEHE. ……..	45
4.5	Dimensiones de la oficina seleccionada para acondicionar. ……..	47
4.6	Temperatura de entrada y salida con velocidad interna de 1.3 m/s, 4.1 m/s, 6.4 m/s, 6.6 m/s. ……..	49
4.7	Temperatura del aire a lo largo del EAHE con velocidad interna de 1.3 m/s, 4.1 m/s, 6.4 m/s, 6.6 m/s. ……..	51
4.8	Temperatura del suelo a 5 cm de la pared del tubo con velocidad interna de 1.3 m/s, 4.1 m/s, 6.4 m/s, 6.6 m/s. ……..	54
4.9	Efectividad y COP del EAHE con velocidad interna de 1.3 m/s, 4.1 m/s, 6.4 m/s, 6.6 m/s. ……..	56
4.10	Temperatura promedio a la entrada y salida, COP y efectividad del EAHE. ……..	58

5.1	Temperatura ambiental anual en el bosque La Primavera.	68
5.2	Representación de la litología del pozo “LP2”.	69
5.3	Esquema del pozo “LP2”.	70
5.4	Esquema del sistema de refrigeración por absorción de medio efecto.	71
5.5	Dominio de estudio: suelo, pozo, paredes del EAHE, material aislante, espacio interno.	72
5.6	Discretización del dominio de estudio.	74
5.7	Temperatura del fluido a lo largo del UEHE modificando la velocidad.	78
5.8	Temperatura del fluido a lo largo del UEHE modificando el diámetro de tubería.	79
5.9	Temperatura del fluido a lo largo del UEHE modificando el espesor del aislante.	79
5.10	Temperatura del fluido a lo largo del UEHE modificando la longitud del aislante.	80
5.11	Temperatura del fluido a lo largo del UEHE modificando la longitud total del intercambiador de calor.	80
5.12	Temperatura del fluido a lo largo del UEHE con las ocho pruebas finales.	82
6.1	Diagrama del SRA de simple efecto.	92
6.2	Diagrama del SRA de medio efecto.	93
6.3	Diagrama del SRA de doble efecto.	93
6.4	Diagrama del SRA de triple efecto.	94
6.5	Ubicación del campo geotérmico Cerritos Colorado.	95
6.6	Litología simplificada de una muestra de roca del campo geotérmico Cerritos Colorado.	96
6.7	Dominio de estudio del modelo matemático.	98
6.8	Temperatura promedio horaria en cada estación del año en Cerritos Colorado.	99
6.9	Temperatura del fluido adentro del intercambiador de calor. Pruebas 1 – 4.	101
6.10	Temperatura del fluido adentro del intercambiador de calor. Pruebas 5 y 6.	101
6.11	Potencia de enfriamiento de cada SRA por estación del año.	102
6.12	Potencia de enfriamiento de cada SRA por estación del año.	103
6.13	COP como función de la temperatura ambiental por estación del año.	103
7.1	Dominio considerado para la simulación numérica durante la afectación y recuperación térmica.	111
7.2	Dispositivo experimental a escala.	112
7.3	Dispositivo impreso en 3D para circular el fluido por el modelo a escala.	113
7.4	Dispositivo experimental para estimar el coeficiente de convección.	113
7.5	Diagrama del dominio considerado en el modelo matemático.	114
7.6	Prueba considerando un tiempo de afectación de 55 s.	114
7.7	Prueba considerando un tiempo de afectación de 55 s.	115
7.8	Prueba considerando un tiempo de afectación de 180 s.	115
7.9	Prueba considerando un tiempo de afectación de 180 s.	116
8.1	Comparación de valores simulados y experimentales de la temperatura del suelo.	121
8.2	Temperatura del suelo medida y simulada con velocidad de 1.3 m/s, 4.1 m/s, 6.5 m/s.	123
8.3	Recta de ajuste entre datos experimentales y simulados durante la afectación térmica del suelo.	125

Lista de tablas.

1.1	Usos directos de la geotermia y porcentaje de aplicación en el mundo……	1
2.1	Conductividad y difusividad térmica del suelo como función del porcentaje de saturación de agua. ……	16
2.2	Densidad aparente y real de las tres muestras de suelo. ……	16
2.3	Microporosidad de las tres muestras de suelo. ……	16
2.4	Valores de la función de mérito de los diferentes modelos. ……	19
3.1	Resumen de los resultados de las pruebas realizadas. ……	34
4.1	Resumen de las temperaturas y configuraciones de EAHE de los trabajos citados……	41
4.2	Profundidad en metros de los pozos. ……	44
4.3	Velocidad del aire, potencia consumida y días de experimentación. ……	46
4.4	Temperatura promedio del aire a la entrada y salida del UEHE. ……	49
4.5	Temperatura promedio a la entrada y salida de cada pozo. ……	52
4.6	Temperatura inicial y diferencia de temperatura en el suelo. ……	54
4.7	Potencia de enfriamiento, efectividad, COP y hora pico de funcionamiento. ……	57
5.1	Espesor y propiedades termo físicas del pozo “LP2”. ……	69
5.2	Datos utilizados para la validación del modelo matemático. ……	75
5.3	Temperaturas reportadas y simuladas para la validación. ……	75
5.4	Difusividad térmica y espesor de cada capa del pozo “LP2”. ……	76
5.5	Potencia térmica de cada generador y temperatura de generación. ……	77
5.6	Parámetros utilizados en el modelo matemático. ……	78
5.7	Valores utilizados en las simulaciones de las figuras 5.7 – 5.11. ……	80
5.8	Valores de las últimas ocho simulaciones. ……	82
6.1	Datos del pozo “PR2”. ……	95
6.2	Valores considerados para la simulación del pozo geotérmico. ……	100
7.1	Posición de los termopares. ……	112
7.2	Desviación estándar y promedio de los parámetros utilizados en las simulaciones. ……	112
7.3	Valores de la función de mérito entre el modelo actualizado. ……	117
7.4	Valores de la función de mérito entre el modelo original. ……	117
8.1	Función de mérito de los distintos modelos para diferentes profundidades. ……	120
8.2	Temperatura simulada y medida para las diferentes profundidades. ……	121
8.3	Datos utilizados para la validación del modelo numérico. ……	121
8.4	Coeficientes de correlación en función de la velocidad del fluido. ……	123
8.5	Función de mérito del modelo original y el modelo mejorado. ……	124
8.6	Coeficiente de determinación y función de mérito. ……	125

Nomenclatura.

e:	Error relativo
EAHE:	Earth to Air Heat Exchanger (intercambiador de calor aire tierra)
GSHP:	Ground Source Heat Pump (bomba de calor geotérmica)
HE-ACS:	Half-Effect Absorption Cooling System (SRA de medio efecto)
M:	Función de Mérito
R^2**:**	Coeficiente de Determinación
SRA:	Sistema de Refrigeración por Absorción
TCS:	Temperatura Constante del Suelo
TEF:	Temperatura Estabilizada de Formación
UEHE:	“U” type Earth Heat Exchanger (intercambiador de calor enterrado tipo “U”)

Capítulo I. "Introducción"

Introducción.

El aprovechamiento de la energía geotérmica por parte de la humanidad comenzó desde su propio inicio. Algunos ejemplos que revelan la amplia relación entre la humanidad y la energía geotérmica son las cuevas y los sitios con aguas termales [Stober, 2013]. Mientras que las grutas, cuevas o cavernas funcionaron como hogares para la especie *Homo sapiens* durante la era paleolítica, los romanos construyeron baños públicos como lugares de esparcimiento en el siglo V a.C. para aprovechar las aguas termales de la zona volcánica de los Apeninos. En la actualidad, según el tipo de aprovechamiento de la energía geotérmica, se divide entre usos directos e indirectos. Los usos indirectos de la geotermia son aquellos en los que se transforma la energía geotérmica en energía eléctrica en plantas geo-termoeléctricas. Hasta el 2020, alrededor del mundo se tenía una capacidad instalada en plantas geo-termoeléctricas de 15.6 GWe [Huttrer, 2020]. En cuanto a los usos directos de la energía geotérmica, sus aplicaciones son más variadas. Hasta el año 2020 se tenía reportado que 88 países hacían uso directo de la energía geotérmica con una capacidad térmica instalada equivalente a 105.2 GWt [Lund & Toth 2021]. En la Tabla 1.1 se desglosa el porcentaje de las distintas tecnologías con las que se aprovecha de manera directa la energía geotérmica alrededor del mundo.

Tabla 1.1. Se muestran los usos directos de la geotermia y su porcentaje de aplicación alrededor del mundo. Con datos de [Lund & Toth, 2021].

Tecnología	(%)
Bombas de calor geotérmicas (GSHP)	58.8
Balneología	18
Calefacción de espacios	16
Acondicionamiento de invernaderos	3.5
Aplicaciones Industriales	1.6
Acuacultura	1.3
Secado de alimentos	0.4
Derretimiento de nieve	0.2
Otros	0.2

Como se observa en la Tabla 1.1, las bombas de calor geotérmicas (GSHP por sus siglas en inglés) son la tecnología más utilizada para aprovechar de manera directa la energía geotérmica, abarcando más de la mitad de las aplicaciones a nivel mundial. Esto es posible ya que a una profundidad entre 2 y 7 metros la temperatura de la tierra alcanza un valor semi constante que no cambia en más de 1°C a lo largo del año debido a fenómenos meteorológicos [Peretti et al., 2013]. A este valor de temperatura semi constante lo llamaremos como temperatura constante del subsuelo (TCS). Esta característica del suelo favorece la implementación de las GSHP a lo largo del mundo, ya que no es necesario contar con recursos geotérmicos de alta temperatura en las cercanías del sitio de instalación. Las GSHP abarcan una gran variedad de dispositivos que tienen como fin aprovechar el suelo en forma de sumidero o fuente de calor. La tecnología de las GSHP presentó un aumento de 26.6 GWt en el periodo 2015 – 2020. Los países líderes en instalación y uso de bombas de calor geotérmicas son: China (25.8 GWt), Estados Unidos (19.8 GWt), Suecia (6.5 GWt), Alemania (4.3

GWt), y Finlandia (2.2 GWt). Es importante recalcar que en estos países el uso de GSHP se encamina a la calefacción de habitaciones y oficinas debido a las bajas temperaturas que se experimentan en algunas zonas.

En la Imagen 1.1 se muestra un esquema general de un equipo GSHP en su funcionamiento como calefacción y como aire acondicionado, respectivamente. En estos equipos el suelo funciona como fuente o sumidero de calor dependiendo de la temperatura ambiental, además de que cuentan con un compresor y una válvula de expansión, como en los equipos de refrigeración convencionales. El fluido de trabajo en las GSHP circula por circuitos cerrados, y es una mezcla de un refrigerante (comúnmente R410A) y agua, y cuya función es transportar la energía entre el suelo y el espacio que se desea climatizar [Noman, 2022]. A diferencia de los las GSHP, los intercambiadores de calor tierra-aire (EAHE por sus siglas en inglés) tienen como fluido de trabajo al aire. Mientras las GSHP tienen un mejor funcionamiento en climas con bajas temperaturas, los EAHE se utilizan en zonas con temperaturas cálidas donde se desea disminuir la temperatura al interior de estancias. Los EAHE tienen un principio de funcionamiento similar a las GSHP, con la principal diferencia de que los EAHE no cuentan con sistema de compresión y expansión, por lo que la transferencia de energía entre la habitación y el suelo se da de manera directa con el aire. Omitir el compresor y válvula de expansión en el circuito de los EAHE y sustituirlo por un ventilador o extractor de aire, da como resultado un menor costo de instalación. A esto se suma que los tubos con los que se hace el arreglo de intercambiadores de calor son generalmente de PVC, ya que esto no influye en el rendimiento de los EAHE [Sakhri et al., 2020] [Rosa et al., 2020].

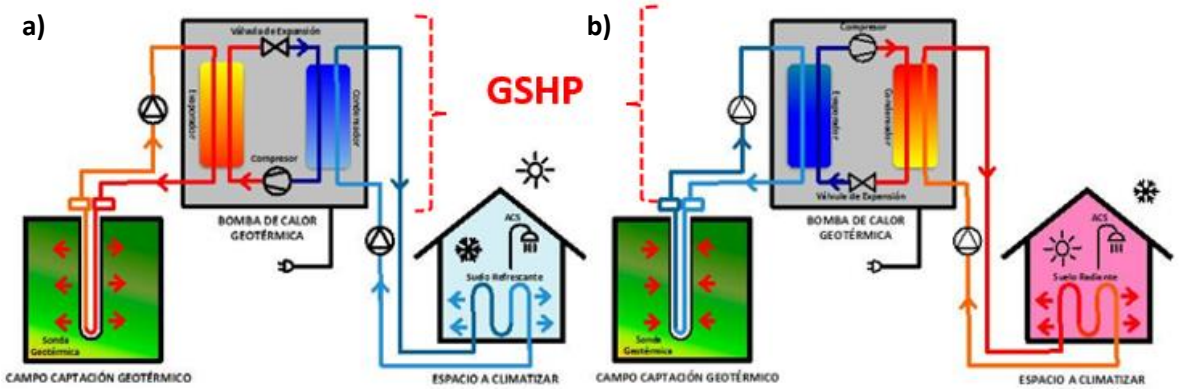

Imagen 1.1. Las imágenes muestran un esquema de GSHP durante su operación como: a) calefacción, b) acondicionamiento. [Geotermia Vertical, s.f.]

Dentro de los parámetros que si influyen en el rendimiento de un EAHE tenemos las características del aire como la velocidad al interior de los tubos, la humedad del aire y la temperatura ambiental [Zajch et al., 2020] [Cuny et al., 2020]. Algunos parámetros relacionados con la tubería que influyen en la temperatura de salida son el diámetro, la longitud total del intercambiador de calor y la presencia de aislante térmico en las tuberías [Amanowicz L. 2018] [Xaman et al., 2014]. Por último, las características del suelo más importantes son el tipo de suelo, sus propiedades termo – físicas, el gradiente geotérmico, la TCS, la porosidad, entre otros [Domingues et al., 2021] [Li et al., 2019].

Los EAHE se pueden clasificar en arreglos horizontales o verticales dependiendo de la instalación y de la zona del intercambiador de calor donde se realiza la mayor transferencia de energía con el suelo [Hou et al., 2022]. Los arreglos horizontales presentan la ventaja de estar en contacto con una temperatura semi constante en la mayor parte de su trayectoria, aunque para conseguir una temperatura por debajo de 21 °C, la excavación debe ser de mayor profundidad, además de que ocupan una mayor área de instalación [Tasdelen & Dagtekin, 2022]. En contraparte, los arreglos verticales están en contacto con un gradiente geotérmico en la mayor parte de su trayectoria, donde las temperaturas menores y cercanas a la TCS se alcanzan a partir de una profundidad de 3 metros, al mismo tiempo que el área utilizada para la instalación es menor en comparación con los arreglos horizontales [Liu et al., 2019]. La clasificación de los EAHE también considera la manera en que los intercambiadores de calor se encuentran conectados con tubos colindantes, ya sea en serie o en paralelo [Darius et al., 2017]. En la Imagen 1.2 y 1.3 se muestra un esquema de EAHE con arreglo horizontal y vertical conectados en serie y en paralelo, respectivamente.

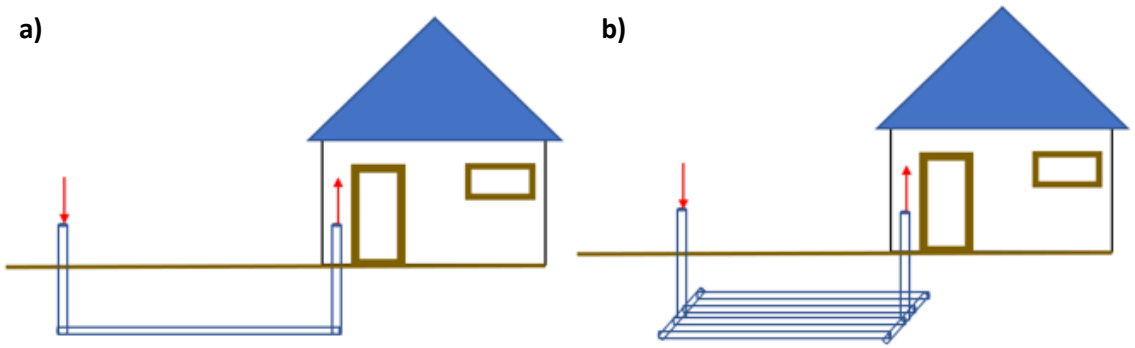

Imagen 1.2.En las imágenes de muestran sistemas EAHE de configuración horizontal con conexión: a) en serie, b) en paralelo [Elaboración propia].

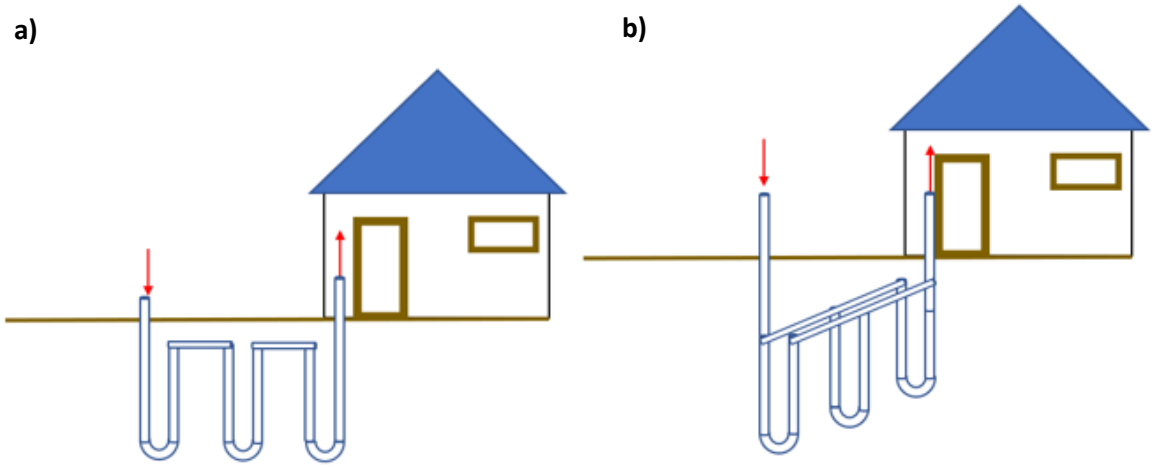

Imagen 1.3. En las imágenes de muestran sistemas EAHE de configuración vertical con conexión: a) en serie, b) en paralelo [Elaboración propia].

México cuenta con un largo historial en el aprovechamiento de los recursos geotérmicos, ya que el 20 de noviembre de 1959 se inauguró en el estado de Hidalgo la primera planta de generación eléctrica en un campo geotérmico en el continente americano [DiPippo, 2022]. Desde esa fecha, y a pesar de la gran cantidad de recursos geotérmicos en el país, el aprovechamiento de la energía

geotérmica se da casi exclusivamente para la producción de energía eléctrica en plantas geo-termoeléctricas. Hasta el año 2022, en el país existen 5 campos geotérmicos en operación: Cerro Prieto, Los Azufres, Los Humeros, Las Tres Vírgenes, y Domo San Pedro, con una capacidad instalada de 1005.8 MWe [Gutiérrez-Negrín, 2020]. El uso de tecnologías para aprovechar de manera directa la energía geotérmica en México se reducen prácticamente a la balneología, y en menor medida, al secado de alimentos y maderas (156.1 MWt). Se estima que para el 2030 esta cantidad llegue a 3800 MWt, de los cuales 63% provendrá de uso en cascada en campos geotérmicos [Gutiérrez-Negrín, 2020].

En México, a lo largo de la última década, se ha comenzado con la investigación de esta tecnología para acoplarla a las características y necesidades del país. Existen estudios publicados en la literatura científica donde se investiga el uso de EAHE para la climatización de espacios en distintos estados de la república mexicana como: Chihuahua, Ciudad de México, Guanajuato, Hidalgo, Nuevo León, Quintana Roo, Sonora, Tabasco y Yucatán. El objetivo de las investigaciones es variado y abarca: **a)** Evaluación numérica del funcionamiento del EAHE bajo distintas condiciones climatológicas [Xamán, 2015] [Rodríguez-Vázquez, 2020] [Ramírez-Dávila, 2014] [Rodríguez-Vázquez, 2018]. **b)** Análisis del efecto del aislante térmico en EAHE [Xamán, 2014]. **c)** Estudio sobre la profundidad de instalación de EAHE [Becerra, 2022]. **d)** EAHE acoplados con sistemas de paneles fotovoltaicos [Maytorena, 2023]. **e)** Comparación tecno – económica con sistemas convencionales de climatización [Díaz-Hernández, 2020].

El atraso en investigación y desarrollo tecnológico de EAHE en México obedece principalmente al hecho de que, a excepción de los estados del norte del país (clima semiárido - cálido), el país gozaba de un clima templado - subhúmedo durante la mayor parte del año. No obstante, es cada vez más frecuente alcanzar marcas históricas de temperaturas altas, lo que se traduce en problemas ambientales, económicos y de salud [Tereshchenko & Filonov, 2001] [Burke et al., 2018] [Thornton, 2014]. Una forma de poder contribuir a la mitigación de emisiones de gases de efecto invernadero es implementando la tecnología de EAHE. Entre las principales dificultades para el uso de esta tecnología en el país encontramos que para poder implementar un sistema de EAHE es necesario el uso y manejo de software especializado, que la gran mayoría de las veces es cara y fuera del alcance de la mayoría de las personas interesadas en implementar esta tecnología [Zhao et al., 2019]. Otro inconveniente que presentan los softwares comerciales es la limitación sobre el trabajo que se puede hacer en ellos, ya que la mayoría de las ocasiones se utiliza como herramienta de análisis en EAHE [Bisoniya, 2015]. Para atender la problemática mostrada anteriormente, en este trabajo se muestra el desarrollo de un simulador numérico para determinar condiciones térmicas de trabajo de intercambiadoras de calor aire – tierra, además de la validación numérica y experimental del mismo.

Planteamiento del problema.

El adecuado dimensionamiento y evaluación de un EAHE es de vital importancia si se quiere aprovechar de manera eficiente la energía geotérmica de baja temperatura para climatizar espacios cerrados [Benhammou & Draoui, 2015]. Para ello, es necesario tomar en cuenta los parámetros de funcionamiento mostrados en la sección anterior con el objetivo de acoplar esta tecnología a los requerimientos y características del sitio específico. Al hacerlo, se podrá contribuir con la reducción de emisiones de gases de efecto invernadero y el consecuente cambio climático, ya que hasta un

40% de la energía que se consume en zonas urbanas corresponde a equipos de calefacción y de aire acondicionado [Pérez-Lombard et al., 2008].

En la actualidad existen herramientas como TRNSYS o EnergyPlus que se utilizan para analizar y modelar sistemas ingenieriles con base en métodos numéricos computacionales aplicados a dinámica de fluidos (CFD por sus siglas en inglés) [Hollmuller & Lachal, 2001] [Lee & Strand, 2006]. En ellos se discretiza el dominio de estudio en pequeños volúmenes de control donde posteriormente se resuelven las ecuaciones que dominan el fenómeno físico en estudio. Con estas herramientas se puede evaluar y tener una idea del funcionamiento real de un sistema EAHE en menor tiempo y con una reducción considerable de costos en comparación con un análisis experimental [Kanaris et al., 2006] [Wang et al., 2007]. Debido a esto, el uso de una herramienta numérica para determinar las condiciones térmicas de trabajo de EAHE es necesaria en las primeras fases de diseño.

Algunas desventajas de las herramientas de CFD comerciales como las que se expusieron previamente surgen del hecho de ser productos que permiten un manejo limitado de sus características (no son de código libre), además de que se requiere una licencia de uso que, por lo regular, tiene un costo alto y requiere personal calificado con dominio en el tema. Otra característica que juega en contra de estos softwares es que no fueron diseñados para evaluar o dimensionar equipos EAHE. Debido a ello, se omiten factores que modifican el comportamiento de estos sistemas de climatización. Por último, el principio de funcionamiento con los que trabajan estos softwares está basado en CFD, por lo que puede ser replicado tomando algunas consideraciones que dependen del alcance del estudio en turno [Bisoniya, 2015] [Muehleisen, 2012] [De Paepe & Janssens, 2003].

Por lo anteriormente expuesto, un modelo numérico capaz de determinar las condiciones térmicas de trabajo de EAHE sería una gran herramienta para poder aprovechar los recursos geotérmicos de baja temperatura en el país. Este modelo numérico debe de atender los problemas mostrados en esta sección, además de ser validado contra datos numéricos y experimentales.

Justificación.

En la actualidad, la mayoría de los sistemas utilizados para la climatización de espacios tienen un alto consumo de energía, lo cual contribuye a la emisión de gases de efecto invernadero. Los equipos de aire acondicionado utilizan hasta un 31% de la electricidad en las casas, mientras que los sistemas de calefacción (eléctricos o a gas) ya consumen en promedio más de 2500 kWh/per cápita en países en vía de desarrollo [Kusiak et al., 2010] [Balaras et al., 2005]. Para contrarrestar este problema, el diseño bioclimático y los sistemas de climatización que aprovechan las energías renovables se muestran como una gran alternativa para controlar los efectos adversos del aumento poblacional [De Assis & Frota, 1999].

Dentro de los sistemas de climatización que han recibido mayor atención durante las últimas décadas se encuentran aquellos que aprovechan el suelo como fuente o sumidero de calor utilizando intercambiadores de calor enterrados. En este rubro se pueden identificar dos grupos, aquellos que utilizan aire como fluido de trabajo (EAHE), y los que utilizan una mezcla de agua y refrigerante (GSHP). Algunas ventajas que se han estudiado de estos sistemas son: **a)** las distintas aplicaciones en el la industria, agricultura y hogar **b)** la posibilidad de instalarlos en cualquier lugar ya que no dependen de la presencia de fuentes geotérmicas de alta temperatura, **c)** la capacidad de

adaptarse al sitio de instalación debido a que se presentan en configuraciones horizontales y verticales, **d)** su aplicación se da en prácticamente cualquier clima, aunque su funcionamiento mejora en climas calurosos y secos, **e)** el consumo de energía es menor comparado con los sistemas convencionales de climatización [Eicker & Vorschulze, 2009]. Todas esas ventajas posicionan a los EAHE como herramientas viables en el ahorro y uso eficiente de la energía. Para el dimensionamiento de estos equipos aún se discuten distintos procedimientos analíticos y numéricos, aunque existe el consenso de que los principales parámetros están relacionados con las características del suelo, las condiciones de trabajo del aire y la configuración del intercambiador de calor [Rodrigues et al., 2015] [Bisoniya, 2015] [Yu et al., 2022].

Conocer las propiedades termo físicas del suelo, así como la TCS del sitio de instalación son de vital importancia en el proceso de dimensionamiento y evaluación de sistemas EAHE ya que el suelo tiene la función de ser fuente o sumidero de calor. Además del valor de temperatura semi constante, es necesario saber con precisión a que profundidad se alcanza esta TCS a fin de poder determinar el gradiente térmico del suelo y la profundidad optima de instalación [Wong & Andaverde, 2010]. Adicionalmente, el conocimiento sobre las condiciones meteorológicas que existen en el sitio de instalación brinda información sobre la temperatura ambiental, que repercute en los perfiles de temperatura del suelo y en las condiciones de trabajo del aire. La configuración geométrica del intercambiador de calor aporta información sobre el diámetro de la tubería, la longitud total del intercambiador de calor, la velocidad del fluido o la presencia de aislante térmico. Al organizar de manera correcta esta información en un modelo numérico, se podría determinar las condiciones térmicas de trabajo del intercambiador de calor. Los datos obtenidos con el modelo numérico deben ser validados. Para ello es importante contar con un sistema de EAHE en operación y funcional que permita la comparación de los datos numéricos y reales.

Objetivos.

General.

Desarrollar un simulador numérico para determinar las condiciones térmicas de trabajo de intercambiadores de calor aire – tierra.

Específicos.

- Analizar la relación entre las condiciones ambientales y la transferencia de calor en el suelo.
- Determinar los mecanismos de transferencia de calor dominantes entre el suelo y el intercambiador de calor enterrado.
- Armar e instalar un dispositivo para medir la temperatura del suelo en función de la profundidad.
- Diseñar y construir un modelo numérico para determinar el perfil de temperaturas del suelo.
- Considerar las limitaciones de espacio y los factores ambientales en el dimensionamiento de intercambiadores de calor aire - tierra.
- Monitorizar y caracterizar un intercambiador de calor aire – tierra para obtener datos experimentales.
- Programar un modelo numérico para determinar las condiciones térmicas de trabajo de intercambiadores de calor aire – tierra.
- Validar experimentalmente el modelo numérico del perfil de temperatura del suelo.

- Validar experimentalmente el modelo numérico de las condiciones térmicas de trabajo de intercambiadores de calor aire – tierra.

Metodología.

El trabajo comenzó con una exhaustiva revisión bibliográfica que se dividió en 5 temas principales: **a)** Estudios sobre los mecanismos de transferencia de calor entre el medio ambiente y el suelo, **b)** Trabajos que integran el diseño, instalación, y evaluación del rendimiento de EAHE, **c)** Review's sobre aplicaciones de EAHE en México y el mundo, **d)** Innovación en tecnologías relacionadas con EAHE, y **e)** Reportes meteorológicos en la zona de experimentación. Con la adecuada revisión bibliográfica se logró delimitar y conocer los alcances del trabajo de investigación.

Durante la revisión bibliográfica se encontró que para estimar los perfiles de temperatura del suelo se generalizaban u omitían algunos parámetros significativos que repercuten en su comportamiento térmico. Para atender este obstáculo, se instaló una sonda de medición en el sitio de experimentación con el objetivo de registrar la temperatura del suelo con distintas condiciones ambientales, a diferentes profundidades y en periodos continuos de tiempo. Al observar y estudiar los registros de temperatura de suelo obtenidos con la sonda de medición, se dio inició con el diseño y elaboración de un modelo numérico que considera los parámetros significativos en el comportamiento térmico del suelo. La validación del simulador se realizó al comparar los resultados numéricos contra datos analíticos y experimentales.

Después de estudiar el perfil de temperatura del suelo, se procedió a delimitar el sitio de instalación de los intercambiadores de calor enterrados, se marcó el sitio de perforación y se realizaron las excavaciones necesarias. Durante el proceso de excavación se tomaron muestras del suelo, las cuales sirvieron para conocer las propiedades termo físicas de interés en el tema de estudio. La instrumentación de los intercambiadoras de calor se realizó durante su ensamblaje con la colocación de termopares en la parte interna y externa de los tubos. Se realizaron pruebas para detectar fugas en el interior de los tubos y se procedió a enterrarlos.

En el transcurso de la experimentación se modificaron distintos parámetros que intervienen en el rendimiento del EAHE. Además de que se tomaron registros continuos de temperatura al interior de los tubos y al exterior en la tierra, se midió la velocidad del aire a la salida del intercambiador y se registró la potencia consumida por el impulsor de aire. Con esta información se evaluó térmicamente a los intercambiadores de calor. Al mismo tiempo, se trabajó en el diseño y construcción del modelo numérico para simular el proceso de transferencia de calor ente el aire y el suelo. En un comienzo, el modelo se validó contra datos publicados por distintos autores de trabajos similares. Posteriormente, la validación del modelo numérico se realizó comparándolo con los datos experimentales obtenidos en el EAHE. De esta manera, al validar ambos modelos numéricos, se dio por concluido el trabajo de investigación.

Estructura de la tesis.

Tomando en cuenta la problemática planteada, así como los objetivos propuestos en este trabajo de investigación, se ha estructurado la tesis de la siguiente forma:

El capítulo I muestra la Introducción al trabajo de investigación. En él se exponen los antecedentes de la energía geotérmica, se muestra su clasificación y aplicaciones, además de la situación de la energía geotérmica en México. Se abre paso a presentar el planteamiento del problema, donde se

exponen algunas limitantes para el aprovechamiento de la energía geotérmica de baja temperatura. Se exponen ventajas y desventajas de herramientas comerciales de CFD, lo que da lugar a la justificación. Posteriormente se fijan el objetivo general y los objetivos específicos para establecer el alcance de la investigación. Por último, se exhibe la metodología seguida para realizar este trabajo.

En el capítulo II se presenta el trabajo "*A new model to predict sub soil thermal profiles based on seasonal rain conditions and soil properties.*" en donde se exhibe la problemática encontrada en la literatura para obtener los perfiles de temperatura del suelo hasta ese momento. Se propone un modelo numérico que considera factores ambientales como las precipitaciones pluviales, así como factores termo físicos del suelo como la difusividad térmica, la porosidad y la permeabilidad. Se delimita el dominio de estudio y se exponen las suposiciones hechas durante el diseño del modelo numérico. Se explica el ensamblaje de la sonda de medición y el alcance que tiene. Se muestran las variables que se consideraron en el estudio y se presenta el modelo matemático. En esta parte se presentan las ecuaciones dominantes, las condiciones iniciales y de frontera, así como la discretización del dominio y la interacción entre nodos. Por último, se presentan los resultados de la validación del modelo numérico.

En el capítulo III se muestra el trabajo "*Application of distinct configurations of vertical earth-to-air heat exchangers for the warm weather population of Temixco, Morelos (Mexico).*" donde se presenta el dispositivo experimental de EAHE utilizado en este trabajo. Se indica el sitio de experimentación donde se incluye una breve descripción de las características del suelo, así como las especificaciones de cada pozo. Se muestran los equipos y herramientas utilizados durante la perforación, la instalación, y la operación de los sistemas. Sobre los EAHE, se expone la configuración y las medidas de cada uno de ellos, al igual que la distribución de termopares al interior y exterior de los tubos. Por último, se presentan algunos resultados de las primeras pruebas realizadas en los EAHE, donde se mide la diferencia de temperatura entre la entrada y la salida, además de la afectación térmica del suelo.

En el capítulo IV se expone el trabajo "*Experimental evaluation of a "U" type earth-to-air heat exchanger planned for a narrow installation space in warm climatic conditions.*" donde se realiza una evaluación experimental del sistema EAHE que tiene como objetivo reducir la temperatura de una oficina durante la época más calurosa. Se realiza una revisión bibliográfica sobre distintos trabajos experimentales donde se evalúan y estudian distintos sistemas EAHE, tanto horizontales como verticales. Se presentan las condiciones climatológicas presentes durante la experimentación y la ubicación del EAHE, junto con las medidas y la carga térmica de la oficina. Se expone la profundidad y separación entre pozos, la configuración geométrica del EAHE, las condiciones en las que se realizaron los experimentos, y las ecuaciones utilizadas para la evaluación del equipo. Por último, se presenta la evaluación experimental realizada junto con las conclusiones del trabajo.

El capítulo V trata sobre el trabajo "*Operational proposal of "U" type earth heat exchanger harnessing a non-producing well for energy supply to an absorption cooling system. Approach with "La Primavera" geothermal field data.*" en el que se expone el modelo numérico desarrollado para determinar las condiciones térmicas de trabajo de intercambiadores de calor enterrados. El trabajo se orientó para extraer energía de pozos abandonados instalando EAHE, por lo que se realizó una revisión bibliográfica sobre aplicaciones hibridas de estos sistemas. Se presentan algunas

características del campo geotérmico como la litología, profundidad de pozos perforados y el gradiente geotérmico estimado, además del sistema de refrigeración por absorción (SRA) propuesto. Al exponer el modelo numérico se presenta el dominio de estudio, las suposiciones hechas en el diseño, las ecuaciones consideradas y la discretización del dominio. También se presenta una validación que se realizó tomando datos publicados de dos trabajos independientes. En la sección de resultados se presentan distintas propuestas de intercambiadores de calor que se obtuvieron con el modelo numérico.

En el capítulo VI se presenta el artículo "*Cooling potential for single and advanced absorption cooling systems in a geothermal field in Mexico.*" En este trabajo se expone una aplicación del modelo numérico presentado en el capítulo anterior con objetivo de proponer un sistema EAHE. El sistema de intercambiadores de calor enterrados tiene el objetivo de suministrar energía a distintos procesos de SRA. Se muestran los distintos sistemas de refrigeración y sus características, junto con la localización y detalles del campo geotérmico. Se explica el análisis de la transferencia de calor en el intercambiador de calor y las suposiciones del modelo matemático. Se calcula el gradiente geotérmico, se exponen los parámetros en cada simulación y se explican los resultados.

El capítulo VII muestra el trabajo titulado "*A new model to determine thermal disturbance and recovery processes during wellbore drilling: Experimental validation with scaled-down wellbore prototype.*" En este artículo se expone la mejora de un modelo numérico utilizado para simular la afectación térmica del suelo ocurrida durante la perforación de pozos. Este mismo modelo numérico se utilizó para conocer la afectación térmica del suelo alrededor de los tubos enterrados del EAHE. En el trabajo se presenta el modelo matemático, el dominio de estudio, las suposiciones hechas durante el diseño, las condiciones iniciales, las condiciones de frontera y las ecuaciones gobernantes. En los resultados se presenta la validación del modelo contra datos experimentales de un modelo a escala.

En el capítulo VIII se presenta la validación experimental del modelo numérico para determinar las condiciones térmicas de trabajo de los intercambiadoras de calor. Se resume la validación del modelo contra datos publicados y se justifica la serie de datos experimentales que se utilizaron. Se calcula el perfil de temperatura del suelo utilizando el modelo numérico presentado en el capítulo II. Se exponen los datos experimentales y el resultado de las simulaciones numéricas. Por último, se muestra el resultado de la validación utilizando distintas métricas estadísticas.

En el capítulo IX se presentan las conclusiones de este trabajo de tesis en términos de los objetivos alcanzados, así como las sugerencias y recomendaciones para trabajos futuros en esta misma línea de investigación.

Capítulo II. “Perfil de temperatura del suelo”

Resumen.

En el trabajo [Molina-Rodea & Wong-Loya, 2021] se da una introducción explicando que la TCS y los perfiles de temperatura del suelo han sido temas estudiados por varias décadas ya que son de gran importancia cuando se quiere aprovechar de manera directa la energía geotérmica. Sus aplicaciones van desde estaciones de tren subterráneas y baños termales, hasta el diseño de EAHE. Para conocer los perfiles de temperatura y la TCS, en un inicio se tomaban mediciones de temperatura por periodos de hasta 3 años. A mediados del siglo XX se desarrollaron soluciones numéricas con series de Fourier para la ecuación de condición de calor. Estas soluciones, aunque han sido utilizadas por bastantes años, difícilmente reproducen perfiles de temperatura reales debido a que no toman en consideración condiciones climatológicas como la lluvia, ni características puntuales del suelo como el tipo de recubrimiento, la porosidad o la permeabilidad. Para atender este problema, en este trabajo se muestra el desarrollo de un modelo numérico capaz de representar adecuadamente el comportamiento térmico del suelo a distintas profundidades, tomando en cuenta factores ambientales como la lluvia y algunas propiedades termo físicas del suelo. El modelo numérico muestra que se pueden conseguir resultados más realistas tomando en cuenta el tipo de suelo, la temperatura ambiental y la lluvia en el sitio. La validación del modelo numérico se realiza al comparar los datos obtenidos con el simulador frente a datos experimentales obtenidos de una sonda de medición. Además, se comparan los resultados contra el modelo analítico utilizado en la mayoría de los trabajos publicados.

En la metodología se define el dominio de estudio, comprendido por la superficie del suelo y la tierra por debajo del él. A continuación, se definen las propiedades del suelo que se tomaron en consideración, que son: difusividad térmica, conductividad térmica, porosidad y permeabilidad. Con las propiedades y el domino de estudio establecidos, se presentan y justifican las suposiciones hechas en el diseño del modelo numérico. El siguiente paso consiste en presentar el dispositivo experimental para medir la temperatura del suelo. Por último, se muestra el modelo matemático junto con las ecuaciones para las condiciones iniciales, de frontera y la interacción entre nodos vecinos. El modelo numérico se presentó en dos partes, primero como un modelo parcial y posteriormente como un modelo completo. En la sección se resultados se expone que el modelo matemático desarrollado es capaz de representar hasta un 80% mejor los perfiles de temperatura comparados con la solución analítica utilizada frecuentemente. Este valor se obtuvo al comparar la función de mérito del modelo analítico contra el modelo parcial y el modelo completo. La función de mérito es una medida de calidad cuantitativa entre datos observados y datos simulados.

Publicación.

Geothermics 97 (2021) 102261

Contents lists available at ScienceDirect

Geothermics

journal homepage: www.elsevier.com/locate/geothermics

A new model to predict subsoil-thermal profiles based on seasonal rain conditions and soil properties

R. Molina-Rodea [a], J.A. Wong-Loya [a,b,*]

[a] Instituto de Energías Renovables, Universidad Nacional Autónoma de México, Priv. Xochicalco s/n, Col. Centro, Temixco, Morelos 62580, México
[b] Colegio de Ciencias y Humanidades, Plantel Vallejo, Universidad Nacional Autónoma de México, Av. Cien Metros s/n, Col. Magdalena de las Salinas, Distrito Federal 07760, México

ARTICLE INFO

Keywords:
Weather conditions
Heat transfer
Soil porosity
Soil permeability

ABSTRACT

In the present work, a novel way to simulate the soil temperature profiles is developed. Soil temperature profiles are essential to know the Stabilized Temperature (ST). In topics related to low depth geothermal energy, sustainable building, renewable energies, and energy efficiency is essential to know both soil temperature profiles and the ST in the design phase. The first way to predict soil temperature profiles was by solving the heat conduction equation by Fourier series. The main problem with the analytical solution is the environmental factors. By omitting these conditions, results agree only with some regions where environmental conditions have less influence on the subsoil temperature. The presented simulator allows using variables used in the analytical solution, likewise environmental factors like relative humidity and rain duration. Besides, the change of thermophysical properties along the year is considered. The results of the simulator are compared against experimental data *in situ* and the analytical solution used previously. The comparison results point out that the new simulator reproduces up to 80% better the soil temperature profiles than the analytical solution by Fourier series.

1. Introduction

The interest in knowing the subsoil temperature variation, and the depth at which the Stabilized Temperature (ST) is found, has been studied for several decades. In topics related to low enthalpy geothermal energy and their direct uses, it is important to know these temperature profiles and the ST value and its depth. Among the different applications in geothermal engineering that take advantage of the knowledge of these profiles is the proper design of earth-air heat exchangers (EAHE) (Kayaci and Demir, 2018) for calculations of heat losses of buildings to the ground (Popiel et al., 2001), underground subway stations (Wong-Loya et al., 2011), greenhouses (Lund and Toth, 2020), and thermal baths (Morales et al., 2021). Initially, it was done by taking soil temperature data over long periods, up to 3 years (Fluker, 1958; Kristensen 1959; Penrod et al., 1960). Subsequently, they tried to make programs and simulators to predict the behavior of the soil throughout the year, but due to the technological limitations of that time, it was decided to solve the one-dimensional heat conduction equation from the development of numerical solutions with Fourier series (Carson, 1963; Kusuda and Achenbach, 1965). Those solutions just included parameters such as the annual average temperature, amplitude of the soil temperature, and the soil's thermophysical properties. Other omitted variables have been included in the analysis over time. Furthermore, it is important to mention that theoretical models hardly reproduce real profiles (Naranjo-Mendoza et al., 2018). Causes of distorted results are buildings, weather conditions, or soil-cover characteristics (Sliwa et al., 2019).

Thermal behavior on the soil surface depends mainly on the type of soil cover and the weather conditions. Therefore, the temperature profiles that are generated below the soil surface will depend on the surface conditions. On this subject, Mihalakakou et al. (1992) analyzed temperature measurements recorded by the Athens National Observatory over 74 years and proposed a model to predict daily surface temperature variation. Their study found that, depending on the site's specific characteristics (with or without grass), differences of up to 8 °C are possible in the soil surface during the hottest months and differences of 2.5 °C for ST. Popiel et al. (2001) conducted a 2-year experiment in which they took temperature measurements at two sites in Poznan, Poland. The first was under an outdoors surface (car parking), and the second was under a grassy surface. When analyzing the data obtained, they observed that in the surface area (up to a depth of 1 m), the

* Corresponding author at: Instituto de Energías Renovables, Universidad Nacional Autónoma de México, Priv. Xochicalco s/n, Col. Centro, Temixco, Morelos 62580, México.
E-mail address: jawol@ier.unam.mx (J.A. Wong-Loya).

https://doi.org/10.1016/j.geothermics.2021.102261
Received 24 June 2021; Received in revised form 20 August 2021; Accepted 13 September 2021
Available online 23 September 2021

temperature difference during the summer was 4 °C greater for the uncovered surface compared to the surface covered with grass. Several other authors agree that the conditions present on the soil surface have a significant impact on the temperature of the surface and below the soil, finding cases of differences of up to 20 °C (Asghar et al., 1990; Bansal et al., 1983; Jayashankar et al., 1989; Nassar et al., 2006).

On the other hand, based on weather conditions, Mihalakakou et al. (1997), developed a model to predict soil surface temperature by comparing their results with data measured in 2 European cities. During their study, they observed that most of the previously published works did not consider some important factors such as the weather conditions of the environment. One of these important variables was rainfall since its effect on the temperature of the soil surface causes changes of up to 4 °C.

Hu et al. (2016) carried out extensive research on numerical and analytical work to obtain the soil temperature profile. In their study, they found that several of the works published up to that time omit the effect of water on the soil and that this leads to inaccuracies when calculating soil temperature during the day and at night (Carson, 1963; Gao et al., 2004; Huang et al., 2014; Kahan et al., 2006;Kusuda, 1975). Besides, they indicated that the duration of rainfall affects the thermo-physical properties of the soil, changing the soil temperature profiles. One of the soil properties most affected by rain and soil moisture is the thermal diffusivity, disturbing soil thermal profiles (Arias--Penas et al., 2015; Horvath et al., 2012; Jiang et al., 2015). The thermal diffusivity has a stark dependence on soil moisture (Agrawal et al., 2018; Ascione et al., 2011; Bansal et al., 2013; Mathur et al., 2015; Misra et al., 1995, 2015).

Damodharan et al. (2020) performed simulations with commercial software to predict the performance of an EAHE system. In their work, they mention that most of the published works are not supported experimentally. Also, they indicate that it is necessary to take temperature measurements of the site to find the depth at which the temperature remains constant throughout the year, despite using mathematical models.

The work presented here shows the development of a numerical simulator capable of adequately representing the soil's thermal behavior at different depths, allowing for environmental variables and soil properties. The numerical simulation shows that more realistic results can be produced by considering variables such as soil type, environmental temperatures, and rainfall at a site.

In this work, the authors calculate and account for the soil's porosity and permeability. These properties depend on the relative humidity of the environment. With these data, numerical simulations were carried out that reproduce the thermal behavior of the soil. To validate the model, the authors compare the data obtained by the simulator against experimental data obtained from a measurement probe installed in Morelos, Mexico. Likewise, they compare the results against the analytical model used in most of the published works to know the temperature of the subsoil. The model describes the thermal behavior of the subsoil throughout the year.

2. Material and methods

This section presents the parameters that were considered when designing the numerical simulator, the assumptions made during the design, the experimental development, the weather conditions, soil properties, and the mathematical model.

The model developed for this simulator allows estimate temperature distribution as a function of the environmental conditions and soil's physical properties. The study domain comprises the soil surface and the subsoil underneath. The soil heat transfer is due to the temperature difference between the ambient temperature at the soil surface and the ST, which is found at a depth that varies in each region (Carson, 1963). This heat transfer produces distinct temperature profiles in the subsoil, which change over time.

The temperature profiles that occur in the lower layers of the soil take different values depending on the ambient temperature on the surface and the weather conditions that arise, such as rain. Rainfall directly affects the heat transfer mechanism due to the change in soil properties, among which the thermal diffusivity, thermal conductivity, porosity, and permeability of the soil stand out.

Due to the above, the assumptions made for the present model are the following:

(1) The problem will be addressed in a one-dimensional way.
(2) The domain is represented as a purely conductive medium.
(3) The study domain is 10 m, which begins to be measured from the soil surface in the vertical direction of depth, and in turn, divided into 2 subdomains.
(4) The first subdomain is represented by an irregular mesh while the second is represented by a regular mesh.
(5) In the first subdomain there are nodes to represent the porosity of the soil.
(6) Thermal diffusivity varies due to the presence of rainfall, and the change in its value depends on permeability.
(7) The surface temperature is the same as the ambient temperature.
(8) The temperature at the lower limit of the domain is equal to the ST.

Assumption 1 was made due to the length and characteristics of the soil since the radial temperature gradients are smaller compared to the axial temperature gradients. Therefore, the dominant direction for heat transfer is in the vertical direction. Assumption 2 and 7 are taken from different works already published (Carson, 1963; Carson and Moses, 1963; Mihalakakou et al., 1992, 1997; Rey-Ronco et al., 2020).

For assumption 3, the lower limit of the domain was set at 10 m-depth since several studies have shown that the depth at which the ST is found is at that depth, or less (Bansal et al., 2012, 2013; Belloufi et al., 2017; Bordoloiet al., 2018; Breesch et al., 2005; Khalajzadeh et al., 2012; Kharbouch et al., 2018; Nethra and Kalidasan, 2021; Patel and Mishra, 2019; Rosa et al., 2020). In addition, a study was conducted to observe if the change in the depth of the lower limit generated any effect on the results, something that will be discussed in Section 2.3. Although the lower boundary condition was established at 10 m-depth, it should be clarified that most of the thermal kinetics occurs in the first meters of depth, as will be shown in Section 3.

2.1. Experimental data

The measurement probe from which the data for the experimental validation of the numerical simulator was obtained was installed in December 2018 at the facilities of the Institute of Renewable Energies (National Autonomous University of Mexico) under a short-grassy surface, and close to vegetation. It should be said that the soil of the site where the measurement probe was installed is of the filling and compaction type, since at the time of the excavation for installation, various fragments of foundations and wall backs were found. Data recording began in January 2019.

The probe is constituted by a PVC tube 2.54 cm in diameter and 1.8 m long, with a total of 27 thermocouples distributed in 9 groups of 3 thermocouples each. Each group of thermocouples is separated by 20 cm from each other; therefore, the last group is 1.8 m deep. Thermocouples are T type (copper – constantan), made with Omega wire, and accuracy of ±0.1 °C.

Further, in each group of thermocouples, the separation on the perimeter of the pipe is 120° between each thermocouple as shown in Fig. 1. When set in 3 thermocouples each group, the number of measurements is increased at each depth, and the uncertainty of the result decreases. It was thus that the value that was taken from each group of thermocouples was the average of the results. In all average values the standard deviation was among the accuracy limits of the thermocouples.

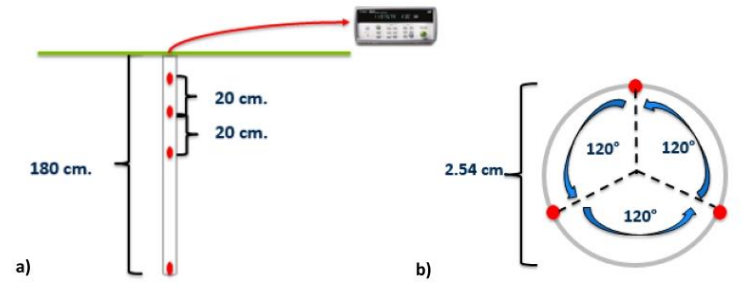

Fig. 1. Scheme of the measurement probe. (a) longitudinal separation of groups of thermocouples, (b) cross-section of the probe, where the radial separation of each group of thermocouples could be observed.

The soil temperature was monitored every 10 min.

2.2. Meteorological data and soil properties

2. 2.1. Relative humidity and environmental temperature

The environmental data used for the numerical simulations were obtained from the ESOLMET-IER meteorological station, which is located inside the Renewable Energies Institute (latitude 18 ◦ 50′25.62″ N, longitude 99 ◦ 14′10.49″ W, altitude 1253 m.a.s.l.) in Temixco, Morelos, Mexico. This solarimetric and meteorological station obtains data with a frequency of 10 min. Later, records can be found on its web page.

From the information available on its website, the meteorological data that it deals with were ambient temperature and relative humidity. Each data was accompanied by the date and time they were registered. The meteorological data of this station were used due to the proximity between the station and the measurement probe with which the experimental validation of the numerical simulator was carried out.

As will be shown in subsequent sections, environmental temperature data was used to define the temperature at the boundary, while relative humidity was the indicator to reveal the presence of rainfall and its duration.

2.2.2. Thermal diffusivity

The thermal diffusivity of the soil at the site where the measurement probe was installed was obtained using the KD2Pro© equipment, which uses the transient line heat source method to estimate thermal conductivity, volumetric specific heat, thermal diffusivity, and thermal resistivity.

Transient thermal diffusivity data as a function of soil water saturation were entered into the simulator when rainfall occurs, starting with a value of 100% and gradually decreasing to 0% until rain happened again. At this moment, the value for thermal diffusivity is reset and returns to 100% saturation. Thus, soil permeability determines the rate of change between thermal diffusivity values.

2.2.3. Porosity

Soil porosity is defined as the space in the soil not occupied by solids, and therefore, it is the space through which water, air, gasses, and nutrients circulate (Ramesh et al., 2019). The amount of porosity that exists in the soil varies significantly according to the type of soil. Thus, soils with a great variety of natural vegetation present a high porosity (up to 50%), while soils used for grazing, cultivation, or open surface have a lower percentage.

The porosity in the soil can be considered constant in the first meters of depth (study domain) and varies drastically only on the surface and at a great depth. The superficial porosity is rapidly reduced when rain occurs since the drops that impact the soil modify and compact the most superficial layers. However, the upper layer has organic residues causing that porosity remains constant during the rain and sometimes after it.

The total porosity of a soil sample (P) can be obtained from Eq. (1), relating the soil's apparent (ρa) and real density (ρr). The apparent density is the quotient between the mass of the sample and its apparent volume (considering the pores between the soil). On the other hand, the real density is the quotient between the mass of the sample and its actual volume (volume excluding the pores).

$$P\ (\%) = \left(1 - \frac{\rho a}{\rho r}\right) \cdot 100 \tag{1}$$

2.2.4. Microporosity

Depending on the size of the pores, those are divided into micropores and macropores. The micropores (storage pores) are less than 0.1 mm in size and retain the water that reaches them against the force of gravity, but the roots of the vegetation cannot absorb it, and they remain there with a pressure of 33 kPa until it is evaporated. This process happens up to 48 h after rain, known as field capacity.

The percentage of microporosity (Mi) must be less than the percentage of total porosity, and this value can be obtained from the difference in masses between the dry landmass (m_d) and the wet landmass (m_w) after 48 h of drainage as shown in Eq. (2).

$$Mi\ (\%) = \left(1 - \frac{m_d}{m_w}\right) \cdot 100 \tag{2}$$

2.2.5. Macroporosity

On the other hand, macropores (drainage pores) have a diameter greater than 0.5 mm and are up to 5 times larger than micropores. Therefore, they allow the passage of water and air through them. These pores do not retain the water against the force of gravity, and consequently, when rain occurs, the water passes through the macropores until it is absorbed by the roots of plants or until it reaches some natural or artificial reservoir. The water that runs through the macropores causes the soil moisture to change for periods after rain. The speed with which the water moves through them is related to the coefficient of permeability of the soil.

The percentage of macroporosity (Ma) of a soil sample is obtained from the percentage of total porosity minus the percentage of microporosity, as shown in Eq. (3).

$$Ma(\%) = P(\%) - Mi(\%) \tag{3}$$

Macroporosity is the type of porosity of interest in the present study since water circulates through them, and therefore, they are responsible for the change in humidity and thermal diffusivity, modifying the thermal dynamics of the soil when it rains.

2.2.6. Permeability

Permeability is the property of the soil to allow water and air to pass through the soil, and it is closely related to porosity (Elhakim, 2016). The units of the soil permeability coefficient are distance over time (velocity). In soils with abundant natural vegetation (porosity up to 50%), their permeability is higher than those without vegetation.

There are numerical methods, field, and laboratory tests to determine soil permeability (Deirieh et al., 2019; Vampa et al., 1988; Zhilenkov et al., 1987). Among the experimental field methods, hydraulic methods are the most used to obtain the filtration characteristics in soils, such as water loss tests. Therefore, in the current work, a constant hydraulic load test was carried out.

The equation that relates the porosity and permeability of the soil to the passage of fluid is Darcy's Law, an empirical equation to determine the flow of water through porous media. Eq. (4) shows the differential and empirical notation of Darcy's Law:

$$Q = \frac{\partial V}{\partial t} = k \cdot i \cdot A \tag{4}$$

where Q is the volumetric flow, ∂V is the fluid quantity, ∂t is the time, k is the permeability coefficient, i is the dimensionless hydraulic gradient, and A area where the water flows.

2.2.7. Hydraulic gradient

The hydraulic gradient is given from the pressure difference at two points on the filtration lines that run through a soil sample. This pressure difference is also known as the hydraulic load. If the hydraulic load is related to the path of the filtration line on a sample with specific length, the hydraulic gradient is obtained as shown in Eq. (5):

$$i = \frac{\Delta h}{L} \tag{5}$$

where Δh is the hydraulic load, and L is the length of the sample.

2.2.8. Permeability coefficient

The coefficient of permeability k is the velocity of water through the ground when subjected to a hydraulic gradient. The k value is in turn a function of the viscosity and the temperature of the water. For the type of problem that is addressed in this work, the temperature variation is between close limits, therefore, the change in the value of the viscosity of water due to the temperature change is disregarded.

Due to the above, the permeability coefficient (k) for these types of problems is a function of the hydraulic gradient, the area perpendicular to the filtration lines, and the volumetric flow that passes through the soil sample as observed in Eq. (6).

$$k = \frac{Q}{i \cdot A} = \frac{\Delta V \cdot L}{h \cdot t \cdot A} \tag{6}$$

2.2.9. Constant load test

In constant load tests, the volume of water (V) flowing through the soil sample of known length (L) is measured, and the hydraulic load (Δh) depends only on the difference between the water levels. Area (A) is measured, and therefore it is only necessary to measure the time (t) in which the volume of water passes through the soil sample and is discharged into a graduated glass.

Due to the lack of reliable literature on porosity and permeability for the type of soil found at the site of installation of the measurement probe, it was decided to find these values with experimental methods. Fig. 2 presents a schematic and a photo of the device to perform the constant load test on a soil sample from the site where the measurement probe was installed.

2.3. Mathematical model

This section presents the mathematical model with the assumptions and spatial considerations mentioned above. The differential equation applicable for the entire domain, the initial conditions, the boundary conditions, and the different stages of interaction between nodes is given. Fig. 3 shows the study domain: the upper limit delimited by the soil surface, the porous media through which the energy is transferred, and the lower limit. Eqs. (8)–(10), Table 4

For this problem, it was considered that the equation that describes the transitory distribution of temperatures through the soil during the year is the one-dimensional Fourier-Biot Eq. (7):

$$\frac{\partial T}{\partial t} = \alpha \cdot \frac{\partial^2 T}{\partial z^2} \tag{7}$$

The initial temperature distribution:

$$T_{(z,t=0)} = T_o \tag{8}$$

where α is the thermal diffusivity, z is the depth measured from the soil surface, and T_o is the initial temperature distribution.

The initial boundary condition for the upper limit could be Dirichlet type or Neumann type, as shown below Eq. (9)

$$T_{(z=0,t)} = T_A \quad \text{or} \quad q''_{(z=0,t)} = J_{(t)} \tag{9}$$

For the lower limit, a Dirichlet-type boundary was considered:

$$T_{(z=L,t)} = T_E \tag{10}$$

where T_A is the air temperature, $J_{(t)}$ is the soil surface heat flux, and T_E is the stabilized temperature, which for this problem was taken as the

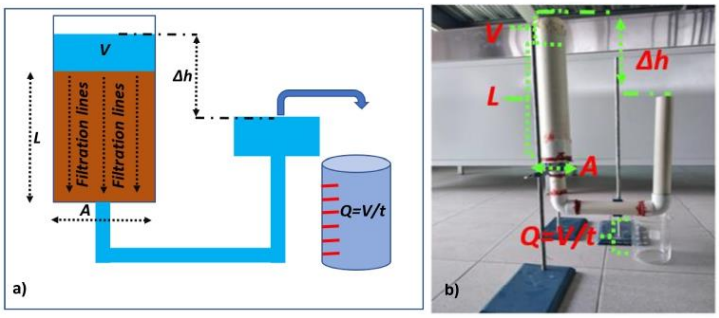

Fig. 2. Experimental device for constant load test, (a) scheme, and (b) picture of the equipment.

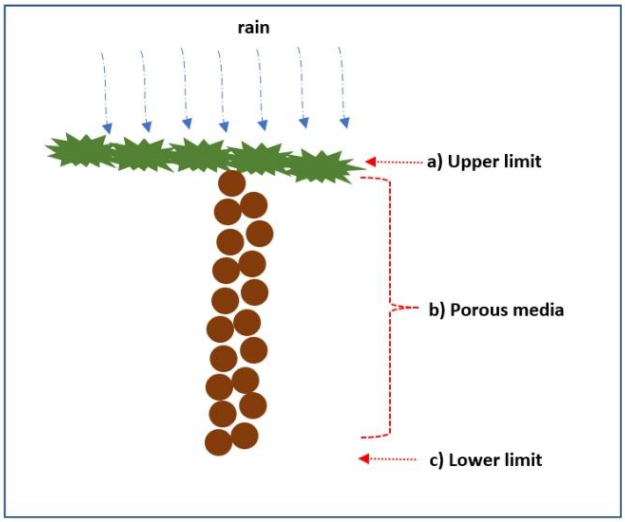

Fig. 3. Scheme of domain considered for the thermal simulation. (a) upper limit, (b) porous media, and (c) lower limit.

average temperature measured from the deepest group of thermocouples of the measurement probe.

In the case of upper limit, a constant temperature value is necessary for a Dirichlet boundary condition, which could be obtained from measures or can be approximated by the air temperature. Whereas for a Neuman boundary condition, it is necessary a heat flux. The accuracy required and the depth where the soil is studied guide the appropriate boundary condition type. A Dirichlet boundary condition was selected for this work due to lack of devices to measure the missing data involved in the heat flux equation at the ground surface. Besides, it is avoided that the uncertainty in the result is more significant due to the large number of variables involved in the heat flux equation. In any case, when selecting Dirichlet or Neumann boundary condition, its parameters are considered time-dependent.

The discretization of Eq. (7) was carried out using the finite approximation method for both the temporal part and the diffusive part. A code was implemented in Fortran 95 to approximate the system of equation's solution resulting from the discretization. Grid-independent and timestep-independent studies were conducted to determine the proper performance of the numerical model. A time-step of 10 min was selected to avoid uncertainty in environmental temperature interpolation from meteorological station. On the other hand, 207 control volumes were required to discretize the domine.

The system of equations was solved using an iterative algorithm by the Jacobi method with 1000 steps. The discretized domain uses an irregular mesh for the first meters of depth and adapts to the porosity of the soil where the measurement probe is installed. In this subdomain, some control volumes represent the soil, and others represent the pores affected when rains occur. After that depth, the mesh has a constant density in the rest of the domain and represents the soil unaffected by weather conditions.

2.4. Interaction between nodes

The simulator considers the changes in thermal diffusivity due to rain; therefore, the interaction between the nodes will be different depending on the time of year. Four periods were identified throughout the year in the experimentation site. Interaction between nodes depends on each period:

- Period without rain: The absence of rain corresponds to the days when no rainfall has occurred, and therefore the land is completely dry, with a constant diffusivity for the entire domain.
- First rain: The first rain instant occurs when rainfall is recorded for long periods, generally in May or June. When this happens, the control volumes representing pores obtain the temperature with which the rain arrived and change the diffusivity of the neighboring nodes.
- Time with rain: The rainy period corresponds to the days with constant rainfall. During this time, the control volumes representing the pores and their neighbors are maintained with a diffusivity equal to 100% saturated soil.
- Short time without rain: From this moment on, the thermal diffusivity of the soil changes its value between the different degrees of saturation until it reaches a value with 0% humidity. The rate of change depends on the permeability of the soil. During this time, the nodes neighboring the pores change their diffusivity, and the nodes representing pores continue with the diffusivity equivalent to 100% saturation.

3. Resutls and discussion

In this section, the model assumptions are validated by evaluating the simulator's precision against the data obtained by the measurement probe. The first subsection presents the thermal diffusivity, porosity, and permeability necessary to carry out the simulation. The second subsection compares the data obtained from the measurement probe and the analytical solution used in most similar studies.

Finally, after independently estimating and validating the relevant parameters, the simulation results are compared with the data produced by the measurement probe at different depths. The main advantage of this approach is that it allows considering factors that affect the heat transfer and the temperature profiles of the subsoil, for which it yields better than the analytical solution.

3.1. Thermophysical properties

This subsection shows the values of thermal diffusivity, porosity, and permeability that were mentioned in assumptions 4, 5, and 6 of the previous section. Knowing the value of these soil properties could make a more realistic simulation of the soil temperature profiles.

Five soil samples were taken from the site where the measurement probe was installed at depth range within 0.5 and 2 m depth. At this range, samples are representative of the study site and allow estimating the ground thermal diffusivity, as shown in Fig. 1. Different amounts of water were added to each portion to achieve different degrees of water saturation, 0, 25, 50, 75 and 100%. Table 1 shows the results of different thermal diffusivity and thermal conductivity values for different percentages of soil water saturation. The strong relationship between soil moisture and soil thermal properties can be seen. For example, when the soil's water saturation in the sample drops to 0%, the value of soil thermal conductivity was up to 4 times less than average moisture value of the leftover soil samples. The change in the thermal diffusivity alters the thermal inertia of the soil during periods of rain.

The different values for the thermal diffusivity of the soil were added to the simulator.

Three samples were taken from the site where the measurement probe was placed to know the total porosity value of the soil. Results are shown in Table 2.

With the data in Table 2, the percentage of total porosity was obtained for the site where the measurement probe is installed. The result is shown in Eq. (11).

$$P(\%) = \left(1 - \frac{985.02 \pm 2.76}{1059.79 \pm 3.58}\right) \cdot 100 = 7.19 \pm 0.44\% \tag{11}$$

With the same soil samples used in Table 2, the microporosity tests were made to later know the macroporosity. The microporosity results are shown in Table 3.

With the data obtained, the microporosity value was 2.56%. As seen previously, to obtain the macroporosity, it is necessary to obtain the difference between total porosity and microporosity. For the soil sample with which we were working, the macroporosity value was 4.63%.

The experimentally obtained porosity, microporosity, and macroporosity determined that the first subdomain should cover 1.9 m-depth and be represented by an irregular mesh. In this irregular mesh, for every 21 units of the domain, 1 unit would represent macroporosity. In this way, a value of 4.76% is obtained, which is very close to the value of 4.63% obtained experimentally. In contrast, the second subdomain would be represented by a regular mesh of 162 control volumes with a size of 0.05 m each.

The last value that was determined experimentally was the permeability of the soil. This was done with the methodology presented in the previous section. Again, three soil samples were taken from the site where the measurement probe was installed, and three constant load tests were carried out. The sample volume of the three samples was 400 cubic centimeters, the length of the sample L was 30.5 cm, the cross-sectional area A in 42.08 square centimeters, and the hydraulic head h in 22 cm.

Table 1
Thermal conductivity and thermal diffusivity as function of water saturation percentage.

Water saturation percentage	Thermal conductivity $(W/m\,K)$	Thermal diffusivity (m^2/s)
0	$1.83_{x10^{-1}} \pm 0.02$	$1.98_{x10^{-7}} \pm 0.01_{x10^{-7}}$
25	$7.44_{x10^{-1}} \pm 0.02$	$2.44_{x10^{-7}} \pm 0.05_{x10^{-7}}$
50	$7.73_{x10^{-1}} \pm 0.19$	$2.62_{x10^{-7}} \pm 0.02_{x10^{-7}}$
75	$7.89_{x10^{-1}} \pm 0.25$	$2.90_{x10^{-7}} \pm 0.04_{x10^{-7}}$
100	$7.94_{x10^{-1}} \pm 0.61$	$3.27_{x10^{-7}} \pm 0.04_{x10^{-7}}$

Table 2
Apparent and real density for three different samples of soil.

Sample	Apparent density (kg/m^3)	Real density (kg/m^3)
1	984.46	1058.70
2	982.59	1062.43
3	988.03	1055.26
Average	985.02 ± 2.76	1059.79 ± 3.58

Table 3
Results of microporosity for the three samples used above.

Sample	Dry landmass (g)	Drained landmass after 48 h (g)	Difference (%)
1	100	102.76 ± 0.26	2.76
2	200	205.63 ± 0.53	2.81
3	300	306.34 ± 0.54	2.11

The result of the three constant load tests was 14,401 ± 23 s. Finally, the permeability value is obtained using the results shown in this section and with Eq. (6).

$$k = \frac{400\ cm^3 \cdot 30.5\ cm}{42.08\ cm^2 \cdot 22\ cm \cdot\ 14,401 \pm 23\ s} = 9.15x10^{-4} \pm 0.2x10^{-4}\ \frac{cm}{s} \tag{12}$$

The result of the permeability coefficient shown in Eq. (12) indicates that when rainfall occurs, the water in the ground will travel 0.8 m per day. Therefore, during the simulations, the permeability was taken as 2.5 days since, according to the value obtained experimentally, the water from rain would take 2.5 days to reach the distance of the last available thermocouple to the comparison between the simulator and the experimental data.

3.2. Analytical solution

Before running the numerical simulations using the parameters obtained in the previous subsection, a comparison was made between the analytical solution and the experimental data of the measurement probe. It is important to mention that the missing experimental data from April and May 2019 were due to problems with the data logger, while data from April 2020 could not been obtained due to Covid-19 pandemic restrictions in Mexico.

The analytical solution to the heat conduction equation presented in Eq. (13) has been used by most of the studies to find the temperature value of the ST and the depth at which it is found (Al-Ajmi et al., 2006; Bisoniya et al., 2015; Kusuda and Achenbach, 1965; Mihalakakou et al., 1992; Rey-Ronco et al., 2020; Rosa et al., 2020). This solution intends to obtain the ST of the soil as a function of time and depth.

The considerations that are taken in the published works to make use of this solution are:

(1) The ground is a semi-infinite and homogeneous medium.
(2) The heat convection in the soil is negligible, therefore the soil is considered a purely conductive medium.
(3) Since the presence of fluids inside the study medium is neglected, the thermal diffusivity of the soil is considered constant throughout the year.

$$T_{(t,z)} = T_m - A_s \cdot e^{\left[-z\sqrt{\frac{\pi}{365\cdot\alpha}}\right]} \cdot cos\left[\left(\frac{2\pi}{365}\right)\cdot\left(t_d - t_o - \left(\frac{z}{2}\cdot\sqrt{\frac{365}{\pi\cdot\alpha}}\right)\right)\right] \tag{13}$$

In Eq. (13) T_m is the average annual temperature of the soil surface

(°C), A_s is the amplitude of the temperature wave at the soil surface (°C), z is the established depth (m), α is the thermal diffusivity of the soil in (m^2/day), and ($t_d - t_o$) is the difference in days between the current day and the first day of the calendar year.

T_m, and A_s were taken from the temperature measurements from the shallowest group of thermocouples of the installed measuring probe, and their values were 21.3 °C and 11.6 °C, respectively. By taking the values from the measured data, more realistic results can be achieved from Eq. (13) due to these measured values are from the study site. While taking values from meteorological data, the soil cover and vegetation make a difference between the temperature from the meteorological data and the experimentation site, inducing uncertainty grows. Ultimately, the thermal diffusivity used is presented in Table 1 with a value of 2.263×10^{-2} (m^2/day). The $t_d - t_o$ interval was 365 days with one-day steps, and the depth was set from 0.6 m to 1.8 m in 0.2 m steps.

Fig. 4 present the graphs with the comparison between analytical solution and experimental data for different depths. In these graphs, it can be observed a discrepancy between the analytical and numerical results during the months that rainfall occurs (May to November). This discrepancy arises from the assumptions made when solving the conduction equation, a constant diffusivity is considered throughout the year, in addition to omitting the climatological aspects.

3.3. Numerical simulator

After estimating the thermal and physical parameters of the soil, the data obtained from the measurement probe were compared against the results of the simulations.

3.3.1. Partial model

The numerical simulation was divided into two parts. The first one was a simulation without considering the rainfall, and consequently, the different values of thermal diffusivity and permeability were omitted. For the first part of the simulation, the thermal diffusivity values were 1.98×10^{-7} (m^2/s), *ST* 20.5, simulation time 22 months, time-step in 10 min, and depth (z) was from 0.6 to 1.8 m in steps of 0.2 m.

In Fig. 5 the experimental data and the simulation result are compared without considering the rainfall from May to November. Compared with Fig. 4, a better fit for the experimental results is shown. The previous is because, although the analytical solution considers a constant thermal diffusivity for the soil, porosity is added to the simulator.

3.3.2. Complete model

The next step was the complete model, including the thermal

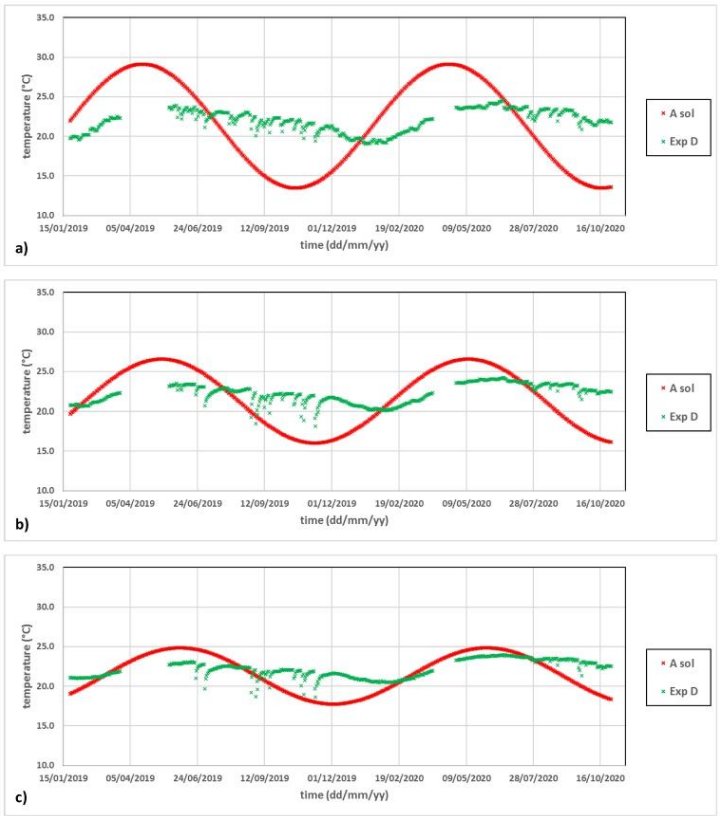

Fig. 4. Comparison between experimental data (Green) and analytical solution (Red) at (a) 0.6 m depth, (b) 1.2 m depth, and (c) 1.8 m depth (For interpretation of the references to color in this figure legend, the reader is referred to the web version of this article.).

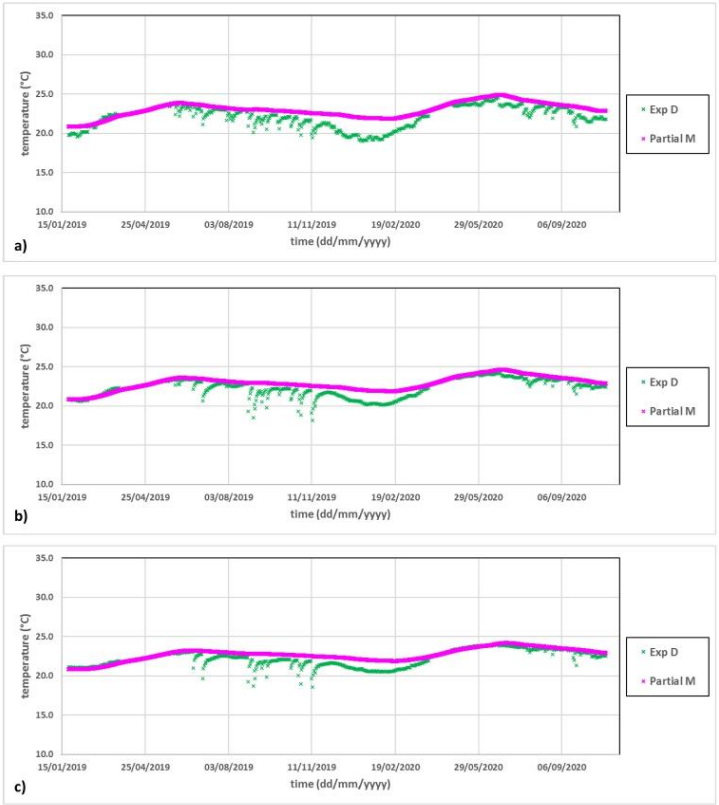

Fig. 5. Comparison between experimental data (Green) and solution of partial model (Pink) at (a) 0.6 m depth, (b) 1.2 m depth, and (c) 1.8 m depth (For interpretation of the references to color in this figure legend, the reader is referred to the web version of this article.).

diffusivity variable as a function of rainfalls with data presented in Table 1. Permeability and porosity presented previously in this section were considered too. ST, simulation time, time step, and depth range were the same as the partial model.

In Fig. 6 the experimental data and the simulation result are compared, including the rainfall over the 2-year study period. In this graph, in comparison with the two previously presented, it can be observed that the simulator replicates the instants of rainfall throughout the year. This consideration results in a better fit to the experimental data, as this simulation time changing thermal diffusivity, i.e., as a function of the presence of rain. Furthermore, this consideration adds up to the fact that permeability indicates how the change occurs between its different values.

For the comparison between the different models (analytical, partial, and complete) and the experimental data, Eq. (14) presents the deviation between the experimental data and the results obtained from the previous models using a merit function as a quantitative quality measure between the experiment and the results as used (Andaverde et al., 2019; Estrada-Wiese and del Río, 2018; Estrada-Wise et al., 2018).

$$N = \sqrt{\frac{\int_{\lambda_1}^{\lambda_f} (E(\lambda) - S(\lambda))^2 d\lambda}{\left(\int_{\lambda_1}^{\lambda_f} E(\lambda) d\lambda\right)^2}} \tag{14}$$

Where $E(\lambda)$ and $S(\lambda)$ are the experimental and analytical data, respectively. The smaller the value of N, the better the fit between the experiment and the model. A value close to 1 denotes deviations close to 100%.

Table 4 shows the results of the merit function (N) for the comparison between the analytical model, partial model, and complete model against the experimental values at different depths. The partial model improves the fit with experimental results against the experimental data to up to 70% compared to the analytical solution; on the other hand, the complete model yields an 80% improvement. These results can be well visualized in Fig. 7.

Finally, Fig. 8a compares the results obtained from the different models and the experimental data at a depth of 0.6 m. The analytical model (red) result does not represent the real temperature profile at any time, while the partial and complete models (pink and blue, respectively) better fit the actual temperature profile. Fig. 8b,c show the attenuation of the thermal wave, and although in the three models, the amplitude of the thermal wave decreases from 1.2 to 1.8 m, again the adjustment is better for the numerical models presented in this work.

4. Conclusion

A numerical simulator was developed that reliably reproduces the

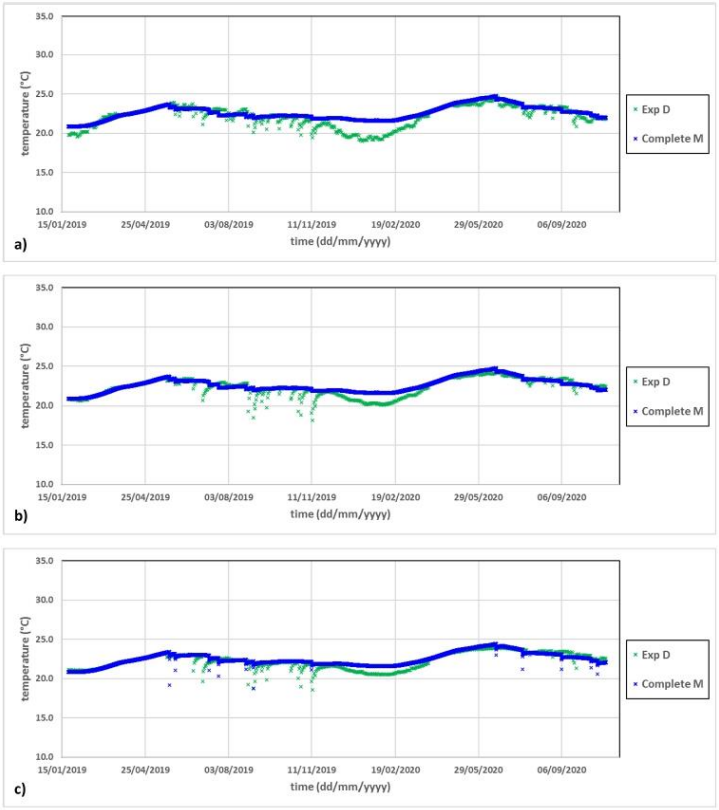

Fig. 6. Comparison between experimental data (Green) and solution of complete model (Blue) at (a) 0.6 m depth, (b) 1.2 m depth, and (c) 1.8 m depth (For interpretation of the references to color in this figure legend, the reader is referred to the web version of this article.).

Table 4
Merit function *N* results for the different models.

Depth	***N*** Analytical solution	***N*** Partial model	***N*** Complete model
0.6	$2.5_{x10^{-1}}$	$6.0_{x10^{-2}}$	$4.5_{x10^{-2}}$
0.8	$2.1_{x10^{-1}}$	$6.6_{x10^{-2}}$	$4.9_{x10^{-2}}$
1.0	$1.8_{x10^{-1}}$	$4.7_{x10^{-2}}$	$3.4_{x10^{-2}}$
1.2	$1.5_{x10^{-1}}$	$4.2_{x10^{-2}}$	$2.9_{x10^{-2}}$
1.4	$1.2_{x10^{-1}}$	$3.7_{x10^{-2}}$	$2.5_{x10^{-2}}$
1.6	$1.1_{x10^{-1}}$	$3.4_{x10^{-2}}$	$2.4_{x10^{-2}}$
1.8	$9.0_{x10^{-2}}$	$3.2_{x10^{-2}}$	$2.1_{x10^{-2}}$

temperature profiles in the soil due to the consideration of environmental and physical parameters of the soil. This simulator was developed because the analytical solution cannot be used in a general way due to the soil's different climatic and physical conditions in different parts of the world. The model used allowed the soil temperature to be reproduced reliably at different depths. With these profiles, the design phase of EAHE, calculations of heat losses of buildings to the ground, greenhouses, and several other direct uses becomes less complicated due temperature values closer to reality are obtained, while when these temperature values are not known, the design must be based on a range of possible temperatures for a given depth.

The simulator was validated against a measurement probe that returned temperature data at different depths for 22 months, showing good agreement between experimental and simulated data. In addition, environmental factors were considered such as rainfall, and the change in the soil's thermal diffusivity throughout the year. On the other hand, some physical parameters such as permeability and porosity were also considered, which helped to better reproduce the soil's thermal phenomenon.

The experiments to determine the diffusivity, porosity, and permeability of the soil have the advantage of allowing us to estimate the parameters independently and with reproducibility. All the above suggests that the assumptions made in Section 2.1 were correct and allow a correct description of the physical phenomena.

For future work, the performance and reproducibility of this new model against different soil type and weather conditions should be checked. In addition, deeper soil temperature data should be obtained to assess the new model improvement. Another area of opportunity lies in comparing the Dirichlet boundary condition used in this work against a Neumann boundary condition using the heat flux equation in the upper limit.

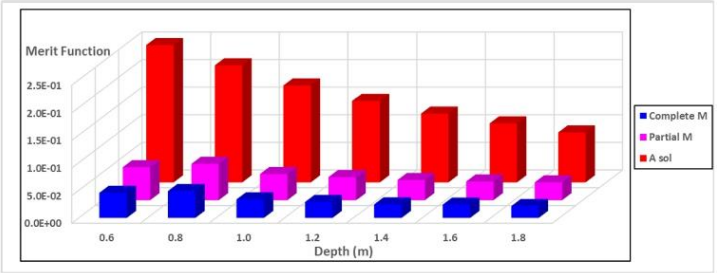

Fig. 7. Complete model (blue), Partial model (pink), and Analytical model (red) merit function results comparison (For interpretation of the references to color in this figure legend, the reader is referred to the web version of this article.).

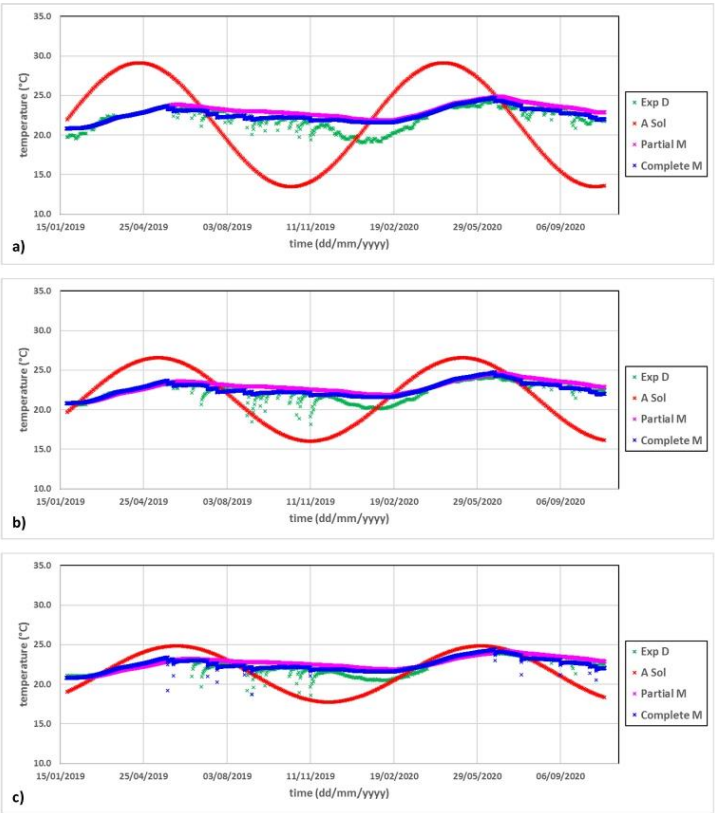

Fig. 8. Comparison between experimental data (Green), analytical solution (Red), solution of partial model (Pink), and solution of complete model (Blue) at (a) 0.6 m depth, (b) 1.2 m depth, and (c) 1.8 m depth (For interpretation of the references to color in this figure legend, the reader is referred to the web version of this article.).

CRediT authorship contribution statement

R. Molina-Rodea: Software, Formal analysis, Writing – original draft. **J.A. Wong-Loya:** Conceptualization, Methodology, Formal analysis, Investigation, Writing – review & editing, Supervision.

Declaration of Competing Interest

The authors declare that they have no known competing financial interests or personal relationships that could have appeared to influence the work reported in this paper.

Acknowledgments

The first author wishes to thank to the Engineering PhD program of UNAM and CONACyT for the financial support provided through the scholarships.

The authors wish to thank the reviewers for their enriching comments and suggestions, which allow improving the present work.

Authors wish to thank to Patricio Valadés Pelayo for his full-text English improvement, to Kevin Alquicira Hernandez for his support in simulation program, and to José de Jesús Quiñones Aguilar for provide data from the ESOLMET-IER meteorological station.

This work was partially financed by the PAPIME-UNAM project (PE108721).

References

Agrawal, K.K., Misra, R., Yadav, T., Agrawal, G.D., Jamuwa, D.K., 2018. Experimental study to investigate the effect of water impregnation on thermal performance of earth air tunnel heat exchanger for summer cooling in hot and arid climate. Renew. Energy 120, 255–265.

Al-Ajmi, F., Loveday, D.L., Hanby, V.I., 2006. The cooling potential of earth–air heat exchangers for domestic buildings in a desert climate. Build. Environ. 41 (3), 235–244.

Andaverde, J.A., Wong-Loya, J.A., Vargas-Tabares, Y., Robles, M., 2019. A practical method for determining the rheology of drilling fluid. J. Pet. Sci. Eng. 180, 150–158.

Arias-Penas, D., Castro-García, M.P., Rey-Ronco, M.A., Alonso-Sanchez, T., 2015. Determining the thermal diffusivity of the ground based on subsoil temperatures. Preliminary results of an experimental geothermal borehole study Q-Thermie-Uniovi. Geothermics 54, 35–42.

Ascione, F., Bellia, L., Minichiello, F., 2011. Earth-to-air heat exchangers for Italian climates. Renew. Energy 36 (8), 2177–2188.

Asghar, A.H., Sharma, A.K., Singh, S.P., 1990. Effect of different earth surface treatments on sub-soil temperatures. Int. J. Energy Res. 14 (9), 911–924.

Bansal, N.K., Sodha, M.S., Bharadwaj, S.S., 1983. Performance of earth air tunnels. Int. J. Energy Res. 7 (4), 333–345.

Bansal, V., Mishra, R., Agarwal, G.D., Mathur, J., 2012. Performance analysis of integrated earth–air-tunnel-evaporative cooling system in hot and dry climate. Energy Build. 47, 525–532.

Bansal, V., Misra, R., Agarwal, G.D., Mathur, J., 2013. Transient effect of soil thermal conductivity and duration of operation on performance of earth air tunnel heat exchanger. Appl. Energy 103, 1–11.

Belloufi, Y., Brima, A., Zerouali, S., Atmani, R., Aissaoui, F., Rouag, A., Moummi, N., 2017. Numerical and experimental investigation on the transient behavior of an earth air heat exchanger in continuous operation mode. Int. J. Heat Technol. 35 (2), 279–288.

Bisoniya, T.S., Kumar, A., Baredar, P., 2015. Energy metrics of earth–air heat exchanger system for hot and dry climatic conditions of India. Energy Build. 86, 214–221.

Bordoloi, N., Sharma, A., Nautiyal, H., Goel, V., 2018. An intense review on the latest advancements of earth air heat exchangers. Renew. Sustain. Energy Rev. 89, 261–280.

Breesch, H., Bossaer, A., Janssens, A., 2005. Passive cooling in a low-energy office building. Sol. Energy 79 (6), 682–696, 3.

Carson, J.E., 1963. Analysis of soil and air temperatures by Fourier techniques. J. Geophys. Res. 68 (8), 2217–2232.

Carson, J.E., Moses, H., 1963. The annual and diurnal heat-exchange cycles in upper layers of soil. J. Appl. Meteorol. Climatol. 2 (3), 397–406.

Damodharan, A., Murugan, R., Abuthakeer, S., 2020. Experimental and numerical analysis of soil-to-air heat exchanger system for domestic buildings. Therm. Sci, 24 (1 Part B), 603–608.

Deirieh, A., Chang, I.Y., Casey, B., Joester, D., Germaine, J.T., 2019. Impact of drying and effective stresses on the pore space and microstructure of mudrocks. J. Geophys. Res. Solid Earth 124 (5), 4290–4304.

Elhakim, A.F., 2016. Estimation of soil permeability. Alex. Eng. J. 55 (3), 2631–2638.

Estrada-Wiese, D., del Río, J.A., 2018. Refractive index evaluation of porous silicon using bragg reflectors. Rev. Mex. Fís. 64 (1), 72–81.

Estrada-Wiese, D., del Río-Chanona, E.A., Del Río, J.A., 2018. Stochastic optimization of broadband reflecting photonic structures. Sci. Rep. 8 (1), 1–9.

Fluker, B.J., 1958. Soil temperatures. Soil Sci. 86 (1), 35–46.

Hu, G., Zhao, L., Wu, X., Li, R., Wu, T., Xie, C., Cheng, G., 2016. New fourier-series-based analytical solution to the conduction–convection equation to calculate soil temperature, determine soil thermal properties, or estimate water flux. Int. J. Heat Mass Transf. 95, 815–823.

Huang, F., Zhan, W., Ju, W., Wang, Z., 2014. Improved reconstruction of soil thermal field using two-depth measurements of soil temperature. J. Hydrol. 519, 711–719 (Amst).

Horvath, K., Koracin, D., Vellore, R., Jiang, J., Belu, R., 2012. Sub-kilometer dynamical downscaling of near-surface winds in complex terrain using WRF and MM5 mesoscale models. J. Geophys. Res. Atmos. 117 (D11) https://doi.org/10.1029/2012JD017432.

Jayashankar, B.C., Sawhney, R.L., Sodha, M.S., 1989. Effect of different surface treatments of the surrounding earth on thermal performance of earth-integrated buildings. Int. J. Energy Res. 13 (5), 605–619.

Jiang, Y., Rocha, A.V., O'Donnell, J.A., Drysdale, J.A., Rastetter, E.B., Shaver, G.R., Zhuang, Q., 2015. Contrasting soil thermal responses to fire in Alaskan tundra and boreal forest. J. Geophys. Res. Earth Surf. 120 (2), 363–378.

Kahan, D.S., Xue, Y., Allen, S.J., 2006. The impact of vegetation and soil parameters in simulations of surface energy and water balance in the semi-arid sahel: a case study using SEBEX and HAPEX-sahel data. J. Hydrol. 320 (1–2), 238–259 (Amst).

Kayaci, N., Demir, H., 2018. Numerical modelling of transient soil temperature distribution for horizontal ground heat exchanger of ground source heat pump. Geothermics 73, 33–47.

Khalajzadeh, V., Farmahini-Farahani, M., Heidarinejad, G., 2012. A novel integrated system of ground heat exchanger and indirect evaporative cooler. Energy Build. 49, 604–610.

Kharbouch, A., El Maakoul, A., Bakhouya, M., El Ouadghiri, D., 2018. Modeling and performance evaluation of an air-soil exchange system in energy efficient buildings. In: Proceedings of the 6th International Renewable and Sustainable Energy Conference (IRSEC), pp. 1–6. IEEE.

Kristensen, K.J., 1959. Temperature and heat balance of soil. Oikos 10 (1), 103–120.

Kusuda, T., 1975. The effect of ground cover on earth temperature. In: Proceedings of the Conference on Alternatives in Energy Conservation: The Use of Earth-Covered Buildings. Fort Worth, TX, pp. 9–12.

Kusuda, T., Achenbach, P.R., 1965. Earth Temperature and Thermal Diffusivity At Selected Stations in the United States. National Bureau of Standards Gaithersburg MD.

Lund, J.W., Toth, A.N., 2020. Direct utilization of geothermal energy 2020 worldwide review. Geothermics 90, 101915.

Mathur, A., Srivastava, A., Mathur, J., Mathur, S., Agrawal, G.D., 2015. Transient effect of soil thermal diffusivity on performance of EATHE system. Energy Rep. 1, 17–21.

Mihalakakou, G., Santamouris, M., Asimakopoulos, D., 1992. Modelling the earth temperature using multiyear measurements. Energy Build. 19 (1), 1–9.

Mihalakakou, G., Santamouris, M., Lewis, J.O., Asimakopoulos, D.N., 1997. On the application of the energy balance equation to predict ground temperature profiles. Sol. Energy 60 (3–4), 181–190.

Misra, A., Becker, B.R., Fricke, B.A., 1995. A theoretical model of the thermal conductivity of idealized soil. HVAC&R Res. 1 (1), 81–96.

Misra, R., Aseri, T.K., Bansal, V., 2015. CFD analysis of thermal influence zone of earth air tunnel heat exchanger under transient conditions. In: Proceedings of the BS2015 14th Conference of International Building Performance Simulation Association. Hyderabad, India, pp. 7–9.

Morales, E., Veroslavsky, G., Manganelli, A., Marmisolle, J., Pedro, A., Samaniego, L., Morales, M., 2021. Potential of geothermal energy in the onshore sedimentary basins of Uruguay. Geothermics 95, 102165.

Naranjo-Mendoza, C., Wright, A.J., Oyinlola, M.A., Greenough, R.M., 2018. A comparison of analytical and numerical model predictions of shallow soil temperature variation with experimental measurements. Geothermics 76, 38–49.

Nassar, Y., ElNoaman, A., Abutaima, A., Yousif, S., Salem, A., 2006. Evaluation of the underground soil thermal storage properties in Libya. Renew. Energy 31 (5), 593–598.

Nethra, M.R., Kalidasan, B., 2021. Earth tube heat exchanger design for efficiency enhancement of PV panel. In: , 2, pp. 587–591.

Patel, A.K., Mishra, P., 2019. CFD analysis of geothermal heat exchanger at different orientation. Int. J. Online Sci. 5, 15–16.

Penrod, E.B., Elliott, J.M., Brown, W.K., 1960. Soil temperature variation (1952–1956) at lexington, kentucky. Soil Sci. 90 (5), 275–283.

Popiel, C.O., Wojtkowiak, J., Biernacka, B., 2001. Measurements of temperature distribution in ground. Exp. Therm. Fluid Sci. 25 (5), 301–309.

Ramesh, T., Bolan, N.S., Kirkham, M.B., Wijesekara, H., Kanchikerimath, M., Rao, C.S.,..., Freeman II, O.W., 2019. Soil organic carbon dynamics: impact of land use changes and management practices: a review. Adv. Agron. 156, 1–107.

Rey-Ronco, M.A., Castro-García, M.P., Marcos-Robredo, G., Alonso-Sánchez, T., 2020. Study of shallow subsoil temperature and its relationship to thermal diffusivity. Geothermics 86, 101821.

Rosa, N., Soares, N., Costa, J.J., Santos, P., Gervásio, H., 2020. Assessment of an earth-air heat exchanger (EAHE) system for residential buildings in warm-summer Mediterranean climate. Sustain. Energy Technol. Assess. 38, 100649.

Sliwa, T., Sojczyńska, A., Rosen, M.A., Kowalski, T., 2019. Evaluation of temperature profiling quality in determining energy efficiencies of borehole heat exchangers. Geothermics 78, 129–137.

Vampa, V., Darderes, E., Sorarrain, Ó., 1988. Metodología para la determinación de la permeabilidad de un yacimiento gasífero aplicando simulación numérica y regresión no lineal. Revista internacional de métodos numéricos 4 (3).
Wong-Loya, J.A., Andaverde, J., Rivera, C.O., 2011. Air conditioning in a station of subway new line in Mexico city using geothermal heat exchangers. Third International Conference on Applied Energy, Perugia, Italy 3223–3232.
Zhilenkov, V.N., Kayakin, V.V., Kotyuzhan, A.I., Parabuchev, I.A., Shelvlyagin, Y.S., Shevchenco, N.I., 1987. Métodos para determinar la permeabilidad de suelos no saturados. Tecnol. Cienc. Agua 59–65.
Z. Gao, N. Chae, J. Kim, J. Hong, T. Choi, & H. Lee (2004). Modeling of surface energy partitioning, surface temperature, and soil wetness in the Tibetan prairie using the simple biosphere model 2 (SiB2). J. Geophys. Res. Atmos., 109(D6).

Capítulo III. “Dispositivo experimental EAHE”

Resumen.

El trabajo que se muestra en este capítulo se envió al Congreso Mundial de Geotermia 2021 [Molina-Rodea & Wong-Loya, 2020] donde se inicia explicando que los EAHE consisten en tubos enterrados a través de los cuales circula aire, desde el exterior hasta el interior de la habitación que se desea climatizar. Al enterrarlos, se aprovecha la energía geotérmica de baja temperatura ya que a pocos metros de profundidad desde la superficie del suelo se encuentra la TCS, que no cambia su valor en más de 1 °C a lo largo del año. Algunas ventajas de los EAHE son el bajo costo operacional cuando se compara la energía eléctrica consumida por el impulsor de aire en lugar de la energía eléctrica consumida por un sistema de acondicionamiento convencional, además de un menor impacto ambiental. Con un adecuado EAHE se puede reducir significativamente el consumo eléctrico en casas, oficinas y edificios ya que es una técnica pasiva de acondicionamiento que ha sido estudiada y aplicada en otras partes del mundo. En regiones con climas cálidos como el que se encuentra en Temixco, es deseable que, durante las horas de trabajo en el día, se alcance la temperatura de confort humano en el interior de espacios. Dependiendo de la configuración geométrica de los EAHE, pueden ser de sección dominante horizontal o vertical.

Posteriormente, en la metodología se expone que los intercambiadores de calor vertical que se instalaron en el IER fueron construidos con tubería de PVC. Se utilizó tubería de PVC ya que es más económica en comparación con la tubería metálica, además de que en el sistema de estudio completo, que comprende el suelo y la tubería enterrada, el suelo es el medio dominante para la transferencia de calor. Cada sistema consta de tres pozos conectados en serie con una separación de 1.5 metros entre cada uno. El primer sistema fue hecho con tubería de dos pulgadas, mientras que el segundo y el tercero fueron construidos con tubería de tres pulgadas. La sección horizontal que conecta a pozos vecinos también fue del mismo diámetro que se utilizó para armar los EAHE, pero aislada térmicamente. A diferencia del primer y tercer sistema que tienen una separación de quince centímetros entre secciones del mismo pozo, el segundo sistema tiene una separación de veinticinco centímetros. La sección más profunda varió en cada pozo ya que el suelo donde se instalaron los sistemas tenía restos de escombro y material de relleno, por lo que durante la fase de perforación se presentaron dificultades. Por el interior de los tubos se hizo circular aire con ayuda de un ventilador. La temperatura del aire y del suelo se midió con termopares tipo “T” instalados en el interior y exterior del EAHE.

Por último, en la sección de resultados se muestran las primeras pruebas realizadas con los EAHE. En total se realizaron 6 pruebas en las que se modificaron algunos parámetros del EAHE. Se utilizaron los intercambiadores de dos y tres pulgadas, además de que se modificó la longitud total del EAHE. La velocidad del aire al interior se fijó en 2.2 m/s, 4.8 m/s y 5.4 m/s, y se utilizó un ventilador de una potencia nominal de 30 W para mover el fluido. La temperatura ambiental osciló cerca de 34 °C durante los días de experimentación. A la salida, la temperatura promedio más baja se registró cuando se utilizó el intercambiador de dos pulgadas de diámetro a una velocidad de 2.2 m/s. Al mismo tiempo, en los resultados se presenta una comparación de costos de la perforación de pozos para EAHE. Se concluye que, en los intercambiadores de tres pulgadas de diámetro, una velocidad superior a 4.8 m/s no genera un cambio significativo en la temperatura del aire a la salida del EAHE. Sin embargo, al aumentar la longitud total del intercambiador de calor en más del 50 %, se genera un cambio de hasta 2 °C a la salida.

Publicación.

Proceedings World Geothermal Congress 2020+1
Reykjavik, Iceland, April - October 2021

Aplication of Distinct Configurations of Vertical Earth-Air Heat Exchangers for the Warm-Weather Population of Temixco, Morelos (México).

Ricardo Molina-Rodea[1], Jorge A. Wong-Loya[1]

[1]Instituto de Energías Renovables, Universidad Nacional Autonoma de México, Priv. Xochicalco s/n Col. Centro, 62580, Morelos

rmr@ier.unam.mx, jawol@ier.unam.mx

Keywords: Thermal comfort, Experimental results, thermal disturbance, heat exchangers.

ABSTRACT

Passive air conditioning techniques are helpful to reduce the electrical consumption of houses, offices, and buildings. Earth-Air Heat Exchangers (EAHE) are part of these techniques. These air conditioning systems consist of buried tubes through which air flows from ambient to inside of a space to be climatized. Depending on their configuration they can be horizontal or vertical. In hot climates such as the one found in Temixco, Morelos, Mexico, it is desirable that, during working hours, the air temperature reaches the temperature of thermal comfort, or close to the stabilized temperature of the ground to be able to condition interior spaces.

This work shows the experimental results of three EAHE systems of vertical pipes made with PVC pipe installed in Temixco, Morelos. Each system consists in a set of three vertical heat exchangers placed in drilled wells, which have a separation of 140 cm between each of them. The first system is 2 inches tubing with a maximum depth of 290 cm, the second is 3 inches tubing with a maximum depth of 285 cm, and the third is 3 inches tubing with a maximum depth of 280 cm. Air at environmental temperature was circulated inside the EAHE tubes with the help of a centrifugal fan. The air temperature inside the exchangers was recorded with the use of thermocouples that were placed over the airflow path. Not only was temperature recorded along the airflow path, but also perpendicular to the tube, into the soil surrounding the buried tubes. In this way, it was possible to observe the thermal disturbance that occurs on the periphery of the tubes due to the circulation of air inside the heat exchangers.

EAHE were operated under various controlled conditions such as airspeed, run time, and overall length of the EAHE. The centrifugal fan used to drive the air into the buried tubes is variable speed, so the air at the outlet of the exchangers had a speed of 2.2 m / s, 4.8 m / s, or 5.4 m / s depending on the diameter of the tubes and the total length of the exchanger. The air velocity at the exit of the exchangers was measured with a rotating anemometer. The duration of the experiments ranged from 2 hours to 12 days. Data collection was carried out during March, April, and May 2020.

With the temperature data obtained, it was possible to observe the temperature difference (ΔT) between the inlet and outlet of the heat exchangers, the coefficient of operation (COP) of the heat exchangers was calculated during the operating hours, and it was observed the thermal impact of the soil during the circulation of air inside the tubes. Results show that it is possible to obtain a ΔT among the inlet and outlet of the EAHE higher than 9 ° C when the diameter of the tubes is 2 inches, while for heat exchangers with tubes of 3 inches diameter the ΔT is 7.3 ° C. The average temperature at the EAHE outlet during the operating periods in all cases was 26 ° C. The average COP for EAHE systems with 3 inches diameter tubes was 6.6, while the experiment where 2 inches tubes were used was 1.6.

1. INTRODUCTION

Geothermal energy, as a renewable and environmentally friendly source of energy, has received an increase in its attention and research during the last decades (Bharadwaj, S. S., & Bansal, N. K. 1981, Esen, H., Esen, M., & Ozsolak, O. 2017, Yu, X., Wang, R. Z., & Zhai, X. Q. 2011). According to its use by humanity, it can be classified into direct and indirect uses. Direct uses are those where the thermal energy of the soil is directly used. This is of great help, since in recent years the energy consumption of buildings has increased, consuming up to 40% of the world's energy consumption (Amanowicz, Ł. 2018, Yang, D., Guo, Y., & Zhang, J. 2016).

The use of geothermal energy to counteract the high energy consumption of buildings is already studied in various parts of the world (Esen, M., & Yuksel, T. 2013, Yu, L., Li, Y. P., & Huang, G. H. 2019, Zhang, X., Zeng, R., Mu, K., Liu, X., Sun, X., & Li, H. 2019). One of the advantages of taking advantage of this energy source to cool or heat a building is that at a depth of no more than 4 meters there is a stabilized temperature (ST), which is the temperature of the ground that remains constant throughout the year (Elminshawy, N. A., Siddiqui, F. R., Farooq, Q. U., & Addas, M. F. 2017, Bharadwaj, S. S., & Bansal, N. K. 1981, Wei, H., Yang, D., Guo, Y., & Chen, M. 2018, Tsilingiridis, G., & Papakostas, K. 2014).

To take advantage of this constant temperature, experimental and numerical investigations of EAHE have been carried out. They have demonstrated the great potential of EAHE as an efficient technology to save energy in the cooling and heating of buildings (Yang, D., Guo, Y., & Zhang, J. 2016, Bisoniya, T. S., Kumar, A., & Baredar, P. 2013, Serageldin, A. A., Abdelrahman, A. K., & Ookawara, S. 2016, Barakat, S., Ramzy, A., Hamed, A. M., & El Emam, S. H. 2016). Among the advantages exposed of these systems is their low operating cost and low environmental impact (Rouag, A., Benchabane, A., & Mehdid, C. E. 2018, Mehdid, C. E., Benchabane, A., Rouag, A., Moummi, N., Melhegueg, M. A., Moummi, A., ... & Brima, A. 2018).

Among the works that have been presented recently Sakhri et. al. (2020) show the behavior of a 60-meter-long horizontal heat exchanger installed in the arid region of Bechar in Algeria at a depth of 1.5 meters. The EAHE managed to obtain a temperature at the outlet of 27 ° C, while at the inlet it was at 39 ° C, achieving a ΔT of up to 12 ° C. Brum et. al. (2019) conducted a numerical

simulation study on the behavior of an EAHE system with up to 5 horizontal pipelines. An important part of their results is that it is preferable and advantageous to install a greater number of exchangers with a smaller radius between tubes, than a single one with a larger diameter, due to the spatial limitations of the place.

Liu et. al. (2019) presented an experimental work of a single U-shaped vertical exchanger for a 16.5-meter deep well. In their work show that with a smaller surface area it is possible to obtain satisfactory results for the temperature at the outlet of the exchanger. Gomat et. al. (2020) showed that the vertical part of a buried heat exchanger has a significant result in the temperature at the exit of the exchanger, even in shallow vertical wells. Díaz-Hernández et. al. (2020) mention that the cost of drilling for the installation of exchangers involves up to 40% of the total, therefore, the deeper the wells, this value will increase. Although for depths greater than 2 meters the change in temperature is not so significant.

However, there are two issues that still need to be addressed. The first is that most of the works presented deal with horizontal tubes, therefore, to have a comfortable temperature at the outlet requires a large heat transfer area, and although there are parallel arrangements of horizontal tubes, they require a large area of land to install them, which represents a limitation in densely populated urban areas (Sarbu, I., & Sebarchievici, C. 2014, Omer, A. M. 2008). The second issue to be addressed is that, to counteract the previous problem, vertical holes have been made to install vertical heat exchangers more than 5 meters deep, which represents a high initial cost if it wants to compare this technology with the cost of install conventional compression conditioning systems.

To address the problems, this work presents the experimental results obtained from three systems of vertical heat exchangers installed in the population with a warm climate of Temixco, Morelos. The area occupied for the installation was 9 m^2. The experimentation was carried out during the months of March, April and May 2020. In addition, a comparison of drilling costs between several wells with a depth of no more than 3 meters is presented, against a drilling of more than 9 meters.

2. METODOLOGY

This study was carried out during the months of March, April and May 2020 at the Institute of Renewable Energies in Temixco, Morelos. During the mentioned months the climate is hot and dry, reaching a temperature during the day up to 35 ° C. The site where the exchangers were installed is at latitude 18 ° 50'25.62 "N, longitude 99 ° 14'10.49" W at a height of 1253 meters above sea level.

2.1 EAHE METODOLOGY

The working fluid is atmospheric air and an S&P TD-250/100 exhaust fan of 30 W was used to drive it. The fan was placed at the inlet of the exchangers and was connected with PVC elbows to the exchangers. At the outlet of the exchangers, the air velocity was measured with rotary anemometers.

The soil of the site where the heat exchangers were installed is of the filling and compaction type, since at the time of the excavations various fragments of foundations and wall backs were found. The average temperature at a depth of 3 meters is 21 ° C ± 0.5 ° C throughout the year. The holes to install the exchangers were made with the help of the PREDATOR pole and extensions made of black steel tubular of Schedule 40; 3 groups of 3 wells were made, in total 9 wells. After inserting the exchangers in each of the wells, the same extracted material was used to fill the wells, avoiding the use of foundation remains or wall backstopping to avoid fracturing the pipe during compaction as the picture 1 shows.

Figure 1: The figure above shows a) the pipe into the well, b) the well backfill with the pipe.

Each group consists of 3 VEAHE made with 2 mm thick PVC pipe connected in series. The horizontal section connecting each well is 140 cm and was thermally insulated with fiberglass duct insulation to prevent the air from increasing its temperature in those areas as shown in picture 2.

Figure 2: The figure above shows the thermal insulation in the horizontal section which connect each exchanger.

The vertical section of each of the exchangers is in a range of 2.6 to 2.9 meters in length. The difference between the lengths of the vertical section of each one is due to the soil conditions at the time of drilling. A scheme with the 3 groups of EAHE and its dimensions are shown in picture 3.

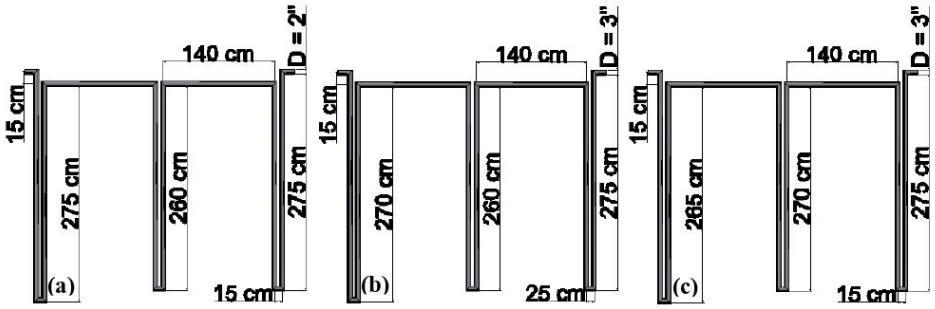

Figure 3: The figure above shows the schemes and dimensions of: a) group 1, b) group 2, and c) group 3.

The characteristics of each EAHE are:

- Group 1 was made with 2-inch pipe and the separation between the centers of the pipe was 15 cm.
- Group 2 was made with 3-inch tubing with a 25 cm spacing between the centers of the tubes.
- Group 3 was also made with 3-inch pipe, but in this case the separation between the centers of the pipes was 15 cm.

2.2 THERMOCOUPLE DISTRIBUTION

The temperature variation of the air along the heat exchanger and the earth surrounding the buried tubes was measured using T-type thermocouples with an error of ± 0.5 ° C. The thermocouples were connected to an AGILENT 34970A data logger. The location of the thermocouples is shown in figure 4. In total, each vertical exchanger consists of 9 thermocouples, 4 inside the tubes to measure the temperature along the path and 5 outside to measure the thermal disturbance that occurs on the ground due to the circulation of air at different temperature.

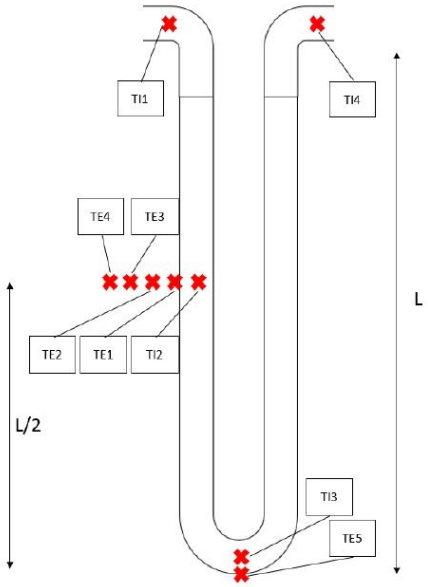

Figure 4: The figure above shows the location of inside thermocouples (TI), and external thermocouples (TE).

Thermocouples that were placed inside the tube were marked TI-1 through TI-4, while thermocouples that measure soil temperature were marked TE-1 through TE-4. TI-1 was placed at the well entrance, TI-2 at the middle of the vertical length of the tube, TI-3 at the lower limit (U) and TI-4 at the well exit. While the outdoor thermocouples, TE-1 to TE-4 were placed at the same distance as TI-2; TE-1 on the outer wall of the tube and from TE-2 to TE-4 in the same direction with a separation of 5 cm between each one. Finally, TE-5 was positioned on the outer wall of the tube at the same depth as TI-3. Some photos of the tubes with the thermocouples are shown below.

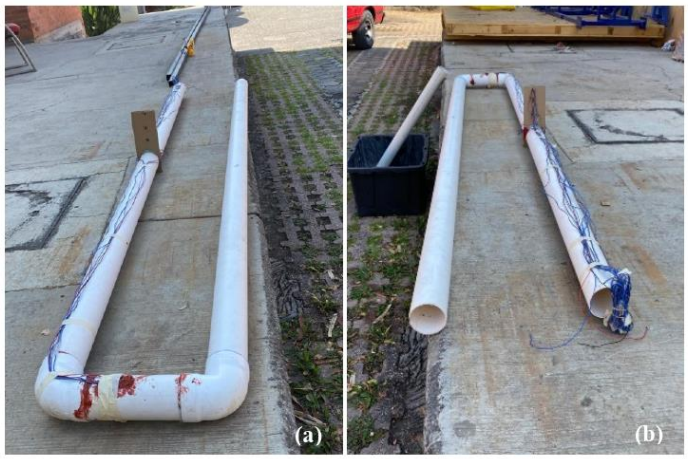

Figure 5: The figure above shows: a) a view from the bottom of the pipe, b) a view from the top of the pipe.

2.3 COP

To know the behavior of the heat exchangers during working hours, the Coefficient of Operation (COP) was used. This coefficient relates the heat power of the exchanger and the electrical power of the air fan. Subsequently, the thermal power of the heat exchanger is calculated from the volumetric flow, the specific heat of the air and the temperature difference between the inlet and the outlet of the buried heat exchanger. The above is observed in the following equation.

$$COP = \frac{P_t}{P_e} = \frac{\dot{m} \cdot Cp \cdot \Delta T}{P_e} \quad (1)$$

Where COP, Pt, Pe, ṁ, Cp, ΔT are Coefficient of Operation, thermal power, electrical power, mass flow, specific heat of the air and the temperature difference.

3. RESULTS

This section will present the results obtained from 6 tests carried out on the heat exchangers. The first 4 tests were performed on the 3-inch exchanger with a 25 cm spacing. The fifth test was carried out with the 2-inch exchanger and the last test was carried out with the 3-inch exchanger with a separation of 15 cm. The experiments were done separately due to two important things. The first one is that, at the time of experimentation, there was only one air impeller; the second is that the drilling of the wells and the installation of the heat exchangers was carried out intermittently.

3.1 TEST 1

The first experiment was conducted on March 23, 2020 on the 3-inch EAHE with a 25-cm separation between the tubes of each well. The total length of the exchanger was 11.8 meters divided into 2 wells. The duration of the experiment was 2 hours and the air speed throughout the experiment was constant equal to 5.4 m / s. During the first experiment, the ambient temperature was maintained at an average of 34.1 ° C. The following graph shows the inlet temperature, the temperature at the outlet of the first well and the temperature at the outlet of the exchanger.

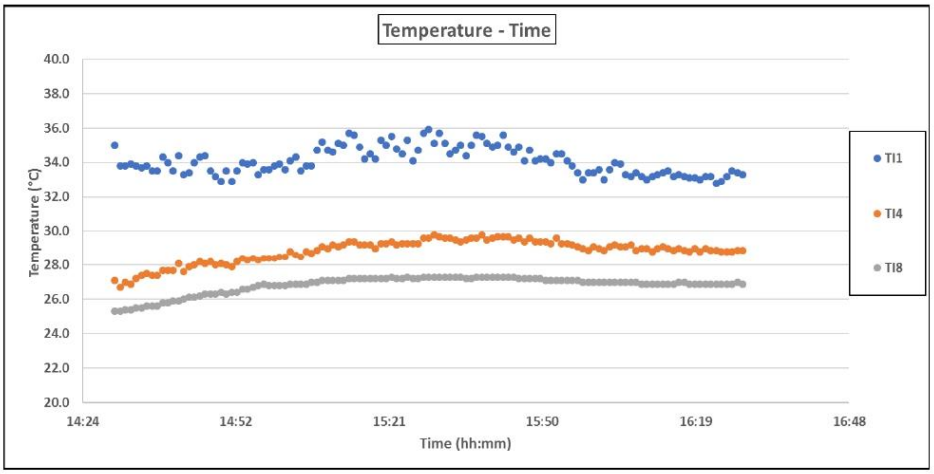

Figure 6: The figure above shows temperature at inlet (blue), first well outlet (orange), and exchanger outlet (grey).

During the first experiment, a temperature at the outlet of the exchanger of 26.8 ° C was obtained. This results in an average ΔT of 7.3 ° C between the inlet and outlet of the exchanger. The COP calculated for the first test was 7.3. The graph in figure 7 shows the thermal disturbance that occurs around the first well. The thermocouple found on the outer wall of the tube (TE1) is the one that has the most change in temperature, as expected. Since the thermocouple that is 15 cm from the wall of the tube (TE4) only changes its temperature by 1.5 ° C.

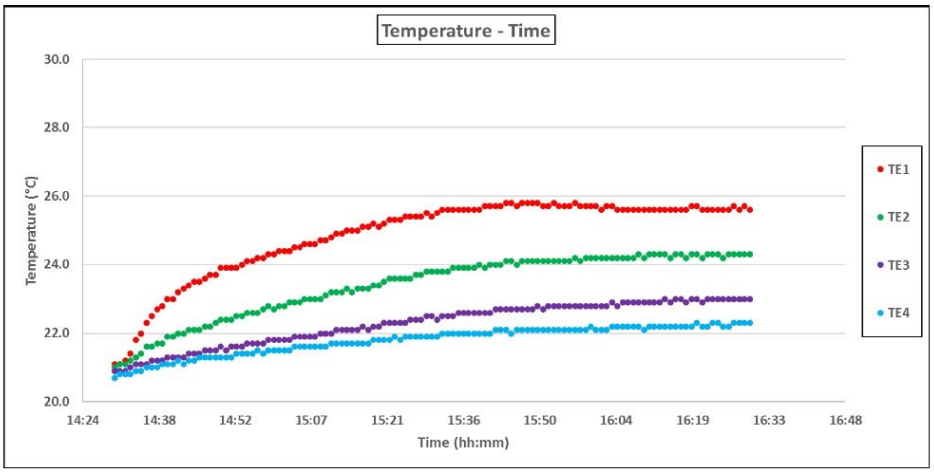

Figure 7: The figure above shows the temperature on the outer wall of the tube (red), to 5 cm (green), 10 cm (purple), and 15 cm (blue) to the pipe.

3.2 TEST 2

The second experiment was carried out on March 24, 2020 on the same EAHE as in the previous test. On this occasion, the duration of the experiment was 3 hours and the air speed throughout the experiment was constant equal to 4.8 m/s. On the second day of experimentation, the average temperature at the inlet of the exchanger (TI1) was 34.6 ° C, while the average temperature measured at the outlet of the exchanger (TI8) was 27.1 ° C. The above results in a COP of 6.7 with a ΔT of 7.5 ° C.

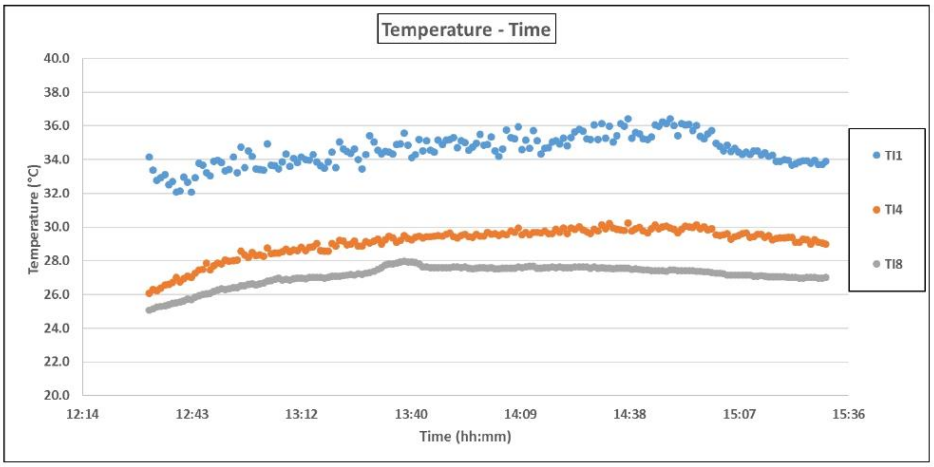

Figure 8: The figure above shows the room temperature between 32°C and 36 °C, and the outlet temperature at 27 °C.

For the thermal disturbance that occurred during the second day of experimentation, the thermocouple furthest from the exchanger wall registered a temperature change of 1.6 ° C during the 3 hours that the experiment lasted. Unlike the previous test, the thermocouple that was placed on the outer wall of the tube measured temperatures above 26.5 ° C for a few moments.

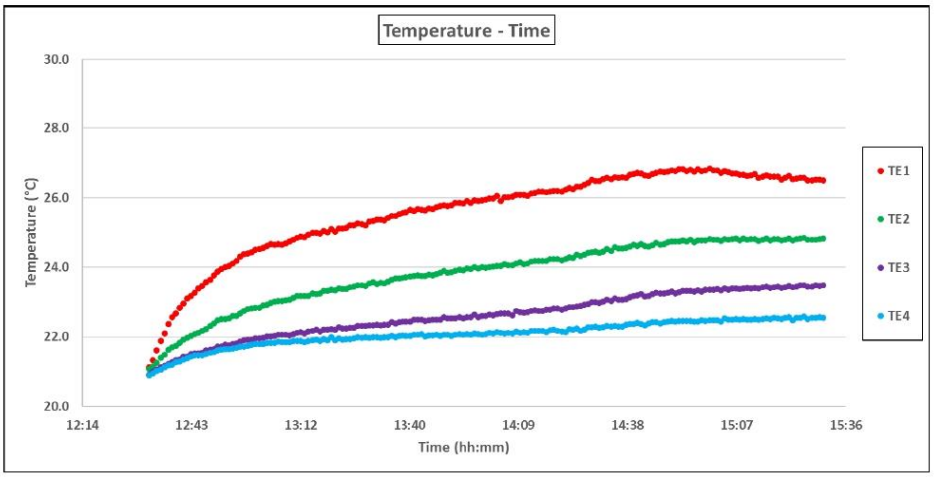

Figure 9: The figure above shows that the thermal disturbance at 15 cm to the pipe was 1.6 °C.

3.3 TEST 3

The third experiment was carried out between March 30 and 31, 2020. For this occasion, work continued with the 3-inch exchanger with a separation of 25 cm, but the total length of the exchanger increased from 11.8 to 18.2 meters by increasing a well more connected in series. The air velocity inside the exchanger was repeated with a value of 4.8 m/s. Although the experiment lasted 20 hours, in this part of the results only the section of time in which the air exchanger operated to lower the ambient air temperature will be presented.

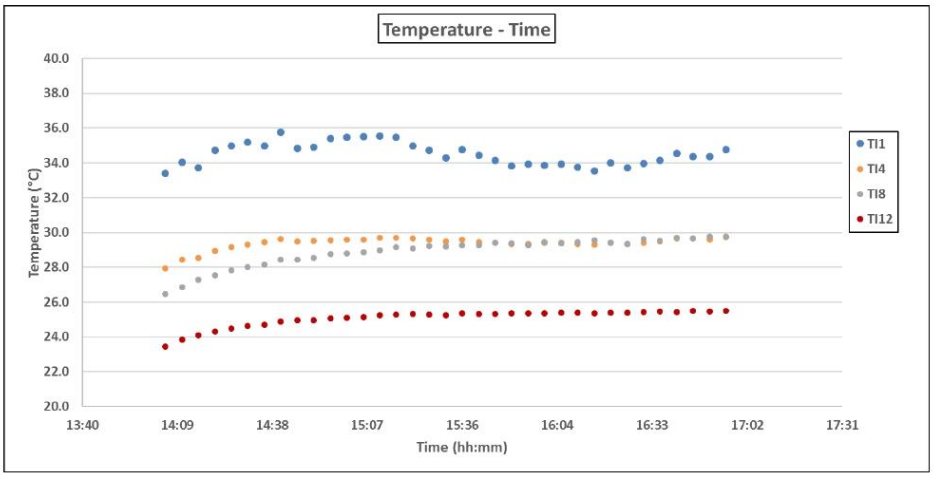

Figure 10: The figure above shows a quasi-constant behavior at outlet of exchanger with a value of 25.7 °C.

On this occasion, an average temperature at the inlet of the exchanger of 34.5 ° C was recorded, while at the outlet of the third well (TI12) the average temperature was 25.1 ° C. In this way, a ΔT of 9.4 ° C and a COP of 8.5 were obtained. The increase in ΔT and COP values are due to the increase in the total length of the exchanger.

On the issue of thermal disturbance, the thermocouple placed 15 cm from the outer wall of the tube registered a change in its temperature of 0.8 ° C, the lowest for the case in which the 3-inch interchange was used with a 25-cm separation. . This is because, unlike previous experiments, in this case the initial temperature of the surrounding earth was 22 ° C and not 21 ° C as in the previous cases.

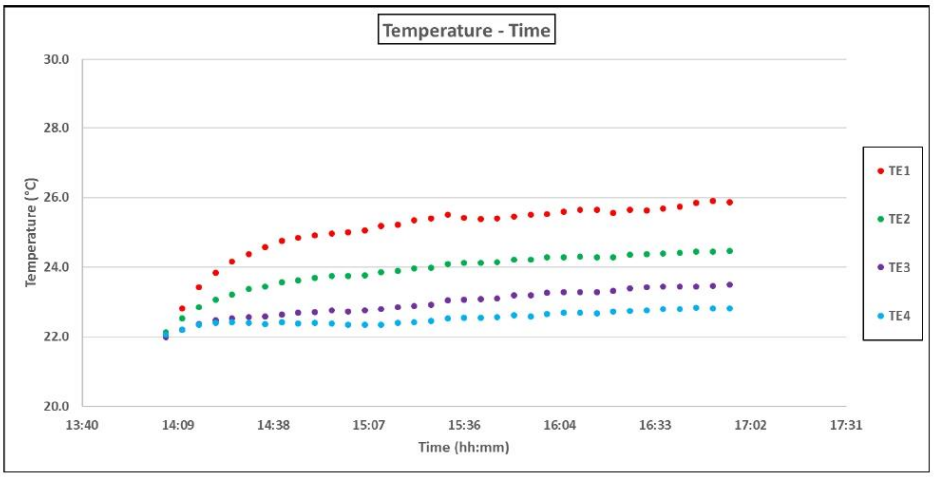

Figure 11: The figure above shows the minimal thermal disturbance in 3-inches pipes tests, with a value of 0.8 °C.

3.4 TEST 4

The fourth experiment took place between April 2 and 13, 2020. The characteristics of the EAHE were the same as in the previous experiment (length and air speed). The duration of this test was 12 days. As in the previous case, the graphs only show the periods in which the heat exchanger worked cooling the outside air.

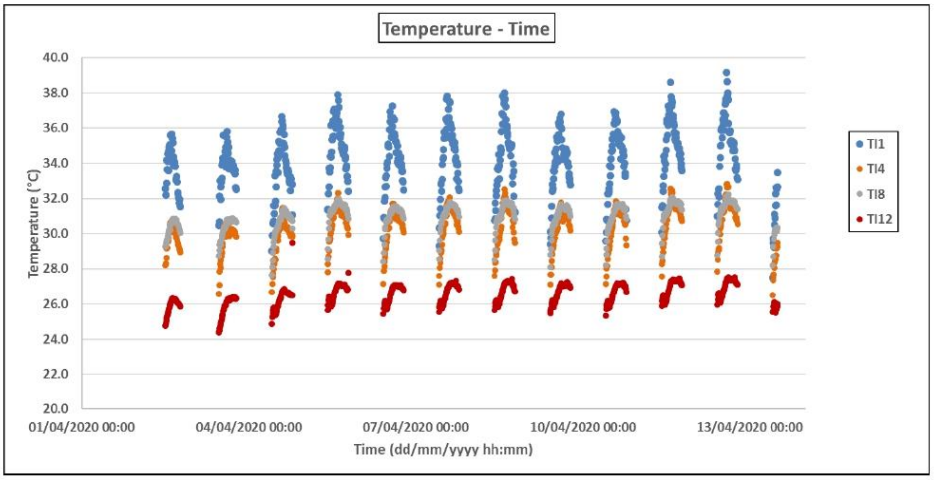

Figure 12: The figure above shows 12 days of performance, with the outlet temperature (red) among 25°C and 27.8 °C.

During the experimentation period of this test, the outside temperature reached 38 ° C on several occasions, while at the exit the temperature was in a range between 25 ° C and 27.8 ° C with an average of 26.6 ° C. The calculated COP was 7.1 with an average ΔT of 7.8 ° C.

The thermal damage of the TE1 thermocouple reached up to 32 ° C, a result that was to be expected due to the temperature that was registered in the TI1 thermocouple. The temperature of the surrounding soil 15 cm from the down comer of the first well registered a change of 1.7 ° C between the first day of experimentation and day 12 as shown in figure 13.

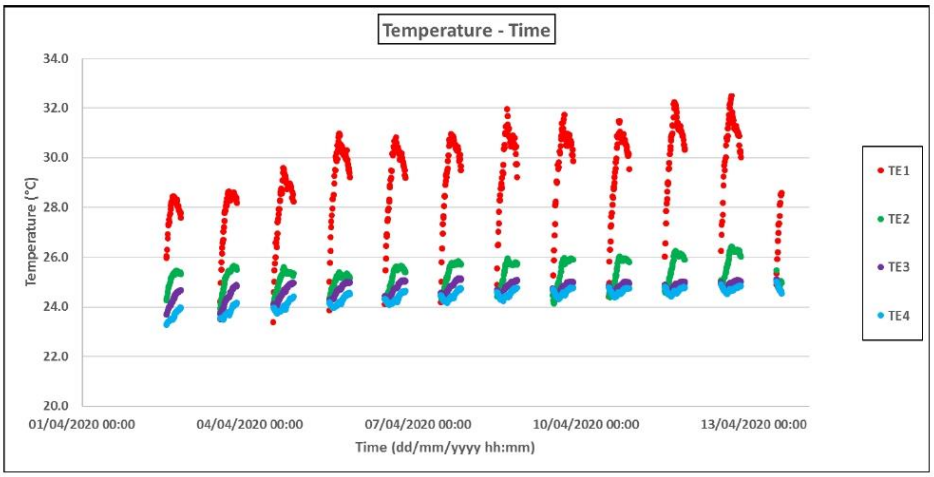

Figure 13: The figure above shows 12 days of performance, the thermal disturbance at 15 cm was about 1.7 °C (blue).

3.5 TEST 5

The fifth test was carried out between April 15 and 27, 2020 with the 2-inch heat exchanger and 25 cm spacing. The 3 wells were used, so the total length of the exchanger was 18.2 meters. The speed measured at the exit of the EAHE was 2.2 m/s, being the lowest of all the tests.

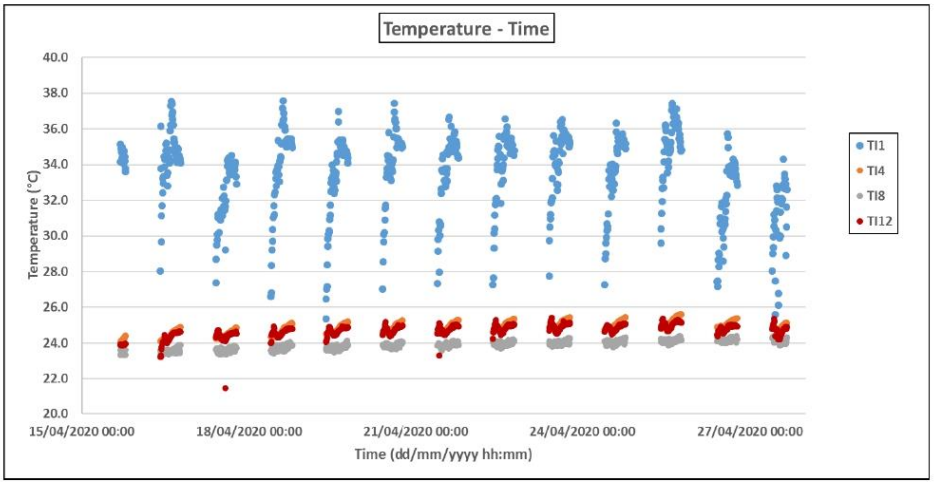

Figure 14: The figure above shows 13 days of performance. Temperature at TI12 is higher than TI8 because the thermal insulator suffered damage.

The graph of this experiment shows that in the first exchanger almost all the decrease in temperature occurs, reaching up to 92% of the total ΔT. It can even be observed that between the second and third wells there is an increase in air temperature of 0.8 ° C on average. This was because the insulation found in the connection between the second and third wells suffered a fault when it was covered with the earth from the excavation. For this test, the calculated COP was 1.6 with a ΔT of 8.9 ° C. The very low value for the COP in this test is due to the decrease in the diameter of the pipe compared to previous experiments and the speed obtained.

In the thermal disturbance that occurs in the soil around the down comer of the first well, it can be observed that an increase in temperature of up to 3.3 ° C occurs at the end of each day that the test lasted. The above is explained because, as shown in the previous graph, almost all the heat transfer of the experiment occurs in the first well, which leads to an increase in soil temperature at 15 cm from the wall of the tube of almost the double compared to previous experiments.

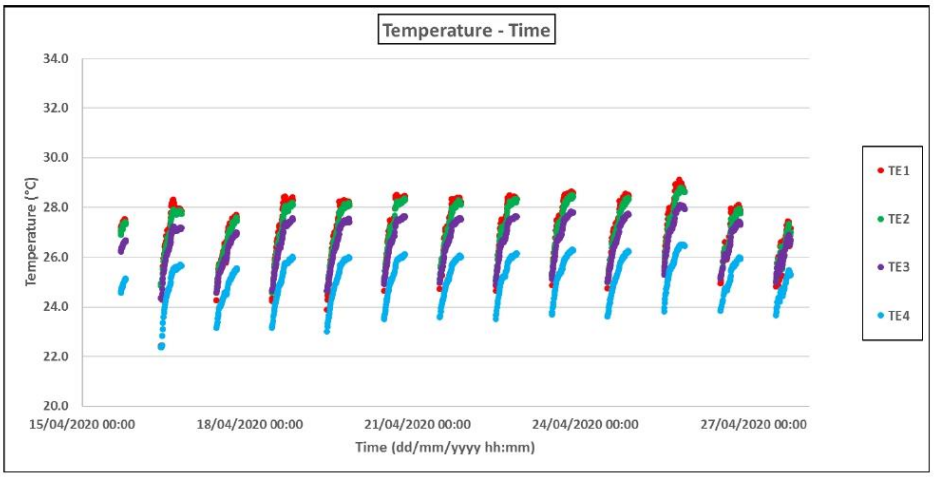

Figure 15: The figure above shows the higher thermal disturbance at 15 cm from the tube with an average value of 3.3 °C.

3.6 TEST 6

The sixth experiment was carried out between May 4 and 11, 2020. The 3-inch heat exchanger was used with a 15 cm separation between the downstream and upstream tubes. The air velocity inside the exchangers was 4.8 m ⁄ s and the total length was 18.2 meters. The average temperature at the entrance was 33.5 ° C, reaching up to 36.8 ° C on the hottest days.

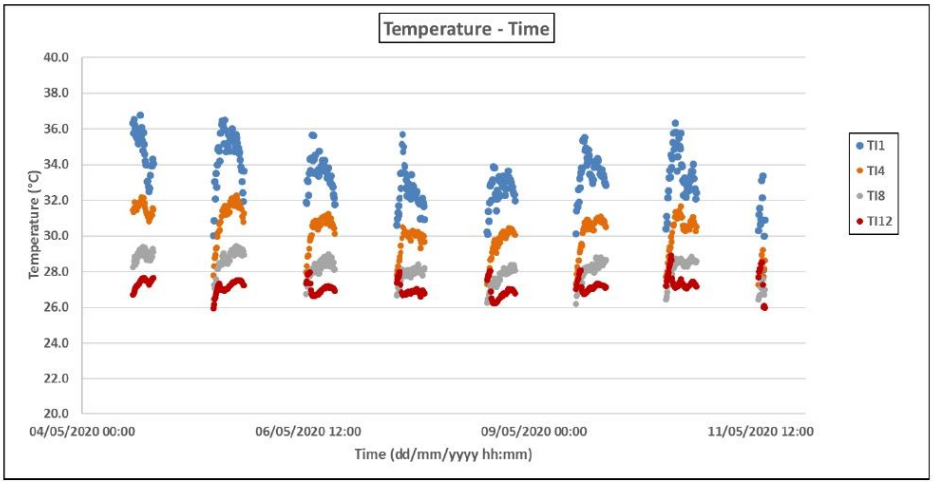

Figure 16: The figure above shows 8 days of performance with an outlet average temperature of 27.2 °C.

In the previous graph it can be seen that at the outlet of each well the air temperature decreased as it progressed inside the exchanger. In this way, at the exit of the third well there was an average temperature of 27.2 ° C, the worst of all the tests. The calculated COP was 5.7 for a ΔT of 6.3 ° C.

The radial disturbance for this test was 1.2 ° C recorded by the TE4 thermocouple. The graph 17 shows that the soil temperature before the thermal impact was 26 ° C. This is explained because the time that was allowed to pass between the installation of the exchangers in the wells and the first test was less compared to the other 2 groups of exchangers, therefore the thermal recovery of the soil after excavation was less.

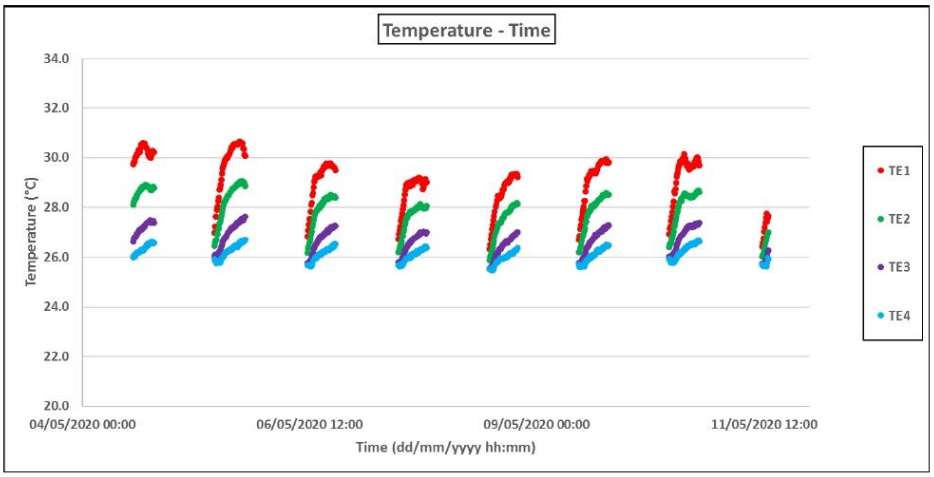

Figure 17: The figure above shows that thermal disturbance begins at 26 °C, as explained in previous paragraph.

To synthesize the data obtained, the following table shows a comparison between the experiments shown in this chapter.

Test #	Test duration	Pipe diameter	Spacing between pipes	Total lenght of the EAHE	Air speed	$\overline{T_i}$	$\overline{T_o}$	ΔT	COP	Thermal disturbance at 15 cm
1	2 h	3"	25 cm	11.8 m	5.4 $^{m}/_{s}$	34.1 °C	26.8 °C	7.3	7.3	1.5 °C
2	3 h	3"	25 cm	11.8 m	4.8 $^{m}/_{s}$	34.6 °C	27.1 °C	7.5	6.7	1.6 °C
3	3 h	3"	25 cm	18.2 m	4.8 $^{m}/_{s}$	34.5 °C	25.1 °C	9.4	8.5	0.8 °C
4	12 d	3"	25 cm	18.2 m	4.8 $^{m}/_{s}$	34.4 °C	26.6 °C	7.8	7.1	1.7 °C
5	13 d	2"	25 cm	18.2 m	2.2 $^{m}/_{s}$	33.6 °C	24.7 °C	8.9	1.6	3.3 °C
6	8 d	3"	15 cm	18.2 m	4.8 $^{m}/_{s}$	33.5 °C	27.2 °C	6.3	5.7	1.2 °C

Table 1: A resume with the results obtained in the tests.

3.7 DRILLING COST COMPARISON

The wells dug to install the heat exchangers were made with the help of a PREDATOR holder and extensions made of Schedule 40 steel tubular. The cost of the holder was $ 3,500.00 MXN, the steel tubular had a cost of $ 1,200.00 MXN, in inputs $ 1,000.00 was spent for the operation of the drilling rig and $ 9,000.00 MXN was spent on personnel to carry out the drilling. In total, $ 14,700.00 MXN was spent to be able to perform the 9 holes with an average depth of 2.8 meters deep.

Budgets were also requested from different companies dedicated to conducting soil studies and drilling wells. The companies were asked the cost of drilling a 10-meter-deep well with a diameter of 50 cm. Of the companies that sent their response, the average cost per drilling was $ 62,400.00 MXN. This represents up to 4 times the cost of drilling up to 9 shallower holes.

4. CONCLUSION

3 groups of EAHE were installed, each one of 3 exchangers connected in series and with different characteristics each. In each group, the total length and speed of the air inside the heat exchanger can be modified. By modifying the total length and air speed, the following conclusions were obtained.

Between tests 1 and 2, when changing the air velocity from 5.4 m / s to 4.8 m / s the change in outlet temperature is not significant. However, when increasing the total length of the exchanger from 11.8 m to 18.2 m and comparing experiments 2 and 3, a difference in the outlet temperature of 2 ° C is shown, in addition, the COP increases from 6.7 to 8.5 and the radial thermal impact it is lower, going from 1.6 ° C to 0.8 ° C.

The lowest heat exchanger outlet temperature of all experiments was achieved in run 5, with the 2-inch tubing. However, it was also the test where the lowest COP was calculated, due to the speed obtained and the diameter of the pipe.

Comparing the cost of drilling a single 10-meter deep well versus 3 wells no more than 3-meters deep, it is shown that by making several shallow wells, up to 75% of the cost of a single well can be saved. which is beneficial when comparing the investment that must be made when installing this type of ventilation system against compression air conditioning equipment.

REFERENCES

Bharadwaj, S. S., and N. K. Bansal. "Temperature distribution inside ground for various surface conditions." Building and Environment 16.3 (1981): 183-192.

Esen, Hikmet, Mehmet Esen, and Onur Ozsolak. "Modelling and experimental performance analysis of solar-assisted ground source heat pump system." Journal of Experimental & Theoretical Artificial Intelligence 29.1 (2017): 1-17.

Yu, X., R. Z. Wang, and X. Q. Zhai. "Year-round experimental study on a constant temperature and humidity air-conditioning system driven by ground source heat pump." Energy 36.2 (2011): 1309-1318.

Amanowicz, Łukasz. "Influence of geometrical parameters on the flow characteristics of multi-pipe earth-to-air heat exchangers–experimental and CFD investigations." Applied energy 226 (2018): 849-861.

Yang, Dong, Yuanhao Guo, and Jinpeng Zhang. "Evaluation of the thermal performance of an earth-to-air heat exchanger (EAHE) in a harmonic thermal environment." Energy Conversion and Management 109 (2016): 184-194.

Esen, Mehmet, and Tahsin Yuksel. "Experimental evaluation of using various renewable energy sources for heating a greenhouse." Energy and Buildings 65 (2013): 340-351.

Yu, L., Y. P. Li, and G. H. Huang. "Planning municipal-scale mixed energy system for stimulating renewable energy under multiple uncertainties-The City of Qingdao in Shandong Province, China." Energy 166 (2019): 1120-1133.

Zhang, Xiaofeng, et al. "Exergetic and exergoeconomic evaluation of co-firing biomass gas with natural gas in CCHP system integrated with ground source heat pump." Energy conversion and management 180 (2019): 622-640.

Elminshawy, Nabil AS, et al. "Experimental investigation on the performance of earth-air pipe heat exchanger for different soil compaction levels." Applied Thermal Engineering 124 (2017): 1319-1327.

Bharadwaj, S. S., and N. K. Bansal. "Temperature distribution inside ground for various surface conditions." Building and Environment 16.3 (1981): 183-192.

Wei, Haibin, et al. "Coupling of earth-to-air heat exchangers and buoyancy for energy-efficient ventilation of buildings considering dynamic thermal behavior and cooling/heating capacity." Energy 147 (2018): 587-602.

Tsilingiridis, G., and K. Papakostas. "Investigating the relationship between air and ground temperature variations in shallow depths in northern Greece." Energy 73 (2014): 1007-1016.

Yang, Dong, Yuanhao Guo, and Jinpeng Zhang. "Evaluation of the thermal performance of an earth-to-air heat exchanger (EAHE) in a harmonic thermal environment." Energy Conversion and Management 109 (2016): 184-194.

Bisoniya, Trilok Singh, Anil Kumar, and Prashant Baredar. "Experimental and analytical studies of earth–air heat exchanger (EAHE) systems in India: a review." Renewable and Sustainable Energy Reviews 19 (2013): 238-246.

Serageldin, Ahmed A., Ali K. Abdelrahman, and Shinichi Ookawara. "Earth-Air Heat Exchanger thermal performance in Egyptian conditions: Experimental results, mathematical model, and Computational Fluid Dynamics simulation." Energy conversion and management 122 (2016): 25-38.

Barakat, S., et al. "Enhancement of gas turbine power output using earth to air heat exchanger (EAHE) cooling system." Energy conversion and management 111 (2016): 137-146.

Rouag, Amar, Adel Benchabane, and Charaf-Eddine Mehdid. "Thermal design of Earth-to-Air Heat Exchanger. Part I a new transient semi-analytical model for determining soil temperature." Journal of Cleaner Production 182 (2018): 538-544.

Mehdid, Charaf-Eddine, et al. "Thermal design of Earth-to-air heat exchanger. Part II a new transient semi-analytical model and experimental validation for estimating air temperature." Journal of Cleaner Production 198 (2018): 1536-1544.

Díaz-Hernández, H. P., et al. "Experimental study of an earth to air heat exchanger (EAHE) for warm humid climatic conditions." Geothermics 84 (2020): 101741.

Gomat, Landry Jean Pierre, Smaël Magloire Elombo Motoula, and Bernard M'Passi-Mabiala. "An analytical method to evaluate the impact of vertical part of an earth-air heat exchanger on the whole system." Renewable Energy 162 (2020): 1005-1016.

Liu, Zhengxuan, et al. "Experimental investigation of a vertical earth-to-air heat exchanger system." Energy Conversion and Management 183 (2019): 241-251.

Brum, Ruth S., et al. "Design evaluation of Earth-Air Heat Exchangers with multiple ducts." Renewable Energy 135 (2019): 1371-1385.

Sakhri, Nasreddine, Younes Menni, and Houari Ameur. "Experimental investigation of the performance of earth-to-air heat exchangers in arid environments." Journal of Arid Environments 180 (2020): 104215.

Sarbu, Ioan, and Calin Sebarchievici. "General review of ground-source heat pump systems for heating and cooling of buildings." Energy and buildings 70 (2014): 441-454.

Omer, Abdeen Mustafa. "Ground-source heat pumps systems and applications." Renewable and sustainable energy reviews 12.2 (2008): 344-371.

Capítulo IV. “Evaluación experimental del EAHE”

Resumen.

El trabajo presentado en este capítulo muestra la evaluación experimental realizada en uno de los intercambiadores de calor tipo “U” presentados en capítulo anterior. En específico, la evaluación se realizó al modificar la velocidad del aire por el interior del UEHE construido con tubería de PVC de 3’’ y con una separación de 0.15 m entre los centros de ambas tuberías. El objetivo de la evaluación es comparar los resultados obtenidos del UEHE con las necesidades de una habitación para ser acondicionada por un sistema como este, pero tomando en consideración las restricciones de espacio de instalación. La introducción comienza con una breve explicación de su funcionamiento y de los principales parámetros de operación, además de recalcar la importancia de estos sistemas para disminuir el consumo eléctrico de sistemas convencionales de acondicionamiento en casas y oficinas. Durante la introducción también se muestra el espacio mínimo que deben de tener los patios de servicio en casas de interés social en México según el INFONAVIT. Posteriormente se resumen distintos trabajos publicados en los que realizan estudios numéricos y experimentales sobre intercambiadores de calor enterrados, ya sea de configuración horizontal o vertical. Se encontró que cuando el arreglo del EAHE es horizontal, la longitud mínima de los tubos enterrados era de 6 m, consiguiendo una disminución en la temperatura del aire de 5.5 °C como máximo. La máxima diferencia de temperatura del aire conseguida con un EAHE horizontal fue de 10.3 °C para una longitud de 53 m. En el caso de los EAHE de arreglo vertical es necesario mencionar que los trabajos experimentales publicados son menos recurrentes. Para este tipo de intercambiador de calor, la máxima diferencia de temperatura alcanzada fue de 8.8 °C con una longitud total de 31 m a una profundidad de 15.5 m. Se observó que, en todos los trabajos revisados, la longitud de los tubos supera el espacio disponible de instalación para casas de interés social.

La sección que muestra la metodología comienza describiendo el sitio de experimentación y el clima predominante durante las fechas en que se realizaron las pruebas. Se retoma del capítulo anterior la descripción del sitio de instalación de los UEHE, la profundidad de cada pozo, las dimensiones del intercambiador de calor y las cotas de los tubos ya instalados. Se presenta un esquema con la ubicación de los termopares para medir la temperatura del aire y de la tierra, se mencionan los equipos y herramientas complementarias para realizar los experimentos, y se resume en una tabla las condiciones de velocidad del aire, potencia consumida por el ventilador, y los días de experimentación. En esta sección también se describe la orientación, longitudes y cargas térmicas de la oficina que se planea climatizar. Por último, se indican las ecuaciones que se utilizaron para realizar la evaluación térmica del UEHE. Los resultados de la evaluación se presentan al realizar cuatro distintos análisis que incluyen la variación de temperatura del aire entre la entrada y salida del sistema, la variación de temperatura del aire a su paso por cada pozo, la afectación térmica del suelo, y el desempeño del sistema. Se encontró que la máxima diferencia de temperatura del aire se consiguió cuando su velocidad era la menor, mientras que cunado la velocidad se aumentó, la diferencia de temperatura conseguida disminuyó. Lo anterior sugiere que a mayor tiempo de residencia del aire al interior de UEHE, su temperatura se acercará cada vez más a la TCS. También se observó que en el primer pozo se consigue hasta un 70% de la diferencia total de temperatura del aire, mientras que el último pozo el aporte es menor al 5%. Para finalizar, la evaluación del UEHE arrojó que, independientemente de la velocidad que tenga el aire por el interior de los tubos, el máximo rendimiento del equipo ocurre cuando la temperatura ambiental alcanza su cenit.

Publicación.

Experimental evaluation of a "U" type earth-to-air heat exchanger planned for narrow installation space in warm climatic conditions.

Molina-Rodea Ricardo[a,1], Wong-Loya Jorge Alejandro[a,*,2] Pocasangre-Chávez Hugo[a,3], Reyna-Guillén Jennifer[a,4].

[a] Institute of Renewable Energies, National Autonomous University of Mexico, Temixco, Morelos, México.

[1] rmr@ier.unam.mx ORCiD: 0000-0001-5583-5310

[2] jawol@ier.unam.mx ORCiD: 0000-0003-4193-112X

[3] hepc@ier.unam.mx

[4] jrg@ier.unam.mx

*Corresponding author. E-mail address: jawol@ier.unam.mx (J. A. Wong-Loya)

Abstract

The thermal performance of a “U” type earth-to-air heat exchanger is presented in this experimental study. The device has a serial-connected vertical configuration. The wells where tubes were installed have a depth of fewer than 3 meters and are separated every 1.5 meters, using an installation area of $3m^2$. The experimentation was carried out in March in Morelos, Mexico when the environmental temperature reaches 35 °C during the day. The performance of the device was measured and compared to the requirements of an office for cooling purposes within a university campus to reproduce the space restrictions found in urbanized areas. By using a small land surface, it is feasible for urbanized areas. The air temperature inside the “U” type earth-to-air heat exchanger, the surrounding soil temperature, the airspeed, and the power consumed by the fan were measured. The air temperature and the fan’s power consumption data were obtained by modifying the airspeed in four constant values, from 1.3 m/s to 6.6 m/s. Results show that the device evaluated in this work has adequate thermal performance for cooling purposes compared to the requirements of an office. A decrease in air temperature was recorded in a range of 5.1 °C to 9.4 °C. Over 70% of the total temperature difference was reached in the first well, where the average soil thermal disturbance at 5 cm was 2.8 °C. The device achieved a maximum COP of 12.8 and a maximum effectiveness of 88.4%. With these results, it is concluded that the system is suitable for cooling purposes in areas with space restrictions. This work is novel since the dimensions available for installation in urbanized areas are considered and compared with the thermal requirements of an office. In addition to the fact that there are no published works with vertical heat exchangers connected in series.

Keywords:

Low temperature geothermal energy. Thermal performance. Vertical heat exchangers. Space restrictions in urbanized areas. Geothermal direct uses.

1. Introduction.

Using the soil as a passive air conditioning technique is feasible because, at a depth of fewer than 10 meters, the soil temperature remains almost constant throughout the year [Elminshawy et. al., 2017] [Baradwaj et. al., 1981] [Wei et. al., 2018] [Tsilingiridis & Papakostas, 2014]. This phenomenon is possible due to the thermal inertia of the soil, which attenuates the temperature fluctuations that occur on the soil surface until reaching a stabilized temperature (ST). Earth-to-air heat exchangers (EAHE) are devices employed to take advantage of the ST, generally built with PolyVinyl Chloride (PVC) pipes [Sakhri et. al., 2020]. Depending on the installation method, EAHE can be horizontal or vertical [Hou et. al., 2022]. Some critical operating parameters are the pipe diameter, the heat exchanger total length, the airspeed, and the installation depth [Benhammou & Draoui, 2015]. During the last years, an increase in experimental research about EAHE as low-energy-consumption system has been observed since it is presented as a low-cost and friendly alternative to the ecosystem [Zeitoun et. al., 2022] [Ahmed et. al., 2022]. This progress is significant since, during the most recent years, the energy consumption in cities for space air conditioning has reached up to 40% of the world's energy consumption [IEA].

In urbanized areas with extreme climates, EAHE systems are placed as an option that contributes to saving and efficient energy use. On the other hand, a recurring problem in these areas with a high population density is the limited space for its installation [Liu et. al., 2019] [Hsu et. al., 2018]. In Mexico, the Institute of the National Housing Fund for Workers (INFONAVIT) is the institution in charge of establishing the minimum housing dimensions according to official regulations. For example, according to the last update found corresponding to 2006, INFONAVIT established 13.6m^2, 7m^2, and 3.3 m^2 as the minimum area for the living room, bedroom, and service yard in low-income housing, respectively [INFONAVIT]. Considering the information above, a literature review was done looking for experimental works with horizontal or vertical EAHE, mainly in cooling operation mode and considering space restrictions in urbanized areas.

Most published papers related to EAHE with air conditioning purposes are horizontal configurations, hence there are many analytical and numerical works where the importance of the different operating parameters in this kind of heat exchanger is discussed [Ghoreishi et. al., 2019] [Nam & Chae, 2014] [Li et. al., 2019] [Dasare & Saha, 2015]. Experimental research that can be found are less due to the costs of drilling, excavation, and installation. Among the experimental studies found with the shortest installation length is the one carried out by [Díaz-Hernández et. al., 2020] where studied the behavior of a 6 m long heat exchanger installed at a depth of 2.5 m to which insulating material was previously installed in the vertical outlet section. The environmental temperature reported was between 31 °C and 36 °C. Most favorable results were obtained during August when a temperature difference of 5.5 °C was achieved. [Becerra et. al., 2022] studied the behavior of two 6-m-long horizontal heat exchangers buried at 1 m and 2 m depths, respectively. During the warmest month, the ambient temperature reached 32°C, and the system achieved a temperature drop of 4°C, with a cooling power of up to 60W. [Belloufi et. al., 2017] investigated the behavior of a EAHE operating in cooling mode under transient conditions in the semi-arid climate of Algeria. EAHE configuration is a single horizontal coil with 53 m in total length and 85 m^2 in surface area. Results show EAHE achieves almost 10 °C in air temperature difference, reducing air temperature to 30 °C. [Sakhri et. al., 2021] conducted experimental research about a single EAHE without external devices in the arid region of Bechar in Algeria. The EAHE consists of a 66 m length pipe buried at 1.5

m depth. The system achieved better performance in cooling mode, with an 11.9 °C drop temperature.

In addition to the single tube configuration, other common configurations are parallel tubes and serpentine. [Mathur et. al., 2017] studied the thermal performance of EAHE for densely populated zones. They compared horizontal and spiral configurations of EAHE installed at 3 m depth occupying 31.8 m^2 (26.5 m x 1.2 m) and 70.9 m^2 (8.7 m x 8.15 m) land space, respectively. The performance of EAHE was measured by calculating the cooling capacity and COP of the system. The average inlet air temperature of the system during the experiments done in the summer was 43.6 °C. The average outlet air temperature was 33.3 °C and 33.5 °C for the horizontal and spiral configurations, respectively. Additional experimental investigation with serpentine configuration is carried out by [Ghosal et. al., 2004] who used experimental data from a horizontal heat exchanger to validate a semi-analytical model. The heat exchangers were buried at 1 m in a 19.2 m^2 land space (4.8 m x 4 m). The total length of the heat exchanger was 4.8 m, and the geometrical configuration was a serpentine. The ambient temperature during the day exceeded 40 °C. The maximum temperature difference during the summer was 4 °C. Works found with parallel tubes correspond to [Li et. al., 2019] who evaluated the cooling performance of a two-layer EAHE accompanied by an irrigation system to affect the soil moisture content. Experiments were conducted from May to August. The deepest section of the EAHE was located 5 m below ground level. The total length of the EAHE was 33.5 m, divided into two horizontal sections of 15 m and 16 m each, and a 2.5 m vertical connection. Air temperature showed an average drop of 14.6 °C. [Congedo et. al., 2020] Carried out a study where the horizontal section length of the EAHE was modified in order to observe the change in temperature at the outlet, as well as the system's behavior when coupled with heat pumps. With an ambient temperature of 33 °C, temperature differences of 1.2 °C, 2.9 °C, and 4.1 °C were obtained for lengths of 10 m, 30 m, and 50 m, respectively, during July in Turin, Italy. [Demir et. al., 2009] Performed the experimental validation of a numerical model. The experimental data were obtained from horizontal heat exchangers buried at a depth of 1.8 m and with a length of 40 m. During the experimental validation, they obtained temperature differences between the inlet and outlet of 1.5 °C. [Ahmed et. al., 2022] Installed 20 tubes for a horizontal heat exchanger system as part of his comparison study between a conventional ventilation system and one coupled with heat exchangers. The horizontal tubes were 7.5-m-long and installed at a depth of 0.6 m on an 8.1 m x 2 m surface. The largest temperature difference was 2.2 °C when the ambient temperature was greater than 34 °C.

It is observed that when the configuration consists of a single horizontal tube, the pipe's length ranges from 6 m to 66 m, or more. Those who change the configuration from single tube to serpentine or parallel require installation surfaces higher than 15 m^2. Both dimensions present a severe problem in urbanized areas due to the space available for installing pipes [Sarbu & Sebarchievici, 2014] [Omer, 2008]. To counteract this problem, vertical heat exchangers have the option of making vertical wells that require less installation surface [Zeng et. al., 2003] [Zeng et. al., 2003]. In this regard, experimental works focused on the vertical configuration of EAHE are less frequent despite research on wellbore heat transfer models considering the heat exchanger has mainly discussed [Li & Lai, 2015] [Yang et. al., 2010] [Cui et. al., 2018] [Ahmadfard & Bernier, 2019] [Florides & Kalogirou, 2007].

[Montagud et. al., 2011] Presented a set of data collected over five years to evaluate the behavior of a conditioning system. The system is made up of 6 wells of 50 m depth each. The maximum ambient temperature was recorded at 26 °C. He observed that the temperature of the working fluid increased by 1.2 °C compared to the same date in the first year of measurement, which reinforces the idea of a large thermal recovery capacity of the soil. [Liu et. al., 2019] proposed a vertical heat exchanger to study the temperature difference reached, the air temperature along the pipe, and the ground temperature. The system consists of a well 15.5 m deep and 1 m in diameter, where two 0.22 m diameter tubes (inlet and outlet) with a separation of 0.7 m were installed. The environmental temperature recorded ranged between 28 °C and 38 °C, and an average difference of 8.8 °C was obtained between the input and output. [Yang et. al., 2009] experimentally validated a mathematical model to observe the heat transfer in vertical heat exchangers. The experimental data were obtained from two vertical heat exchangers installed in wells 30 m deep. At the end of the experimental validation, it was found that the average fluid temperature difference between the inlet and outlet is 2 °C. Other authors have highlighted the importance of any configuration's vertical section of heat exchangers. [Gao et. al., 2020] studied the behavior of a vertical heat exchanger coupled to a 190 m^3 underground refuge chamber that is used in case of mine accidents. The vertical heat exchangers were installed in wells 300 m deep, through which air circulated at 2 m/s. The test lasted 109 h between July 16th and 21st. Inlet temperature peaks were recorded at 27 °C. While at the outlet, the temperature decreased by an average of 4 °C. Other published studies talk about the importance of vertical sections in any type of buried heat exchanger [Ahmed et. al., 2021]. They mention that the vertical inlet section has a considerable impact on the thermal behavior of the entire system since it is subject to periodic fluctuations in temperature of both the ambient air and the soil itself [Gomat et. al., 2020] [Wei et. al., 2020] [Soares et. al., 2021]. Table 1 summarizes the dimensions and temperature drops reported in the cited works.

Table 1. Summary of configuration and temperatures reported in cited works, dashes mean that the information is not available.

	Configuration	Total length	Depth	Ambient temperature	Temperature difference reached
Horizontal configuration - EAHE					
Díaz-Hernández et. al., 2020	Single tube	6 m	2.5 m	31 °C ~ 36 °C	5.5 °C
Becerra et. al., 2022	Single tube	6 m	1 m / 2 m	32 °C	4 °C
Belloufi et. al., 2017	Single tube	53 m	--	40.3 °C	10.3 °C
Sakhri et. al., 2021	Single tube	66 m	1.5	39 °C	11.4 °C
Mathur et. al., 2017	Single T. / Serpentine	26.5 m / 8.7 m	3 m	43.6 °C	33.3 °C / 33.5 °C
Ghosal et. al., 2004	Serpentine	4.8 m	1 m	40 °C	4 °C
Li et. al., 2019	Parallel	33.5 m	5 m	25.6 °C	14.6 °C
Congedo et. al., 2020	Parallel	10 m / 30 m / 50 m	--	33 °C	1.2 °C / 2.9 °C / 4.6 °C
Demir et. al., 2009	Parallel	40 m	1.8 m	---	1.5 °C

Ahmed et. al., 2022	Parallel	7.5 m	0.6 m	34 °C	2.2 °C
Vertical configuration - EAHE					
Montagud et. al., 2011	U concentric tubes	600 m	50 m	26 °C	--- °C
Liu et. al., 2019	Single U tube	31 m	15.5 m	28 °C ~ 38 °C	8.8 °C
Yang et. al., 2009	Single U tube	60 m	30 m	---	2 °C
Gao et. al., 2020	Underground chamber	300 m	300 m	27 °C	4 °C

As can be seen, to counteract the limitation of the large installation area required for horizontal heat exchangers, vertical heat exchangers require wells with a depth greater than 15 m. Unfortunately, this switch generates a high installation cost since specialized equipment is required to conduct the drilling [Díaz-Hernández, et. al., 2020]. Both issues, the large installation area required and the depth of the well, are essential aspects that must be addressed for the use of low-temperature geothermal energy in cities.

In this work, an experimental evaluation of an 'U' type earth to air heat exchanger (UEHE) planned for a narrow installation space is shown. The heat exchanger has a vertical configuration with "U" tubes connected in series. A significant aspect of this configuration is that the land space used for the installation is smaller than that used in different configurations of horizontal EAHE. In addition, the deepest section of the heat exchangers is also lower than that found in similar works. It is necessary to emphasize that few works address this issue [Agrawal et. al., 2019]. The UEHE's target is to decrease the air temperature to achieve temperature comfort conditions in an adjacent room and consider limited installation space. The experimentation was conducted under ambient conditions during one of the warmest months in Morelos, Mexico. During the evaluation, the inlet and outlet air temperature was measured along with soil temperature, airspeed, and power consumed by the fan to calculate the coefficient of performance (COP), and the effectiveness of the UEHE.

2. Material and methods.

This section describes the weather and the experimental site, the geometric configuration, the selected room, and the characteristics of the heat exchangers with which the experiments were carried out. The equipment and tools used during the experimentation, the variables under consideration, and the equations used for data analysis are presented too.

2.1 Experimentation site and weather.

The experimentation was carried out in March 2022 at the UNAM - Institute of Renewable Energies (IER) (18°50'22'' N, 99°14'06'' W, 1253 m.a.s.l.), located in Temixco, Morelos, Mexico. According to the National Water Commission (CONAGUA), the prevailing climate throughout the year is warm and sub-humid, with rainfall from May to October [CONAGUA]. Figures 1a) and 1b) show the average precipitation and maximum and minimum temperature for each month of the year in Temixco. The maximum temperatures during the day are reached between 14:00 and 16:00.

The heat exchangers are in the IER-UNAM facilities in Temixco, Morelos, Mexico. The wells where the heat exchangers were placed were drilled in a garden between two buildings. In total, three

wells of different depths were drilled with a separation of 1.5 m between neighboring wells, as shown in figure 2. The soil surface used for installation is 3 m^2. The difference in the depth of the wells is due to the filling of the soil, which was with rubble and compaction material. The ground surface is covered with a layer of grass.

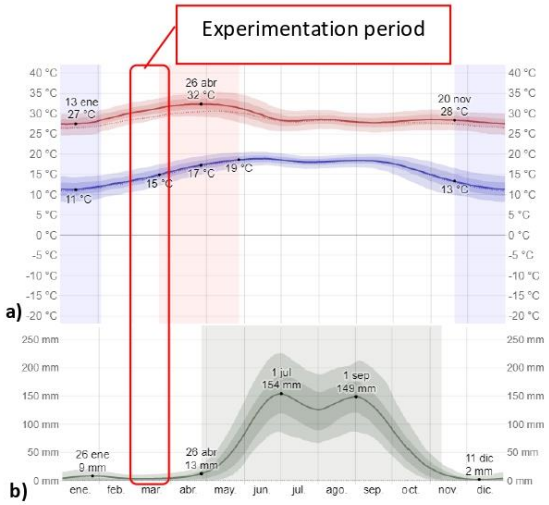

Figure 1. a) Maximum and minimum temperatures reached in Temixco, b) Average monthly rainfall in Temixco.

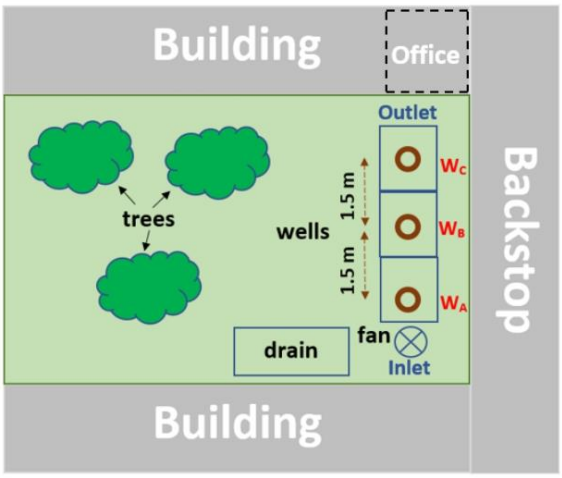

Figure 2. Location and geometric configuration scheme of wells.

2.2 UEHE configuration.

The experimentation was carried out in a system of UEHE installed in the arrangement of wells in figure 2. The diameter of the wells is 0.4 m, and they are connected in series by a 0.15 m deep trench. Henceforth, the wells will be identified by the letters shown in figure 2 (subscript A, B, C). Table 2 shows the depths of each well.

Table 2. Depth in meters by wells A, B, and C.

Wells	Depth (m)
W_A	2.80
W_B	2.85
W_C	2.75

The heat exchangers were built with PVC pipe with a diameter of 0.076 m (3 inches) and a thickness of 0.002 m. The horizontal section that connects the wells W_A - W_B and W_B - W_C is buried 0.15 m from the ground surface and thermally insulated with fiberglass for ducts to prevent the increase in air temperature in those sections. Figure 3 shows a cross-section of the well (Fig. 3a) and a general scheme of the heat exchanger connected in series (Fig. 3b). The material used for the filling is the same that was extracted in the drilling, but without construction remains.

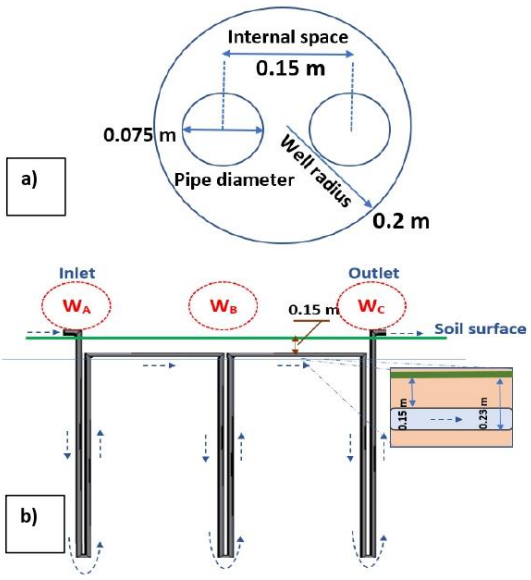

Figure 3. Scheme of the UEHE, a) Cross section of the well with the heat exchanger, b) UEHE schematic connected in series and airflow direction (dotted arrows).

T-type thermocouples (Omega, ±0.5°C) were used to measure the air temperature inside the exchangers and the surrounding ground temperature. The system consists of eighteen thermocouples divided into six thermocouples per well. Thermocouple 1 measures the temperature of the air at the inlet well. Thermocouple 2 measures the temperature of the air in the middle of the downward vertical section. Thermocouples 2' and 2'' measure the soil's temperature at 5 and 15 cm from the tube external wall in a radial direction and are placed at the same depth as thermocouple 2. Thermocouple 3 measures the air temperature in the deepest section of the well. Finally, thermocouple 4 measures the air temperature at the outlet well. This same configuration is repeated for wells W_B and W_C. Figure 4 shows a diagram of the location of the thermocouples mentioned above.

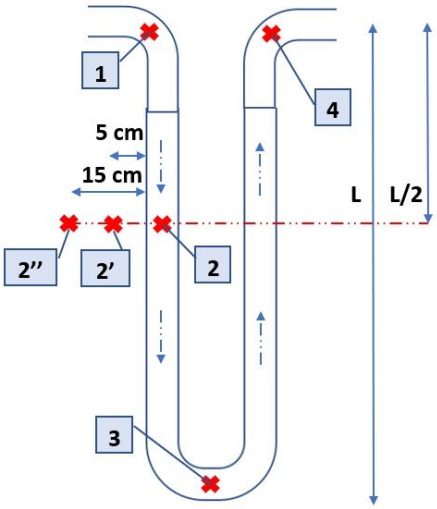

Figure 4. Thermocouple location inside de UEHE and into the surrounding soil.

2.3 Equipment and tools.

The following equipment was used during the tests:

- S&P TD-800/200 fan (185 W) to blow air inside the UEHE placed at the W_A inlet.
- LVYUAN 0-130 V (500 VA) voltage controller connected to the fan to manipulate the power supplied to the fan and control the airspeed inside the UEHE.
- HER-440 Digital Air Flow and Speedometer (0.8~40.0 m/s, ± 2.0% accuracy) to measure the average air speed at the UEHE outlet. Velocity was measured at the beginning and the end of each experiment.
- AGILENT 3497A data logger to collect temperature data from the thermocouples installed in the UEHE.
- Wattmeter HER-432 (120 V~, 0.001~15 A) to measure the voltage and current used by the fan and the potentiometer during the experimentation.

2.4 Experiment conditions.

As mentioned above, the experimentation was carried out during one of the warmest months at the IER. In total, measurements were made on 15 different days. The experiments began around 11:00 a.m. and ended at approximately 6:00 p.m. since the highest ambient temperatures occur during this period. During the experimentation, temperature measurements were taken every 5 minutes, for a total of 86 measurements for each thermocouple. In addition, as part of the analysis of the UEHE performance, the power supplied to the fan was manipulated, with which it was possible to have four different airspeeds inside the UEHE. The different airspeeds, power consumed by the fan, and the days of experimentation are shown in table 3.

Table 3. Air speed inside the UEHE, power consumed by the fan, and tests days.

Air speed (v)	Fan's power (W)	Days (day/month)
1.3 *m/s*	7 W	03/03, 11/03, 25/03
4.1 *m/s*	33.9 W	02/03, 10/03, 16/03, 24/03
6.4 *m/s*	54.9 W	01/03, 09/03, 15/03, 23/03
6.6 *m/s*	74.8 W	28/02, 08/03, 14/03, 22/03

2.5 Office selected.

The office selected for air-cooling, whose location was shown in figure 2, occupies an area of 23.6 m^2 and an approximate volume of 74.4 m^3. The office dimensions are shown in detail in figure 5. The office roof inclines 5.3°, with the north wall 0.44 m higher than the south wall to favor rainwater drainage. The office door is located on the west wall, which also connects to another adjacent office, so the west wall has the condition of 'no sun' and 'no wind'. On the south wall, there is a window that occupies an area of 5.7 m^2 that is partially shaded by a projection located at the top of the wall, therefore in this wall, there are 'sun' and 'wind' conditions. The north and east walls have the condition of 'no sun' and 'wind' since they are located on corridors that allow the passage of air but are shaded by other structures. These conditions are used to generate the thermal simulation of the office. It is important to mention that the sunshine hours received by the office are on average 10.3 per day.

In accordance with the official Mexican norm NOM-001-STPS-1999 that deals with the ventilation requirements in closed spaces, it is necessary at least 5 air changes per hour to avoid a space with stale air.

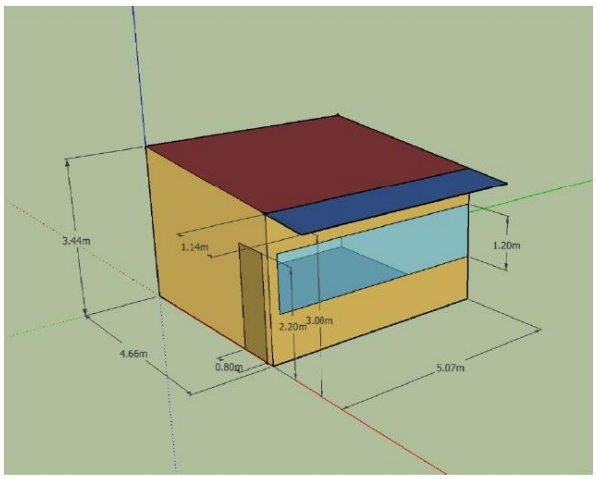

Figure 5. Dimensions of the office selected for air conditioning.

2.6 UEHE calculations.

The performance of the UEHE was evaluated using the coefficient of operation (COP) [Lim & Lee, 2021] [Ozgener & Ozgener, 2010] [Pfafferott, 2003] and the effectiveness ($\mathcal{E}$) [Manik et. al., 2019] [Ahmadi et. al., 2021] [Bisoniya, 2015] [De Paepe & Janssens, 2003]. The COP relates the energy transferred by the air to the ground (Q) and the energy used to move the air inside the UEHE (W) (Eq. 1). On the other hand, $\mathcal{E}$ relates the temperature change reached in the UEHE (Ti - To) and the difference between the air temperature at the inlet and the ground ST (Ti - Tg) (Eq. 2), where Tg, Ti, To are the temperature of the ground, the air at the inlet and outlet of the UEHE, respectively.

$COP = Q/W$	(1)
$\varepsilon = \frac{Ti - To}{Ti - Tg}$	(2)

The total energy transferred by the air to the ground is obtained with equation 3, where Q is the energy transferred by the air, $\dot{m}$ is the mass flow rate of the air, Cp_{air} is the specific heat of the air, and ΔT is the temperature difference between the inlet and outlet of the heat exchanger.

$\dot{Q} = \dot{m}_{air} \cdot Cp_{air} \cdot \Delta T = \dot{m}_{air} \cdot Cp_{air} \cdot (Ti - To)$	(3)

The mass flow of air that passes through the interior of the UEHE is given by the ratio between the volumetric flow of air ($\dot{V}_{air}$) multiplied by the air density at ambient conditions (ρ_{air}).

$\dot{m}_{air} = \dot{V}_{air} \cdot \rho_{air}$	(4)

The air volumetric flow depends on the speed at which it is driven by the fan placed at the inlet (v), the pipe's diameter (D), and the cross-sectional area of the pipe (A).

$A = \pi \cdot \frac{D^2}{4}$	(5)

3. Result and Discussion.

This section shows the results obtained during the experimentation done with the heat exchangers, and the comparison with the thermal requirements of the selected office. The comparison between the inlet and outlet air temperature of the UEHE, the change in air temperature in each well, the soil's thermal disturbance, and the system's performance for each speed is shown.

From here on, to refer to the temperature of a specific thermocouple, reference will be made to the well with the letters shown in figure 2 and to the number of the thermocouple shown in figure 4. For example, the air temperature at the inlet and outlet of the system were measured by thermocouples T_{A1} and T_{C4}, respectively. The temperature of thermocouple 3 in well W_B will be referred to as T_{B3}.

3.1 Inlet and outlet temperature variation.

Figures 6a), 6b), 6c), and 6d) show the air temperature variation at the inlet and outlet of the system ($T_{A1} - T_{C4}$) at the average speed of 1.3 m/s, 4.1 m/s, 6.4 m/s, and 6.6 m/s respectively during the tests days.

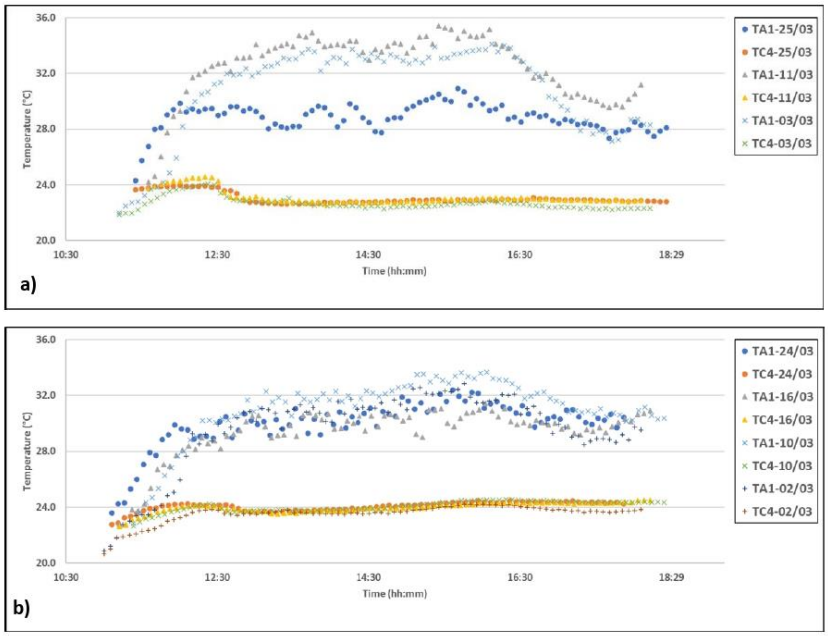

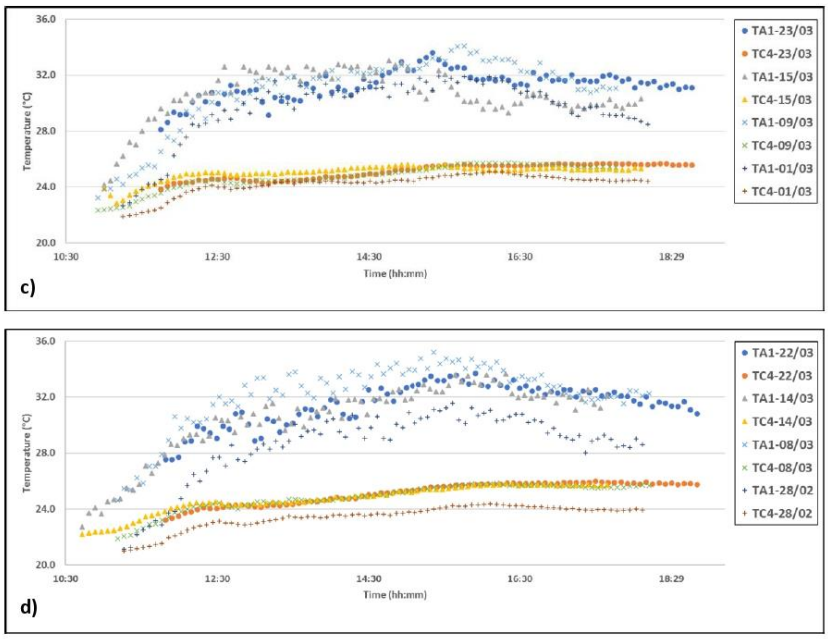

Figure 6. The inlet and outlet temperatures are shown on the different days of experimentation for the airspeed a) 1.3 m/s, b) 4.1 m/s, c) 6.4 m/s, y d) 6.6 m/s.

It was observed that the system's inlet and outlet air temperature average was 30.5 °C with a variation of ± 2.5 °C during all the days of experimentation. Therefore, it can be considered that similar environmental conditions were present during all the days of experimentation. Furthermore, the air temperature at the UEHE outlet depended on the air speed change. At lower airspeeds, outlet air temperature was lower, while when the airspeed increased, the outlet air temperature was also higher. In addition, it was observed that the temperature variation decreased, going from ± 2.5 °C at the inlet to ± 0.8 °C at the output. Table 4 shows the temperature summary for this subsection.

Table 4. The average temperature at the inlet and outlet of the UEHE is shown, as well as the temperature difference reached with the different airspeeds.

		Inlet	Outlet	
Speed (m/s)	Day (dd/mm)	T_{A1} avg. (°C)	T_{C4} avg. (°C)	ΔT avg. (°C)
1.3				
	03/03	30.7 ± 3.3	22.7 ± 0.5	8.1 ± 3.3
	11/03	32.5 ± 2.4	23.1 ± 0.5	9.4 ± 2.6
	25/03	28.8 ± 1.0	23.0 ± 0.4	5.8 ± 1.1
4.1				

	02/03	29.5 ± 2.9	23.5 ± 0.7	6.0 ± 2.3
	10/03	31.0 ± 2.3	24.1 ± 0.4	7.0 ± 2.0
	16/03	29.4 ± 1.8	24.0 ± 0.4	5.4 ± 1.6
	24/03	30.0 ± 1.7	24.0 ± 0.3	5.9 ± 1.5
6.4				
	01/03	29.6 ± 2.2	24.2 ± 0.7	5.4 ± 1.6
	09/03	30.7 ± 2.7	24.7 ± 0.9	6.0 ± 1.9
	15/03	30.6 ± 1.8	25.0 ± 0.6	5.6 ± 1.5
	23/03	31.3 ± 1.0	24.2 ± 0.5	6.2 ± 0.7
6.6				
	28/02	28.6 ± 2.5	23.4 ± 0.9	5.1 ± 1.7
	08/03	32.2 ± 2.3	24.8 ± 1.0	7.3 ± 1.6
	14/03	30.4 ± 2.7	24.7 ± 1.0	5.7 ± 1.7
	22/03	31.5 ± 1.5	25.2 ± 0.8	6.3 ± 0.9

The lowest air temperature at the outlet was recorded when the airspeed was 1.3 m/s with an average of 22.9 °C ± 0.5 °C. The most significant temperature difference was achieved with this speed, with an average of 7.7 °C ± 2.9 °C. On the other hand, when the airspeed was above 6 m/s, the highest temperature of the air at the outlet was recorded, on average 24.5 ± 1.1 °C. The lowest temperature difference was also recorded with this speed, with a value of 6.0 ± 1.7 °C. The outlet air temperature values are within the temperature range for human comfort [Mishra & Ramgopal, 2013].

3.2 Temperature variation by well.

Figures 7a), 7b), 7c), and 7d) show the air temperature variation in each well (T_{A1}-T_{A4}, T_{B1}-T_{B4}, T_{C1}-T_{C4}) and the connections between wells (T_{A4}-T_{B1}, T_{B4}-T_{C1}) at the average speed of 1.3 m/s, 4.1 m/s, 6.4 m/s, and 6.6 m/s respectively during the days of experimentation.

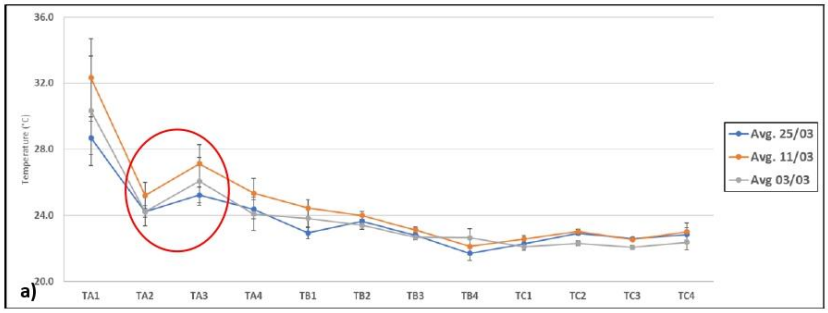

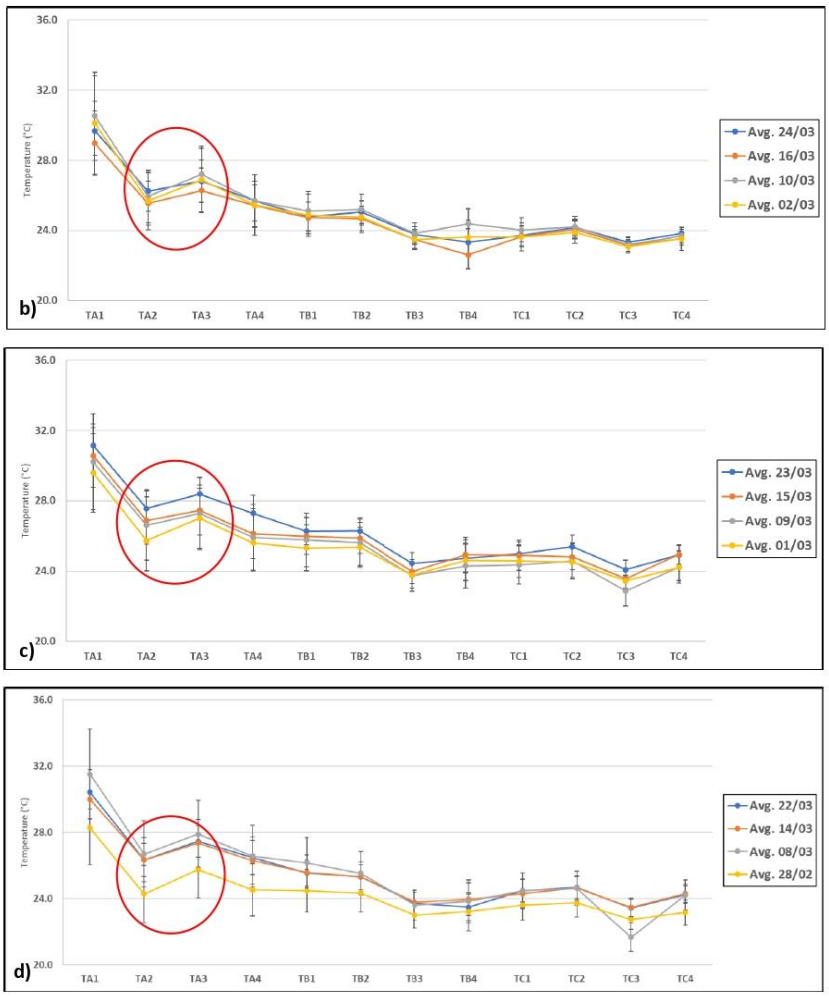

Figure 7. The average air temperature record along the UAEHE is shown on the different days of experimentation for the airspeed of a) 1.3 m/s, b) 4.1 m/s, c) 6.4 m/s, and d) 6.6 m/s.

In all the tests carried out, the air temperature increased by an average of 1.1 °C between thermocouples T_{A2} and T_{A3}. This phenomenon is due to a drain near the W_A affecting the ground temperature around it, as shown in figure 2. An average increase of 0.8 °C in air temperature was also recorded at the connection between wells W_B and W_C since, after carrying out the tests, it was found that the insulating material in that area was poorly installed. Table 5 shows the temperature summary for this subsection.

Table 5. The average inlet and outlet temperatures for wells W_A, W_B, and W_C are shown, and the temperature difference in the sections connecting wells A – B and B – C.

		W_A		W_B		W_C		W_A - W_B	W_B - W_C
		Inlet	Outlet	Inlet	Outlet	Inlet	Outlet		
Speed (m/s)	Day (dd/mm)	T_{A1} avg. (°C)	T_{A4} avg. (°C)	T_{B1} avg. (°C)	T_{B4} avg. (°C)	T_{C1} avg. (°C)	T_{C4} avg. (°C)	ΔT_{A-B} avg. (°C)	ΔT_{B-C} avg. (°C)
1.3									
	03/03	30.7 ± 3.3	23.7 ± 1.0	23.5 ± 0.6	22.0 ± 0.5	22.0 ± 0.2	22.7 ± 0.5	0.2 ± 0.5	0.1 ± 0.4
	11/03	32.5 ± 2.4	24.7 ± 0.9	24.1 ± 0.5	22.3 ± 0.5	22.4 ± 0.2	23.1 ± 0.5	0.6 ± 0.4	0.0 ± 0.4
	25/03	28.8 ± 1.0	23.7 ± 0.6	23.0 ± 0.4	22.0 ± 0.4	22.3 ± 0.2	23.0 ± 0.4	0.7 ± 0.3	-0.3 ± 0.3
4.1									
	02/03	29.5 ± 2.9	25.1 ± 1.7	24.7 ± 1.2	23.2 ± 1.0	23.4 ± 0.8	23.5 ± 0.7	0.4 ± 0.6	-0.2 ± 0.4
	10/03	31.0 ± 2.3	26.3 ± 1.5	25.5 ± 1.1	23.9 ± 0.8	24.1 ± 0.7	24.1 ± 0.4	0.7 ± 0.4	-0.2 ± 0.4
	16/03	29.4 ± 1.8	25.6 ± 1.2	25.1 ± 0.9	23.8 ± 0.8	24.1 ± 0.6	24.0 ± 0.4	0.6 ± 0.3	-0.3 ± 0.4
	24/03	30.0 ± 1.7	25.6 ± 1.1	24.8 ± 0.8	23.7 ± 0.8	24.0 ± 0.5	24.0 ± 0.3	0.8 ± 0.4	-0.3 ± 0.4
6.4									
	01/03	29.6 ± 2.2	25.9 ± 1.6	25.3 ± 1.3	24.0 ± 1.2	24.3 ± 0.9	24.2 ± 0.7	0.6 ± 0.4	-0.3 ± 0.3
	09/03	30.7 ± 2.7	26.7 ± 1.9	26.1 ± 1.5	24.6 ± 1.3	24.8 ± 1.1	24.7 ± 0.9	0.6 ± 0.4	-0.2 ± 0.4
	15/03	30.6 ± 1.8	27.0 ± 1.4	26.3 ± 1.0	24.8 ± 1.0	25.1 ± 0.9	25.0 ± 0.6	0.7 ± 0.4	-0.3 ± 0.3
	23/03	31.3 ± 1.0	27.3 ± 1.0	26.3 ± 0.8	24.9 ± 0.8	25.3 ± 0.7	24.2 ± 0.5	1.0 ± 0.3	-0.4 ± 0.4
6.6									
	28/02	28.6 ± 2.5	25.2 ± 1.8	24.7 ± 1.4	23.5 ± 1.1	23.8 ± 1.0	23.4 ± 0.9	0.4 ± 0.4	-0.3 ± 0.3
	08/03	32.2 ± 2.3	27.6 ± 1.8	26.8 ± 1.5	25.1 ± 1.2	25.4 ± 1.1	24.8 ± 1.0	0.8 ± 0.4	-0.3 ± 0.4
	14/03	30.4 ± 2.7	26.7 ± 2.0	26.0 ± 1.7	24.5 ± 1.3	24.8 ± 1.2	24.7 ± 1.0	0.7 ± 0.4	-0.2 ± 0.3
	22/03	31.5 ± 1.5	27.5 ± 1.4	26.6 ± 1.1	25.2 ± 1.1	25.7 ± 0.9	25.2 ± 0.8	0.9 ± 0.4	-0.4 ± 0.4

The largest temperature difference in the W_A well was obtained when the airspeed was 1.3 m/s, with an average value of 6.6 °C ± 2.2 °C. The smallest difference in the W_A well was obtained with a airspeed of 6.4 m/s, with an average temperature of 3.8 °C ± 0.9 °C. Something different was observed in W_B since the airspeed change did not generate a difference between the temperature change achieved. The temperature difference reached was 1.4 °C ± 0.6 °C for all velocities, although what was different was the inlet and outlet temperatures in that well. Finally, in W_C well, it was observed that depending on the airspeed, a positive or negative effect was achieved on the change in air temperature. When the airspeed was 1.3 m/s, 4.1 m/s, 6.4 m/s, and 6.6 m/s, a temperature difference of -0.7 °C ± 0.5 °C, 0.0 °C ± 0.4 °C, 0.1 °C ± 0.3 °C, and 0.4 °C ± 0.3 °C respectively.

During all the experimentation days, 71.8% and 22.3% of the total temperature difference are achieved in W_A and W_B. The WC well presented the same average temperature at the inlet and outlet, indicating that the last well's heat input under the conditions shown is insignificant or null.

3.3 Soil thermal disturbance.

Figures 8a), 8b), 8c), and 8d) show the thermal affectation of the soil in the WA well at 5 cm from the tube wall with an average airspeed of 1.3 m/s, 4.1 m/s, 6.4 m/s, and 6.6 m/s respectively during the days of experimentation.

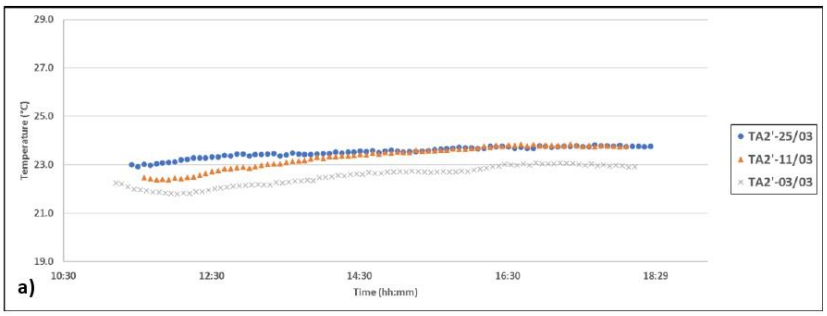
29.0
27.0
25.0
23.0
21.0
19.0
Temperature (°C)
10:30
12:30
14:30
16:30
18:29
Time (hh:mm)
TA2'-25/03
TA2'-11/03
TA2'-03/03

a)

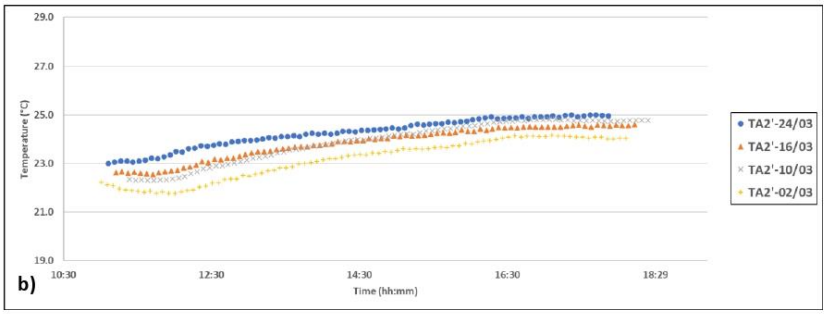
29.0
27.0
25.0
23.0
21.0
19.0
Temperature (°C)
10:30
12:30
14:30
16:30
18:29
Time (hh:mm)
TA2'-24/03
TA2'-16/03
TA2'-10/03
TA2'-02/03

b)

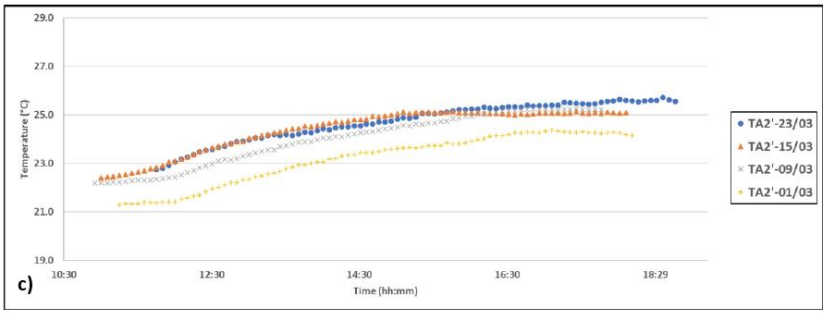
29.0
27.0
25.0
23.0
21.0
19.0
Temperature (°C)
10:30
12:30
14:30
16:30
18:29
Time (hh:mm)
TA2'-23/03
TA2'-15/03
TA2'-09/03
TA2'-01/03

c)

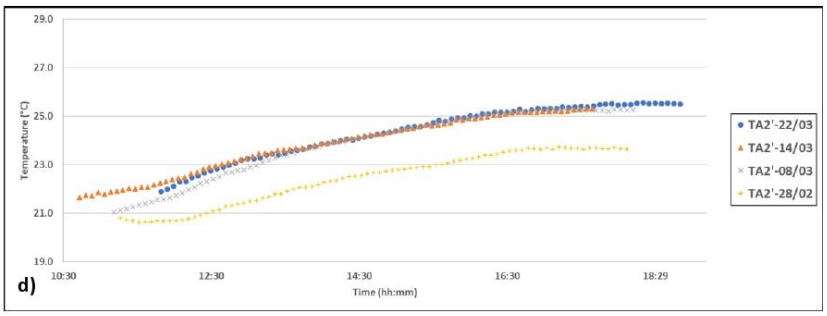

Figure 8. The temperature record is shown at 5 cm from the external wall of the tube in well A on the different days of experimentation for the speed of a) 1.3 m/s, b) 4.1 m/s, c) 6.4 m /s, and d) 6.6 m/s.

It was observed that the soil temperature at position $T_{A2'}$ at instant $t_{=0}$ changed throughout the days of the experiment. The first days of experimentation corresponded to a speed of 6.6 m/s, soil's average temperature was 21.6 °C ± 0.5 °C. The last days of experimentation corresponded to a speed of 1.3 m/s, soil's average temperature was 22.6 °C ± 0.4 °C. This change in soil temperature means that after four days of continuous use for at least 8 hours, the soil temperature increased by an average of 1.0 °C ± 0.9 °C. It should also be mentioned that the soil temperature returns to its ST after three days without using the system. Table 6 shows the temperature summary for this subsection.

Table 6. The initial temperature and the temperature difference at the end of the experiments are shown at positions $T_{A2'}$ y $T_{A2''}$.

Speed (m/s)	Day (dd/mm)	$T_{A2'}$ t=0 (°C)	$\Delta T_{A2'}$. (°C)	$T_{A2''}$ t=0 (°C)	$\Delta T_{A2''}$. (°C)
1.3					
	03/03	22.2	0.8	21.8	0.0
	11/03	22.5	1.4	22.0	0.4
	25/03	23.0	0.8	22.7	0.2
4.1					
	02/03	22.2	1.9	21.9	0.1
	10/03	22.3	2.5	22.0	0.6
	16/03	22.6	2.0	22.3	0.5
	24/03	23.0	2.0	22.7	0.5
6.4					
	01/03	21.3	3.1	21.1	0.8
	09/03	22.2	3.1	21.7	0.8
	15/03	22.4	2.7	22.1	0.9
	23/03	22.7	3.0	22.2	1.1

6.6					
	28/02	20.8	2.9	20.7	0.7
	08/03	21.1	4.2	20.9	1.3
	14/03	21.7	3.7	21.5	1.1
	22/03	21.9	3.7	21.8	1.2

In position $T_{A2'}$ the final temperature of the soil was different for the four speeds evaluated. When the airspeed was more significant than 6 m/s, the ground temperature reached 24.9 °C ± 0.1 °C, while when the speed was 1.3 m/s, the ground temperature reached 23.5 °C ± 0.1 °C. It is explained that the soil temperature difference was greater as the airspeed increased and decreased when the airspeed was lower. On the other hand, the difference in soil temperature at position $T_{A2''}$ was four times lower compared to that previously analyzed. The final temperature was similar for all experiments, with 22.5 °C ± 0.5 °C.

3.4 UEHE performance.

System performance was measured using equations 1 and 2 presented in the previous section. Calculations for equations 3 and 4, the values of Cp_{air} = 1000 (J/kg K), y ρ_{air} = 1.2 (kg/m^3) were used, which were obtained from [Cengel & Boles, 2015]. In the calculation of the COP, the electric power of the fan was taken from table 3. In equation 2, Ti and To are equal to T_{A1} and T_{C4}, respectively, in each test. The Tg value was set at 21.1 °C and was taken using the mathematical model presented by [Molina-Rodea & Wong-Loya, 2021]. Figures 9a), 9b), 9c), and 9d) show the effectiveness (ε) and the coefficient of operation (COP) of the system with an average speed of 1.3 m/s, 4.1 m/s, 6.4 m/s, and 6.6 m/s during the days of experimentation.

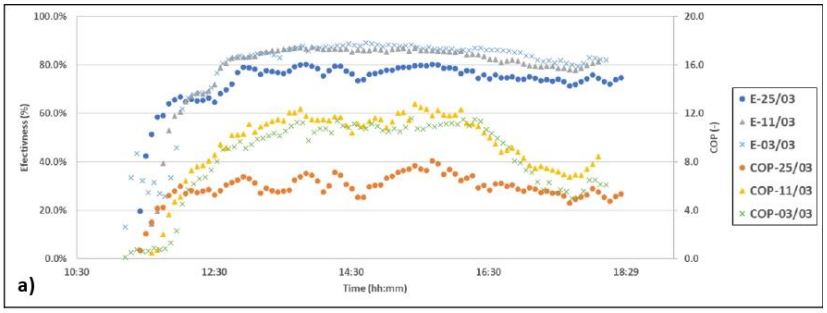

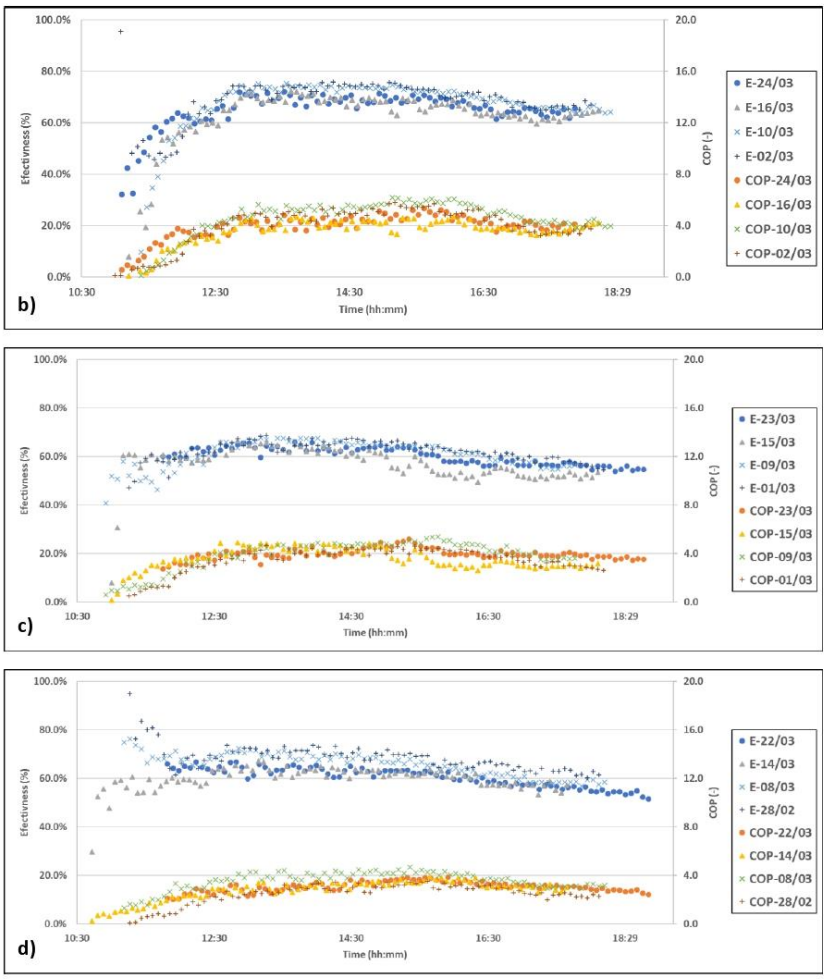

Figure 9. The effectiveness and the COP are shown on the different days of experimentation for the speed of a) 1.3 m/s, b) 4.1 m/s, c) 6.4 m/s, and d) 6.6 m/s.

It was observed that the speed of the air influences both the effectiveness and the COP. For example, when the airspeed was 1.3 m/s, the highest effectiveness and COP values were obtained, 76.7% ± 14.1% and 7.8 ± 3.0 on average, respectively. Similar in almost all the tests was the hour of peak performance that occurred between 3:00 p.m. and 4:00 p.m. Table 7 shows the temperature summary for this subsection.

Table 7. The system's cooling capacity and maximum and average COP are shown, with the peak performance hour for each day.

						Peak performance			
Air speed (m/s)	Day (d/m)	$\dot{v}$ (m³/h)	$\dot{Q}$ avg. (W)	ε avg. (%)	COP avg. (-)	$\dot{Q}$ max. (W)	ε max. (%)	COP max. (-)	Time (hh:mm)
1.3		19.8							
	03/03		57.4 ± 23.5	77.6 ± 18.1	8.2 ± 3.4	81.0	88.4	11.6	15:23
	11/03		66.9 ± 18.8	79.4 ± 13.2	9.6 ± 2.7	89.2	87.0	12.7	15:26
	25/03		41.1 ± 7.9	73.3 ± 8.7	5.9 ± 1.1	56.6	80.3	8.1	15:41
4.1		62.6							
	02/03		134.1 ± 52.0	65.0 ± 27.5	4.0 ± 1.5	196.1	75.6	5.8	15:11
	10/03		156.3 ± 45.1	67.3 ± 10.7	4.6 ± 1.3	209.6	74.8	6.2	15:09
	16/03		121.1 ± 35.6	62.0 ± 12.8	3.6 ± 1.1	160.5	68.7	4.7	16:03
	24/03		133.1 ± 32.8	64.8 ± 7.5	3.9 ± 1.0	180.9	70.8	5.3	15:37
6.4		97.8							
	01/03		189.8 ± 54.9	62.0 ± 4.3	3.5 ± 1.0	255.8	68.8	4.7	13:16
	09/03		211.5 ± 67.1	60.8 ± 5.6	3.9 ± 1.2	295.2	64.4	5.4	15:46
	15/03		195.1 ± 50.9	57.0 ± 7.8	3.6 ± 0.9	270.3	66.5	4.9	12:51
	23/03		216.7 ± 24.9	60.1 ± 3.4	3.9 ± 0.5	283.9	64.3	5.2	15:21
6.6		100.8							
	28/02		185.5 ± 61.6	68.6 ± 5.5	2.5 ± 0.8	264.8	69.4	3.5	15:37
	08/03		265.4 ± 56.6	65.9 ± 4.7	3.5 ± 0.8	349.1	68.0	4.7	15:22
	14/03		206.5 ± 62.9	59.9 ± 4.9	2.8 ± 0.8	289.6	63.7	3.9	15:39
	22/03		229.1 ± 31.8	60.6 ± 3.9	3.1 ± 0.4	287.1	62.6	3.8	15:55

The temperature difference in the UEHE and the mass flow influence the cooling capacity. The increase in air mass flow is more significant than the change in temperature difference. That is why, as the airspeed increases, the cooling power increases as well. In the calculation of the COP, although the cooling and electrical power increase with speed, the electrical power does so to a greater extent, so the COP decreases. The effectiveness goes hand in hand with the temperature difference in the UEHE. The highest effectiveness was obtained when the temperature difference was more significant and vice versa. Figure 10 shows the UEHE's average inlet and outlet temperature and compares the effectiveness and the COP depending on the air speed.

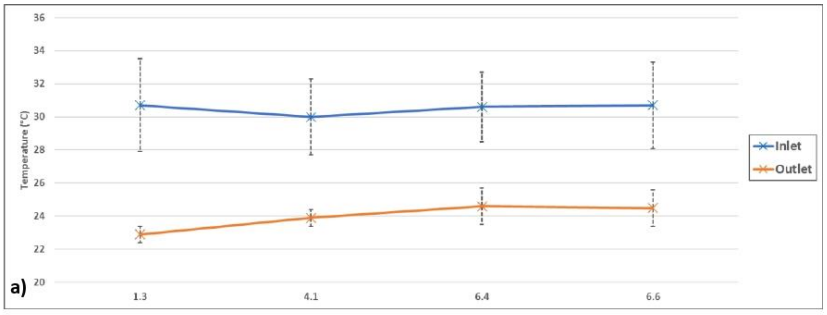

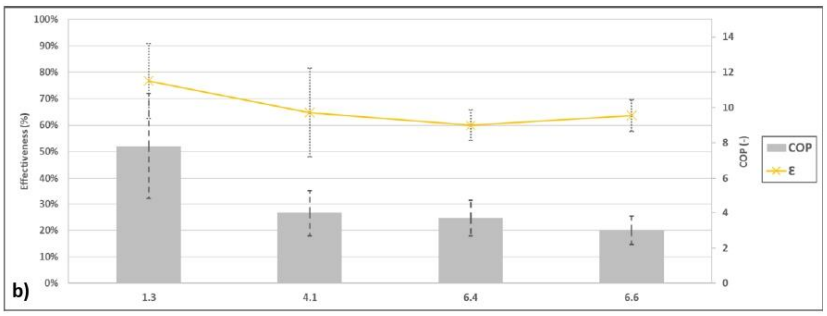

Figure 10. It shows a) the average inlet (blue) and outlet (orange) temperature of the system, b) the COP (grey), and the effectiveness of the system (yellow) for the different air speeds.

3.5 Office thermal comparison.

As shown in section 2.5, the 'wind' or 'no wind', and 'sun' or 'no sun' conditions on each wall were used to run the office thermal simulations in SketchUp and OpenStudio, along with the dimensions and thermal loads generated inside. Regarding the thermal load generated inside, a single person makes use of the office using their personal computer equipment throughout the day (9:00 a.m. to 6:00 p.m.), with natural lighting and without any other equipment that generates a significant thermal load, so 108 W are produced inside. In total, adding the internal thermal load and that generated by exposure to the sun, the selected office has a thermal load of 181.9 W to remove, with a replacement of 372 m^3 per hour to reach thermal comfort.

Comparing the results shown in table 7 with the office requirements just mentioned, the higher volumetric flow achieved in the heat exchangers is not enough to cover the necessary air changes in the office. On the other hand, with an airspeed greater than 6.4 m/s, it is possible to remove the thermal load generated in the office.

4. Conclusions.

In this work, an experimental evaluation of an UEHE planned for a narrow installation space was conducted. The UEHE comprises three vertical wells drilled on a 3 m^2 land surface. The deepest section of the UEHE is less than 3 m. The experimentation was carried out in March, one of the warmest months at the experimentation site, and aims to supply fresh air to an office. During the experimentation period, airspeed was modified as follows: 1.3 m/s, 4.1 m/s, 6.4 m/s, and 6.6 m/s. After the analysis of the results, the following conclusions are reached:

- The outlet air temperature was affected by the airspeed. The lower the airspeed inside the UEHE, the lower the outlet temperature, which implies that the outlet air temperature depends on the residence time inside the heat exchanger. Temperature drops ranged from 5.1 °C to 9.4 °C depending on the airspeed fixed.
- Outlet air temperature remained below 26 °C. This temperature is close to the human comfort range.
- Most heat loss from the air to the ground occurs at the beginning. Into the first well take place 71% of the total temperature dropped on average. On the other hand, results show

that third well performance is occasionally adverse. A reengineering must be considered attending the last well performance.

- Soil temperature rises after continuous days of operation. It is concluded that the thermal affectation of the soil around well A is more significant when the airspeed increases, reaching an increase of up to 4.3 °C when the airspeed was 6.6 m/s. The importance of this point is notorious for numerical simulation works where they consider the soil temperature with a constant value during the operation time.
- The highest COP, cooling power, and effectiveness were reached between 15:00 and 16:00 when the inlet temperature was at its zenith. It is concluded that the operation of UEHE equipment has a strong dependence on the ambient temperature.
- The cooling power and the COP are affected by the airspeed and vary inversely. The lowest cooling power (54.9 W ± 20.8 W) was obtained with the lowest mass flow (25.6 kg/m3). On the other hand, for the same mass flow, the COP registers the highest values obtained (7.8 ± 0.3) since the power consumed by the fan is the lowest.
- The performance of the UEHE covers the thermal needs of the selected office, although they do not cover the necessary number of air changes. For this it would be necessary to put more heat exchangers in parallel to increase the volumetric flow. It could also be considered to avoid the use of the last well, since thermally its contribution is not significant, but it could increase the air flow to the office.
- The UEHE presented in this work has the advantage that the installation surface and the depth of the wells are smaller than those found in published works. Comparing it with the minimum space of a service yard in low-income houses, it could be installed since it does not exceed the 3.3 m2 indicated by INFONAVIT.

5. Declarations.

Availability of data and materials.

The datasets used and/or analyzed during the current study are available from the corresponding author upon reasonable request.

Competing interests.

The authors declare that there is no conflict of interest regarding the publication of this article.

Funding.

This work was partially financed by the PAPIME-UNAM project (PE108721).

Authors' contribution.

Molina-Rodea R.: Conceptualization, Data curation, Investigation, Methodology, Validation, Writing – original draft.

Pocasangre-Chávez H.: Data curation, Investigation, Methodology, Software.

Reyna-Guillén J.: Investigation, Software, Validation.

Wong-Loya J.A.: Conceptualization, Formal analysis, Investigation, Validation, Writing – review & editing.

Acknowledgments.
Molina-Rodea R., Pocasangre-Chávez H., and Reyna-Guillén J. wish to thank the Engineering Ph.D. program of UNAM and CONACYT for the financial support provided through the scholarships.

6. References

1. Elminshawy, N. A., Siddiqui, F. R., Farooq, Q. U., & Addas, M. F. (2017). Experimental investigation on the performance of earth-air pipe heat exchanger for different soil compaction levels. Applied Thermal Engineering, 124, 1319-1327.
2. Bharadwaj, S. S., & Bansal, N. K. (1981). Temperature distribution inside ground for various surface conditions. Building and Environment, 16(3), 183-192.
3. Wei, H., Yang, D., Guo, Y., & Chen, M. (2018). Coupling of earth-to-air heat exchangers and buoyancy for energy-efficient ventilation of buildings considering dynamic thermal behavior and cooling/heating capacity. Energy, 147, 587-602.
4. Tsilingiridis, G., & Papakostas, K. (2014). Investigating the relationship between air and ground temperature variations in shallow depths in northern Greece. Energy, 73, 1007-1016.
5. Sakhri, N., Menni, Y., & Ameur, H. (2020). Effect of the pipe material and burying depth on the thermal efficiency of earth-to-air heat exchangers. Case Studies in Chemical and Environmental Engineering, 2, 100013.
6. Hou, G., Taherian, H., Song, Y., Jiang, W., & Chen, D. (2022). A systematic review on optimal analysis of horizontal heat exchangers in ground source heat pump systems. Renewable and Sustainable Energy Reviews, 154, 111830.
7. Benhammou, M., & Draoui, B. (2015). Parametric study on thermal performance of earth-to-air heat exchanger used for cooling of buildings. Renewable and Sustainable Energy Reviews, 44, 348-355.
8. Zeitoun, W., Lin, J., & Siroux, M. (2022, July). A Review–Earth-air Heat Exchanger: Applications, Advances and Challenges. In IOP Conference Series: Earth and Environmental Science (Vol. 1050, No. 1, p. 012005). IOP Publishing.
9. Ahmed, A. A., Assadi, M., Kalantar, A., Sliwa, T., & Sapińska-Śliwa, A. (2022). A Critical Review on the Use of Shallow Geothermal Energy Systems for Heating and Cooling Purposes. Energies, 15(12), 4281.
10. International Energy Agency. Renewables. 2019. Available online: www.iea.org/renewables2019 (accessed in January 2022).
11. Liu, Z., Xie, M., Zhou, Y., He, Y., Zhang, L., Zhang, G., & Chen, D. (2023). A state-of-the-art review on shallow geothermal ventilation systems with thermal performance enhancement system classifications, advanced technologies and applications. Energy and Built Environment, 4(2), 148-168.
12. Hsu, C. Y., Chiang, Y. C., Chien, Z. J., & Chen, S. L. (2018). Investigation on performance of building-integrated earth-air heat exchanger. Energy and Buildings, 169, 444-452.
13. INFONAVIT. Investigación y Análisis. Available online: www.portalmx.infonavit.org.mx (accessed in January 2022).
14. Ghoreishi-Madiseh, S. A., Kuyuk, A. F., & de Brito, M. A. R. (2019). An analytical model for transient heat transfer in ground-coupled heat exchangers of closed-loop geothermal systems. Applied Thermal Engineering, 150, 696-705.

15. Nam, Y., & Chae, H. B. (2014). Numerical simulation for the optimum design of ground source heat pump system using building foundation as horizontal heat exchanger. Energy, 73, 933-942.
16. Li, C., Mao, J., Peng, X., Mao, W., Xing, Z., & Wang, B. (2019). Influence of ground surface boundary conditions on horizontal ground source heat pump systems. Applied Thermal Engineering, 152, 160-168.
17. Dasare, R. R., & Saha, S. K. (2015). Numerical study of horizontal ground heat exchanger for high energy demand applications. Applied Thermal Engineering, 85, 252-263.
18. Díaz-Hernández, H. P., Macias-Melo, E. V., Aguilar-Castro, K. M., Hernández-Pérez, I., Xamán, J., Serrano-Arellano, J., & López-Manrique, L. M. (2020). Experimental study of an earth to air heat exchanger (EAHE) for warm humid climatic conditions. Geothermics, 84, 101741.
19. Becerra, G., Picazo, M., Aguilar, J. O., Xamán, J., Osorio, E., Hernandez, J., & Ledesma-Alonso, R. (2022). Experimental study of a geothermal earth-to-air heat exchanger in Chetumal, Quintana Roo, Mexico. Energy Efficiency, 15(4), 1-13.
20. Belloufi, Y., Brima, A., Zerouali, S., Atmani, R., Aissaoui, F., Rouag, A., & Moummi, N. (2017). Numerical and experimental investigation on the transient behavior of an earth air heat exchanger in continuous operation mode. International Journal of Heat and Technology, 35(2), 279-288.
21. Sakhri, N., Menni, Y., Ameur, H., & Chamkha, A. J. (2021). Experimental study of a stand-alone earth to air heat exchanger for heating and cooling in arid regions. Journal of Thermal Engineering, 7(5), 1206-1215.
22. Mathur, A., Mathur, S., Agrawal, G. D., & Mathur, J. (2017). Comparative study of straight and spiral earth air tunnel heat exchanger system operated in cooling and heating modes. Renewable Energy, 108, 474-487.
23. Ghosal, M. K., Tiwari, G. N., & Srivastava, N. S. L. (2004). Thermal modeling of a greenhouse with an integrated earth to air heat exchanger: an experimental validation. Energy and Buildings, 36(3), 219-227.
24. Li, H., Ni, L., Yao, Y., & Sun, C. (2019). Experimental investigation on the cooling performance of an Earth to Air Heat Exchanger (EAHE) equipped with an irrigation system to adjust soil moisture. Energy and Buildings, 196, 280-292.
25. Congedo, P. M., Baglivo, C., Bonuso, S., & D'Agostino, D. (2020). Numerical and experimental analysis of the energy performance of an air-source heat pump (ASHP) coupled with a horizontal earth-to-air heat exchanger (EAHX) in different climates. Geothermics, 87, 101845.
26. Demir, H., Koyun, A., & Temir, G. (2009). Heat transfer of horizontal parallel pipe ground heat exchanger and experimental verification. Applied thermal engineering, 29(2-3), 224-233.
27. Ahmed, S. F., Khan, M. M. K., Amanullah, M. T. O., Rasul, M. G., & Hassan, N. M. S. (2022). Thermal performance of building-integrated horizontal earth-air heat exchanger in a subtropical hot humid climate. Geothermics, 99, 102313.
28. Sarbu, I., & Sebarchievici, C. (2014). General review of ground-source heat pump systems for heating and cooling of buildings. Energy and buildings, 70, 441-454.

29. Omer, A. M. (2008). Ground-source heat pumps systems and applications. Renewable and sustainable energy reviews, 12(2), 344-371.
30. Zeng, H., Diao, N., & Fang, Z. (2003). Efficiency of vertical geothermal heat exchangers in the ground source heat pump system. Journal of Thermal Science, 12(1), 77-81.
31. Zeng, H., Diao, N., & Fang, Z. (2003). Heat transfer analysis of boreholes in vertical ground heat exchangers. International journal of heat and mass transfer, 46(23), 4467-4481.
32. Li, M., & Lai, A. C. (2015). Review of analytical models for heat transfer by vertical ground heat exchangers (GHEs): A perspective of time and space scales. Applied Energy, 151, 178-191.
33. Yang, H., Cui, P., & Fang, Z. (2010). Vertical-borehole ground-coupled heat pumps: A review of models and systems. Applied energy, 87(1), 16-27.
34. Cui, Y., Zhu, J., Twaha, S., & Riffat, S. (2018). A comprehensive review on 2D and 3D models of vertical ground heat exchangers. Renewable and sustainable energy reviews, 94, 84-114.
35. Ahmadfard, M., & Bernier, M. (2019). A review of vertical ground heat exchanger sizing tools including an inter-model comparison. Renewable and Sustainable Energy Reviews, 110, 247-265.
36. Florides, G., & Kalogirou, S. (2007). Ground heat exchangers—A review of systems, models and applications. Renewable energy, 32(15), 2461-2478.
37. Montagud, C., Corberan, J. M., Montero, Á., & Urchueguia, J. F. (2011). Analysis of the energy performance of a ground source heat pump system after five years of operation. Energy and Buildings, 43(12), 3618-3626.
38. Liu, Z., Yu, Z. J., Yang, T., Li, S., El Mankibi, M., Roccamena, L., ... & Zhang, G. (2019). Experimental investigation of a vertical earth-to-air heat exchanger system. Energy Conversion and Management, 183, 241-251.
39. Yang, W., Shi, M., Liu, G., & Chen, Z. (2009). A two-region simulation model of vertical U-tube ground heat exchanger and its experimental verification. Applied Energy, 86(10), 2005-2012.
40. Gao, X., Zhang, Z., & Xiao, Y. (2020). Modelling and thermo-hygrometric performance study of an underground chamber with a long vertical earth-air heat exchanger system. Applied Thermal Engineering, 180, 115773.
41. Ahmed, S. F., Khan, M. M. K., Amanullah, M. T. O., Rasul, M. G., & Hassan, N. M. S. (2021). A parametric analysis of the cooling performance of vertical earth-air heat exchanger in a subtropical climate. Renewable Energy, 172, 350-367.
42. Gomat, L. J. P., Motoula, S. M. E., & M'Passi-Mabiala, B. (2020). An analytical method to evaluate the impact of vertical part of an earth-air heat exchanger on the whole system. Renewable Energy, 162, 1005-1016.
43. Wei, H., Yang, D., Wang, J., & Du, J. (2020). Field experiments on the cooling capability of earth-to-air heat exchangers in hot and humid climate. Applied Energy, 276, 115493.
44. Soares, N., Rosa, N., Monteiro, H., & Costa, J. J. (2021). Advances in standalone and hybrid earth-air heat exchanger (EAHE) systems for buildings: A review. Energy and Buildings, 253, 111532.
45. Agrawal, K. K., Misra, R., Agrawal, G. D., Bhardwaj, M., & Jamuwa, D. K. (2019). The state of art on the applications, technology integration, and latest research trends of earth-air-heat exchanger system. Geothermics, 82, 34-50.

46. SMN.CONAGUA. (2022). Normal Climatológica por Estado. México. Obtained from: https://smn.conagua.gob.mx/es/informacion-climatologica-por-estado?estado=mor (accessed in January 2022).
47. Lim, K., & Lee, C. (2021). Coefficient of performance and heating and cooling thermal performance characteristics using a standing column well and cross-mixing balancing well heat exchanger methods. Energy Reports, 7, 1444-1459.
48. Ozgener, L., & Ozgener, O. (2010). An experimental study of the exergetic performance of an underground air tunnel system for greenhouse cooling. Renewable Energy, 35(12), 2804-2811.
49. Pfafferott, J. (2003). Evaluation of earth-to-air heat exchangers with a standardised method to calculate energy efficiency. Energy and buildings, 35(10), 971-983.
50. Manik, T. U. H. S. G., Sitorus, T. B., Panjaitan, M. L., & Saragih, Y. O. (2019, May). The experimental and simulation study of an earth-air heat exchanger in Medan city. In *IOP Conference Series: Materials Science and Engineering* (Vol. 505, No. 1, p. 012104). IOP Publishing.
51. Ahmadi, S., Irandoost Shahrestani, M., Sayadian, S., Maerefat, M., & Haghighi Poshtiri, A. (2021). Performance analysis of an integrated cooling system consisted of earth-to-air heat exchanger (EAHE) and water spray channel. Journal of Thermal Analysis and Calorimetry, 143(1), 473-483.
52. Bisoniya, T. S. (2015). Design of earth–air heat exchanger system. Geothermal Energy, 3(1), 1-10.
53. De Paepe, M., & Janssens, A. (2003). Thermo-hydraulic design of earth-air heat exchangers. Energy and buildings, 35(4), 389-397.
54. Mishra, A. K., & Ramgopal, M. (2013). Field studies on human thermal comfort—an overview. Building and Environment, 64, 94-106.
55. Cengel, Y. A., & Boles, M. A. (2015). Gas-vapor mixtures and air-conditioning. Thermodynamics and Engineering Approach, 8th ed.; McGraw Hill: New York, NY, USA, 725-729.
56. Molina-Rodea, R., & Wong-Loya, J. A. (2021). A new model to predict subsoil-thermal profiles based on seasonal rain conditions and soil properties. Geothermics, 97, 102261.

Capítulo V. “Modelo de comportamiento térmico de EAHE”

Resumen.

El trabajo que se presenta en este capítulo expone propuestas de EAHE de configuración vertical tipo “U” con el objetivo de aprovechar la energía residual en el interior de un pozo de exploración geotérmica ubicado en el bosque “La Primavera”, en Jalisco, México. La energía obtenida del pozo de exploración es transportada y cedida al generador de un ciclo de refrigeración por absorción. Utilizar intercambiadores de calor tipo “U” con este objetivo es una manera innovadora de aprovechar la energía remanente de los pozos geotérmicos, además de que se aprovechan tres importantes ventajas: el ahorro económico en la fase de perforación, que puede llegar a ser de hasta un 80% del presupuesto inicial de esta fase; la gran variedad de procesos industriales que requieren la energía que se obtiene de los pozos; y la disminución de gases contaminantes en comparación si la energía se hubiera obtenido con métodos convencionales. Durante la introducción se exponen diversos trabajos publicados donde se acoplan sistemas de refrigeración por absorción con intercambiadores de calor enterrados. Sin embargo, se menciona que durante la revisión bibliográfica se encontraron dos importantes inconvenientes. El primer problema recurrente consiste en omitir las características geométricas y los parámetros de funcionamiento de los intercambiadores de calor utilizados para extraer la energía del pozo. Este problema es común de encontrarse en trabajos teóricos donde calculan la energía que se puede ceder desde la formación rocosa hacia el fluido. El segundo problema consiste la falta de información sobre las características puntuales del sitio de instalación como el gradiente geotérmico o la composición del suelo. Esto provoca que se omitan o supongan algunos factores importantes que son cruciales en la fase de diseño del intercambiador de calor. Para dar solución a estos puntos, en este trabajo se presenta el modelo numérico que determina las condiciones térmicas de trabajo de EAHE. Tanto las dimensiones del EAHE como los parámetros de funcionamiento se obtuvieron con el simulador que reproduce el cambio de temperatura de un fluido que circula por el interior de un intercambiador de calor.

En la metodología se presenta el modelo físico, donde se incluyen la ubicación y la profundidad del pozo de exploración, la temperatura ambiental promedio en la zona, la litología del sitio, y las propiedades termo físicas de las distintas capas de roca. Del HE-ACS se expone su funcionamiento y los equipos que componen el sistema completo, se muestran el rango de temperaturas que se alcanza en el evaporador y se presenta un esquema de este. Posteriormente se presenta el modelo matemático, comenzando por delimitar el dominio de estudio que comprende la formación rocosa, el pozo, las paredes del UEHE, el espacio interior por donde circula el fluido, y el aislante. Se presentan las suposiciones hechas en el diseño del modelo y se justifica su aplicación con trabajos previos. Se señalan las ecuaciones que modelan el problema junto con las ecuaciones para las condiciones iniciales y de frontera. Al presentar el modelo matemático se incluye la información sobre el método numérico utilizado, el lenguaje de programación, las variables consideradas y la discretización del dominio. Antes de pasar a los resultados se presenta una validación realizada al comparar datos publicados en otros artículos. La sección de resultados comienza presentando las distintas difusividades térmicas por capa litológica, el modelo matemático que representa el gradiente geotérmico, y las características del SRA. Por último, se presentan las distintas propuestas de UEHE con sus características geométricas y de operación y se muestra la temperatura del fluido a la salida, además de que se compara con los requerimientos del HE-ACS.

Publicación.

Operational proposal of “U” type earth heat exchanger harnessing a non-producing well for energy supply to an absorption cooling system. Approach with “La Primavera” geothermal field data.

Molina-Rodea R.[a], Saucedo-Velázquez J.[a], Gómez-Franco W.R.[a], Wong-Loya J.A.[a,b*]

[a] Instituto de Energías Renovables, Universidad Nacional Autónoma de México, Priv. Xochicalco s/n, Col. Centro, Temixco, Morelos, 62580, México.

[b] Colegio de Ciencias y Humanidades, Plantel Vallejo, Universidad Nacional Autónoma de México, Av. Cien Metros s/n, Col. Magdalena de las Salinas, Distrito Federal, 07760, México.

*Corresponding author. E-mail address: jawol@ier.unam.mx (J. A. Wong-Loya)

Abstract

This paper proposes the operation of "U" type heat exchangers to harness the remaining energy in a non-producing well and use it in an absorption cooling system. The operational proposals are obtained with a previously validated numerical model that takes information from the non-producing well, from the absorption cooling system, and that can modify heat exchanger parameters to estimate the fluid temperature throughout pipes. By taking information from the well, such as the geothermal gradient, the thickness of each stratum, and its thermophysical properties, in addition to the requirements of the absorption cooling system, it is possible to reach more realistic results compared to omitting or assuming any information. In total, 31 different simulations were carried out in which the fluid velocity, the diameter and total length of the heat exchanger, or the length and thickness of the insulator material were modified. As a result, 4 different operation proposals are obtained that meet the requirements of the absorption cooling system. In this way, it is possible to combine, in a novel way, the properties of the well, the characteristics of the absorption cooling system, and the operating parameters of the "U" type heat exchanger.

Keywords:

Geothermal energy direct uses.

Wellbore heat transfer.

“U” type earth heat exchanger coupled with absorption cooling system.

Heat exchanger performance.

1. Introduction.

The increase in the world's population and the need to cover basic requirements of feeding, housing, transportation, and entertainment have increased global energy consumption [1]. Most of the energy consumed globally comes from fossil fuels. A negative effect of hydrocarbon combustion is the generation of greenhouse gases, which lead to various environmental and health problems [2]. Therefore, renewable energies are essential in combating climate change and global pollution, as they present an alternative to cover energy requirements. A way that looks quite promising in the future is the use of non-producing wells, whether oil, gas, or geothermal [3], which represents three significant advantages:

1. Savings in costs and working time during the drilling phase due to the well already drilled [4] [5].
2. A wide range of industries can benefit from the remaining energy of non-producing wells [6].
3. Using the remaining energy from the non-producing well contributes to mitigating the pollution caused by burning fossil fuels [7].

An innovative way to harness the remaining energy from non-producing wells is by installing "U" type earth heat exchangers (UEHE). The extracted energy can be used by coupling the UEHE with other devices, for example, the generator in an absorption cooling system (ACS), which replaces the compressor in conventional cooling systems. There are several works where the behavior of various configurations of ACS powered by solar energy has been studied. Those powered by geothermal energy are limited. However, we mention: [8] conducted a theoretical analysis of the operating coefficients to examine the efficiency of a working fluid. In this work, they found that with generation temperatures between 60 °C – 80 °C, evaporator temperatures of -10 °C could be reached. [9] conducted a thermodynamic analysis of a half–effect ACS (HE-ACS) driven by a low enthalpy geothermal source. The authors conclude that with a generator temperature between 55 and 70 °C, temperatures up to -16 °C can be reached in the evaporator. [10] conducted an experimental study on HE-ACS with 1 kW cooling power and evaporator temperatures down to -7 °C. Generator temperatures up to 75°C were required to achieve that cooling power. The authors also mention that low-temperature sources, such as geothermal energy, would make these systems even more efficient. Finally, [11] studied the possibility of extracting energy from wells using heat exchangers and mentioned that the fluid velocity, the insulator material's characteristics, and the fluid's inlet temperature play an important role. Some works compare the thermal behavior of distinct ACS, such as the one presented by [12] which conducted a theoretical study. They mentioned that the lowest possible evaporation temperatures could be achieved with HE-ACS with generation temperatures close to 50°C and that one way to reduce the electrical consumption of these systems is to take advantage of the waste heat from other energy sources.

On the other hand, some authors focus on the geometrical and operational characteristics of UEHE harnessing the remaining energy in non–producing wells. [13] performed a numerical study of a UEHE installed in a non-producing well, paying attention to fluid inlet pressure and temperature. Nevertheless, the heat exchanger was overestimated because they considered the ground temperature constant. [14] developed a mathematical model to evaluate the heat transfer between the heat exchanger, the wellbore, and the surroundings. They concluded that it is possible to obtain more realistic results by knowing the geothermal gradient accurately. [15] investigated the behavior of non-producing wells using numerical simulations. They concluded that geothermal site information such as geothermal gradient and heat exchanger data such as length of insulator material and fluid velocity is essential to know the behavior of heat transfer and energy production. [16] studied, through numerical simulation, the performance of a UEHE installed in a geothermal

well analyzing the mass flow and total length of the heat exchanger. They concluded that by modifying the total length of the exchanger, geothermal energy could be extracted more efficiently. [17] developed an analytical model for heat extraction rate prediction in shallow wells. This study used a parametric analysis with 12 variables, including geothermal gradient, thermophysical soil properties, fluid velocity, ambient temperature, and heat exchanger total length. They conclude that knowledge of surrounding soil temperature is a significant factor in the heat extraction rate and heat exchanger design stage. As is shown, the geothermal gradient, soil thermophysical properties, or stratum thickness from the non-producing well are crucial information that should be considered in the design stage. Omitting this information leads to underestimating or overestimating the dimensions of the heat exchanger [18].

The bibliographic review shows that two paths have been taken in research to couple the UEHE with ACS. The first focuses on the operation of the ACS, where the operating temperature ranges in the generator and the evaporator has been studied. However, the authors do not provide information on the characteristics of the UEHE or the well. The second group focuses on studying the characteristics and behavior of the UEHE in non-producing wells. Again, however, they do not delve into the information about the ACS or the well.

In this paper, different UEHE operation proposals are presented and discussed, harnessing the remaining energy in a non-producing geothermal well and supplying energy to the generator of an ACS for food preservation. To approximate both lines of investigation, the authors consider the properties and characteristics of the well, the operating conditions of the UEHE, and the working conditions of the ACS. The properties and characteristics of the non-producing well were taken from the “La Primavera” geothermal field in Jalisco, Mexico. The total depth and diameter of the well, the geothermal gradient of the site, the thermophysical properties of each stratum, and the environmental temperature of the site are considered. The operating conditions of the UEHE were obtained with a previously validated mathematical model that allows estimating the temperature of the fluid as it passes through the UEHE. With the mathematical model, it is possible to modify the total length of the UEHE, the diameter of the pipe, the characteristics of the thermal insulation, and the velocity of the fluid. The operation of the ACS is simulated with software that allows knowing the generator and evaporator temperature and the thermal power required in the generator. Finally, the best operating proposals are presented considering the above conditions. Thus, in this work, for the first time, the operating characteristics of the UEHE, requirements of the ACS, and properties of the non-producing well are considered to avoid errors in overestimating or underestimating the UEHE.

2. Material and Methods.

This section presents the properties of the non-producing well, the characteristics of the ACS, and the mathematical model of the UEHE.

2.1 Non-producing well.

The LP2 well located in the "La Primavera" geothermal field is considered in this work. The location of the geothermal field, also known as "Cerritos Colorados," corresponds to the "La Primavera" forest, 20 km from Guadalajara city, in Jalisco, Mexico. The prevailing climate throughout the year is mild sub-humid with an average annual temperature of 21.6 °C, as the National Water Commission (CONAGUA) reported. Figure 1 shows the average hourly ambient temperature for each year's season in the "La Primavera" forest. Currently, the geothermal field is commissioned by the Federal Electricity Commission (CFE) for exploration. Thirteen wells with depths greater than 100 m have been drilled in the geothermal field [19]. Figure 2 shows a representation of the lithology of the "La Primavera" geothermal site, and Table 1 shows the thickness and thermophysical properties of each stratum shown in the lithology [20].

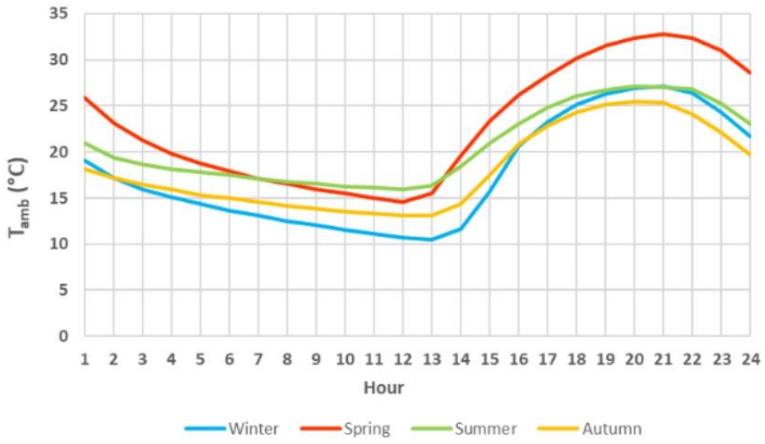

Figure 1. Average annual ambient temperature of each season in "La Primavera" forest. [21].

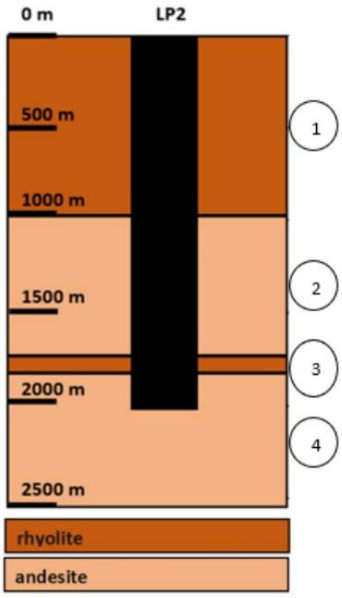

Figure 2. Representation of the lithology of the well "LP2"

Table 1. Thickness and thermo-physical properties of "LP2" well.

Layer	Thickness *(m)*	Specific heat *(J/kg K)*	Thermal conductivity *(W/m K)*	Density *(kg/m³)*
1 rhyolite	1000	900	2.08	2200
2 andesite	750	1073	1.28	2460
3 rhyolite	100	1074	2.68	2460
4 andesite	1150	1151	1.28	2180

The LP2 well has an approximate depth of 2000 m and a diameter of 0.216 m (8 ½") at its deepest part, as seen in Figure 3. The geothermal gradient of the site is 114.9 °C/km, reported by [22, 23].

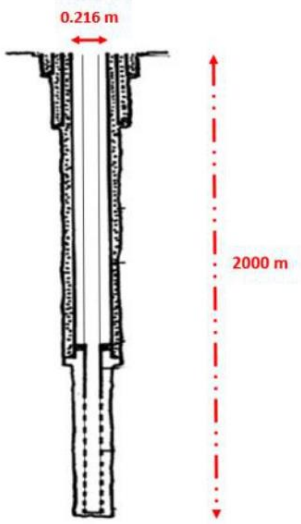

Figure 3. Scheme of the "LP2" well.

2.2 Absorption Cooling System.

In the literature review, it was found that the "half-effect" configuration is the one that requires the lowest generation temperature among all the types of ACS. For example, to produce an evaporator temperature below 0 °C, the generation temperature is in the range of 70 °C to 90 °C [Domínguez-Izunza, 2014]. By having the lowest generation temperatures, it is intuited that UEHE total length must also be the shortest. Therefore, a half-effect absorption cooling system (HE-ACS) with a mixture of H_2O/LiBr was used in this work to couple with UEHE from the "LP2" well. In addition, the H_2O/LiBr mixture was chosen as the refrigerant and absorbent solution, respectively, since the range of refrigeration temperatures is sufficient to achieve food preservation [24, 25].

As can be seen in Figure 4, the HE-ACS consists of a refrigerant solution circuit (delimited by the dotted red line) and two mixed solution circuits, one at low pressure and the other at high pressure (delimited by the green dotted line). In this system, the enriched mixture of refrigerant and LiBr found in the absorber (A_1) is pumped (P_1) to the low-pressure generator (G_1), previously passing through the solutions heat exchanger (SHE_1) to increase cycle efficiency. In the low-pressure generator, water evaporation occurs due to the managed energy (Q_2). Then, the mixture passes to the absorber of the high-pressure circuit (A_2). In the high-pressure absorber, the evaporated water is again mixed with the LiBr solution, which is pumped (P_2) to the high-pressure generator (G_2), which, as in the low-pressure circuit, previously passes through the solutions exchanger heat (SHE_2). The energy supplied (Q_4) in the high-pressure generator causes the evaporation of the water fraction, which passes to the condenser (C). A phase change occurs in the condenser (Q_5). Now in a liquid state, the water passes through the expansion valve (V_3), where the pressure and temperature decrease to reach the evaporator (E) and produce the cooling effect. Subsequently, the refrigerant reaches the low-pressure absorber, and the cycle is repeated. The LiBr mixture that did not

evaporate in both generators passes through the respective solution heat exchangers (SHE_1 and SHE_2), passes to the expansion valves (V_1 and V_2), and reaches their respective absorbers. In a HE-ACS, the energy obtained from the non-producing well is delivered to both generators (Q_1 and Q_2).

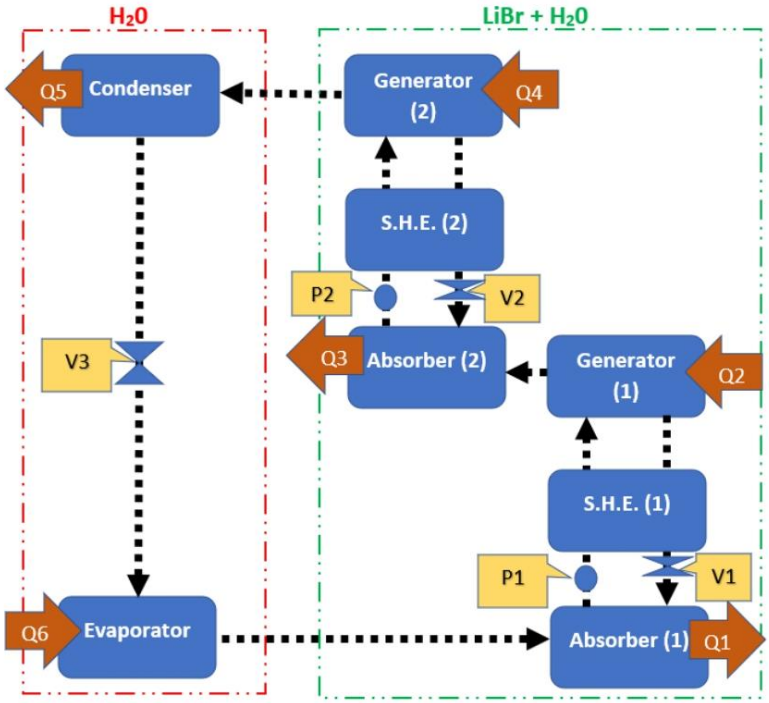

Figure 4. Scheme of a half-effect absorption cooling system.

2.3 UEHE mathematical model.

2.3.1 Study domain.

Figure 5 shows the study domain, which includes the ground, the well, the walls of the UEHE, the insulator material, and the internal space of the UEHE. The heat transfer phenomenon occurs due to the temperature difference between the ground around the pipes and the fluid circulating through the pipes. Since the temperature of the soil increases as a function of depth, the outlet fluid temperature will also be a function of the path through the UEHE and its geometric characteristics.

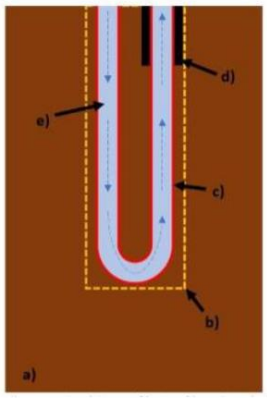

Figure 5. Study domain: a) ground (brown), b) well walls (yellow), c) UEHE walls (red), d) insulator material (black), e) UEHE internal space (blue).

2.3.2 Assumptions.

Considering mentioned above, the assumptions considered for the mathematical model are:

1. The mean fluid velocity is considered as the velocity profile inside the pipes.
2. Inside the UEHE, heat convection is the leading heat transfer mechanism.
3. The ground around the UEHE is considered in two dimensions.
4. Outside the UEHE, heat conduction is the dominant heat transfer mechanism.
5. The UEHE wall thickness is negligible.
6. The thermophysical properties of the soil change depending on the soil type.
7. The initial temperature distribution and the boundary temperature is equal to the geothermal gradient.
8. The inlet fluid temperature remains constant.
9. The effect of environmental factors on soil surface temperature is negligible.
10. The phase change of the fluid as it passes through the pipes is omitted.

Assumptions 1 and 2 are considered since some authors who have studied the EAHE performance have simplified the fluid velocity profile with a mean fluid velocity and a pure convective heat transfer mechanism [26, 27, 28]. In this regard, with a constant velocity value, it was established that the internal space of the UEHE is one-dimensional since the fluid moves in a fixed direction with a selected velocity. Besides, considering that the fluid flows under a turbulent regime (Reynolds >

2300) to benefit heat transfer [29], a purely convective energy transfer regime is selected. In assumption 3, it was considered that the energy is transferred predominantly in the radial direction because the thermal gradients in that direction are more significant than the axial gradients, although they are also considered. Assumption 4 is supported by several published papers that similarly analyze heat transfer in the soil [30, 31, 32]. Furthermore, the convective flows in that specific region have not yet been established. Assumption 5 is considered since the thickness of the pipe wall is very small compared to the soil layer. It is also known that when the heat transfer is in series, the section where it occurs at the slowest rate is the most critical [33, 34]. In assumption 6, the thermophysical properties of each stratum were obtained from the presented lithology. Furthermore, it is assumed that the filling of the well is made with the same material from each stratum. Assumption 7 was taken from the geothermal gradient information, the most realistic temperature data available. Assumptions 8 y 9 are considered in the absence of specific information, taking the temperature value shown in section 2.1. In other works, an average inlet temperature has also been considered in the absence of information [35]. Finally, assumption 10 is taken because this work does not focus on studying the phase change in the fluid, in addition to the fact that the same consideration has been taken in other published works [34].

2.3.3 Numerical model.

For this problem, the equation that describes the transient distribution of temperatures inside the UEHE and in the surrounding ground is the general energy equation (1), where T is the temperature, υ is the fluid velocity, and α is the thermal diffusivity.

$$\frac{\partial T}{\partial t} + \nabla \cdot (\upsilon T) = \alpha \cdot \nabla^2 T \quad (1)$$

The initial temperature distribution is:

$$T_{(X,Z,t=0)} = T_{i(z)} \quad (2)$$

where $T_{i(z)}$ is the temperature given by the geothermal gradient as a function of depth.

The boundary conditions used in this problem are Dirichlet type as shown below, where T_0 and T_n are the average annual temperature and bottom hole temperature, respectively.

$$T_{(X=0=n,Z,t)} = T_{i(z)} \quad (3)$$

$$T_{(X,Z=0,t)} = T_0 \quad (4)$$

$$T_{(X,Z=n,t)} = T_n \quad (5)$$

This type of boundary uses a constant temperature value. For the present problem, it is applicable since the information on the geothermal gradient of the study site is available. In addition, the

boundary is located at a considerable distance from the well walls so that the thermal disturbance does not affect this fixed value.

The finite volume numerical method was used to analyze the heat transfer inside and around the UEHE. This computational numerical method divides the study domain into a finite number of control volumes. Subsequently, all the terms in equation 1 (temporal, convective, and diffusive) are discretized and solved for each control volume [36, 37]. The discretization method consists of integrating the differential equation for each control volume. This way, a discrete equation is obtained for each control volume involving the variable under study and its relationship with the adjacent control volumes. Therefore, the discretized equation expresses the conservation principle for a control volume, just as the differential equation does for an infinitesimal point.

A numerical code in the Fortran90 programming language was implemented to approximate the solution of the resulting system of discretized equations. In total, 7,000 control volumes were used to represent the study domain; 2,000 to represent the internal space and the rest for the surrounding soil. Figure 6 shows that the distribution of the control volumes is irregular, presenting greater density in the surroundings of the UEHE walls, which is the place where the energy transfer occurs on a larger scale. The resulting system of equations for each control volume is ordered into a system of linear equations. This system of equations is solved using the iterative tridiagonal matrix algorithm (TDMA) that solves the resulting system in each dimension separately [38].

The main advantage of this mathematical model is that it allows estimating the temperature of the fluid as it passes through the UEHE as a function of the diameter and total length of the pipe, the fluid velocity, the length and thickness of the insulator material, soil thermophysical properties, and geothermal gradient.

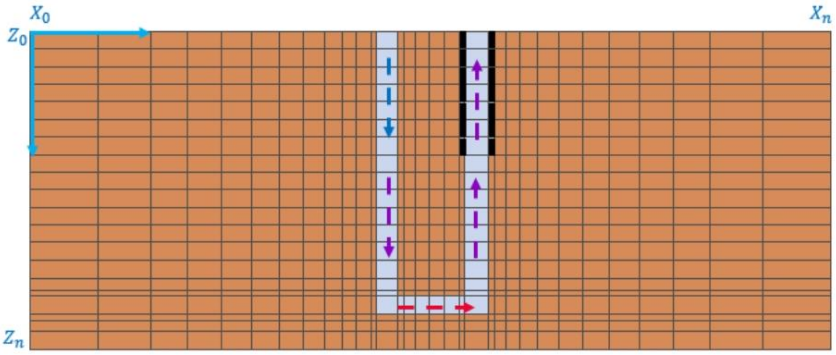

Figure 6. The discretized study domain is shown with an increase in the density of control volumes in the vicinity of the UEHE.

2.3.4 Model validation.

The mathematical model presented in this section was validated against numerical results by [9], who presented 2 study cases. The first corresponds to a UEHE proposed for a 100 m depth well. Geometrical and dynamical parameters are diameter = 0.0254 m, total length = 200 m, fluid velocity = 1 m/s, insulator thickness and length = 0 m. In this study case, the soil was compounded in 3 layers,

Table 2 shows the thermophysical properties of each one. The bottom hole temperature was 68.6 °C. The authors reported temperatures to correspond at the heat exchanger outlet, and at 112 m of total length, with 28.2 °C and 65 °C, respectively.

Table 2. Data used for the numerical model validation. [9]

Layer	Specific heat *(J/kg K)*	Thermal conductivity *(W/m K)*	Density *(kg/m³)*
Pumice	885	1.77	2360
Ash	920	1.54	2180
Basalt	880	0.22	2700

The second was a thermal analysis in the "Las Tres Virgenes" geothermal field. This study was done with the "W-LV5" well, which has 1850 m depth. The bottom hole temperature estimated was 219.3 °C at 1800 m depth. Geometrical and dynamical parameters are diameter = 0.0254 m, total length = 3700 m, fluid velocity = 7 m/s, and insulator thickness and length = 0 m. [20] reported a 156.7 °C/km geothermal gradient and the following thermophysical properties ($CP_4 = 1000\ J/kg\ K$, $\rho_4 = 2670\ kg/m^3$). The outlet fluid temperature simulated was 72.8 °C. Table 3 presents a detailed comparison of each study case's parameters, results, and relative error. As can be seen, the outlet air temperature predicted by the model used in this work corresponds with the reported temperature. Furthermore, the maximum relative error and the maximum temperature difference are 4.6% and 1.6 °C, respectively. Therefore, the mathematical model is suitable for predicting the thermal performance of the UEHE.

Table 3. Prognosticated temperatures and reported temperatures for the model validation.

	Geometrical and dynamical properties			Inlet air temperature (°C)	Outlet air temperature (°C)		Relative Error (%)
	D (m)	T_L (m)	V (m/s)		Reported	Model	
Study case 1	0.0254	200	1	24.0	28.2 65	26.9 63.4	4.6 2.5
Study case 2	0.0254	3700	7	30.0	72.8	74.3	2.1

3. Results.

This section presents the results of this work. First, the data from the non-producing well used in the numerical modeling and the characteristics of the HE-ACS are shown. Before showing the results of the simulations, the properties of the working fluid and the variables that affect the temperature of the fluid at the outlet are presented.

3.1 Non-producing well characteristics.

The information used from the non-producing well corresponds to the geometry of the well, the thermophysical properties of each stratum, and the geothermal gradient. From the geometry of the well shown in section 2.1, the diameter and depth are obtained, which limits the total length of the UEHE and the diameter of the pipe. Regarding the thermophysical properties, the thermal diffusivity per layer is calculated from the information shown in Table 1 with equation 6, in addition to delimiting each layer by its thickness. Table 4 shows the thickness of each layer and its thermal diffusivity.

$$\alpha_r = \frac{k_r}{\rho_r \cdot CP_r} \quad (6)$$

Table 4. Thermal diffusivity and thickness of each stratum presented in the lithology.

Layer	Thickness *(m)*	Thermal diffusivity *(m^2/s)*
1 rhyolite	1000	$1.05_{x10}{}^{-6}$
2 andesite	750	$4.89_{x10}{}^{-7}$
3 rhyolite	100	$1.01_{x10}{}^{-6}$
4 andesite	1150	$5.11_{x10}{}^{-7}$

As shown in section 2.1, the geothermal gradient in "La Primavera" is 114.9 °C/km. Considering that the average annual ambient temperature for the site where the geothermal well is located is 21.6 °C and that the total depth of the well is 2000 meters, the mathematical expressions of the geothermal gradient in the downward and upward directions correspond to equations 7 y 8, respectively. The information from Table 4 and equations 7 and 8 is used in the numerical model to carry out the simulations.

$$T_{i\,(X,0<Z<2000,t)} = 21.6 + (0.115 \cdot Z) \quad (7)$$

$$T_{i\,(X,2000<Z<4000,t)} = 481.6 - (0.115 \cdot Z) \quad (8)$$

3.2 HE-ACS proposed.

The HE-ACS proposed for this work has a cooling capacity of 380 kW and an evaporation temperature of 5 °C, which are sufficient for food preservation. With the help of the Engineering Equation Solver (EES) software, it is possible to know the amount of energy that must be supplied to both HE-ACS generators and the inlet fluid temperature to achieve evaporation of the water fraction. Table 5 shows the values of Q_2, Q_4, and the generation temperature (T_G) obtained from the EES.

Table 5. The power in each generator (Q_2 and Q_4) and the generation temperature (T_G) are shown.

Q_2 (kW)	Q_4 (kW)	T_G (°C)
399.7	396.4	60.0
398.9	396.5	62.2
398.1	396.4	64.4
397.2	396.3	66.7
396.2	396.3	68.9
395.3	396.1	71.1
394.5	395.7	73.3
393.5	395.5	75.6
391.9	396.5	77.8
391.2	396.3	80.0

The thermal power in both generators must be covered for the energy delivered by the UEHE to achieve the desired evaporation temperature. Obtaining the average of both generators results in a power of 791.9 kW with a generation temperature of 70 °C. Furthermore, from the same software (EES), it was obtained that the temperature at which the H_2O/LiBr mixture enters both generators is 35 °C on average. This information helps compare the numerical simulation results with the HE-ACS requirements.

3.3 UEHE operational proposals.

In this work, water at ambient temperature was chosen as the working fluid to circulate inside the UEHE. It was chosen in this way since there is information on the average ambient temperature for the well site, as shown above. The inlet water temperature value used was 21.6 °C. This value was kept constant (assumption 9). The thermophysical properties of water used in the mathematical model were taken from [39]. The values used belong to the range of temperatures shown in Figure 1 and are as follows: $\rho_{H_2O} = 1000\ kg/m^3$, $CP_{H_2O} = 4187\ J/kg\,K$, $k_{H_2O} = 0.582\ W/m\,K$, $\alpha_{H_2O} = 1.4_{x10}{}^{-7}\ m^2/s$. For the insulating material, thermal diffusivity of $\alpha_{insulator} = 1.08_{x10}{}^{-9}\ m^2/s$ was set.

With the information collected from the well and the working fluid, various simulations were carried out to find the operational proposal for the UEHE that meets the requirements of the HE-ACS, and that is also the one with the lowest cost in materials. The UEHE operational proposals are based on modifying any of the parameters of the mathematical model. Parameters are shown below in Table 6:

The first model, or base model, was made with the following values:

- Pipe diameter was established at D = 0.076 m (3'') since it is the maximum allowable diameter considering the characteristics of the "LP2" well presented above.
- The UEHE total length was set at T_L = 4000 m to use the maximum depth of the well.
- The fluid velocity was set at v = 6 m/s, close to the recommended limit for water flow in pipes.
- The characteristics of the insulating material were taken as l_L = 1000 m and l_T = 1'' freely.

The base model gave as a result that the outlet fluid temperature of the UEHE is 174.7 °C. Taking this result as the starting point, the value of each parameter was modified separately to observe the difference in the results. In total, 31 tests were carried out, each with different values for each parameter.

The variation of each parameter was carried out as explained below:

- The fluid velocity was changed in steps of 2 m/s starting at 2 m/s, and going up to 12 m/s. It is known that the velocity of water inside a pipe is not recommended to exceed 6 m/s, but in this work, some values above that value were taken only as comparison points.
- The pipe diameter was changed in 0.025 m (1") steps from 0.05 m (2") to 0.125 m (5"). As with velocity, some values are outside of what is allowable, precisely due to the well diameter, but again, they are used only as a point of comparison.
- The thickness of the insulator material was changed from 0.025 m (1'') to 0.075 m (3'') in 0.025 m (1'') steps.
- The total length of the insulator material started at 250 m and went up to 1000 m with differences of 250 m. Modeling without insulator material was also carried out.
- The UEHE total length was fixed from 2,000 m to 4,000 m in steps of 500 m.

Table 6. Parameters used in the mathematical model.

Parameter	Range	Step
Fluid velocity (v)	*2 m/s – 12 m/s*	*2 m/s*
Pipe diameter (D)	*0.025 m – 0.125 m*	*0.025 m*
UEHE total length (T_L)	*2000 m – 4000 m*	*500 m*
Insulator length (I_L)	*0 m – 1000 m*	*250 m*
Insulator thickness (I_T)	*0.025 m – 0.075 m*	*0.025 m*

The graphs presented in Figures 7 - 11 show the results of the outlet fluid temperature depending on the variation of each exposed parameter. Table 7 shows the different parameters used in each simulation and the outlet fluid temperature.

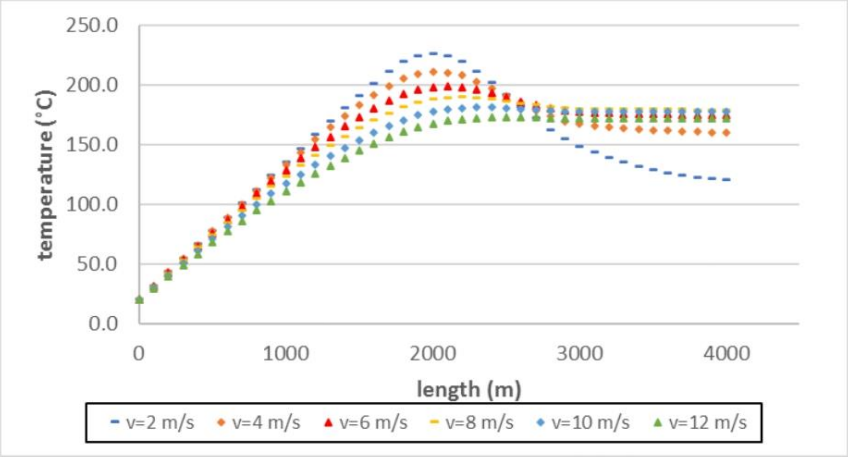

Figure 7. Fluid temperature through the UEHE as function of fluid velocity.

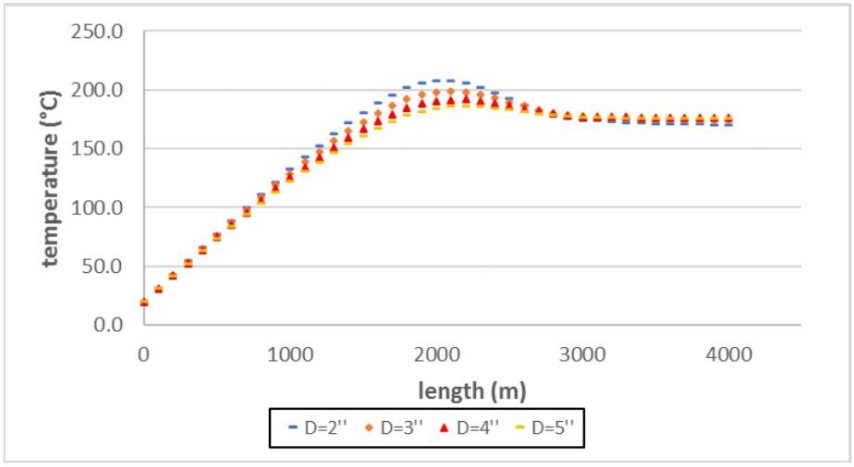

345

346 *Figure 8. Fluid temperature through the UEHE as function of pipe diameter.*

347

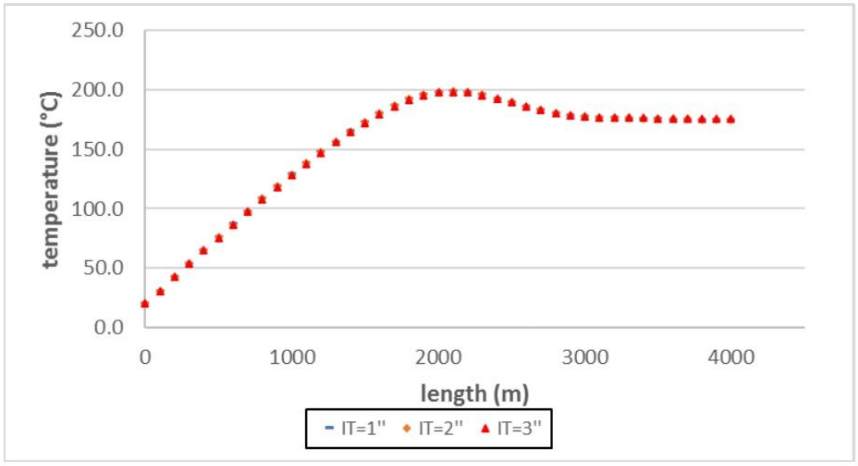

348

349 *Figure 9. Fluid temperature through the UEHE as function of insulator thickness.*

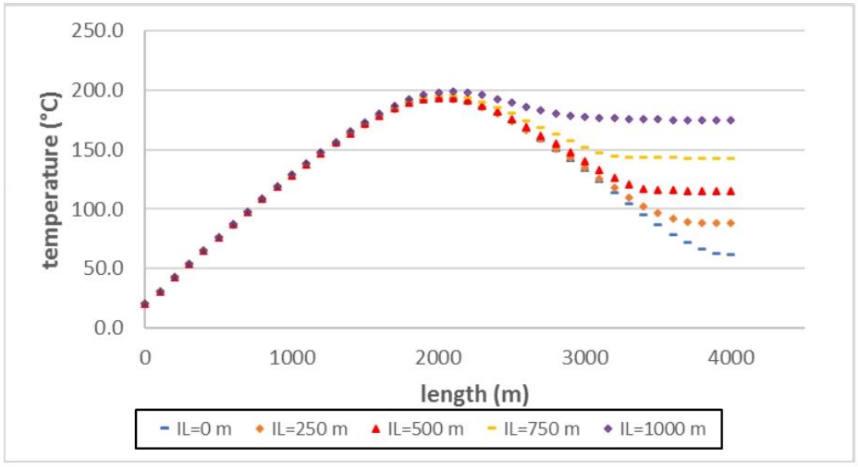

350

351 *Figure 10. Fluid temperature through the UEHE as function of insulator length.*

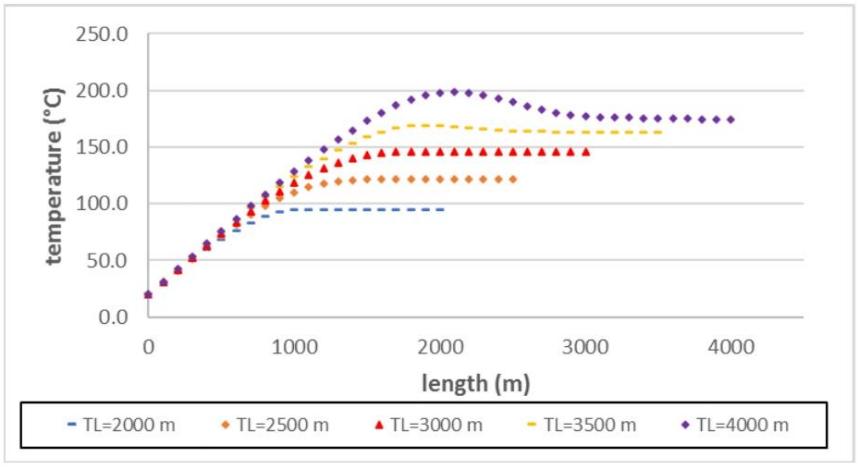

352

353 *Figure 11. Fluid temperature through the UEHE as function of heat exchanger total length.*

354 *Table 7. Values for the simulations presented in figures 6 to 10.*

Test	(v)	(D)	(l_T)	(l_L)	(T_L)	(T_O)
v=2 m/s	2	3	1	1000	4000	120.4
v=4 m/s	4	3	1	1000	4000	160.0
v=6 m/s	6	3	1	1000	4000	174.7
v=8 m/s	8	3	1	1000	4000	178.7
v=10 m/s	10	3	1	1000	4000	177.1

v=12 m/s	12	3	1	1000	4000	172.0
D=2''	6	2	1	1000	4000	170.0
D=3''	6	3	1	1000	4000	174.7
D=4''	6	4	1	1000	4000	175.8
D=5''	6	5	1	1000	4000	175.1
I_T=1''	6	3	1	1000	4000	174.7
I_T=2''	6	3	2	1000	4000	175.1
I_T=3''	6	3	3	1000	4000	175.4
I_L=0 m	6	3	1	0	4000	60.8
I_L=250 m	6	3	1	250	4000	88.6
I_L=500 m	6	3	1	500	4000	115.5
I_L=750 m	6	3	1	750	4000	142.4
I_L=1000 m	6	3	1	1000	4000	174.7
T_L=2000 m	6	3	1	1000	2000	94.7
T_L=2500 m	6	3	1	1000	2500	121.9
T_L=3000 m	6	3	1	1000	3000	145.9
T_L=3500 m	6	3	1	1000	3500	162.2
T_L=4000 m	6	3	1	1000	4000	174.7

Figure 7 shows that the gradual increase in fluid velocity from 2 m/s to 8 m/s generates an increase in the outlet fluid temperature. Conversely, outlet fluid temperature decreases when the fluid velocity changes from 10 m/s to 12 m/s. The above is because, although the necessary turbulence occurs inside the UEHE, the residence time of the fluid is shorter, and therefore, its temperature is also lower compared to the previous cases.

The change in the pipe diameter is presented in Figure 8, and it is observed that when going from 2'' to 5'', the change in the outlet fluid temperature is insignificant, going from T_O = 170.0 °C to T_O = 175.1 °C, respectively. The change in the insulator material thickness is shown in Figure 9 and shows the same as in the previous case. The outlet fluid temperature goes from T_O = 174.7 °C, T_O = 175.1 °C, and T_O = 175.4 °C when analyzing an insulator thickness of 1'', 2'', and 3'', respectively.

On the other hand, when modifying the UEHE and insulator's total length, significant changes are generated at the outlet fluid temperature. For example, in Figure 10, when the length of the insulator material is evaluated, it is observed that the outlet fluid temperature goes from T_O = 60.8 °C in the absence of the insulator, up to T_O = 174.7 °C when the length of the insulator material was 1000 m. The same phenomenon is observed in Figure 11 with the change in total length of the UEHE, since when the length is equal to 2000 m, the outlet fluid temperature was T_O = 94.7 °C. In comparison, covering the entire well, the temperature increases to T_O = 174.7 °C. These results show that the numerical model has greater sensitivity to the change of T_L and I_L.

The next step is to give the best UEHE operational proposal based on the previous results, and with the objective of meeting the needs of the HE-ACS generators, and for this, another 8 simulations were carried out. On this occasion, some parameters were delimited based on previous results. For example, the total length of the UEHE was set at 2000 m since it was observed that with a greater length, the outlet fluid temperature exceeds the requirements of the HE-ACS generators. A similar case occurs with the thickness of the insulator material, which was set at 0.025 m (1'') since it was observed that no significant changes are generated with a greater thickness. Regarding the pipe diameter, simulations were carried out only with 0.05 m and 0.076 m (2'' and 3'') since with values

greater than 0.101 m (4''), the size of the well would be exceeded. The fluid velocity was changed between 4 m/s and 6 m/s, not to exceed the recommended limit. Finally, the length of the insulator material was changed between 0 m and 250 m. Figure 12 and Table 7 show the results and values used in the eight final simulations, respectively.

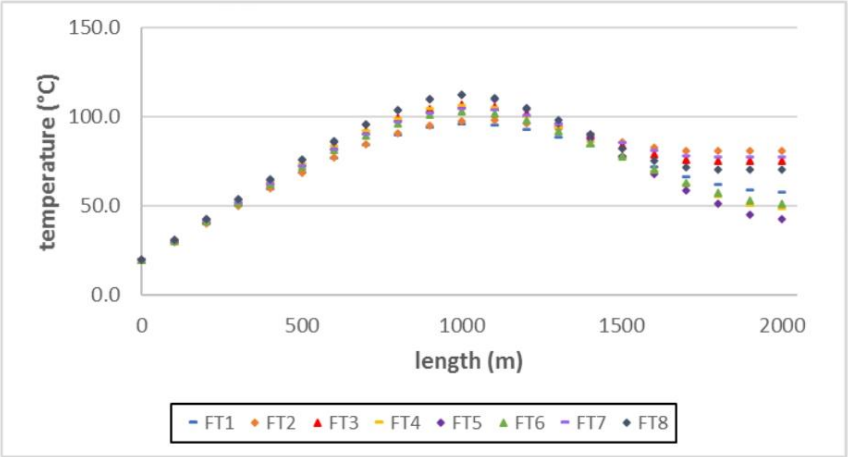

Figure 12. Fluid temperature through the UEHE in the 8 final tests.

Table 8. Values for the simulations presented in figure 11.

Test	(*v*)	(*D*)	(I_T)	(I_L)	(T_L)	(T_O)
FT1	6	3	1	0	2000	57.2
FT2	6	3	1	250	2000	80.7
FT3	4	3	1	250	2000	75.0
FT4	4	3	1	0	2000	48.5
FT5	4	2	1	0	2000	42.8
FT6	6	2	1	0	2000	51.2
FT7	6	2	1	250	2000	77.3
FT8	4	2	1	250	2000	70.5

Table 8 shows that the conditions given in FT1, FT4, FT5, and FT6 are not adequate to supply energy to the generators of the HE-ACS. Furthermore, in all these tests, the repeated parameter is the insulator length, which was 0 m. Therefore, these design proposals were discarded.

The remaining operational proposals were compared to the HE-ACS requirements to compare if they met the required heat flow. Equations 7 and 8 were used, where Q_2 and Q_4 are the power of both generators, Q_T is the total power of the generators, and T_A is the temperature of the H_2O/LiBr mixture before entering the generators.

$$Q_2 + Q_4 = Q_T = \dot{m}_{H_2O} \cdot Cp_{H_2O} \cdot (T_O - T_A) \quad (7)$$

$$v \cdot A \cdot \rho_{H_2O} = \frac{Q_T}{Cp_{H_2O} \cdot (T_O - T_A)}$$	(8)

By using equation 8 for each of the pipe diameters used, it is obtained that the minimum fluid velocity is 2.7 m/s and 1.2 m/s for 0.05 m and 0.076 m (2'' and 3'') pipe diameter, respectively. Comparing these results with those obtained in Table 7, the fluid velocity values of FT2, FT3, FT7, and FT8 comply with the mass flow necessary to supply energy to the HE-ACS generators. Of these 4 remaining tests, FT8 is the one that best meets the requirements since it uses a smaller diameter pipe and a lower fluid velocity, which translates into less power for the device in charge of moving the fluid. While in FT2, both the fluid velocity and the pipe diameter are overestimated.

Therefore, it is concluded that the values of fluid velocity, pipe diameter, length and thickness of the insulator material, and UEHE total length of the FT2, FT3, FT7, and FT8 tests achieve the final temperature requirements (T_O) and heat flow (Q_T) necessary for the operation of a HE-ACS with refrigeration capacity and temperature in the evaporator of 791.9 kW and 5 °C, respectively.

4. Conclusions

This paper presents different UEHE operational proposals to harness the remaining energy of a non-producing well and use it in an ACS for food preservation. To obtain more realistic results, in this work, the authors gather information from the non-producing well, the ACS, and the UEHE, which is later used in a mathematical model. The non-producing well is in the "La Primavera" geothermal field. The information gathered corresponds to the diameter and total depth of the well, the composition of each stratum and its thickness, the geothermal gradient, and the ambient temperature of the site. Regarding the information collected from the ACS, the cooling power, the evaporation and generation temperature, the power required in both generators, and the refrigerant inlet temperature are considered. On the UEHE, its total length, the diameter of the pipe, the thickness and total length of the insulating material, and the fluid's velocity are also considered.

The operational proposals are obtained with a mathematical model in Fortran90 language that uses the information mentioned above and estimates the temperature of the fluid as it passes through the UEHE tubes. The mathematical model is previously validated with published results on the operation of two UEHEs under different operating conditions, with a maximum relative error of 4.6%. However, the limitations of the mathematical model are shown in the assumptions made during the design phase, which include a constant fluid velocity, a constant inlet fluid temperature, the wall thickness of buried pipes, and the effect of environmental factors on the ground surface are neglected, among others.

To obtain the best operational proposals, 31 simulations were carried out in which one of the following UEHE parameters was modified: total length, pipe diameter, fluid velocity, and geometry of the insulator material, while the information from the non-producing well and the ACS remained constant in each one. The first 23 simulations were carried out to observe the sensitivity of the mathematical model to the change of each parameter separately, where a greater sensitivity to the change in the total length of the UEHE and the insulating material was found. Subsequently, 8 more simulations were carried out where some parameters were defined, such as the UEHE total length and the insulating material's thickness based on the first simulations' results. In this way, the UEHE operational proposals that best meet the ACS requirements under the conditions given by the non-producing well were reached. Therefore, the results are more realistic than those obtained with assumed or omitted information on the non-producing well, the ACS, or the UEHE.

For future work, it is proposed to consider the phase change of the fluid as it passes through the UEHE to obtain results that are even closer to reality.

5. Declarations.

Funding.

This work was partially financed by the CONACYT through the scholarships.

Acknowledgments.

Authors wish to thank to Kevin Alquicira Hernandez for his support in simulation program.

Data availability

The datasets used and/or analyzed during the current study are available from the corresponding author upon reasonable request.

References

1. Mohsin, M., Abbas, Q., Zhang, J., Ikram, M., & Iqbal, N. (2019). Integrated effect of energy consumption, economic development, and population growth on CO 2 based environmental degradation: a case of transport sector. Environmental Science and Pollution Research, 26(32), 32824-32835.
2. Shindell, D., & Smith, C. J. (2019). Climate and air-quality benefits of a realistic phase-out of fossil fuels. Nature, 573(7774), 408-411.
3. Caulk, R. A., & Tomac, I. (2017). Reuse of abandoned oil and gas wells for geothermal energy production. Renewable energy, 112, 388-397.
4. Sui, D., Wiktorski, E., Røksland, M., & Basmoen, T. A. (2019). Review and investigations on geothermal energy extraction from abandoned petroleum wells. Journal of Petroleum Exploration and Production Technology, 9(2), 1135-1147.
5. Soares, N., Rosa, N., Monteiro, H., & Costa, J. J. (2021). Advances in standalone and hybrid earth-air heat exchanger (EAHE) systems for buildings: A review. Energy and Buildings, 253, 111532.
6. Nian, Y. L., & Cheng, W. L. (2018). Evaluation of geothermal heating from abandoned oil wells. Energy, 142, 592-607.
7. Medhi, N., & Das, M. (2018, December). A study on abandoned oil/gas wells as sustainable sources of geothermal energy. In International Conference on Renewable & Alternate Energy (ICRAE–2018) (pp. 04-06).
8. Pilatowsky, I., Rivera, W., & Romero, R. J. (2001). Thermodynamic analysis of monomethylamine–water solutions in a single-stage solar absorption refrigeration cycle at low generator temperatures. Solar energy materials and solar cells, 70(3), 287-300.
9. Hernández-Magallanes, J. A., Ibarra-Bahena, J., Rivera, W., Romero, R. J., Gómez-Arias, E., Dehesa-Carrasco, U., ... & Kozhiparambil Chandran, S. (2019). Thermodynamic analysis of a half-effect absorption cooling system powered by a low-enthalpy geothermal source. Applied Sciences, 9(6), 1220.
10. Arivazhagan, S., Saravanan, R., & Renganarayanan, S. (2006). Experimental studies on HFC based two-stage half effect vapour absorption cooling system. Applied Thermal Engineering, 26(14-15), 1455-1462.
11. Kujawa, T., Nowak, W. & Stachel, A.A. Analysis of the exploitation of existing deep production wells for acquiring geothermal energy. J Eng Phys Thermophys 78, 127–135 (2005).
12. Domínguez-Inzunza, L. A., Hernández-Magallanes, J. A., Sandoval-Reyes, M., & Rivera, W. (2014). Comparison of the performance of single-effect, half-effect, double-effect in series and inverse and triple-effect absorption cooling systems operating with the NH3–LiNO3 mixture. Applied thermal engineering, 66(1-2), 612-620.
13. Davis, A. P., & Michaelides, E. E. (2009). Geothermal power production from abandoned oil wells. Energy, 34(7), 866-872.
14. Bu, X., Ma, W., & Li, H. (2012). Geothermal energy production utilizing abandoned oil and gas wells. Renewable energy, 41, 80-85.
15. Noorollahi, Y., Pourarshad, M., Jalilinasrabady, S., & Yousefi, H. (2015). Numerical simulation of power production from abandoned oil wells in Ahwaz oil field in southern Iran. Geothermics, 55, 16-23.

16. Lyu, Z., Song, X., Li, G., Hu, X., Shi, Y., & Xu, Z. (2017). Numerical analysis of characteristics of a single U-tube downhole heat exchanger in the borehole for geothermal wells. Energy, 125, 186-196.
17. Tang, F., Nowamooz, H., Wang, D., Yang, E., Luo, J., Wang, W., & Tan, Y. (2022). A simplified approach to predicting the Heat Extraction Rate of Borehole Heat Exchangers from parametric analysis. Geothermics, 101, 102358.
18. Gharibi, S., Mortezazadeh, E., Bodi, S. J. H. A., & Vatani, A. (2018). Feasibility study of geothermal heat extraction from abandoned oil wells using a U-tube heat exchanger. Energy, 153, 554-567.
19. Gutiérrez-Negrín, L. C., Canchola Félix, I., Romo-Jones, J. M., & Quijano-León, J. L. (2020). Geothermal energy in Mexico: update and perspectives. In Proceedings world geothermal congress.
20. Verma, S. P., Arredondo-Parra, U. C., Andaverde, J., Gómez-Arias, E., & Guerrero-Martínez, F. J. (2012). Three-dimensional temperature field simulation of a cooling of a magma chamber, La Primavera caldera, Jalisco, Mexico. International Geology Review, 54(7), 833-843.
21. Velázquez, J. I. S., Franco, W. R. G., Gómez-Arias, E., & Urueta, G. G. (2020). Evaluation of the cooling potential for a single effect absorption cooling system in the PR2 well of Cerritos Colorados geothermal field, Mexico. Energy Exploration & Exploitation, 38(6), 2521-2540.
22. L.C.A. Gutierrez-Negrin, The La Primavera, Jalisco, Mexico, Geothermal Field, in: Geotherm. Resour. Counc. Trans., Geothermal Resources Council, San Diego, California, 1988.
23. Prol-Ledesma, R. M., Carrillo-de la Cruzb, J. L., Torres-Verab, M. A., Membrillo-Abadb, A. S., & Espinoza-Ojedac, O. M. (2018). Heat flow map and geothermal resources in Mexico $ Mapa de flujo de calor y recursos geotérmicos de México. Terra Digitalis, 2(2), 1-38.
24. Khan, M. M. A., Saidur, R., & Al-Sulaiman, F. A. (2017). A review for phase change materials (PCMs) in solar absorption refrigeration systems. Renewable and sustainable energy reviews, 76, 105-137.
25. Chidambaram, L. A., Ramana, A. S., Kamaraj, G., & Velraj, R. (2011). Review of solar cooling methods and thermal storage options. Renewable and sustainable energy reviews, 15(6), 3220-3228.
26. Ozgener, O., Ozgener, L., & Goswami, D. Y. (2011). Experimental prediction of total thermal resistance of a closed loop EAHE for greenhouse cooling system. International Communications in Heat and Mass Transfer, 38(6), 711-716.
27. Li, H., Ni, L., Liu, G., Zhao, Z., & Yao, Y. (2019). Feasibility study on applications of an Earth-air Heat Exchanger (EAHE) for preheating fresh air in severe cold regions. Renewable Energy, 133, 1268-1284.
28. Gomat, L. J. P., Motoula, S. M. E., & M'Passi-Mabiala, B. (2020). An analytical method to evaluate the impact of vertical part of an earth-air heat exchanger on the whole system. Renewable Energy, 162, 1005-1016.
29. De Paepe, M., & Janssens, A. (2003). Thermo-hydraulic design of earth-air heat exchangers. Energy and buildings, 35(4), 389-397.
30. Belloufi, Y., Zerouali, S., Rouag, A., Aissaoui, F., Atmani, R., Brima, A., & Moummi, N. (2022). Transient assessment of an earth air heat exchanger in warm climatic conditions. Geothermics, 104, 102442.

31. Mihalakakou, G., Santamouris, M., & Asimakopoulos, D. (1992). Modelling the earth temperature using multiyear measurements. Energy and Buildings, 19(1), 1-9.
32. Mihalakakou, G., Santamouris, M., Lewis, J. O., & Asimakopoulos, D. N. (1997). On the application of the energy balance equation to predict ground temperature profiles. Solar Energy, 60(3-4), 181-190.
33. Ramírez-Dávila, L., Xamán, J., Arce, J., Álvarez, G., & Hernández-Pérez, I. (2014). Numerical study of earth-to-air heat exchanger for three different climates. Energy and buildings, 76, 238-248.
34. Zhou, T., Xiao, Y., Liu, Y., Lin, J., & Huang, H. (2018). Research on cooling performance of phase change material-filled earth-air heat exchanger. Energy Conversion and Management, 177, 210-223.
35. Sodha, M. S., Buddhi, D., & Sawhney, R. L. (1993). Optimization of pipe parameters of an underground air pipe cooling system. Energy conversion and management, 34(6), 465-470.
36. Serageldin, A. A., Abdelrahman, A. K., & Ookawara, S. (2016). Earth-Air Heat Exchanger thermal performance in Egyptian conditions: Experimental results, mathematical model, and Computational Fluid Dynamics simulation. Energy Conversion and management, 122, 25-38.
37. Liu, Q., Du, Z., & Fan, Y. (2018). Heat and mass transfer behavior prediction and thermal performance analysis of earth-to-air heat exchanger by finite volume method. Energies, 11(6), 1542.
38. Borah, A. K., Singh, P. K., & Goswami, P. (2013). Advances in numerical modeling of heat exchanger related fluid flow and heat transfer. American Journal of Engineering Science and Technology Research, 1(9), 156-166.
39. Çengel, Y. A., & Boles, M. A. (2015). Termodinámica. McGraw-Hill.

Capítulo VI. “Aplicación del modelo numérico”

Resumen.

El trabajo [Saucedo-Velázquez et al., 2022] muestra una colaboración realizada con el equipo de refrigeración del IER en el que se presenta el análisis de un campo geotérmico con el objetivo de comparar el funcionamiento de distintos SRA acoplados a fuentes de calor geotérmicas. La contribución consiste en utilizar el modelo numérico desarrollado para determinar las condiciones térmicas de trabajo de intercambiadores de calor enterrados que se presentó en el capítulo anterior. Utilizando el modelo numérico se dimensiona un intercambiador de calor enterrado tipo “U” capaz de suministrar de energía al generador de distintos tipos de SRA. En la introducción se da un panorama general de las aplicaciones directas de la geotermia, poniendo especial énfasis en la aplicación híbrida de SRA acoplados con fuentes renovables de energía como la solar. En cuanto a los estudios relacionados con SRA acoplados con sistemas geotérmicos, estos son escasos, además de que los existentes no analizan la fuente geotérmica. En este trabajo se comparan distintas configuraciones de SRA suministrados por energía obtenida de un pozo geotérmico localizado en México. En el análisis se incluye las temperaturas que se podrían obtener del pozo geotérmico, la potencia de enfriamiento, y el COP para los distintos casos propuestos.

En la sección que sigue a la introducción se muestran los distintos SRA. Se exponen los componentes principales de cada uno de ellos, así como las condiciones de operación y las principales diferencias con los demás. Se dan las características del pozo geotérmico, donde se incluye la localización del campo geotérmico y del pozo en estudio. Como información específica del pozo se conoce la litología, el gradiente geotérmico, la profundidad del pozo y la temperatura de fondo. Se muestran las ecuaciones para calcular la energía térmica total contenida en el campo geotérmico y para calcular la potencia de enfriamiento para SRA. En esta misma sección se describe brevemente el análisis de transferencia de calor en un intercambiador de calor tipo “U”. Se describe el método numérico, el lenguaje en que fue programado, consideraciones tomadas, ecuaciones, ventajas y el dominio de estudio.

En la sección de resultados se muestra la representación matemática del gradiente geotérmico y se fijan las variables en estudio que incluyen la velocidad del fluido, la longitud total del intercambiador, la longitud y espesor del aislante. Después de realizar las simulaciones numéricas se analizan cada uno de los resultados obtenidos y se presenta la temperatura del fluido a la salida del intercambiador de calor. Por último, se concluye que un intercambiador de calor sin material aislante en la sección de salida es capaz de satisfacer los requerimientos de un SRA de medio efecto.

Publicación.

processes

MDPI

Article

Cooling Potential for Single and Advanced Absorption Cooling Systems in a Geothermal Field in Mexico

Juliana Saucedo-Velázquez [1], Geydy Gutiérrez-Urueta [2], Jorge Alejandro Wong-Loya [1], Ricardo Molina-Rodea [1] and Wilfrido Rivera Gómez Franco [1,*]

[1] Instituto de Energías Renovables, Universidad Nacional Autónoma de México, Privada Xochicalco S/N, Col. Centro, Temixco C.P. 62580, Morelos, Mexico; jusave@ier.unam.mx (J.S.-V.); jawol@ier.unam.mx (J.A.W.-L.); rmr@ier.unam.mx (R.M.-R.)

[2] Facultad de Ingeniería, Universidad Autónoma de San Luis Potosí, Av. Dr. Manuel Nava No. 8, Col. Zona Universitaria Poniente, San Luis Potosí C.P. 78290, San Luis Potosí, Mexico; geydy.gutierrez@uaslp.mx

* Correspondence: wrgf@ier.unam.mx

Abstract: Climate change is one of the main problems humanity is currently facing due to the use of fossil fuels. At present, 20% of the total electricity consumed in buildings worldwide is for air conditioning. The development and use of thermally driven cooling systems is very important, since they can be activated by renewable energies, such as geothermal, reducing the consumption of electricity produced by fossil fuels. In this paper, we analyze a geothermal field located in the state of Jalisco, Mexico, with the aim of comparing the performance of different advanced absorption cooling systems driven by a geothermal heat source. The analysis includes the influence of water temperature obtained from an abandoned geothermal well, using a U tube heat exchanger inside the well. The results show that this well can reach temperatures from 59 °C to 190 °C, depending on the depth of the U tube and the insulation thickness. At a T_E = 8 °C, the operating range temperatures were 59–80 °C, 77–110 °C, 135–162 °C, and 180–187 °C for the half-effect, single-effect, double-effect and triple-effect systems, respectively. The maximum cooling potential was 99,334 GW obtained with the double-effect system, followed by 92,995 GW with the triple-effect system, 70,939 GW with the single-effect system, and 38,721 GW with the half-effect system.

Keywords: absorption cooling systems; geothermal cooling; cooling potential

Citation: Saucedo-Velázquez, J.; Gutiérrez-Urueta, G.; Wong-Loya, J.A.; Molina-Rodea, R.; Rivera Gómez Franco, W. Cooling Potential for Single and Advanced Absorption Cooling Systems in a Geothermal Field in Mexico. *Processes* **2022**, *10*, 583. https://doi.org/10.3390/pr10030583

Academic Editor: Ahmad Arabkoohsar

Received: 22 February 2022
Accepted: 15 March 2022
Published: 17 March 2022

1. Introduction

Climate change is one of the main problems humanity is currently facing due to the use of fossil fuels for different applications. Currently, 20% of the total electricity consumed in buildings worldwide is for air conditioning [1]. In 2018 it was estimated that refrigeration systems consumed 3900 TWh/year of electricity worldwide, and this energy is mainly produced by the consumption of fossil fuels [2]. Therefore, it is important that alternative cooling systems capable of operating with renewable energies, such as geothermal, are used.

A geothermal resource is the portion of heat released from the interior of the Earth that can be used in the appropriate technical and economic conditions available [3]. The potential of the Earth's geothermal resources is enormous, considering their current use and prospects, given the energy needs of humanity. The total heat content of the Earth is estimated to be around 1013 EJ (1 EJ = 1018 J) and it would take more than 109 years to deplete it, through a current global terrestrial heat flux of 40 million MW [4]. Therefore, the geothermal resource base is large enough and is practically everywhere. In 2020, the total global electricity production was 26,000 TWh, of which geothermal energy supplied an estimated 225 TWh (97 TWh of electricity and the rest in the form of heat) [5]. These amounts represent a low contribution to the total energy consumed around the world, even with the known potential.

The distribution of thermal energy used by category is approximately 58.8% for geothermal heat pumps, 18.0% for bathing and swimming, 16.0% for space heating, 3.5% for greenhouse heating, 1.6% for industrial applications, 1.3% for aquaculture pond and raceway heating, 0.8% for other applications [6].

In Mexico, the indirect use of geothermal energy almost entirely encompasses electricity production. Its direct uses are still restricted to bathing and swimming in recreational facilities and some of them for therapeutic uses (reported in 20 locations), including the geothermal field studied in this work, La Primavera. Likewise, Mexico's Federal Electricity Commission developed some of the direct uses of geothermal resources in the Los Azufre field, including a wood dryer, a fruit and vegetable dehydrator, a greenhouse, and a heating system of offices [7]. National studies related to geothermal energy and absorption cooling systems are presented next. Galindo-Luna et al. [8] proposed a hybrid system using a parabolic-trough collector field coupled to a low-enthalpy geothermal well to drive an absorption air conditioning system. A coefficient of performance (COP) of 0.71 was obtained for a generator temperature of 90 °C. The results of the modeling of a half-effect absorption system were reported using an ammonia/lithium nitrate mixture driven by a low-enthalpy geothermal source from two geothermal wells [9]. The results showed that at the wells temperatures, the cooling system can operate but obtaining low cooling effects. The potential that can be obtained from a geothermal well to operate a single-effect system was presented considering seasonal variations [10]. The COP values varied between 0.91 and 0.97. Ambriz-Díaz et al. [11] analyzed a cascade hybrid system operating in different modes. The system was composed in the first thermal level by an organic Rankine cycle to produce electricity, in the second level by an absorption refrigeration cycle to produce ice, and on the third level by a dehydrator for drying agricultural products. The results indicated that the dehydration process significantly improved the economic benefits of all the alternatives, achieving payback periods of around one year and reducing greenhouse emissions. Also, it was reported that the production of electricity alone was undesirable because it had the worst energy efficiencies and payback periods.

At an international level, several studies have been realized using geothermal energy to drive cooling systems or hybrid systems to produce cooling and an extra output. These studies are mainly based on single-effect, half-effect, and double-effect systems. Rogowska et al. [12] modeled a 10 kW single-stage absorption cooling system to produce air conditioning. The results were applied to a more advanced design of 500 kW refrigeration units in the studied region. An absorption refrigeration unit for the storage of agricultural products driven by geothermal hot water [13] reported a COP of 0.49, reaching a maximum value of 0.6 by using an extra heat exchanger. A dynamic simulation study to evaluate the performance of a new heating and cooling system was made based on the coupling between a low or medium-enthalpy geothermal source, an air handling unit, and a desiccant wheel [14]. The analysis demonstrated the technical and economic feasibility of the proposed system. The performance of an absorption refrigeration cycle and an ejector cycle using data from a low-enthalpy geothermal well were compared [15], deducing that at specific conditions, both systems were feasible as alternatives to conventional refrigeration systems. Arreola Núñez [16] modeled a commercial absorption machine driven by geothermal energy instead of gas. The results showed the thermodynamic feasibility of the system operating with geothermal energy but obtaining slightly lower coefficients of performance. Two works [17,18] have performed a parametric exergy and economic analysis of a combined cogeneration system to produce cooling and power using geothermal energy as a heat source. The results determined the most optimal operating conditions of the proposed systems. An integrated power and absorption cooling system was modeled including the waste heat from the power generation process as heat input in the cooling system, which in turn supplied the cooling water to the power plant [19]. It was concluded that it was not feasible, since it required a larger cooling capacity, increasing the total investment costs. Regarding advanced absorption cooling systems, a study presented a performance comparison of four different configurations for water/LiBr absorption cooling systems,

being these a single-effect, a half-effect, a double-effect in series, and a double-effect in reverse [20]. The maximum COPs achieved were 0.89, 0.4, 1.5, and 1.48, respectively. Similarly, calculations of the COPs and exergy analysis for single, double, triple, and half-effect water/LiBr absorption cycles were performed in another work [21]. It was observed that the COP significantly increased with the double and triple-effect cycles with values of 1.65 and 2.32, respectively. In the last two studies, the authors did not consider a special heat source, they only analyzed the performance of the systems at different operating temperatures. Shirazi et al. [22] analyzed the feasibility of single, double, and triple-effect heating and cooling absorption systems operating with solar collectors. The most favorable results were obtained with the double-effect system. The influence of various operating parameters on the COP and exergy efficiencies of the system were evaluated in [23]. The COPs for the single, double, and triple-effect chillers were in the range of 0.73–0.79, 1.22–1.42, and 1.62–1.90, respectively, while the maximum exergy efficiencies were in the range of 12.5–23.2%, 14.3–25.1%, and 17.7–25.2%, respectively. Best and Rivera [24] carried out a review analyzing both theoretical and experimental studies on absorption refrigeration systems operated with renewable energies such as geothermal. It was observed that the studies on absorption cooling systems driven partially or totally by geothermal energy in Mexico were very scarce. The installation of a thermo-chiller was described [25] operating with a double-effect ammonia absorption cycle at the Aurora Ice Museum in Chena Hot Springs, Alaska. The thermo-chiller was powered by thermal spring water providing 52.8 kW of cooling at −29 °C. Han et al. [26], proposed a double-effect water/LiBr absorption cooling system, based on an enhanced geothermal system (EGS) using concentric circle wells. The influence of key parameters such as well depth and injection rates in the cooling system were analyzed. The results showed that the driven temperature of EGS hot water can reach more than 150 °C steadily for 20 years. A thermodynamic analysis of a parallel-flow water/LiBr double-effect absorption system powered by geothermal energy was performed by using the Engineering Equation Solver (EES) software [27]. The results showed the behavior of the chiller at different operating conditions. A COP of up to 1.43 and a cooling load of 420 kW were obtained. Another thermodynamic study to utilize an existing low-temperature geothermal heat source was presented including six different models, with simple and half-effect systems [28]. The COP obtained with the half-effect system was approximately half (0.424) of the COP obtained with single-effect chillers (0.825). The results showed that the geothermal heat source can be used to drive both single and half-effect systems.

This bibliographic review showed that several studies have been carried out to compare the performance of advanced systems (half, double, and triple-effect systems) operating with solar energy. However, studies related to advanced absorption systems directly operating with a geothermal heat source are very scarce. Specifically, no studies were found for double and triple-effect systems driven by geothermal energy in which the geothermal well was analyzed.

The purpose of this article is to compare different configurations of absorption cooling systems driven by a geothermal field located in Mexico. The analysis includes the temperatures that can be obtained from a geothermal well considering different cases, and the variation of the cooling potential and COP for each one of the systems over the course of the year as a function of the driven and ambient temperatures. Real ambient temperatures were used in the analysis obtained from a meteorological station installed in the geothermal field.

2. Systems Description

2.1. Single-Effect Cooling System

A single-effect water/LiBr refrigeration system is mainly integrated by two circuits: a refrigerant circuit formed by a condenser, an expansion valve, and an evaporator, and a solution circuit integrated by a generator, an absorber, a solution heat exchanger, a pump, and a valve. Figure 1 shows a schematic diagram of the system.

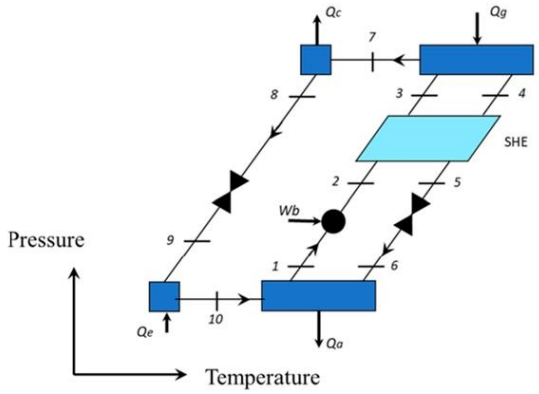

Figure 1. Schematic diagram of a single-effect absorption cooling system.

A solution with a high amount of refrigerant leaving the absorber (1) is pumped (2) to the generator, passing first through the solution heat exchanger, where it is preheated before entering the generator (3). In this component, an amount of heat Q_g is supplied to separate part of the water from the water/LiBr solution. The water in a vapor phase (7) goes to the condenser where it is condensed by means of an amount of heat removed Q_c. The liquid leaving this component (8) passes through an expansion valve reducing its pressure and temperature (9) and then to the evaporator producing the cooling effect Q_e. The water in a vapor phase leaving the evaporator (10) goes to the absorber where it is absorbed by the solution coming from the generator (4). The solution leaving the generator passes through the solution heat exchanger (5), preheating the solution going to the generator, and then through the valve reducing its pressure before entering the absorber (6). In the absorber, an amount of heat Q_a is delivered due to the exothermic reaction from the water absorption process. The solution with a high amount of refrigerant formed is then ready to be pumped to the generator starting the cycle again.

2.2. Half-Effect Cooling System

As can be seen in Figure 2, the half-effect cycle has one refrigerant circuit and two water/LiBr solution circuits, one of them at high pressure and the other one at low pressure. The refrigerant produced in the high-pressure generator passes through the condenser, the expansion valve, the evaporator, and the absorber similarly to the single-effect system. The solution low-pressure circuit also operates in the same way as previously described but with the difference that the refrigerant produced in the low-pressure generator is absorbed in the high-pressure absorber to produce a solution with a high amount of refrigerant which is used in the high-pressure circuit. Because in this system the heat is supplied into the two generators and produces only one stream of refrigerant which passes to the evaporator to produce the cooling effect, this system is called half-effect.

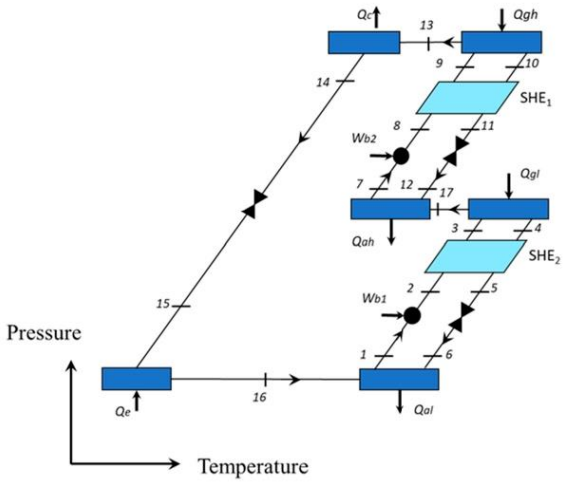

Figure 2. Schematic diagram of a half-effect absorption cooling system.

2.3. Double-Effect Cooling System

A double-effect system is shown in Figure 3. In the low part of the schematic diagram, it can be observed a single-stage system as described in Figure 1 but additionally, it has a second generator (Q_{g2}) operating at higher pressure and temperature, and a second solution heat exchanger (SHE_2). Although a second condenser appears in the diagram (Q_{c2}), this component and Q_{g1} is the same component. The shell part of a heat exchanger operates as a generator, while the side tubes operates as a condenser. As will be seen, the objective of adding the components above mentioned is to improve the system *COP*.

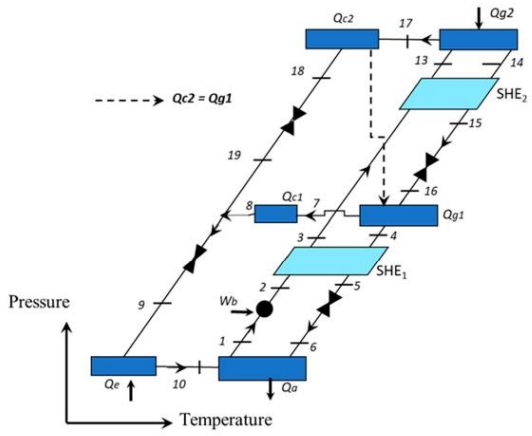

Figure 3. Schematic diagram for a double-effect absorption cooling system.

In this system, an amount of heat is supplied to Q_{g2} at a higher temperature than that supplied to a single-stage system to produce the refrigerant. The water in a vapor phase is then condensed in Q_{c2} leaving as a saturated liquid. The heat removed from the condensation processes is used as heat input to Q_{g1} to produce an extra amount of

refrigerant which is then condensed in Q_{c1}. Both condensed streams join before passing through the expansion valve and the evaporator. The rest of the cycle operates similarly to the single-stage system with the difference that the solution leaving from the absorber is pumped to Q_{g2} to produce the refrigerant at the highest pressure, and the solution leaving this component passes to Q_{g1} to produce more refrigerant. The two solution heat exchangers SHE_1 and SHE_2 are used to preheat the solution going from the absorber to the generator to reduce the heat supplied to Q_{g2}.

As can be seen from Figure 3, and the above explained, the heat is supplied to this system only in Q_{g2}, since Q_{g1} uses the heat delivered from the condensation process in Q_{c2}. Because the heat is supplied in only one component and produces two refrigerant streams, this system is denominated as a double-effect.

2.4. Triple-Effect Cooling System

A triple-effect system is shown in Figure 4. This system is similar to the double-effect system previously described but additionally, it has a third generator (Q_{g3}) and a third solution heat exchanger (SHE_3). The operation of this system is analogous to the double-effect system but in this case, the heat source is supplied to Q_{g3} at an even higher temperature than the second-stage system to produce the first stream of refrigerant. The other two streams of refrigerants are produced in Q_{g2} and Q_{g1}, using the heat delivered from the condensation processes in Q_{c3} and Q_{c2}. Because this system has the capability of producing three streams of refrigerant by suppling heat in only one component, this system is called a triple-effect system.

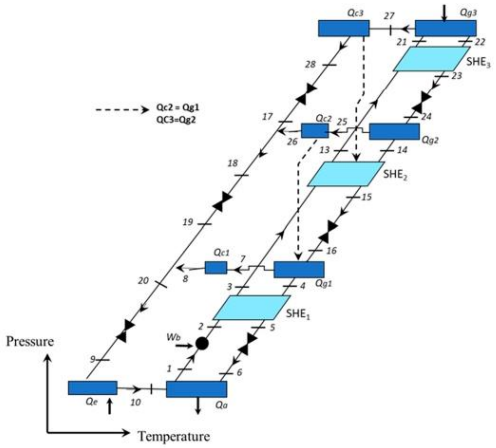

Figure 4. Schematic diagram of a triple-effect absorption cooling system.

3. Location and Solution Methods

3.1. Geothermal Source

The "Cerritos Colorados" geothermal field is located in the central-southern portion of the "La Primavera forest" [29] which is located 20 km west of the city of Guadalajara, in the state of Jalisco, between the extreme coordinates 103°28′ to 103°42′ West longitude and 20°32′ to 20°44′ North latitude (Figure 5).

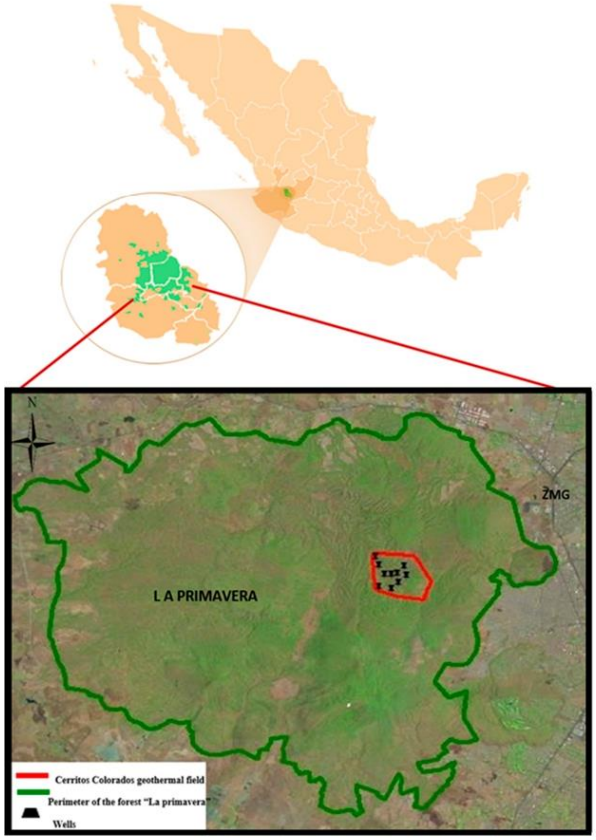

Figure 5. Location map of the Cerritos Colorado geothermal field [30].

In the present study, the data of the PR2 well are used. This well was chosen due to all the necessary data for analysis were available [31]. In Table 1 the characteristics of the well are presented, and Figure 6 presents its lithology.

Table 1. Data from PR2 geothermal well in the geothermal field Cerritos Colorados [29,31].

Well	Latitude	Longitude	Geothermal Gradient (°C/km)	Depth (m)	Temperature (°C)
PR2	20.66423	−103.53115	114.9	1988	320

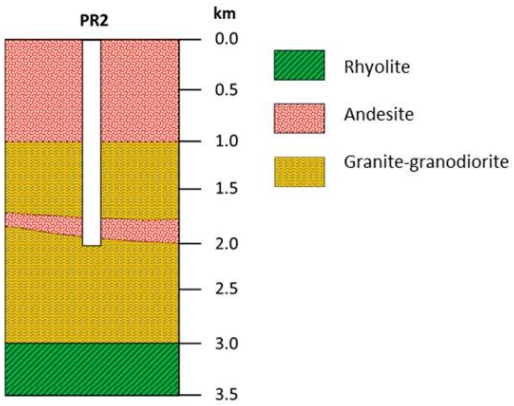

Figure 6. Simplified lithology based on core drilled wells from Cerritos Colorados geothermal field.

3.2. Calculation of Total Thermal Energy

To determine the energy gained by the fluid circulating through the well, the volumetric method was used. This method takes into consideration the energy contained in a certain volume of rock containing a hot water reservoir which supplies the energy to the fluid circulating through the pipe. The energy gained by the fluid is determined by using heat transfer equations and energy balances [32]. The procedure is repeated again for each control volume.

The energy stored in the rock volume (Q_r) can be determined by

$$Q_r = AH(1 - \varnothing)\rho_r C_r(T_i - T_m) \quad (1)$$

where A is the area of the control volume; H is the thickness of the reservoir; ρ_r is the density of the rock; C_r the specific heat of the rock; ϕ the porosity of the rock, defined as the relationship between the volume of empty spaces in the host rock or spaces occupied by the water in it and the total volume of the material [33]; and T_i and T_m, the initial and minimum temperatures, respectively.

The fluid energy Q_f can be estimated by Equation (2)

$$Q_f = AH\rho_f C_f \varnothing(T_i - T_m) \quad (2)$$

where p_f and C_f, represent the density and specific heat of the rock, respectively.

Thus, the total energy is calculated as:

$$Q_t = Q_f + Q_r \quad (3)$$

Some of these parameters can be known with acceptable accuracy, but others, such as the area and thickness of the well, are uncertain even with extensive drilling, due to underground phenomena and morphology. Therefore, study areas of 1 km^2, 2 km^2, and 3 km^2, were considered as a minimum, probable, and maximum areas, respectively. For the majority of the reservoirs, the uncertainties regarding the depth are small compared with those of the respective area [34].

In Equations (1) and (2) H was considered as 2000 m which is an average value of divers well of the geothermal field. ϕ was established as 10%, which is related to the type of rock which is predominantly constituted by a volcanic igneous rock of intermediate composition [35]. The values of ρ_r and C_r of each type of rock were used according to the stratigraphic column of the Cerritos Colorados geothermal field (Figure 6). In the case of the fluid, the specific heat water values C_f = 4.18 kJ/kg°C and a density p_f = 1000 kg/m^3

are used. T_m is set according to the technology used. For geothermal power plants, a temperature of 135 °C for single cycles and 90 °C for binary cycles are assumed in general [36]. For the present study, T_m varied according to the requirements of each absorption cycle. From the modeling of each one of the systems, it was found that for the specified conditions, T_m was 58 °C, 77 °C, 134 °C and 170 °C for the half, single, double, and triple-effect systems, respectively, and T_i was taken from the recorded temperatures of the analyzed geothermal well. It is important to mention that although a T_m of 58 °C for the half-effect cycle seemed to be a low temperature to drive an absorption cooling system, the double solution circuit used in this cycle (see Figure 2), allows the system to operate at such low temperature.

To define the reservoir initial temperature (T_i), an average of the temperatures recorded in the well PR2 was taken based on the data in Table 1.

3.3. Calculation of the Cooling Potential (CP) for the Absorption Cooling Systems

The power (P) produced by a geothermal power plant can be calculated by Equation (4) using the volumetric method [36].

$$P = \frac{Q_t \, R_f \, C_e}{F_p t} \tag{4}$$

where Q_t is the total energy obtained by Equation (3), R_f is the recovery factor, which represents the fraction of the energy that could be recovered, C_e is the efficiency factor, F_p is the plant factor, and t the operation time in hours. Values of R_f up to 25% have been reported for good conditions of porosity and permeability into the well but normally lower values are reported [35]. For the present study, an R_f of 12.5% and an F_p of 90% were considered since they are typical values reported in the literature [36].

Based on this equation, the cooling potential (CP) can be estimated by Equation (5) as:

$$CP = \frac{Q_t \, R_f \, COP}{F_p t} \tag{5}$$

where the efficiency factor (C_e) is replaced by the COP for each one of the cooling analyzed systems.

3.4. Simulation of the Water/LiBr Absorption Cooling Systems

To obtain the COP of each system, mathematical models were developed based on the first-law of thermodynamics, and then the simulation was carried out by using the Engineering Equation Solver (EES) software.

The following assumptions were considered in the modeling of each one of the cooling cycles:

- There is thermodynamic equilibrium in the cycles.
- The cycles operate under steady-state conditions.
- The solution is saturated at the exit of the generators and absorbers.
- The refrigerant is saturated at the exit of the condensers and evaporators.
- Heat losses and pressure drops in piping and components are negligible.
- The flow through the valves is isenthalpic.
- The effectiveness of the heat exchangers was 0.8.
- A ΔT = 7 °C was considered between the ambient temperature and the temperature of the condensers and absorbers.
- The evaporation temperature T_E was 8 °C.

The value of T_E = 8 °C was chosen since it was the optimum value of the evaporation temperature obtained from the analysis of diverse absorption cooling systems [10]. These authors also reported that the values of CP and COP are directly proportional to T_E. However, higher values of T_E were not considered in the present study, since higher temperatures cannot provide good air condition temperatures.

Appendix A shows the tables with the energy balances for each one of the components integrating the four analyzed systems [20].

3.5. Heat Transfer Analysis in a U-Tube Heat Exchanger

The heat transfer analysis inside the "U" type heat exchanger was performed using a mathematical model developed with the finite volume numerical method and implemented in Fortran 90 programming language. This computational mathematical method consists of dividing the study domain into a finite quantity of control volumes. The equation which models the physical phenomena is discretized and solved for each control volume [37]. The main advantage of this mathematical model is that allows the estimation of fluid temperature through the heat exchanger based on pipe diameter, fluid velocity, boundary temperatures, the total length of the heat exchanger, the total length of the insulator, and soil thermo-physical characteristics. The study domain includes the soil, the well, the heat exchanger walls, the insulator material, and the space inside the heat exchanger where the fluid flows. Figure 7 shows a schematic diagram of the underground U tube heat exchanger.

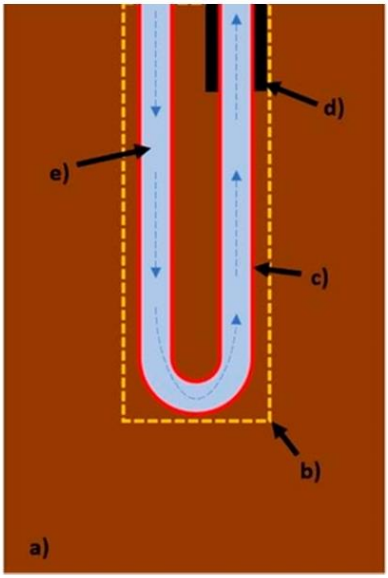

Figure 7. Study domain: (**a**) soil (brown), (**b**) well (yellow), (**c**) heat exchanger walls (red), (**d**) insulator (black), and (**e**) space inside the heat exchanger (blue).

In total, 1400 control volumes were used to represent the study domain. These control volumes are organized irregularly, presenting a greater density near the pipe walls of the heat exchanger.

The assumptions considered for the mathematical model are:

- The fluid viscosity is neglected, thus, the fluid velocity profile inside the heat exchanger is constant.
- The space inside the heat exchanger is represented as one-dimensional due to the constant fluid velocity.
- Inside the heat exchanger, the convection is the main heat transfer phenomenon; therefore, the conduction heat transfer among the fluid and the pipe walls is neglected.

- Outside the heat exchanger, the conduction is the main heat transfer phenomenon; therefore, the convection heat transfer through the soil porous is neglected.
- The heat exchanger walls thickness is neglected as the thermal dynamic is led by the soil.
- The soil thermal diffusivity changes as a function of the soil type presented in the lithology [32].
- The boundary temperature is equal to the temperature calculated with the geothermal gradient.
- The inlet fluid temperature remains constant.
- Environmental factors are neglected in soil surface temperature.
- Condensation and phase change for the fluid are omitted.

The energy equation (Equation (6)) is used for modeling purposes. All the terms in this equation (temporal, convective, and diffusive) are discretized for each node in the mesh represents the study domain [38].

$$\frac{\partial T}{\partial t} + \nabla \cdot (vT) = \alpha \cdot \nabla^2 T \tag{6}$$

In the previous equation, v and α represent the fluid velocity and thermal diffusivity, respectively. When Equation (6) is discretized, and the coefficients are arranged for each mesh node, a linear equation system results. This equations system is solved using an iterative Tridiagonal Matrix Algorithm (TDMA), which solves each dimension separately [39].

4. Results and Discussion

To determine the *CP* and *COP* for each of the systems driven with the energy provided by the geothermal well, first it is necessary to know the ambient temperatures in the zone since the geothermal well temperatures and the systems cooling performance depend upon these.

4.1. Ambient Temperature Data per Hour

The ambient temperature data used for the analysis were requested from the National Water Commission, CONAGUA. The data from the meteorological station "La Primavera" was used since it is the nearest station to the geothermal field.

Figure 8 shows the average ambient temperature per hour for the entire year 2018 for Spring, Summer, Autumn, and Winter. As can be seen, the temperatures varied between 10.3 °C and 33 °C for the whole year.

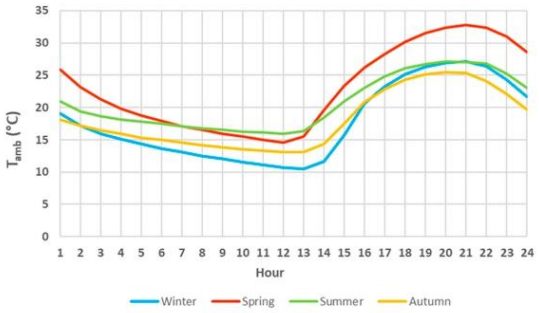

Figure 8. Average temperature per hour for each season.

4.2. Determination of the Geothermal Well Temperature

As stated in the assumptions, the initial temperature distribution is equal to the geothermal gradient for the specific site, which is equal to the boundary temperature.

Equations (7) and (8) show temperature correlations used in this study as a function of depth z.

$$T_{(z,t=0)} = 20 + (0.115 \cdot z),\ 0 < z < 2000 \quad (7)$$

$$T_{(z,t=0)} = 480 - (0.115 \cdot z),\ 2000 < z < 4000 \quad (8)$$

Six different cases were simulated changing the fluid velocity, the heat exchanger total length, the insulator length, and thickness. The thermal diffusivity for each type of soil used in the simulations was calculated using data from the stratigraphic column presented previously (Figure 6) and is constant for each test. The thermal diffusivity of the insulator material was considered equal to $1.08x10^{-9}$ $\left(m^2/s\right)$. For all the tests carried out, the fluid inlet temperature was fixed at 20 °C, which is the average value of the seasonal environmental temperature. Finally, a "U" tube heat exchanger with a 3" pipe diameter was considered for the 6 cases. This value is considered because this is the maximum allowable diameter to cover the largest contact area inside the well. Table 2 shows the values of total length (TL), insulator length (IL), insulator thickness (IT), and fluid velocity (v) for each one of the 6 tests. The outlet fluid temperature is also reported (T_O).

Table 2. Values considered for the simulations of the geothermal well.

Case	TL (m)	IL (m)	IT(in)	v (m/s)	T_O (°C)	Cooling System Possible to Activate
1	4000	-	-	6	60.8	half-effect
2	4000	1000	1	6	174.7	triple-effect
3	4000	500	2	6	116.2	single-effect
4	4000	1000	1	4	160	double-effect
5	3000	1000	1	6	145.9	double-effect
6	3000	-	-	6	59.6	half-effect

The base case (first) was done without insulation, resulting in a temperature of 60.8 °C. This outlet temperature is enough to be used in a half-effect cooling system and was set as the starting point to compare subsequent results. Afterward, distinct values of total length, insulator length, insulator thickness, and air velocity were used to analyze their effects on the outlet fluid temperature, which is used to drive the absorption systems.

For the second case, insulator material was considered with 1000 m length and 1" of thickness, keeping the remaining parameters as in the first case. The result shows that the fluid outlet temperature was 174.7 °C.

The insulator material was considered again for the third case but changing the length and thickness. As result, the outlet fluid temperature was 116.2 °C. Compared with the first one, simulating 500 m less insulator material, allows the fluid to continue exchanging energy with its surroundings.

The fourth case considers 1000 m of insulator material, 1" of insulator thickness but a fluid velocity of 4 m/s. The result shows that the change in the velocity caused less turbulence, but the outlet fluid temperature was greater compared with the first case achieving a temperature of 160 °C.

Figure 9 illustrates the results obtained for cases 1 to 4. It shows the initial temperature condition in blue, equal to the temperature at the boundary obtained with the geothermal gradient. The fluid temperature profile is also shown, along with the heat exchanger for examples 1 to 4 (all 4000 m in total length). It is observed that the energy gain occurs in the first 2000 m, which is the downward section of the exchanger, while, depending on the simulator conditions, the energy gained was different.

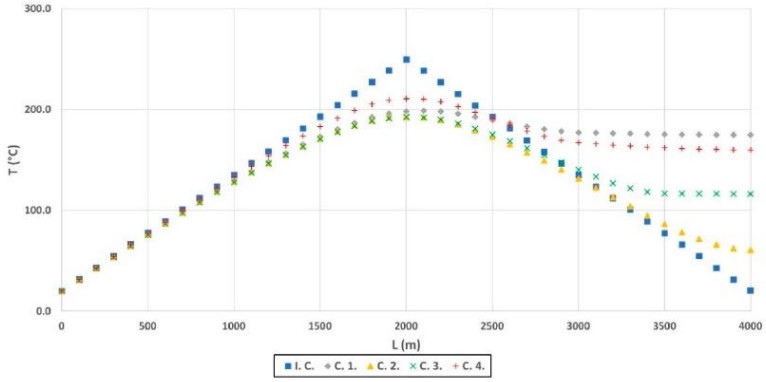

Figure 9. Fluid temperature inside the exchanger: I.C. initial condition (blue), C.1 (orange), C.2. (grey), C.3. (green), C.4. (red).

For the fifth case, the total length of the heat exchanger was reduced, while in the sixth one the insulator material was omitted. The results showed that both cases´s temperature for were 145.9 °C and 59.6 °C, respectively. As in the first 2 cases, there is a difference of almost 100 °C in the final temperature of the fluid caused by the absence of the insulator material. Figure 10 shows the results for cases 5 and 6 (3000 m total length).

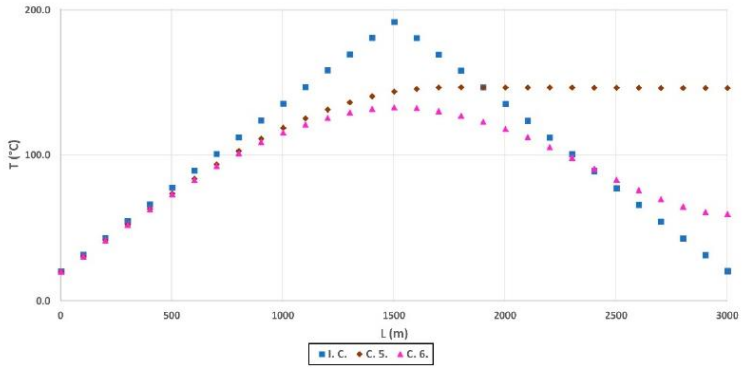

Figure 10. Fluid temperature inside the exchanger: I.C. initial condition (blue), C.5. (coffee), C.6. (pink).

4.3. Determination of the Cooling Potential (CP)

The *CP* can be determined for each one of the proposed systems by using Equation (5). The hourly results for the four seasons are presented in Figure 11a–d at a T_E = 8 °C. It can be observed that the *CP* is higher for the double-effect system with a maximum cooling potential of 99,334 GW, followed by the triple-effect with 92,995 GW, 70,939 GW for simple-effect, and 38,721 GW for the half-effect system. These maximum potentials are obtained in winter when the ambient temperature is lower. For the double and triple-effect system, when the environmental temperatures are very high, the systems cannot operate. This happened since the absorber and condenser temperatures were fixed 7 °C above the ambient temperature, and at considerably high absorber temperatures and low pressures, a crystallization phenomenon occurs.

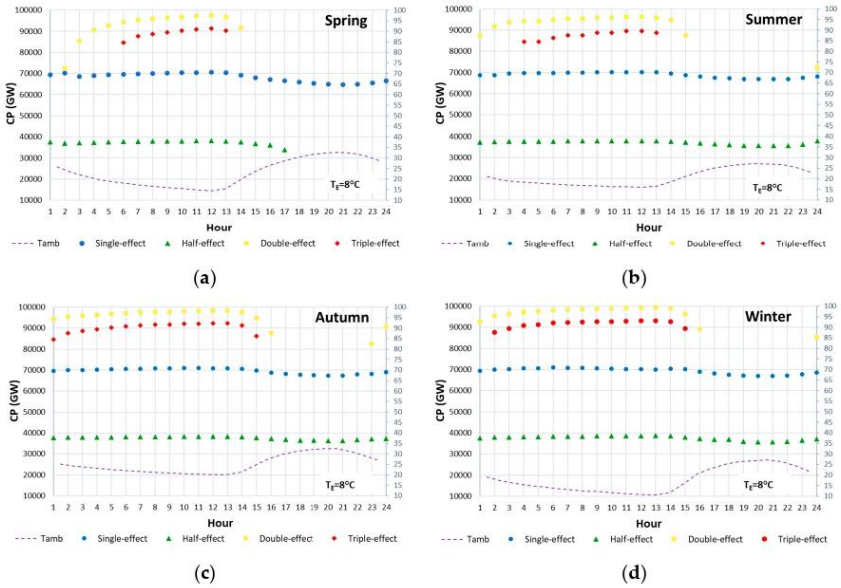

Figure 11. Cooling potential per hour for each absorption system for the season, (**a**) Spring, (**b**) Summer, (**c**) Autumn, and (**d**) Winter.

From the analysis carried out in Section 4.2, it was clear that the geothermal well can produce useful heat at temperatures up to 175 °C, depending on the analyzed case as it was shown in Table 2 and in Figures 9 and 10. Figure 12a–d show the cooling potential for each one of the proposed systems at a T_E = 8 °C for Spring, Summer, Autumn, and Winter, respectively. First, it is noticeable that the triple-effect system cannot operate in the Spring and Summer seasons due to the high ambient temperatures. The rest of the systems may operate for all seasons. Although it was expected that with the triple-effect system the highest cooling potential could be reached, due to its limited operating ranges the *CP* values are slightly lower than those obtained with the double-effect system. So, the highest potentials are obtained with the double-effect system, followed by the triple-effect system, and then for the single-effect system. The lowest *CP* values are obtained with the half-effect system, but with the advantage that these type of system may operate at very low temperatures from 59 °C to 79 °C. The single-effect system operates at temperatures between 77 °C and 112 °C, while the other systems require temperatures higher than 140 °C to operate, which can be only obtained for the analyzed cases 2, 4, and 5.

Figure 13a–d show the coefficients of performance for each one of the systems for Spring, Summer, Autumn, and Winter, respectively. As it was expected, according to the data reported in the literature [21], the highest *COPs* are obtained with the triple-effect system. However, this system has a more limited operating temperature range in contrast to the other systems. The lowest *COP* values were obtained for the half-effect system varying from 0.43 to 0.49. For the single-effect system, the *COPs* varied between 0.89 and 0.97, while for the double-effect and triple-effect systems varied from 1.27 to 1.47, and from 1.78 to 1.95, respectively. The maximum *COPs* are obtained in the Winter and Autumn seasons.

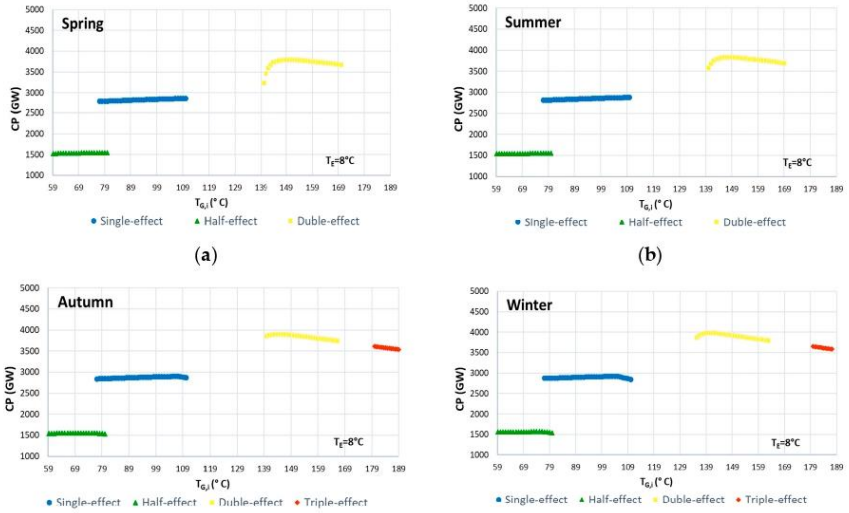

Figure 12. Cooling Potential per hour for each absorption system for the season, (**a**) Spring, (**b**) Summer, (**c**) Autumn, and (**d**) Winter.

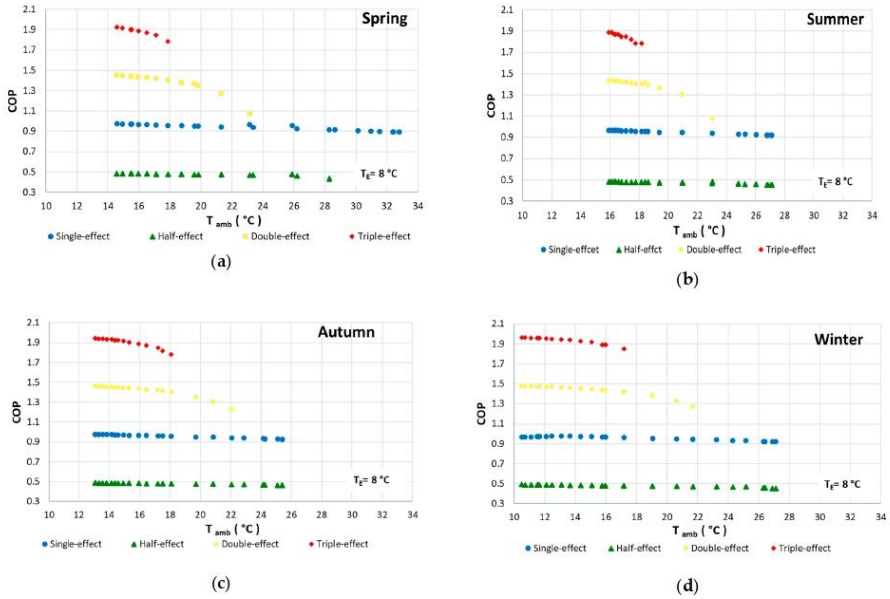

Figure 13. COP as a function of the Tamb for each absorption system for (**a**) Spring, (**b**) Summer, (**c**) Autumn, and (**d**) Winter.

5. Conclusions

A geothermal field located in Mexico was studied with the purpose to assess the performance of the four advanced absorption cooling systems driven by a geothermal heat source.

From the analysis of the geothermal well, it was found that without placing an insulation layer in the tube of return, it is possible to obtain temperatures around 60 °C, which are enough to drive a half-effect system; however, it is necessary the insulation to reach higher temperatures to drive the other systems, especially the double-effect and triple-effect systems.

At a T_E = 8 °C, the operating range temperatures were 59–80 °C, 77–110 °C, 135–162 °C, and 180–187 °C, with the half-effect, single-effect, double-effect, and triple-effect systems, respectively.

The range of the coefficients of performance for the four systems were: 0.43–0.49 for the half-effect system, 0.89–0.97 for the single-effect system, 1.27–1.47 for the double-effect, and 1.78–1.95 for the triple-effect system. The maximum values of the coefficients of performance were obtained in Autumn and Winter when the ambient temperatures were the lowest. This occurs since at low ambient temperatures, the condenser and absorber temperatures are also lower, thus reducing the operating pressures of the systems. The lower operating pressures cause an increase of the refrigerant production and therefore an increase of the coefficients of performance.

The maximum cooling potential was obtained with the double-effect system, achieving values up to 99,334 GW, followed by the triple-effect system with 92,995 GW. With the single-effect and half-effect systems the cooling potentials were up to 70,939 GW and 38,721 GW, respectively.

From the analysis, it was demonstrated that the triple-effect system does not present any advantage over the double-effect system, since it is more complex, it requires higher operating temperatures, it has a more limited operating range, and achieved lower cooling potentials.

The technical feasibility to produce cooling at temperatures as low as 58 °C by using geothermal energy was also demonstrated. This fact is very important because around the world there are numerous geothermal wells which can be used for these purposes. However, it is important to consider both the distance from the wells to towns and the possible applications. This is relevant since long distance result in the economic infeasibility because the geothermal areas (hydrothermal) are, in many cases, located far from urban areas.

Author Contributions: Conceptualization, J.S.-V., G.G.-U. and W.R.G.F.; methodology, J.S.-V., G.G.-U. and W.R.G.F.; geothermal well modeling, J.A.W.-L. and R.M.-R.; formal analysis, J.S.-V., G.G.-U. and W.R.G.F.; writing—original draft preparation, J.S.-V., G.G.-U.,W.R.G.F., J.A.W.-L. and R.M.-R.; writing—review and editing, J.S.-V. and W.R.G.F.; visualization, W.R.G.F. and G.G.-U.; supervision, W.R.G.F. All authors have read and agreed to the published version of the manuscript.

Funding: This research received no external funding.

Institutional Review Board Statement: Not applicable.

Informed Consent Statement: Not applicable.

Data Availability Statement: The data presented in this study are available in the article.

Conflicts of Interest: The authors declared no potential conflict of interest with respect to the research, authorship, and/or publication of this article.

Nomenclature

A	area
Ce	efficiency factor
C	specific heat
COP	coefficient of performance
CP	cooling potential

F_p	plant factor
h	enthalpy
H	thickness of the reservoir
IL	insulator length
IT	insulator thickness
$\dot{m}$	mass flow
p	pressure
P	geothermoelectric potential
Q	heat load
Q_t	total energy
R_f	recovery factor
SHE	solution heat exchanger
T	temperature
TL	total length
t	time
W	work
v	fluid velocity
Z	depth
Subscripts	
a	absorber
b	pump
c	condenser
e	evaporator
f	fluid
g	generator
G,I	introduced to the generator
i	initial
m	minimum
o	outlet
r	rock
w	wall
Greek letters	
α	thermal diffusivity
ρ	density
ε	effectiveness
v	volume
Ø	porosity of the rock

Appendix A

Table A1. Energy balances for each one of the components of the single-effect absorption cooling system.

Component	Balances
Generator	$Q_g = \dot{m}_4 h_4 + \dot{m}_7 h_7 - \dot{m}_3 h_3$
Condenser	$Q_c = \dot{m}_7 (h_7 - h_8)$
Evaporator	$Q_e = \dot{m}_{10} (h_{10} - h_9)$
Absorber	$Q_a = \dot{m}_{10} h_{10} + \dot{m}_6 h_6 - \dot{m}_1 h_1$
Effectiveness of the SHE	$\varepsilon_{SHE} = \frac{h_3 - h_2}{h_4 - h_2}$
Pump Work	$W_b = v_1 (P_8 - P_{10})$
COP	$COP = \frac{Q_e}{Q_g + W_b}$

Table A2. Energy balances for each one of the components of the half-effect absorption cooling system.

Component	Balances
Generator	$\dot{Q}_{gh} = \dot{m}_{13}h_{13} + \dot{m}_{10}h_{10} - \dot{m}_9h_9$ $\dot{Q}_{gl} = \dot{m}_4h_4 + \dot{m}_{17}h_{17} - \dot{m}_3h_3$
Condenser	$\dot{Q}_c = \dot{m}_{13}(h_{13} - h_{14})$
Evaporator	$\dot{Q}_e = \dot{m}_{16}(h_{16} - h_{15})$
Absorber	$\dot{Q}_{al} = \dot{m}_6h_6 + \dot{m}_{16}h_{16} - \dot{m}_1h_1$ $\dot{Q}_{ah} = \dot{m}_{17}h_{17} + \dot{m}_{12}h_{12} - \dot{m}_7h_7$
Effectiveness of the SHE	$\varepsilon_{SHE_1} = \frac{h_3 - h_2}{h_4 - h_2}$ $\varepsilon_{SHE_2} = \frac{h_9 - h_8}{h_{10} - h_8}$
Pump Work	$\dot{W}_{b1} = v_1(P_2 - P_1)$ $\dot{W}_{b1} = v_7(P_8 - P_7)$
COP	$COP = \frac{\dot{Q}_e}{\dot{Q}_{gh} + \dot{W}_{b1} + \dot{Q}_{gl} + \dot{W}_{b2}}$

Table A3. Energy balances for each one of the components of the double-effect absorption cooling system.

Component	Balances
Generator	$\dot{Q}_{g2} = \dot{m}_{14}h_{14} + \dot{m}_{17}h_{17} - \dot{m}_3h_3$
Condenser	$\dot{Q}_{c1} = \dot{m}_7h_7 - \dot{m}_8h_8$
Generator-Condenser	$\dot{Q}_{g1} = \dot{m}_7h_7 + \dot{m}_4h_4 - \dot{m}_{16}h_{16}$ $\dot{Q}_{c2} = \dot{m}_{17}h_{17} - \dot{m}_{18}h_{18}$
Evaporator	$\dot{Q}_e = \dot{m}_{10}(h_{10} - h_9)$
Absorber	$\dot{Q}_a = \dot{m}_6h_6 + \dot{m}_{10}h_{10} - \dot{m}_1h_1$
Effectiveness of the SHE	$\varepsilon_{SHX} = \frac{h_3 - h_2}{h_4 - h_2}$ $\varepsilon_{SHX} = \frac{h_{13} - h_3}{h_{14} - h_3}$
Pump Work	$\dot{W}_b = v_1(P_2 - P_1)$
COP	$COP = \frac{\dot{Q}_e}{\dot{Q}_{g2} + \dot{W}_b}$

Table A4. Energy balances for each one of the components of the triple-effect absorption cooling system.

Component	Balances
Generator	$\dot{Q}_{g3} = \dot{m}_{22}h_{22} + \dot{m}_{27}h_{27} - \dot{m}_{21}h_{21}$
Condenser	$\dot{Q}_{c1} = \dot{m}_7h_7 - \dot{m}_8h_8$
Generator-Condenser	$\dot{Q}_{g2} = \dot{m}_{25}h_{25} + \dot{m}_{14}h_{14} - \dot{m}_{24}h_{24}$ $\dot{Q}_{c3} = \dot{m}_{27}(h_{27} - h_{28})$ $\dot{Q}_{g1} = \dot{m}_7h_7 + \dot{m}_4h_4 - \dot{m}_{16}h_{16}$ $\dot{Q}_{c2} = \dot{m}_{25}(h_{25} - h_{26})$
Evaporator	$\dot{Q}_e = \dot{m}_{10}(h_{10} - h_9)$
Absorber	$\dot{Q}_a = \dot{m}_6h_6 + \dot{m}_{10}h_{10} - \dot{m}_1h_1$
Effectiveness of the SHE	$\varepsilon_{SHE\ 1} = \frac{h_3 - h_2}{h_4 - h_2}$ $\varepsilon_{SHE\ 2} = \frac{h_{13} - h_3}{h_{14} - h_3}$ $\varepsilon_{SHE\ 3} = \frac{h_{21} - h_{13}}{h_{22} - h_{13}}$
Pump Work	$\dot{W}_b = v_1(P_2 - P_1)$
COP	$COP = \frac{\dot{Q}_e}{\dot{Q}_{g3} + \dot{W}_b}$

References

1. International Energy Agency (IEA). *The Future of Cooling Opportunities for Energy-Efficient Air Conditioning*; IEA: Paris, France, 2018; p. 92. Available online: https://iea.blob.core.windows.net/assets/0bb45525-277f-4c9c-8d0c-9c0cb5e7d525/The_Future_of_Cooling.pdf (accessed on 10 October 2021).
2. United Nations Environment Programme; International Energy Agency. *Cooling Emissions and Policy Synthesis Report*; UNEP, Nairobi and IEA: Paris, France, 2020.
3. IGME; IDEA. *Manual de Geotermia*; Instituto para la Diversificación y Ahorro de la Energía- Instituto Geológico y Minero de España: Madrid, Spain, 2008; Available online: http://geoatlantic.eu/portfolio/wp-content/uploads/2020/06/10952_manual_geotermia_a2008.pdf (accessed on 12 August 2021).
4. Rybach, L.; Mongillo, M. Geothermal Sustainability—A Review with Identified Research Needs. *GRC Trans.* **2006**, *30*, 1083–1090.
5. Renewable Supply and Demand. Available online: https://www.c2es.org/ (accessed on 11 January 2022).
6. Lund, J.W.; Boyd, T.L. Direct Utilization of Geothermal Energy 2015 Worldwide Review. In Proceedings of the World Geothermal Congress 2015, Melbourne, Australia, 19–24 April 2015.
7. Gutiérrez-Negrín, L.C.A.; Maya-González, R.; Luis Quijano-León, J. Present Situation and Perspectives of Geothermal in Mexico. *Proc. World Geotherm. Congr.* **2015**, *2015*, 19–25.
8. Galindo-Luna, Y.; Gómez-Arias, E.; Romero, R.; Venegas-Reyes, E.; Montiel-González, M.; Unland-Weiss, H.; Pacheco-Hernández, P.; González-Fernández, A.; Díaz-Salgado, J. Hybrid Solar-Geothermal Energy Absorption Air-Conditioning System Operating with NaOH-H2O—Las Tres Vírgenes (Baja California Sur), "La Reforma" Case. *Energies* **2018**, *11*, 1268. [CrossRef]
9. Hernández-Magallanes, J.A.; Ibarra-Bahena, J.; Rivera, W.; Romero, R.J.; Gómez-Arias, E.; Dehesa-Carrasco, U.; Espinoza-Ojeda, O.M.; Chandran, S.K. Thermodynamic Analysis of a Half-Effect Absorption Cooling System Powered by a Low-Enthalpy Geothermal Source. *Appl. Sci.* **2019**, *9*, 1220. [CrossRef]
10. Saucedo Velázquez, J.I.; Rivera Gómez Franco, W.; Gómez-Arias, E.; Gutiérrez Urueta, G.G. Evaluation of the cooling potential for a single effect absorption cooling system in the PR2 well of Cerritos Colorados geothermal field, Mexico. *Energy Explor. Exploit.* **2020**, *38*, 2521–2540. [CrossRef]
11. Ambriz-Díaz, V.M.; Rubio-Maya, C.; Pacheco Ibarra, J.J.; Galván González, S.R.; Martínez Patiño, J. Analysis of a sequential production of electricity, ice and drying of agricultural products by cascading geothermal energy. *Int. J. Hydrog. Energy* **2017**, *42*, 18092–18102. [CrossRef]
12. Rogowska, A.; Szaflik, W. Cooling Load Production in Sorption Cycles Supplied by a Geothermal Heat Source for Air. *Proc. World Geotherm. Congr.* **2005**, *2005*, 24–29.
13. Uwera, J.; Itoi, R.; Jalilinasrabady, S.; Jóhannesson, T.; Benediktsson, D.Ö. Design of a cooling system using geothermal energy for storage of agricultural products with emphasis on Irish potatoes in Rwanda, Africa. *Trans.—Geotherm. Resour. Counc.* **2015**, *39*, 157–164.
14. Angrisani, G.; Diglio, G.; Sasso, M.; Calise, F.; Dentice d'Accadia, M. Design of a novel geothermal heating and cooling system: Energy and economic analysis. *Energy Convers. Manag.* **2016**, *108*, 144–159. [CrossRef]
15. Ramirez Sanchez, R. *Refrigeración Térmica con Geotermia de baja Entalpía*; Universidad Nacional Autónoma de México: Manzanilla, Mexico, 2016.
16. Arreola Núñez, M. *Aprovechamiento de Calor Geotérmico de Mediana y baja Entalpía para la Producción de Frío*; Universidad Michoacana de San Nicolás de Hidalgo: Morelia, Mexico, 2016.
17. Akbari Kordlar, M.; Mahmoudi, S.M.S.; Talati, F.; Yari, M.; Mosaffa, A.H. A new flexible geothermal based cogeneration system producing power and refrigeration, part two: The influence of ambient temperature. *Renew. Energy* **2019**, *134*, 875–887. [CrossRef]
18. Parikhani, T.; Ghaebi, H.; Rostamzadeh, H. A novel geothermal combined cooling and power cycle based on the absorption power cycle: Energy, exergy and exergoeconomic analysis. *Energy* **2018**, *153*, 265–277. [CrossRef]
19. Tesha. Absorption Refrigeration System as an Integrated Condenser Cooling Unit in Geothermal Power Plant. MSc Thesis, Department of Mechanical and Industrial Engineering, University of Iceland, Reykjavík, Iceland, 2010; pp. 25–29.
20. Domínguez-Inzunza, L.A.; Sandoval-Reyes, M.; Hernández-Magallanes, J.A.; Rivera, W. Comparison of the Performance of Single Effect, Half Effect, Double Effect in Series and Inverse Absorption Cooling Systems Operating with the Mixture H2O-LiBr. *Energy Procedia* **2014**, *57*, 2534–2543. [CrossRef]
21. Gebreslassie, B.H.; Medrano, M.; Boer, D. Exergy analysis of multi-effect water–LiBr absorption systems: From half to triple effect. *Renew. Energy* **2010**, *35*, 1773–1782. [CrossRef]
22. Shirazi, A.; Taylor, R.A.; White, S.D.; Morrison, G.L. A systematic parametric study and feasibility assessment of solar-assisted single-effect, double-effect, and triple-effect absorption chillers for heating and cooling applications. *Energy Convers. Manag.* **2016**, *114*, 258–277. [CrossRef]
23. Gomri, R. Investigation of the potential of application of single effect and multiple effect absorption cooling systems. *Energy Convers. Manag.* **2010**, *51*, 1629–1636. [CrossRef]
24. Best, R.; Rivera, W. A review of thermal cooling systems. *Appl. Therm. Eng.* **2015**, *75*, 1162–1175. [CrossRef]
25. Erickson, D.C.; Kyung, I.; Holdmann, G.P. Geothermal powered absorption chiller for Alaska Ice Hotel. *Trans.—Geotherm. Resour. Counc.* **2005**, *29*, 57–59.
26. Han, B.; Li, W.; Li, M.; Liu, L.; Song, J. Study on Libr/H2O absorption cooling system based on enhanced geothermal system for data center. *Energy Reports* **2020**, *6*, 1090–1098. [CrossRef]

27. El Haj Assad, M.; Said, Z.; Khosravi, A.; Salameh, T.; Albawab, M. Parametric study of geothermal parallel flow double-effect water-LiBr absorption chiller. In Proceedings of the 2019 Advances in Science and Engineering Technology International Conferences (ASET), Dubai, United Arab Emirates, 26 March–10 April 2019; IEEE: Piscataway, NJ, USA, 2019; pp. 1–6.
28. Masheiti, S.; Agnew, B. Thermodynamic Simulation Modelling of Low-Temperature Geothermal Source Located in Arid-Zone Area North Africa. *Jordan J. Mech. Ind. Eng.* **2010**, *4*, 61–68.
29. Gutierrez-Negrin, L.C.A. The La Primavera, Jalisco, Mexico, Geothermal Field. In Proceedings of the Geothermal Resources Council Transactions; Geothermal Resources Council, San Diego, CA, USA, 9–12 October 1988.
30. Saucedo Velazquez, J.I. *Propuesta para el Desarrollo de un Proyecto Geotérmico Sustentable en el Bosque de la Primavera*; Universidad Autónoma de San Luis Potosí: San Luis Potosí, Mexico, 2017.
31. Prol-Ledesma, R.M.; Carrillo-de la Cruz, J.L.; Torres-Vera, M.A.; Membrillo-Abad, A.S.; Espinoza-Ojeda, O.M. Heat flow map and geothermal resources in Mexico. *Terra Digit.* **2018**, *2*, 1–15. [CrossRef]
32. Verma, S.P.; Arredondo-Parra, U.C.; Andaverde, J.; Gómez-Arias, E.; Guerrero-Martínez, F.J. Three-dimensional temperature field simulation of a cooling of a magma chamber, La Primavera caldera, Jalisco, Mexico. *Int. Geol. Rev.* **2012**, *54*, 833–843. [CrossRef]
33. Muffler, P.; Cataldi, R. Methods for regional assessment of geothermal resources. *Geothermics* **1978**, *7*, 53–89. [CrossRef]
34. Muffler, L.J.P. Assessment of geothermal resources of the United States -1978. In *Geological Survey Circular 790*; Geological Survey: Reston, VA, USA, 1979; Volume 2.
35. Dipippo, R. *Geothermal Power Plants: Principles, Applications, Case Studies and Environmental Impac*, 4th ed.; Butterworth-Heinemann: Oxford, UK, 2015; ISBN 978-0081008799.
36. Hiriart, G. Evaluación de la Energía Geotérmica en México. 2011. Available online: https://www.cre.gob.mx/documento/2027.pdf (accessed on 3 July 2021).
37. Serageldin, A.A.; Abdelrahman, A.K.; Ookawara, S. Earth-Air Heat Exchanger thermal performance in Egyptian conditions: Experimental results, mathematical model, and Computational Fluid Dynamics simulation. *Energy Convers. Manag.* **2016**, *122*, 25–38. [CrossRef]
38. Liu, Q.; Du, Z.; Fan, Y. Heat and Mass Transfer Behavior Prediction and Thermal Performance Analysis of Earth-to-Air Heat Exchanger by Finite Volume Method. *Energies* **2018**, *11*, 1542. [CrossRef]
39. Kumar Borah, A.; Singh, P.K.; Goswami, P. Advances in Numerical Modeling of Heat Exchanger Related Fluid Flow and Heat Transfer. *Am. J. Eng. Sci. Technol. Res. Am. J. Eng. Sci. Technol. Res.* **2013**, *1*, 156–166.

Capítulo VII. “Afectación térmica del suelo”

Resumen.

En el trabajo [Molina-Rodea et al., 2020] se presenta la mejora de un simulador numérico utilizado para modelar la afectación y recuperación térmica del suelo, a fin de conocer la temperatura estabilizada de formación (TEF) de un pozo geotérmico. La mejora se realiza precisamente sobre el módulo de perturbación térmica del simulador, con el cual se reproducen los perfiles de temperatura del suelo que surgen por la circulación de fluidos de perforación en el fondo del pozo. En la introducción se exponen distintos modelos desarrollados en 1D, 2D y 3D que consideran distintas suposiciones en sus modelos de transferencia de calor conductivos y convectivos. Se encontró que la gran mayoría de modelos desprecian el efecto de la masa térmica y la transferencia de calor que ocurre por debajo del fondo del pozo, y en su lugar asumen una frontera con un valor de temperatura fija. Esto produce unos perfiles de temperatura alejados de la realidad sobre todo en el suelo de la sección inferior del pozo. El simulador WELLTHER-SIM se desarrolló precisamente para atender este problema, ya que es posible estimar la difusividad térmica de la formación a partir de la observación de la fase de recuperación térmica de la roca. Este simulador numérico ha sido validado contra datos experimentales obtenidos en campo. Sin embargo, la validación se había realizado únicamente durante el proceso de recuperación térmica. En este trabajo se muestra la mejora del modelo numérico capaz de representar adecuadamente los fenómenos de perturbación térmica de la formación cuando circula el fluido de perforación y arrastre. La mejora resulta de cambiar el tipo de frontera en el modelo numérico, de una frontera con temperatura fija, a una frontera mixta.

En la metodología se muestran el dominio de estudio que comprende la formación rocosa, el fondo del pozo, la sección interna y el fluido de perforación. Se explica el mecanismo de circulación del fluido en el interior del pozo, el tipo de frontera establecida, la forma de transferencia de calor en cada etapa y se explican las suposiciones tomadas en cuenta. Se expone el dispositivo experimental con las medidas y distribución de termopares, además de que se justifican sus dimensiones. Durante la presentación del proceso para realizar los experimentos se justifican las suposiciones hechas en torno al fluido de perforación y su comportamiento térmico durante las fases de afectación y recuperación térmica. También se presenta el dispositivo experimental construido para estimar el coeficiente de transferencia de calor del fluido de perforación junto con la ecuación que representa este fenómeno en particular. Al presentar el modelo numérico se muestran las ecuaciones a discretizar, la ecuación para la distribución inicial de temperatura, las ecuaciones en las fronteras internas y externas, y la cantidad de nodos utilizados para la simulación.

La sección de resultados inicia mostrando la validación experimental de las suposiciones del modelo numérico. Posteriormente se presentan los experimentos realizados con el modelo a escala para un tiempo de afectación térmica de 55 y 180 segundos, respectivamente. La validación del modelo se realiza al comparar los resultados numéricos y los resultados experimentales con una función de mérito que muestra una mejora de hasta 60% comparado con el módulo original del simulador WELLTHER-SIM.

Publicación.

Computers & Geosciences 135 (2020) 104359

Contents lists available at ScienceDirect

Computers and Geosciences

journal homepage: www.elsevier.com/locate/cageo

A new simulator to determine thermal disturbance and recovery processes during wellbore drilling: Experimental validation with a scaled-down wellbore prototype

R. Molina-Rodea [a], J.A. Wong-Loya [a,b,*], P.J. Valades-Pelayo [a]

[a] Instituto de Energías Renovables, Universidad Nacional Autónoma de México, Priv. Xochicalco s/n, Col. Centro, Temixco, Morelos, 62580, Mexico
[b] Colegio de Ciencias y Humanidades, Plantel Vallejo, Universidad Nacional Autónoma de México, Av. Cien Metros s/n, Col. Magdalena de las Salinas, Distrito Federal, 07760, Mexico

ARTICLE INFO

Keywords:
Borehole prototype
Geothermal energy
Heat transfer
Thermal disturbance process
Drilling process

ABSTRACT

In the present study, a novel simulator is developed. The simulator is built upon the model presented by (Wong et. al. 2017) but considering a Robin boundary condition at the interphase between the rock formation and the bottom-hole. Additionally, simulation results are compared against experiments in a scaled-down bore-hole set-up, emulating the most relevant aspects of a real perforation, such as: behaving as a semi-infinite media and considering sequential circulation and shut-in times with varying durations. Moreover, all thermal parameters are independently estimated, such as to diminish cross-correlation between model parameters. Deviations between experiments and the simulations of the proposed model are below 1.2%, for all cases. Deviations for the present model are about an order of magnitude smaller than those obtained by Wong et. al. 2017).

1. Introduction

According to its installed capacity in 2017, geothermal energy yearly potential is 12,913 MWe (IRENA, 2018), although it is still relatively underused. One of the main problems regarding geothermal energy usage, lays in estimating the thermal potential of a geothermal reservoir as well as its behavior during its exploitation period, to determine the suitability for a given application (Tinti et al., 2018). In turn, estimating the thermal potential implies using geochemical and geophysical analysis, along with transient thermal models for estimating formation properties (Wong-Loya et al., 2017).

Estimating thermophysical formation properties requires either using thermal laboratory measurements or in-situ wellbore temperature measurements. The former involves drilling tasks and extracting rock sample cores, which tends to affect sample properties (Fuchs et al., 2015) while being significantly more expensive and time-consuming than in-situ temperature measurements (Fuchs et al., 2015). On the other hand, using thermal models has proven more practical, although less accurate (Bording et al., 2016). The main reason, stemming from limitations on the wellbore thermal models used for predicting transient temperature profiles during disturbance and shut-in times.

Various types of numerical simulation models to predict thermal processes under drilling and shut-in conditions have been developed (Lee, 1982; Espinosa-Paredes et al., 2001 and 2009; Ricard and Chanu, 2013). Models developed consider different assumptions, such as using heat conduction and convection models together with bottom-hole temperatures and thermophysical properties of solid and fluid materials while using 1D, 2D and 3D domains (e.g., Espinosa-Paredes et al., 2001; Yang et al., 2013; Sanaz et al., 2013; Wu et al., 2014; Li et al., 2015; Liu et al., 2016). In 1986, Shen & Beck elaborated a 1D transient analytical model, considering finite circulation time into the wellbore and shut-in time, accounting for radial heat transport. Waples et al. (2004) and Zare-Reisabadi et al. (2015) showed a 1D numerical model to determine bottom hole temperature in shallow wells (<3500 m) from measured temperature data. One dimensional model accounting for temperature variations as a function of depth can only account for a limited amount of input parameters, such as surface temperature, bottom-hole measured temperature, shut-in time, and depth. Due to these limitations, 1D models, are used to yield rough estimates on the bottom hole stabilized temperature.

In recent times, You et al. (2016) modeled heat transfer in the wellbore and the formation considering two separate sub-domains with

* Corresponding author. Instituto de Energías Renovables, Universidad Nacional Autónoma de México, Priv. Xochicalco s/n, Col. Centro, Temixco, Morelos, 62580, Mexico.
E-mail address: jawol@ier.unam.mx (J.A. Wong-Loya).

https://doi.org/10.1016/j.cageo.2019.104359
Received 17 May 2019; Received in revised form 26 September 2019; Accepted 11 November 2019
Available online 12 November 2019
0098-3004/

a refined grid in the region near the wellbore. Model validation was carried out against idealized analytic cases. Pan and Oldenburg (2014) used a numerical method to simulate the interaction between the wellbore and the surroundings accounting for non-isothermal, multiphase, and multicomponent phenomena. The formation temperature profiles are a function of fluid flow rate for the production stage; however, well recuperation is not studied. Furthermore, model validation is carried out only for the hydrodynamic model using both on-site measurements and an idealized analytical case; validation for the thermal model is missing.

Cao et al. (1988) developed a mathematical model that simulates the thermal affectation and thermal recovery that occurs during the drilling of the well, obtaining synthetic series of temperature data in the bottom of the well, mud temperature data during the shut-in time and the radius of thermal disturbance in the formation. Some of the assumptions made in their work are: during thermal recovery process the heat transfer is radial in the direction of the formation towards the well; the vertical temperature gradient is negligible and; the formation and the drilling mud are homogeneous. Their work focuses on the lower boundary of the bottom of the well.

On the other hand, Van Oort et al. (2018) simulated a 2D transient thermal model that decouples the heat equation from the momentum and mass conservation equations, assuming steady-state and plug flow along the pipe before solving the energy equation for both the well and the formation. Model validation considers a (1) steady-state analytical model and (2) software data from Drillbench® (Schlumberger). However, no formal validation was carried out, as the presented data sets were also used to fit the model thermal diffusivity and heat transfer coefficients.

All these 2D studies disregard the effects of thermal mass and heat transfer below the bottom hole and instead assume a Dirichlet boundary condition, artificially limiting the shape of the temperature profiles near the bottom hole. To overcome these limitations, our research group developed a 3D wellbore simulator (WELLTHER-SIM), where the model domain accounts for the thermal phenomena at depths up to two times the depth of the bottom hole (Wong-Loya et al., 2017). This model was designed to estimate the rock formation effective thermal diffusivity for two different geothermal wellbores. Parameter estimation was carried out by fitting the simulation to experimental shut-in temperature profiles (Wong-Loya et al., 2017). However, while results showed that the heat conduction model is accurate for shut-in time processes, no formal comparison was made against data obtained during the fluid circulation process.

In this regard, from Wong-Loya et al. (2017), it can be concluded that using Dirichlet boundary conditions and setting them at carefully selected temperatures is reasonable under certain circumstances. However, it is clear from these transient thermal simulations that considering the thermal mass below the bottom hole, yields quite different temperature distributions in regions near the bottom hole, both below and above it.

To analyze the thermal behavior of the formation when a well is drilled, there are two main approaches (Cao et al., 1988). The first one studies radial disturbances from the Well wall towards the rock formation omitting the bottom-hole (Espinosa-Paredes et al., 2001; García--Valladares et al., 2006; Hasan and Kabir, 2012; Pan and Oldenburg, 2014; You et al., 2016). The second one focuses on the bottom-hole, taking into account the thermal disturbances below the bottom-hole and around nearby walls (Bullard, 1947; Luheshi, 1983; Shen and Beck, 1986; Wong-Loya et al., 2017).

The work carried out presents a numerical simulator capable of adequately representing the phenomena of thermal affectation and recovery of the formation surrounding the bottom of the well during drilling. The fact that it can adequately reproduce both phenomena helps in geoscience to validate the works where a new methods have been developed in order to obtain the stabilized temperature of formation such as: (Bassam et al 2010, 2015; Wong-Loya et al., 2012; Wong-Loya et al., 2015; Espinoza-Ojeda and Santoyo, 2016; Jiang et al., 2016; Liu et al., 2016; Chang et al., 2018), by the fact of being able to create synthetic series of temperature data (BHT) at different times (shut-in), which are data required by most analytical methods and numerical simulators for that purpose. Numerical simulations show that the change of a Dirichlet-type boundary for a Robin type generates satisfactory results compared to experimental results.

In this work, authors account for the mass below the bottom hole as this affects the overall thermal transient behavior of the formation when compared to a Dirichlet boundary condition in the lower borehole limit. Besides comparison against an analytical solution, model validation and parameter estimation consider independent sets of experiments, carried out in a scaled-down laboratory set-up that emulates the bottom of a borehole. The model describes the transient thermal behavior during the disturbance and the recuperation stages.

2. Methodology

2.1. Physical considerations

The model developed for the simulator estimates the heat transfer and temperature distributions during the disturbance and recuperation processes of the borehole drilling operation. Fig. 1 (a and b) presents the two distinct subdomains considered by the model, namely; the drilling mud (a) and the surrounding rock formation (b).

The heat transfer analysis in the mud subdomain is different depending on the process considered. During thermal disturbance (a.k.a. circulation time), forced convection is assumed to be the dominant heat transfer mechanism. The thermal disturbance stage duration ranges from two to 5 h (Wong-Loya et al., 2017; Andaverde et al., 2005), starting right after borehole drilling stop; hence, mud heating can only occur by exchanging heat with the rock formation through the borehole.

Due to the high circulation rates, the drilling fluid temperature is considered time-independent, set at 30 °C. A boundary condition of the third kind (Robin type) between the mud and the formation subdomains accounts for Heat Exchange. The heat transfer coefficient used is estimated from experiments on a scaled down set-up (as explained in the next subsection).

From the perspective of the formation, the mud removes heat, lowering temperature profiles in the vicinity of the well. As circulation time passes (and depending on the mud thermophysical properties) low-temperature contours extend away from the borehole. In this regard, the model considers 3D heat conduction within the rock formation domain,

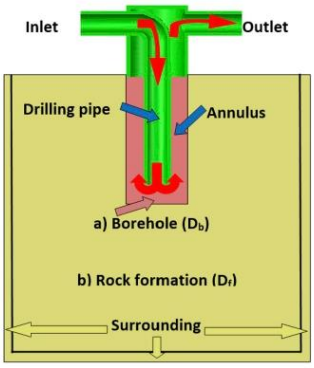

Fig. 1. Domain considered for the thermal simulation during the recuperation and disturbance stages. (a) the borehole and (b) the rock formation subdomains.

Table 1
Thermocouples positions.

Thermocouple	Position x,y,z (cm)
T_{1a} (axial)	(4, 4, 4.3)
T_{2a} (axial)	(4, 4, 3.5)
T_{3a} (axial)	(4, 4, 2.1)
T_{1r} (radial)	(7.5, 4, 5.9)
T_{2r} (radial)	(7.9, 4, 5.9)

while convection (i.e. due to the drilling fluid permeating through the rock), is neglected.

On the other hand, while the shut-in stage takes place, conductive transport within the mud is considered the main thermal transport mechanism; convection is negligible given that fluid forced circulation stops, while the mud transport properties hinder any heat transport effects arising due to natural convection.

Within the rock formation subdomain, the same considerations used during the disturbance process hold for the Shut-in time (i.e. conduction is the dominant mechanism). After a (usually long) given time, the fluid within the bottom hole subdomain reaches the so-called Static Formation Temperature (SFT). As a summary, the model assumptions are as follows:

1. Drilling mud and rock formation physical properties are different, but homogeneous and isotropic within each subdomain.
2. Physical properties are time-independent and equal for both stages.
3. Thermal resistance between the bottom hole and the rock formation is negligible.
4. During the circulation time heat exchange between the drilling mud and rock formation is through forced convection.
5. Drilling mud is assumed incompressible.
6. During circulation time, the drilling fluid temperature entering the bottom hole is time-independent and homogeneous.
7. During circulation time, no temperature gradients exist within the mud.
8. During recovery, natural convection on the bottom hole is negligible.
9. During recovery, axial heat transfer between the bottom hole and the surface above is negligible.

Assumptions 1, 2, 3 and 5, were experimentally and numerically validated by Shen and Beck (1986) and Wong-Loya et al. (2017). This study, based on the simulator presented by Wong-Loya et al. (2017), presents three improvements to the description of the disturbance and recovery processes. Additionally, assumptions 4, 6, 8 and 9 are experimentally validated as shown in the upcoming sections.

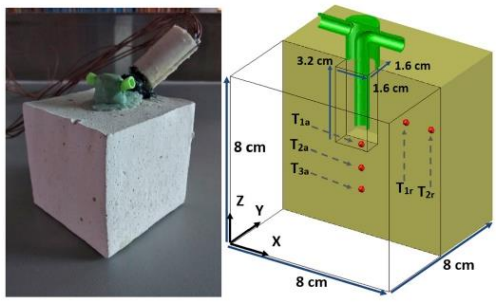

Fig. 2. Scaled-down experimental set-up. Red dots indicate the locations for the five T thermocouples. Thermocouples were located at three axial and two radial positions. (For interpretation of the references to colour in this figure legend, the reader is referred to the Web version of this article.)

Table 2
Average and standard deviations of the thermal parameters used within the simulations used to describe the disturbance and shut-in time.

Thermocouple	Position x,y,z (cm)
T_{1a} (axial)	(4, 4, 4.3)
T_{2a} (axial)	(4, 4, 3.5)
T_{3a} (axial)	(4, 4, 2.1)
T_{1r} (radial)	(7.5, 4, 5.9)
T_{2r} (radial)	(7.9, 4, 5.9)

2.2. Experimental set-up

Validation of the model assumptions presented in the past section is carried out with the assistance of a scaled-down set-up. Given that the present work focuses on modelling the bottom hole during drilling operations (in accordance to the approach from Bullard, 1947; Luheshi, 1983; Shen and Beck, 1986; Wong et al. 2017), the set-up considers a homogeneous cubic domain of 8 cm length, with a rectangular borehole zone of 1.6 by 1.6 by 3.2 cm depth, emulating the bottom hole.

The rock formation, during large-scale operation, behaves as a semi-infinite conducting media. Hence, the main criteria for selecting the prototype dimensions was so that this assumption remains valid, at least for the duration of the experimental thermal disturbance stage. As such, cube size and material selection consider that the disturbances coming from the emulated bottom hole (thermal wavefronts) can travel in any direction (excepting upwards) without significant interaction with the lateral and lower boundaries. In this regard, taking the plaster thermal diffusivity (α) from Table 1, experiment durations (t) from Table 2, and a minimum distance from the bottom-hole to the boundary (L) of 4 cm, (refer to Fig. 2), yields a Fourier Number ($Fo = \alpha t/L2$) between 0.1 and 0.4. Thus, allowing us to assure that the interaction with the prototype boundaries remains negligible (excepting the upper boundary). Within the set-up, five type T thermocouples were inserted at three different axial and two different radial positions, as shown in Fig. 2. Plaster emulates the rock formation; its conductivity and thermal diffusivity were estimated using a K2D Pro device, presented in Fig. 2. Due to its low porosity, the plaster permeability was negligible.

To avoid any deformations during drying, the plaster casting was carried out in a 3D printed cubic mold (emulating the rock formation subdomain), and a piping header was also 3D printed, with an inlet and outlet as presented in Fig. 3. The fluid inlet was 3 cm below the plaster surface.

Before the experiment started, the scaled-down set-up was submerged for 5 h in a temperature-controlled thermal bath ensuring thermal equilibrium and, hence, a known (homogeneous) initial temperature distribution. During the experiment, 3 L of ambient-temperature motor oil (SAE 25W-50), was circulated between the pre-heated set-up and the oil reservoir and back, with a pump for high-density fluids (WINTEK 12V 6A).

In a real drilling operation, the drilling mud exchanges heat with a relatively small horizon within the rock, i.e., a (radial) distance of 20–80 cm away from the mud (Cao et al., 1988). Hence, within this horizon, both the drilling mud and rock formation thermal mass are roughly on the same order of magnitude — explaining why most models consider that the temperatures of both domains change in time. However, when considering only the borehole bottom thermal mass (and brief fluid residence time), as is the case of the present article, a time-independent fluid temperature (Shen and Beck, 1986) and gradient-free perforation mud can be assumed; i.e., assumptions 6 and 7, respectively. In this respect, our scaled-down experimental set-up considers an oil reservoir (3 l and a volumetric specific heat of 1.75 kJ/l k), with a thermal mass around 7 times bigger than that of the system (volume of 0.5 l and volumetric specific heat of 1.7 kJ/l K), rendering these assumptions physically sound. Furthermore, the heat transfer

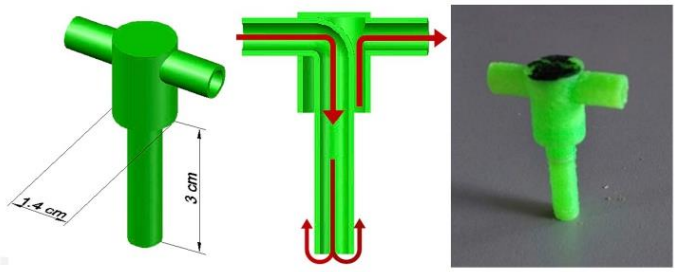

Fig. 3. 3D printed piping header used in the scaled-down experimental set-up. Red arrows outline the fluid flow through the header. (For interpretation of the references to colour in this figure legend, the reader is referred to the Web version of this article.)

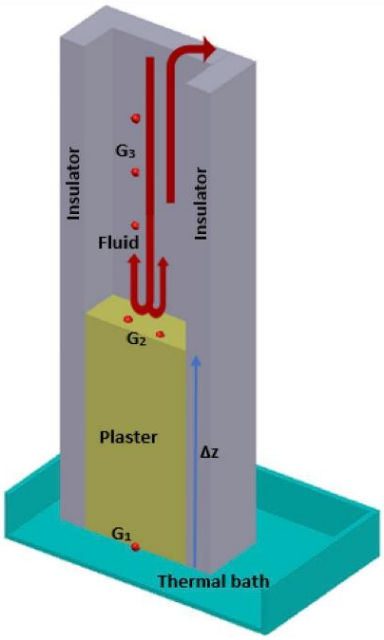

Fig 4. Presents the experimental set up used to estimate the heat transfer coefficient. The insulating lining, plaster and fluid region are present. Groups of thermocouples labeled as T1, T2 and T3, are used to estimate parameters from equation (1).

coefficient (during circulation time) was estimated by placing thermocouples at the fluid inlet and outlet while assessing the energy exchanged by the recirculating fluid.

Experiments were performed to assess the validity of assumption 6, lasting 55, 80 and 180 s. Each experiment was repeated three times, and the temperature readings within the solid were recorded and compared with the results obtained by the simulator.

2.3. Estimation of the heat transfer coefficient

Given that there are no correlations available in the open literature, valid under similar thermal and hydrodynamic operating conditions, an experimental set up (Fig. 4) was devised to estimate the convective heat transfer coefficient, as described in the methodology section.

The experimental set up, presented in Fig. 4, for estimating the heat transfer coefficient considers a rectangular plaster in the bottom, with an adiabatic Styrofoam lining, covering the side walls. The adiabatic lining allows assuming heat transfer is unidirectional, while the cavity shape along the inlet and outlet allows us assuming the flow pattern will remain close to the one in the prototype, which considers the header from Fig. 3. Red dots in Fig. 4, represent the location of the thermocouples. During the experiments to estimate the heat transfer coefficient, the fluid recirculation is maintained, until thermal transient processes stabilize both in the plaster and the fluid, yielding the following equation valid:

$$\kappa_r \frac{\Delta T}{\Delta z} = h\left(T_w - T_f\right) \tag{1}$$

Where κ_r is the plaster thermal conductivity, estimated by using the KD2Pro; T_w is the temperature in the solid cube right at the fluid-solid interphase, estimated by averaging temperature from the two thermocouples labeled as G2; T_f is the fluid bulk temperature, estimated by averaging the three thermocouples labeled as G3. Finally, $\frac{\Delta T}{\Delta z}$ is estimated by the difference between thermocouples labeled as G2 and G1 divided by the axial distance between them, label in Fig. 4 as Δz.

2.4. Mathematical model

In this section, a mathematical model is presented, which follows the assumptions and geometric considerations mentioned in the past subsection. The differential equations applicable for both subdomains, initial and boundary conditions are given, for each stage of the perforation process. Fig. 5 presents the interphases connecting the model subdomains (Fig. 1): The interphase connecting the Formation (D_f) with the Borehole (D_b), represented by the red surface, I_b; and the bounding interphase between the Formation subdomain (D_f) and its surroundings, defined by the blue surface, I_s.

The equations describing the transient temperature distribution for the rock formation (D_f) subdomain during the disturbance process are:

$$\alpha_r \left(\frac{\partial^2 T_r}{\partial x^2} + \frac{\partial^2 T_r}{\partial y^2} + \frac{\partial^2 T_r}{\partial z^2} \right) = \frac{\partial T_r}{\partial t} \tag{2}$$

The boundary condition for the interphase between the rock formation and the borehole (I_b), as presented in Fig. 5, is described by:

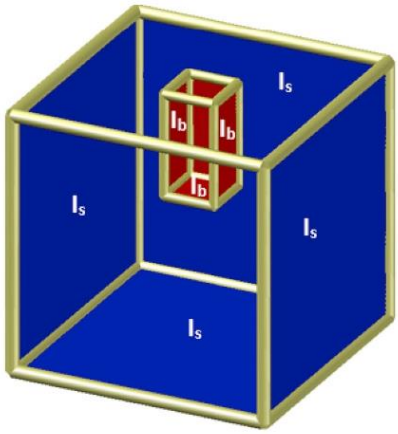

Fig. 5. Diagram of the domain considered in the mathematical model, presenting main boundary conditions for both subdomains. The red surfaces denote the borehole-formation interphase (I_b); the blue ones, the formation-surroundings interphase. (For interpretation of the references to colour in this figure legend, the reader is referred to the Web version of this article.)

$$-k\left(\frac{\partial T_r}{\partial \bar{n}}\right)\Big|_{\bar{x}=I_b} = h\left(T_{fl} - T_r|_{\bar{x}=I_b}\right) \tag{3}$$

And the initial temperature distribution of the rock formation is:

$$T_r(x, y, z, t=0) = T_o \tag{4}$$

where α_r and k are the formation thermal diffusivity and conductivity, respectively, while $T_r|_{\bar{x}=I_b}$ is the temperature of the rock formation adjacent to the borehole and h the drilling fluid convective coefficient. T_o is the formation initial temperature and T_{fl} is the drilling fluid temperature (within the Borehole subdomain). The temperature within the borehole subdomain (D_b) is assumed constant in space and during the whole disturbance process, in accordance with model assumption 7.

For the thermal recovery process, diffusion heat transfer prevails within the rock formation subdomain (D_f), and as such, equation (2) is still applicable. On the other hand, given that the perforation mud is now stagnant within the borehole and following assumptions 8, equation ## now applies within the borehole subdomain (D_b):

$$\alpha_b\left(\frac{\partial^2 T_b}{\partial x^2} + \frac{\partial^2 T_b}{\partial y^2} + \frac{\partial^2 T_b}{\partial z^2}\right) = \frac{\partial T_b}{\partial t} \tag{5}$$

Where α_b is the thermal diffusivity of the drilling mud. Additionally, equation (5) is solved considering the following boundary condition for the interphase between the rock formation and the borehole (I_b):

$$T_r|_{\bar{x}=I_b} = T_b|_{\bar{x}=I_b} \tag{6}$$

The initial conditions for the temperature distribution in the rock formation during the recovery stage (T_r^e) is:

$$T_r^e(x, y, z, t=0) = T_r(x, y, z, t=t_s) \tag{7}$$

Where t_s is the time when the fluid circulation stops. Finally, for both stages the boundary conditions between the formation subdomain (D_f) and the surrounding interphase (I_s), are defined as:

$$T_r|_{\bar{x}=I_s} = T_o \tag{8}$$

Where T_o is both the surroundings temperature and the formation initial temperature.

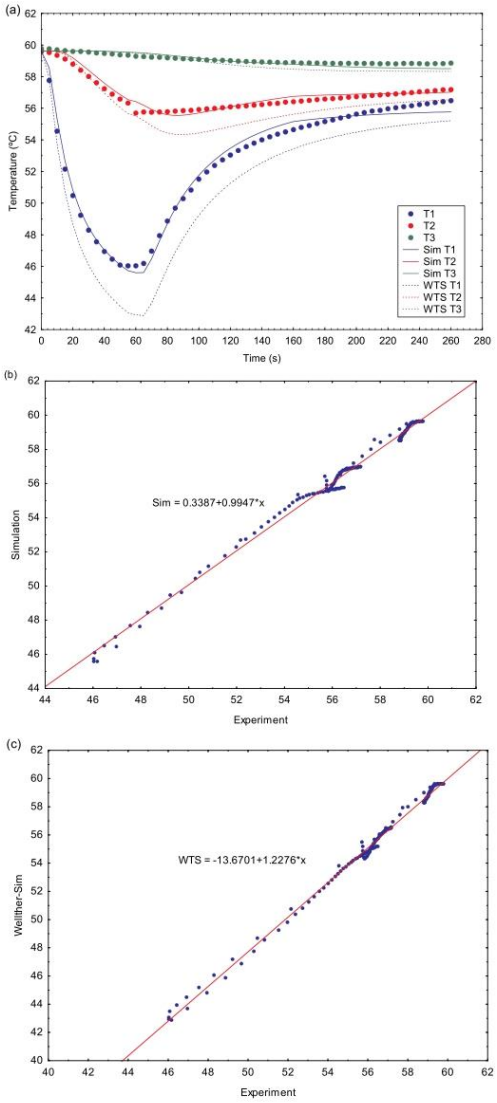

Fig. 6. Experiment considering a disturbance time of 55 s and 205 s of shut-in time. (a)Experimental and simulated thermal behavior for thermocouples at different axial positions, (b) comparison between simulated and experimental data, and (c) comparison between Wellther-Sim and experimental data.

To approximate the solution of these coupled systems of equations and in-house first order finite volume discretization scheme was implemented in Fortran 95. The linear equations system was solved using an iterative splitting algorithm that reduces the problem to three subsequent Tridiagonal Matrix Algorithms (TDMA); each one runs in every dimension. The domain discretization uses a constant density,

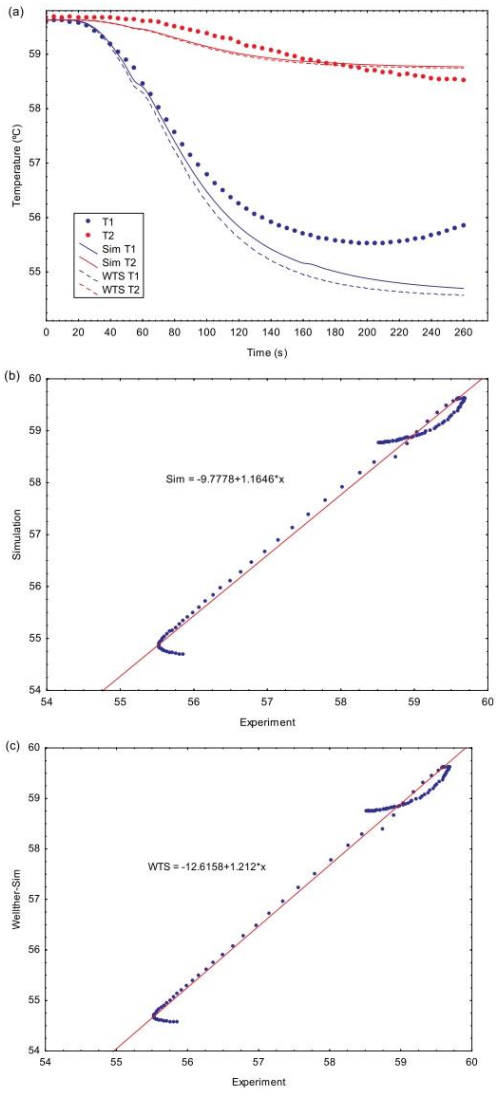

Fig. 7. Experiment considering a disturbance time of 55 s and 205 s of shut-in time. (a) Experimental and simulated thermal behavior for thermocouples at different radial positions, (b) comparison between simulated and experimental data, and (c) comparison between Wellther-sim and experimental data.

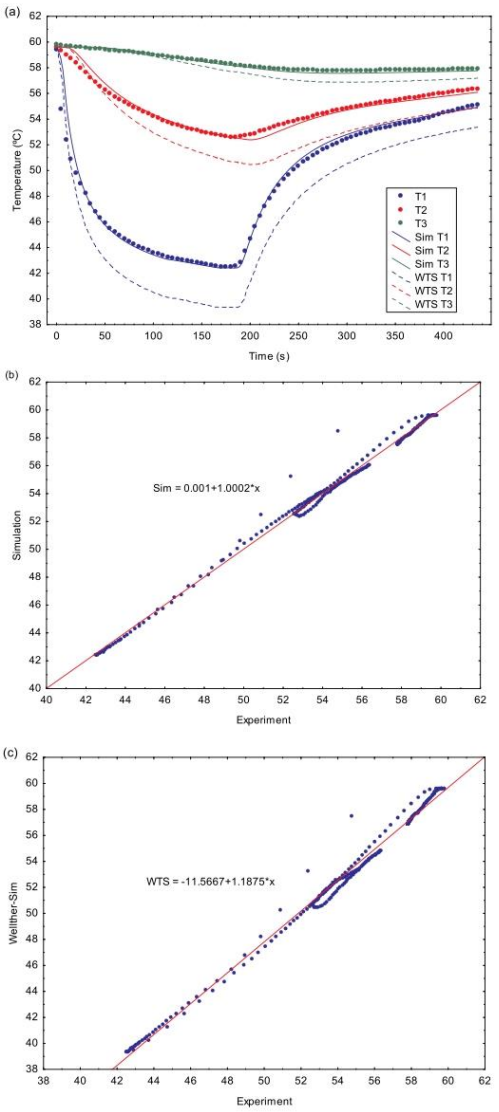

Fig. 8. Experiment considering a disturbance time of 180 s and 250 s of shut-in time. (a) Experimental and simulated thermal behavior for thermocouples at different axial positions, (b) comparison between simulated and experimental data, and (c) comparison between Wellther-sim and experimental data.

structured mesh in each subdomain made of hexahedral control volumes (i.e. a cubic domain discretized into smaller cubic control volumes). Mesh independency (variability <1%) for all output variables considered in this study, was attained by discretizing each axis in 90 subdivisions, hence yielding $\sim 7.3 \times 10^5$ control volumes. Figure # presents the mesh used during the disturbance process.

3. Results

In the present section, the validation of model assumptions is carried out by assessing the accuracy of the simulator against experiments that emulate the drilling process in a scaled down bottom-hole prototype. The first subsection presents two distinct transient thermal experiments in a solid block, heated and cooled in a thermal bath, and compared

against model simulations; the second subsection presents an experimental set-up along with a regression analysis that allows the independent estimation of the drilling fluid forced convection coefficient within the Borehole prototype.

Finally, after relevant parameters are independently estimated and validated, the simulation results are compared against experiments that emulate the thermal processes occurring during the drilling operations (for both the circulation time and the shut-in time). The main advantage of this approach is that it allows isolating the effect of different heat transfer processes (and the parameters involved), hence, shedding more light in the improvement of the simulator assumptions.

The independent estimation of the diffusive and convective parameters used within the simulation to describe the Bottom-hole thermal behavior. Table 2 presents the average and standard deviations of experimentally obtained values.

The plaster thermal properties were estimated using a KD2 Pro device, which uses a Transient Line Heat Source Method to estimate thermal conductivity, volumetric heat capacity, thermal diffusivity and thermal resistivity. The convective heat transfer coefficient was estimated, as explained in the methodology section.

After estimating the thermal parameters, the experiments emulating a typical drilling operation are compared against simulations for the five thermocouples presented in Fig. 2. The process of emulating a typical drilling operation in a scaled-down bottom-hole considers the stages of disturbance and shut-in sequentially; two experiments are presented with different disturbance times of 55 and 180 s.

Fig. 6 presents (a) and compares (b and c) experimental and simulations data obtained at different axial positions for the scaled-down prototype with disturbance and shut-in times of 55 and 205 s, respectively. As expected, the closest the thermocouple is to the Bottom-hole surface, the closer its temperature is to the drilling fluid temperature (T_{fl}); T1 is closest, and T3 is the furthest. The furthest thermocouple (T3) from the bottom-hole perforation presents only slight variations in temperature; as it was still 2.1 cm from the lower boundary, it can be implied that thermal perturbations never reached the bottom boundary, hence, the finite cube behaves as a semi-infinite domain.

Fig. 7 considers the same experiment presented in Fig. 6, however, the experimental and simulations data belong to thermocouples located at two different radial positions. With respect to the distance from the well, the same behavior is observed: the thermocouple with a radial position further away from the well (T2) presents a slighter temperature variation than that of the thermocouple closer to the well (T1). Again, from the data collected by thermocouple T2 (Fig. 7a), it can be seen that thermal perturbations do not reach the boundaries in the radial direction. Moreover, From Fig. 7 (a and b and c), it can be seen that Thermocouple T1, deviations from simulation and experimental data growing with time; however, deviations for thermocouple T2 remain bounded.

Finally, Fig. 8 and Fig. 9 present and compare experimental and simulation data for disturbance and shut-in times of 180 and 250 s, respectively. Fig. 8 presents thermocouples located at different axial positions; Fig. 9, for different radial positions. When compared against shorter disturbance and shut-in times (Figs. 6 and 7), simulation results for different axial (Fig. 8) and radial (Fig. 9) positions, better represent the experimental data. This is also expected, given that longer disturbance times yield a temperature distribution within the emulated rock formation that is closer to a steady state; i.e. longer times imply temperatures that are less dependent on time itself. This in turn, means that deviations between the model and real temperature profiles for should be closer to each other before the recuperation stage starts, hence, increasing the chances that both the affectation and recuperation stage are well described by the simulation results.

Additionally, as seen in Fig. 7, in Fig. 9(a and b and c), it is observed that, for thermocouple T1, deviations between simulations and experimental data also grow with time while deviations for thermocouple T2 remain bounded. Table 3 presents deviations between simulation and

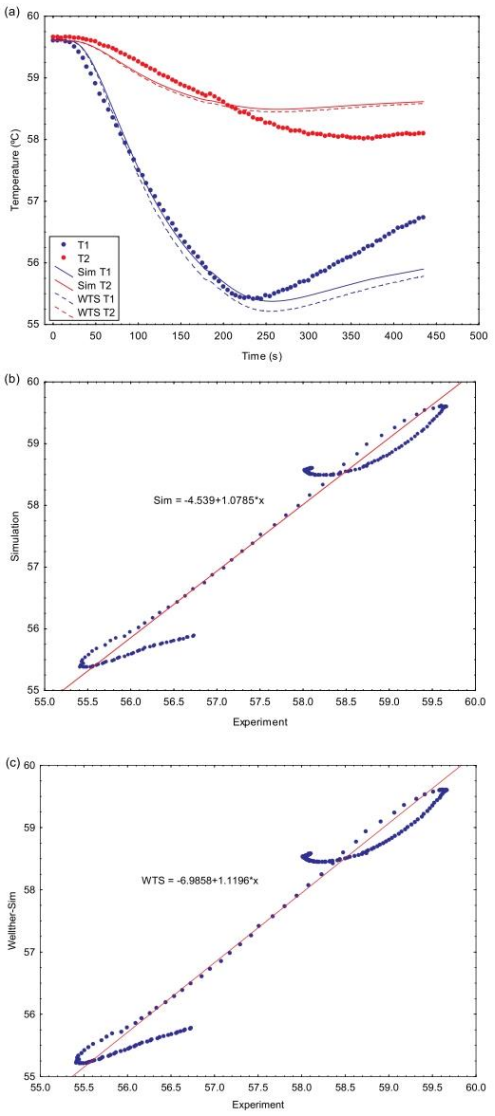

Fig. 9. Experiment considering a disturbance time of 180 s and 250 s of shut-in time. (a) Experimental and simulated thermal behavior for thermocouples at different radial positions, (b) comparison between simulated and experimental data, and (c) comparison between Wellther-sim and experimental data.

experimental data using a merit function as a quantitative quality measure between simulation and experiment, as used by Andaverde et al., (2019), Estrada-Wiese and del Rio, 2018 and Estrada-Wiese et al., 2018.

Table 3
Merit function computed by this work simulator for all five thermocouples and both experiments.

Simulation	Axial			Radial		Average
	T1	T2	T3	T1	T2	
1 (55 s)	7.6×10^{-3}	4.4×10^{-3}	3.1×10^{-3}	9.4×10^{-3}	2.6×10^{-3}	5.4×10^{-3}
2 (180 s)	1.19×10^{-2}	5.8×10^{-3}	2.6×10^{-3}	5.9×10^{-3}	5.6×10^{-3}	6.3×10^{-3}

Table 4
Merit function computed by Welltherm-Sim for all five thermocouples and both experiments.

Experiment	Axial			Radial		Average
	T1	T2	T3	T4	T5	
1 (55 s)	3.5×10^{-2}	1.5×10^{-2}	5.6×10^{-3}	1.2×10^{-2}	2.7×10^{-3}	1.4×10^{-2}
2 (180 s)	5.1×10^{-2}	3.0×10^{-2}	1.1×10^{-2}	7.5×10^{-3}	5.1×10^{-3}	2.1×10^{-2}

$$N = \sqrt{\frac{\int_{\lambda_1}^{\lambda_f} \left(E(\lambda) - S(\lambda)\right)^2 d\lambda}{\left(\int_{\lambda_1}^{\lambda_f} E(\lambda) d\lambda\right)^2}} \tag{9}$$

in which $E(\lambda)$ and $S(\lambda)$ are the experimental and simulated data, respectively. The smaller N becomes, the better the fit between the experiments and the model. Merit functions were computed for each experiment and each thermocouple, the obtained values are presented in Table 3. A value of N close to 1, denote deviations of about 100%. For the emulated drilling operation, values around 0.5% are observed; the largest ones being 1.2% for experiment 2 with the thermocouple 1 (T1).

Figs. 6b, 7b and 8b, 9b, and the merit functions values show a good agreement between the simulator and the experiment, in the mentioned figures are expected that regression model was a straight line with a slope value of 1 and intercept value of 0, while the value of the merit function is expected a value near to 0.

Also, the results obtained in this work were compared with the results obtained by Wellther-Sim (Wong-Loya et al., 2017) (Table 4). Figs. 6 (b and c), 7 (b and c), 8 (b and c) and 9 (b and c) shown better agreement of this simulator than Wellther-Sim. Also the merit function values obtained by the simulator presented in this work are better than those obtained by Wellther-Sim by about an order of magnitude. Hence, model assumptions 4 is physically sound and better suited.

4. Conclusions

A simulator for thermal processes during the wellbore drilling was developed for a reliable reproduction of the thermal disturbance and recovery process. The heat model used enabled the drilling fluid circulation and shut-in processes to be accurately described in the wellbore and the surrounding rock-formation.

The simulator was validated by an experiment, using a devised prototype, showing good agreement between the experimental and simulated data. It this seen that considering the thermal mass below the drilled bottom-hole allows better representing the thermal behavior of the prototype, i.e. locating the domain boundary far enough so that the thermal fronts can travel freely for the duration of the experiment. Moreover, a Robin type boundary condition at the borehole-rock formation interface allows better representing thermal disturbance process, hence, better representing the temperature distribution at the beginning of the recovery process.

Although experiments are not directly obtained from a real perforation, the scale-down Bottom-hole presents advantages such as: independent estimation of involved parameter, reproducibility of experiments. Ultimately the model is able to capture the main features for both, disturbance and recovery, suggesting that the model assumptions allow a better description of the physical phenomena and as such, for future work, the model is to be validated considering prototypes with non-homogeneous rock formations.

Computer code availability

The program "Thermal_behavior" was written in Fortran 90 programming language. The program estimates the temperature profiles of the rock formation during the processes of disturbance and thermal recovery, occurring during the geothermal well drilling process. The code is available for download from the following public repository: https://github.com/Ricardo-IER/thermal-behavior.git.

In the link, there are three files: the file "code", presenting the uncompiled source code; the "user's manual", that explains how to use the code; and the file "Computer code information", that presents general information.

Author contribution

Molin-Rodea R.: PhD Student, Conducted experimentation and data analysis.

Wong-Loya J.A.: Researcher, Simulator design, data analysis, job supervision and article writing.

Valades-Pelayo P.J.: Researcher, Analysis of heat transfer and results, writing of the article.

Declaration of competing interest

None.

Acknowledgements

The first author wishes to thank to the Engineering PhD programme of UNAM and CONACyT for the financial support provided through the scholarships.

This work was partially financed by the PAPIME-UNAM project (PE110319).

References

Andaverde, J., Wong-Loya, J.A., Vargas-Tabares, Y., Robles-Perez, M., 2019. A practical method for determining the rheology of drilling fluid. J. Pet. Sci. Eng. 180, 150–158. https://doi.org/10.1016/j.petrol.2019.05.039 (December 2018).

Andaverde, J., Verma, S.P., Santoyo, E., 2005. Uncertainty estimates of static formation temperatures in boreholes and evaluation of regression models. Geophys. Geophys. J. Int. 160, 1112–1122.

Bassam, A., Santoyo, E., Andaverde, J., Hernandez, J.A., Espinoza-Ojeda, O.M., 2010. Estimation of static formation temperatures in geothermal wells by using an artificial neural network approach. Comput. Geosci. 36, 1191–1199.

Bassam, A., Del Castillo, A.Á., García-Valladares, O., Santoyo, E., 2015. Determination of pressure drops in flowing geothermal wells by using artificial neural networks and wellbore simulation tools. Appl. Therm. Eng. https://doi.org/10.1016/j.applthermaleng.2014.05.048.

Bording, T.S., Nielsen, S.B., Balling, N., 2016. The transient divided bar method for laboratory measurements of thermal properties. Geophys. J. Int. 207 (3), 1446–1455. https://doi.org/10.1093/gji/ggw278.
Bullard, E.C., 1947. Time necessary for a borehole to attain temperature equilibrium Astron. Soc. Geophys. Suppl. 5, 125–130.
Cao, S., Lerche, I., Hermanrud, C., 1988. Formation temperature estimation by inversion of borehole measurements. Geophysics 53 (7), 979–988. Retrieved from. http://geophysics.geoscienceworld.org/cgi/content/abstract/53/7/979.
Chang, X., Zhou, J., Guo, Y., He, S., Wang, L., Chen, Y., Jian, R., 2018. Heat transfer behaviors in horizontal wells considering the effects of drill pipe rotation, and hydraulic and mechanical frictions during drilling procedures. Energies 11 (9), 2414.
Espinosa-Paredes, G., Morales-Díaz, A., Olea-González, U., Ambriz-García, J.J., 2009. Application of a proportional-integral control for the estimation of static formation temperatures in oil wells. Mar. Pet. Geol. 26 (2), 259–268.
Espinosa-Paredes, G., Garcia, A., Santoyo, E., Hernandez, I., 2001. TEMLOPI/V. 2: a computer program for estimation of fully transient temperatures in geothermal wells during circulation and shut-in. Comput. Geosci. 27 (3), 327–344.
Espinoza-Ojeda, O.M., Santoyo, E., 2016. A new empirical method based on log-transformation regressions for the estimation of static formation temperatures of geothermal, petroleum and permafrost boreholes. J. Geophys. Eng. 13 (4), 559–596.
Estrada-Wiese, D., del Río-chanona, E.A., del Río, J.A., 2018. Stochastic optimization of broadband reflecting photonic structures. Sci. Rep. 1–9. https://doi.org/10.1038/s41598-018-19613-6 (November 2017).
Estrada-Wiese, D., del Rio, J.A., 2018. Refractive index evaluation of porous silicon using bragg reflectors. Rev. Mex. Fis. 64 (February), 72–81.
Fuchs, S., Balling, N., Förster, A., 2015. Calculation of thermal conductivity, thermal diffusivity and specific heat capacity of sedimentary rocks using petrophysical well logs. Geophys. J. Int. 203 (3), 1977–2000. https://doi.org/10.1093/gji/ggv403.
García-Valladares, O., Sánchez-Upton, P., Santoyo, E., 2006. Numerical modeling of flow processes inside geothermal wells: an approach for predicting production characteristics with uncertainties. Energy Convers. Manag. 47 (11–12), 1621–1643.
Hasan, A.R., Kabir, C.S., 2012. Wellbore heat-transfer modeling and applications. J. Pet. Sci. Eng. 86, 127–136.
International Renewable Energy Agency, 2018. Renewable Energy Highlights - July 2018.
Jiang, G., Li, W., Rao, S., Shi, Y., Tang, X., Zhu, C., Hu, S., 2016. Heat flow, depth–temperature, and assessment of the enhanced geothermal system (EGS) resource base of continental China. Environ. Earth Sci. 75 (22), 1432.
Lee, T.C., 1982. Estimation of formation temperature and thermal property from dissipation of heat generated by drilling. Geophysics 47 (11), 1577–1584.
Li, M., Liu, G., Li, J., Zhang, T., He, M., 2015. Thermal performance analysis of drilling horizontal wells in high temperature formations. Appl. Therm. Eng. 78, 217–227.
Liu, C., Li, K., Chen, Y., Jia, L., Ma, D., 2016. Static formation temperature prediction based on bottom hole temperature. Energies 9 (8), 646.
Luheshi, M.N., 1983. Estimation of formation temperature from borehole measurements. Geophys. J. 74, 747–776.
Pan, L., Oldenburg, C.M., 2014. T2Well-An integrated wellbore-reservoir simulator. Comput. Geosci. 65, 46–55. https://doi.org/10.1016/j.cageo.2013.06.005.
Ricard, L.P., Chanu, J.B., 2013. GeoTemp™ 1.0: a MATLAB-based program for the processing, interpretation and modelling of geological formation temperature measurements. Comput. Geosci. 57, 197–207.
Sanaz, S., Rafid, A.-K., Frans, B., et al., 2013. An efficient computational model for deep low-enthalpy geothermal systems. Comput. Geosci. 51, 400–409. https://doi.org/10.1016/j.cageo.2012.08.019. In this issue.
Shen, P.Y., Beck, a.E., 1986. Stabilization of bottom hole temperature with finite circulation time and fluid flow. Geophys. J. Int. 86 (1), 63–90. https://doi.org/10.1111/j.1365-246X.1986.tb01073.x.
Tinti, F., Kasmaee, S., Elkarmoty, M., Bonduà, S., Bortolotti, V., 2018. Suitability evaluation of specific shallow geothermal technologies using a GIS-Based multi criteria decision analysis implementing the analytic hierarchic process. Energies 11 (2). https://doi.org/10.3390/en11020457.
Van Oort, E., Incedalip, O., Vajargah, A.K., 2018. Thermal wellbore strengthening through managed temperature drilling – Part I: thermal model and simulation. J. Nat. Gas Sci. Eng. 58, 275–284. https://doi.org/10.1016/j.jngse.2018.06.046 (May).
Waples, D.W., Pacheco, J., Vera, A., 2004. A method for correcting log-derived temperatures in deep wells, calibrated in the Gulf of Mexico. Pet. Geosci. 10, 239–245.
Wong-Loya, J. a, Andaverde, J., Santoyo, E., 2012. A new practical method for the determination of static formation temperatures in geothermal and petroleum wells using a numerical method based on rational polynomial functions. J. Geophys. Eng. 9 (6), 711–728. https://doi.org/10.1088/1742-2132/9/6/711.
Wong-Loya, J.A., Santoyo, E., Andaverde, J.A., Quiroz-Ruiz, A., 2015. RPM-WEBBSYS: a web-based computer system to apply the rational polynomial method for estimating static formation temperatures of petroleum and geothermal wells. Comput. Geosci. 85, 45–59. https://doi.org/10.1016/j.cageo.2015.09.001.
Wong-Loya, J.A., Santoyo, E., Andaverde, J., 2017. A 3-D wellbore simulator (WELLTHER-SIM) to determine the thermal diffusivity of rock-formations. Comput. Geosci. 103 (July 2016), 204–214. https://doi.org/10.1016/j.cageo.2017.03.016.
Wu, B., Zhang, X., Jeffrey, R.G., 2014. A model for downhole fluid and rock temperature prediction during circulation. Geothermics 50, 202–212.
Yang, M., Meng, Y., Li, G., Li, Y., Chen, Y., Zhao, X., Li, H., 2013. Estimation of wellbore and formation temperatures during the drilling process under lost circulation conditions. Math. Probl. Eng. 2013.
You, J., Rahnema, H., McMillan, M.D., 2016. Numerical modeling of unsteady-state wellbore heat transmission. J. Nat. Gas Sci. Eng. 34, 1062–1076. https://doi.org/10.1016/j.jngse.2016.08.004.
Zare-Reisabadi, M., Kamali, M.R., Mohammadnia, M., Shabani, F., 2015. Estimation of true formation temperature from well logs for basin modeling in Persian Gulf. J. Pet. Sci. Eng. 125, 13–22. https://doi.org/10.1016/j.petrol.2014.11.009.

Capítulo VIII. "Validación experimental"

En este capítulo se presenta la validación de los modelos numéricos desarrollados para determinar las condiciones térmicas de trabajo de EAHE. Se incluye la validación del modelo numérico para determinar el perfil de temperatura del suelo visto en el capítulo II, la validación del modelo numérico para determinar las condiciones térmicas de trabajo de EAHE visto en el capítulo V, y la validación del modelo numérico para reproducir la afectación térmica del suelo visto en el capítulo VII. Para referirnos a ellos, en este capítulo los llamaremos modelo 1, 2 y 3 a los modelos numéricos presentados en los capítulos II, V y VII, respectivamente.

Dado que no existe una sola métrica estadística para la validación de modelos numéricos desarrollados para predecir fenómenos físicos, es preferible utilizar una combinación de ellos tomando en cuenta el propósito para el que el modelo fue conceptualizado y desarrollado [Tedeschi 2006]. Debido a ello, para realizar la validación de los distintos modelos presentados en este trabajo se utilizaron las siguientes medidas de ajuste:

- Error relativo porcentual (*e*): $$e = \left|\frac{T_R - T_S}{T_R}\right| \cdot 100$$ [8.1]

- Coeficiente de determinación (R^2): $$R^2 = \frac{(\sigma T_R T_S)^2}{\sigma {T_R}^2 \cdot \sigma {T_S}^2}$$ [8.2]

- Función de mérito (*M*): $$M = \sqrt{\frac{\sum_{i=1}^{n}(T_R - T_S)^2}{\sum_{i=1}^{n}(T_R)^2}}$$ [8.3]

En las ecuaciones 8.1, 8.2 y 8.3 T_R y T_S son la temperatura real (medida durante los experimentos con termopares) y la temperatura simulada en °C, respectivamente. En la ecuación 8.3 $\sigma T_R T_S$ es la covarianza y σT_R y σT_S las varianzas de las temperaturas comparadas.

El error relativo porcentual (***e***) es la relación entre el error absoluto y el valor real multiplicado por cien, y sirve para indicar la diferencia de entre la temperatura real y la temperatura simulada en la escala del valor real. En trabajos publicados sobre validación experimental de modelos numéricos, un error relativo porcentual menor al 10% representa una fuerte relación entre la observación experimental y los resultados simulados [Amanowicz & Wojtkowiak, 2018] [Bisoniya et al., 2015] [Wang et al., 2018]. En el presente trabajo se utiliza el error relativo porcentual para comparar el modelo 1 y 2 contra datos publicados en otros trabajos ya que en ellos solo fueron expuestos algunos valores puntuales.

Por su parte, el coeficiente de determinación (***R²***), o bondad del ajuste, se utiliza para conocer la precisión de un modelo al momento de predecir o replicar resultados experimentales. Este coeficiente se obtiene con la relación entre varianzas y covarianzas de dos variables. Para el caso de modelos lineales entre dos variables, el coeficiente de determinación se obtiene de multiplicar el coeficiente de correlación de Pearson al cuadrado. A diferencia del coeficiente de correlación, el coeficiente ***R²*** se puede utilizar para modelos lineales o no [Bisoniya et al., 2014] [Serageldin et al., 2016]. Su valor se encuentra entre cero y uno, donde un valor cercano a uno representa una

adecuada concordancia entre el modelo y los datos experimentales. En este trabajo se utiliza para comparar los resultados obtenidos con los modelos 2 y 3.

Por último, la función de mérito (***M***) es una medida de calidad cuantitativa entre datos observados y datos simulados [Andaverde et al., 2019]. Esta métrica muestra la desviación entre el modelo y los experimentos, al considerar la sumatoria de las diferencias entre ambos valores. En específico, la función de mérito mostrada en la ecuación 8.3 ha sido utilizada previamente para determinar la concordancia entre series de datos simulados y experimentales [Estrada-Wiese, 2018]. A valores para ***M*** más cercanos a cero, es mejor el ajuste entre el experimento y el modelo [Estrada-Wiese et al., 2010]. En el presente trabajo se utilizó la función de mérito para validar los tres modelos numéricos presentados en este trabajo.

Validación del modelo 1.

La validación del modelo para determinar los perfiles de temperatura del suelo se realizó en dos partes. En ambas se compararon los datos simulados contra los datos obtenidos con la sonda de medición y con los EAHE instalados. La primera parte de la validación se presentó en el artículo expuesto en el capítulo II haciendo uso de la función de mérito para comparar los datos simulados con la sonda de medición. En la Tabla 8.1 se muestran los valores de la función de mérito vista en la ecuación 8.3 para el modelo completo, el modelo parcial, y la solución analítica utilizada comúnmente. Se observa que los valores de ***M*** para la solución analítica presentan los peores resultados, con un promedio de $1.5_{x10^{-1}}$. Por el otro lado, el modelo completo presentó los mejores resultados de ***M***, con un valor promedio de $3.2_{x10^{-2}}$. Incluso el modelo parcial arrojó mejores resultados que la solución analítica, con un valor promedio de $4.5_{x10^{-2}}$.

*Tabla 8.1. Se presentan la profundidad de medición y los distintos valores de la función de mérito (**M**) para la solución analítica, el modelo parcial y el modelo completo.*

Profundidad	***M*** Solución analítica	***M*** Modelo parcial	***M*** Modelo completo
0.6 m	$2.5_{x10^{-1}}$	$6.0_{x10^{-2}}$	$4.5_{x10^{-2}}$
0.8 m	$2.1_{x10^{-1}}$	$6.6_{x10^{-2}}$	$4.9_{x10^{-2}}$
1.0 m	$1.8_{x10^{-1}}$	$4.7_{x10^{-2}}$	$3.4_{x10^{-2}}$
1.2 m	$1.5_{x10^{-1}}$	$4.2_{x10^{-2}}$	$2.9_{x10^{-2}}$
1.4 m	$1.2_{x10^{-1}}$	$3.7_{x10^{-2}}$	$2.5_{x10^{-2}}$
1.6 m	$1.1_{x10^{-1}}$	$3.4_{x10^{-2}}$	$2.4_{x10^{-2}}$
1.8 m	$9.0_{x10^{-2}}$	$3.2_{x10^{-2}}$	$2.1_{x10^{-2}}$

La segunda parte de la validación del modelo numérico se realizó al comparar los resultados del simulador y los valores de temperatura que se midieron alrededor de los tubos enterrados antes de realizar las pruebas que se expusieron en el capítulo IV. Para esta parte de la validación se utilizó el error relativo como métrica de comparación. En la primera columna de la Tabla 8.2 se muestran las distintas profundidades de comparación, en la segunda se muestra el promedio de temperatura registrada durante marzo 2019 y 2020, en la tercera la temperatura obtenida con el modelo numérico, y en la cuarta el error relativo porcentual. Se observa que el error relativo porcentual promedio es de 2.7 %, mientras que el valor máximo es de 3.3 %. Lo anterior indica un adecuado ajuste entre los resultados del modelo numérico y las mediciones en el sitio de experimentación. La

Imagen 8.1 muestra una comparación entre la temperatura simulada y la temperatura registrada durante marzo a distintas profundidades.

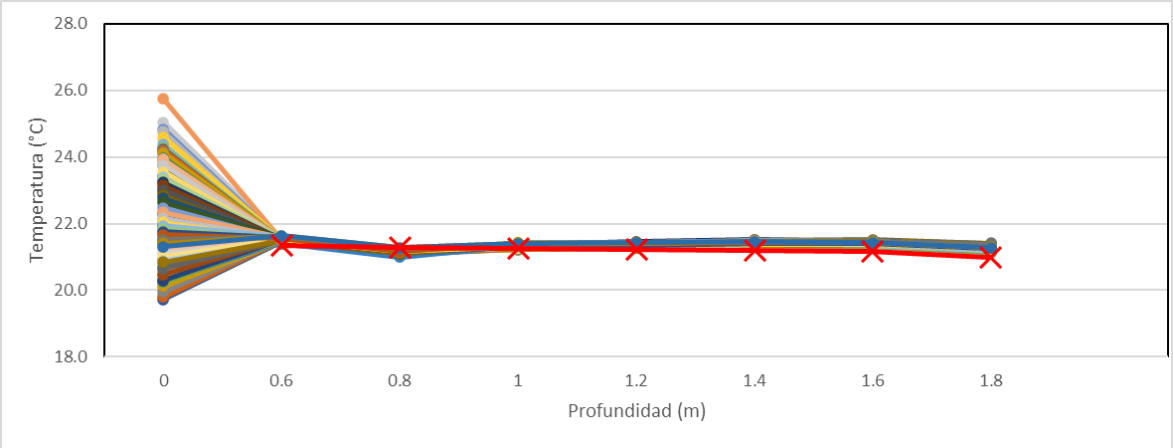

Imagen 8.1. Se presenta una comparación entre los valores simulados (rojo) y el registro de la sonda de medición (resto de colores) hasta una profundidad de 1.8 m.

*Tabla 8.2. Se presentan las distintas profundidades de comparación, así como la temperatura registrada, la temperatura simulada y el error relativo porcentual (**e**)*

Profundidad	Temperatura registrada (°C)	Temperatura simulada (°C)	***e*** (%)
0.6 m	22.1 ± 0.5	21.4	3.3
0.8 m	21.7 ± 0.5	21.3	2.0
1.0 m	21.9 ± 0.5	21.2	2.8
1.2 m	21.8 ± 0.5	21.2	2.8
1.4 m	21.8 ± 0.5	21.2	2.9
1.6 m	21.8 ± 0.5	21.2	2.8
1.8 m	21.5 ± 0.5	21.1	2.6

Validación del modelo 2.

La validación del modelo para determinar las condiciones térmicas de trabajo de intercambiadores de calor presentado en el capítulo V también se realizó en dos partes. Se compararon las temperaturas obtenidas con el modelo matemático contra datos numéricos y datos experimentales. La primera parte de la validación se presentó en el artículo expuesto en el capítulo V utilizando el error relativo porcentual como medida de ajuste. En esta parte se muestra la comparación del modelo contra valores numéricos publicados por un autor quien presentó dos casos de estudio sobre intercambiadores de calor instalados en pozos geotérmicos profundos [Hernández-Magallanes et al., 2019]. En la Tabla 8.3 se muestran los valores utilizados en la simulación, así como la temperatura reportada por el autor, la obtenida con el modelo matemático, y el error relativo porcentual. Se observa que para los 3 puntos de comparación el error no excede el 5%, lo cual indica un adecuado ajuste.

Tabla 8.3. Datos utilizados para la validación del modelo numérico.

Caso de estudio	Parámetros de funcionamiento				Resultados		***e*** (%)
	Diámetro (in)	Longitud total (m)	Velocidad (m/s)	T. de entrada (°C)	Reportados (°C)	Simulador (°C)	

1	1	200	1	24.0	28.2	26.9	4.6
					65.0	63.4	2.5
2	1	3700	7	30.0	72.8	74.3	2.1

La segunda parte de la validación se realizó utilizando la evaluación experimental hecha en los EAHE que se mostró en el capítulo IV de este trabajo, en donde se presentaron distintos experimentos modificando la velocidad del aire al interior de los tubos. Durante las pruebas se seleccionaron cuatro distintas velocidades, 1.3 m/s, 4.1 m/s, 6.4 m/s y 6.6 m/s. Mientras que para la validación se seleccionaron tres velocidades 1.3 m/s, 4.1 m/s y 6.5 m/s. Los resultados obtenidos a 6.4 m/s y 6.6 m/s se promediaron ya que el cambio de 0.2 m/s no generó cambios significativos, como se observó en el capítulo IV. En el mismo capítulo se explica que alrededor del pozo de entrada se encontró una anomalía térmica producida por una alcantarilla ubicada en las cercanías. Debido a esta razón, y a que no se cuenta con información precisa sobre su temperatura y ubicación, se decidió tomar los datos del segundo pozo para la validación del modelo numérico. En esta sección se utilizó la función de mérito de la ecuación 8.3 para determinar el nivel de ajuste entre el modelo y los datos experimentales. Las Imágen 8.2 muestran una comparación gráfica de la temperatura a la entrada, en la sección más profunda y a la salida del segundo pozo, entre los valores simulados y los valores medidos a distintas velocidades.

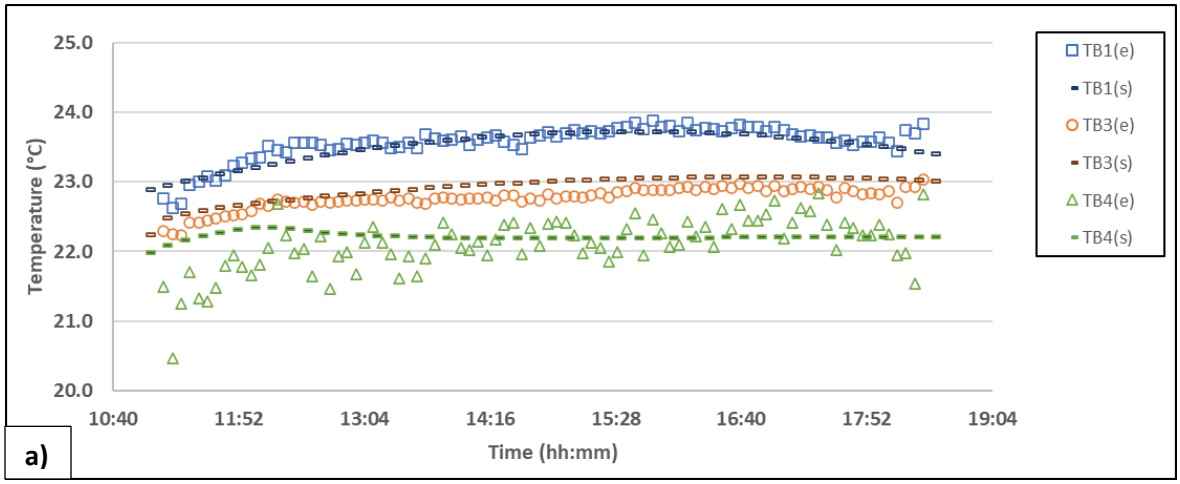

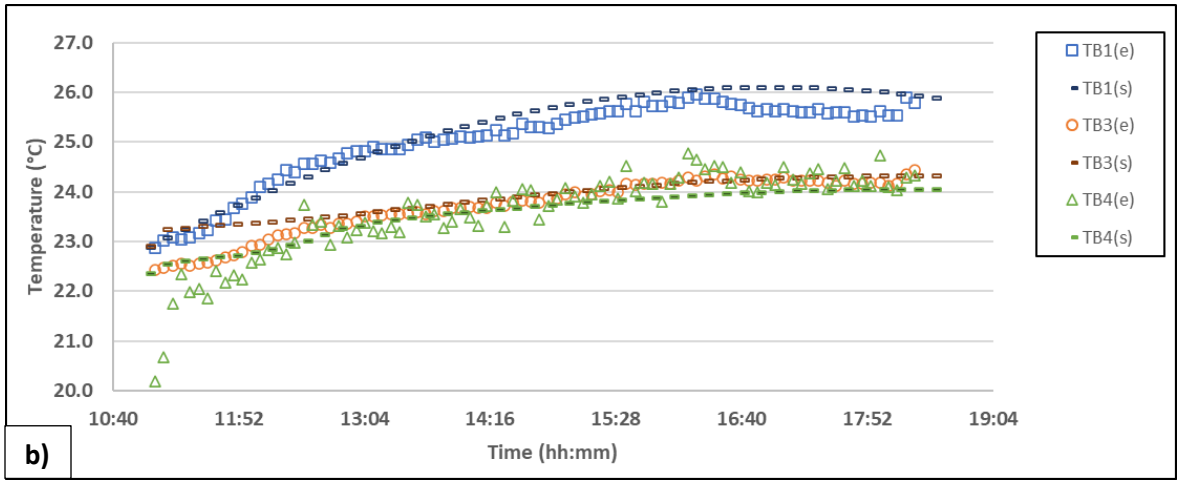

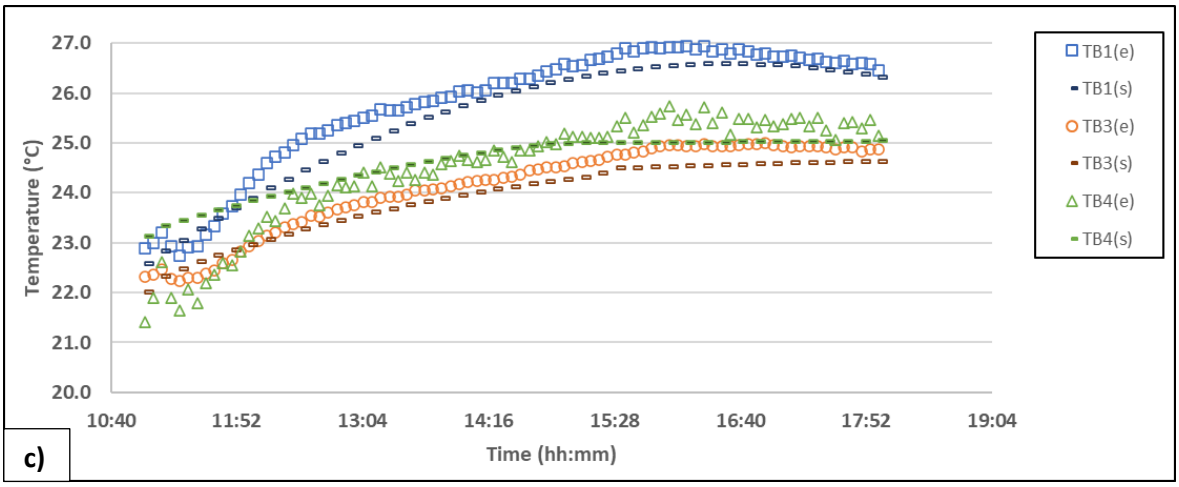

Imagen 8.2. Se muestra la comparación entre datos experimentales (e) y datos simulados (s) para una velocidad de a) 1.3 m/s, b) 4.1 m/s, c) 6.5 m/s.

En las gráficas que se muestran en la Imagen 8.2 se observa que el modelo presenta un mejor ajuste con las temperaturas registradas al pasar de un estado no estacionario a uno *cuasi* estacionario. Esto tiene explicación ya que el modelo presentado en el capítulo V de este trabajo, aunque utiliza condiciones iniciales que asemejan a la realidad y toma en consideración el gradiente geotérmico del suelo, no se enfoca en el régimen transitorio, más bien en las condiciones térmicas de trabajo durante ciclos de operación. En la Tabla 8.4 se muestran los valores del coeficiente de determinación para las velocidades y posiciones mencionadas anteriormente. Se observa que cuando se utiliza el coeficiente R^2 como métrica de comparación, los resultados obtenidos a una velocidad de 6.5 m/s son los que tienen un mejor ajuste.

Tabla 8.4. Se muestran los valores del coeficiente de determinación para las distintas velocidades utilizadas.

	R^2@1.3 m/s	R^2@4.1 m/s	R^2@6.5 m/s
TB1	0.7991	0.9696	0.9768
TB3	0.8611	0.9468	0.9823
TB4	0.0164	0.8604	0.9654

Validación del modelo 3.

El modelo numérico que reproduce la afectación térmica del suelo producida por la circulación de un fluido que se expuso en el capítulo anterior también se validó en dos partes. Se realizaron comparaciones contra datos tomados en el laboratorio y en el sitio de experimentación de los EAHE. La primera parte se expone en el artículo presentado en el capítulo VII, en el cual se hace uso de la función de mérito y del coeficiente de determinación a fin de establecer la calidad del modelo para reproducir los fenómenos de perturbación térmica en el suelo. Los datos obtenidos con el modelo numérico se comparan con datos de laboratorio de un modelo a escala por el que se hizo circular un fluido. En la Tabla 8.5 se muestran los valores de la función de mérito para el modelo original y el modelo mejorado. Se observa que en el primer experimento el valor promedio de la función de mérito para modelo original tuvo un valor de $1.4_{x10^{-2}}$, mientras que el modelo mejorado tuvo un valor de $5.4_{x10^{-3}}$. En el segundo experimento también se observó una mejora, ya que el modelo original presenta un valor promedio de la función de mérito de $2.1_{x10^{-2}}$, mientras que el nuevo

modelo arroja un valor de $6.3_{x10^{-3}}$. Lo anterior refleja un mejor ajuste del modelo mejorado en comparación con el modelo original.

Tabla 8.5. Valores de la función de mérito del modelo original y el modelo utilizado en este trabajo.

		Dirección axial			Dirección radial	
		T1	T2	T3	T4	T5
Caso de estudio 1	M. original	$3.5_{x10^{-2}}$	$1.5_{x10^{-2}}$	$5.6_{x10^{-3}}$	$1.2_{x10^{-2}}$	$2.7_{x10^{-3}}$
	M. mejorado	$7.6_{x10^{-3}}$	$4.4_{x10^{-3}}$	$3.1_{x10^{-3}}$	$9.4_{x10^{-3}}$	$2.6_{x10^{-3}}$
Caso de estudio 2	M. original	$5.1_{x10^{-2}}$	$3.0_{x10^{-2}}$	$1.1_{x10^{-2}}$	$7.5_{x10^{-3}}$	$5.1_{x10^{-3}}$
	M. mejorado	$1.2_{x10^{-2}}$	$5.8_{x10^{-3}}$	$2.6_{x10^{-3}}$	$5.9_{x10^{-3}}$	$5.6_{x10^{-3}}$

La segunda parte de la validación se realizó utilizando los datos experimentales de los EAHE del capítulo IV. En específico, se utilizaron los datos de la temperatura del suelo que se registraron con los termopares colocados en dirección radial del tubo por donde fluyó el aire. Al igual que se explicó en la sección anterior, para realizar la validación del modelo se utilizaron únicamente tres distintas velocidades, 1.3 m/s, 4.1 m/s y 6.5 m/s. Otra declaración que se retoma de la sección anterior es la que explica que para la comparación se utilizaron los datos registrados en el segundo pozo debido a la alteración térmica producida por la alcantarilla. En este caso se utilizó el coeficiente de determinación y la función de mérito para determinar el nivel de ajuste entre el modelo y los datos experimentales.

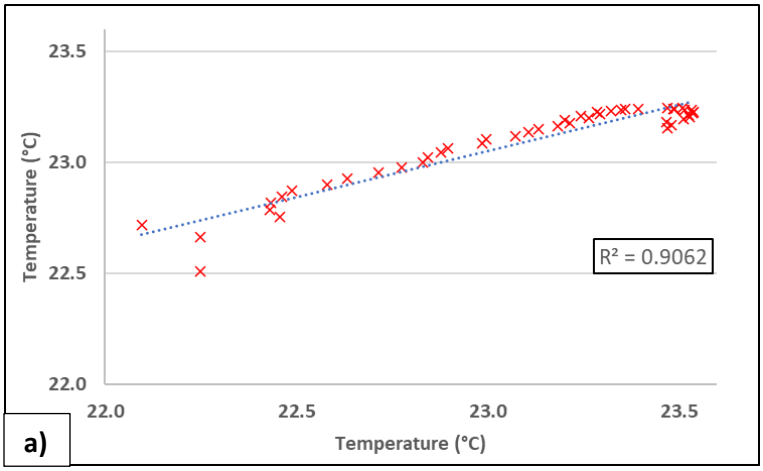

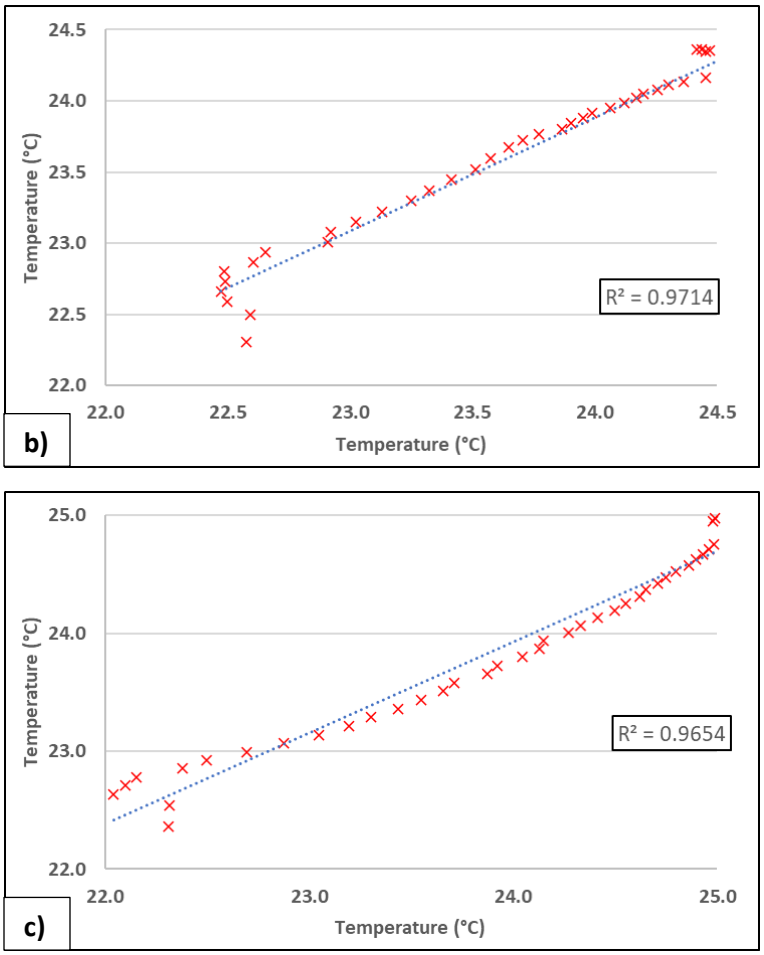

Imagen 8.3. Recta de ajuste entre datos experimentales y datos simulados durante la afectación térmica del suelo.

Tabla 8.6. Valores del coeficiente de determinación y función de mérito durante la afectación térmica del suelo.

Velocidad	R^2	M
1.3 m/s	0.9062	$1.1_{x10^{-2}}$
4.1 m/s	0.9714	$8.3_{x10^{-3}}$
6.5 m/s	0.9654	$1.2_{x10^{-2}}$

Las Imagen 8.3 muestran una comparación gráfica de la temperatura registrada con los termopares y la temperatura simulada para las velocidades fijadas. Se observó que en los tres casos el modelo presenta problemas para reproducir los primeros instantes de la afectación térmica, que es cuando la temperatura del suelo se encuentra en los valores mínimos. En la Tabla 8.6 se presentan los valores del coeficiente de determinación y de la función de mérito para los tres casos expuestos. Utilizando ambas métricas de comparación, el modelo reprodujo de mejor manera los resultados observados cuando la velocidad era 4.1 m/s. El resultado de la validación indica un adecuado ajuste entre el modelo numérico y los datos experimentales.

En este capítulo se exhibieron las validaciones realizadas a los modelos numéricos desarrollados y utilizados en este trabajo. La validación se realizó utilizando el error relativo, el coeficiente de

determinación, y la función de mérito que se detallaron al comienzo. De cada uno de los modelos se dio una breve explicación de su uso, los valores utilizados en la comparación y los resultados de la validación.

Capítulo IX. "Conclusiones"

Conclusiones

En el trabajo realizado durante el doctorado se desarrolló un simulador numérico que funciona con tres módulos y que sirve para determinar las condiciones térmicas de trabajo de intercambiadores de calor aire tierra (EAHE). Las conclusiones se exponen a continuación.

1. La energía geotérmica se ha posicionado como una alternativa viable para contribuir a la mitigación de gases de efecto invernadero y sus efectos adversos. En específico, para disminuir el consumo energético de equipos de acondicionamiento convencionales, los EAHE se presentan como una opción que ha sido demostrada y aplicada, pero que aún tiene un amplio campo de investigación. El desempeño de un equipo EAHE depende de factores ambientales, características del sitio de instalación, configuración geométrica y características de operación. Su rendimiento durante periodos de operación se puede conocer de manera experimental o numérica. Las simulaciones numéricas tienen la ventaja de consumir menos recursos económicos en comparación con el método experimental, pero es necesario conocer el problema de estudio y sus limitaciones al momento de diseñar el modelo numérico. Se llegó a esta conclusión después de realizar la revisión bibliográfica durante el estudio de doctorado.
2. En el proceso de transferencia de calor que ocurre entre el ambiente y el suelo influyen varios factores, desde las condiciones meteorológicas hasta el tipo de recubierta que tiene el suelo. La solución analítica utilizada frecuentemente para predecir la temperatura del suelo que se describió en el capítulo II toma en consideración algunas propiedades como la temperatura promedio anual del suelo, la amplitud de onda y la difusividad térmica del suelo. Un problema de esta solución es que, dependiendo de las condiciones puntuales de cada sitio de implementación, los perfiles de temperatura pueden tener valores y formas distintas. Debido a ello, esta solución puede ser utilizada en una forma general, pero tomando algunas consideraciones. Al considerar otros factores como la lluvia y su efecto en la dinámica térmica del suelo durante el diseño del modelo numérico, que también considera la porosidad y permeabilidad, se logró obtener resultados hasta un 80% con mejor ajuste en comparación con la solución analítica. Se llegó a esta conclusión después de analizar la transferencia de calor en el suelo, desarrollar el modelo numérico y validarlo.
3. Para aprovechar el bajo consumo energético que tienen los sistemas EAHE en comparación con sistemas de acondicionamiento convencional es necesario poder acercar esta tecnología a los lugares donde se pueda aprovechar. El principal objetivo de los EAHE es disminuir el consumo eléctrico de casas y oficinas en ciudades grandes, pero un problema de la urbanización es, precisamente, el poco espacio disponible para la instalación. Durante el desarrollo de este trabajo se instalaron diversos sistemas EAHE con configuración vertical. De este modo se consideraron las limitaciones de espacio al no pasar de $3.3m^2$ de superficie de instalación. Durante la evaluación se encontró que conforme aumenta el tiempo de residencia, la diferencia de temperaturas alcanzadas en el EAHE es mayor. También se encontró que, a mayor velocidad del aire, el funcionamiento del último pozo puede resultar contraproducente. En cuanto a la afectación térmica del suelo, se concluye que durante el transcurso de los días de funcionamiento la temperatura del suelo aumenta, por lo que es preferible una operación en modo intermitente para favorecer la recuperación térmica del

suelo. Estas conclusiones se obtuvieron después de instalar y evaluar experimentalmente el sistema EAHE.

4. La modelación numérica presenta la gran ventaja de ahorrar tiempo en comparación con la toma de datos en el sitio de experimentación. Durante la etapa de diseño de un modelo numérico es importante establecer de manera adecuada las suposiciones hechas, ya que de esta manera se tendrá una idea del alcance y objetivo de la simulación. El modelo numérico desarrollado para determinar las condiciones térmicas de funcionamiento de intercambiadores de calor aire tierra toma en consideración suposiciones del fluido de circulación, del mecanismo dominante de transferencia de calor en cada sección y del sitio de instalación. Con estas suposiciones durante la fase de diseño se logró modelar la temperatura del aire a lo largo del EAHE con un error relativo menor al 5% y un coeficiente de determinación promedio superior a 0.8. Se observó que el modelo se ajusta de mejor manera a los datos experimentales cuando se pasa de un estado transitorio a uno estacionario. Esto se explica por las consideraciones hechas en el fluido durante la fase de diseño del modelo numérico. Se concluye que las suposiciones del modelo son correctas y que reproduce con certeza las condiciones térmicas de trabajo.
5. La afectación térmica del suelo en temas relacionados a intercambiadores de calor enterrados es un tema al que aún no se le ha dado la importancia necesaria. En la gran mayoría de trabajos publicados en los que consideran el suelo como parte del domino de estudio, se considera que el suelo permanece con una temperatura constante a lo largo del periodo de funcionamiento del EAHE. Por la modelación y los experimentos realizados a lo largo del doctorado, se sabe que esta suposición dista mucho de la realidad, ya que se registró hasta 4.0 °C de diferencia en la temperatura del suelo antes y después de su funcionamiento. Se concluye que el modelo numérico desarrollado para reproducir la afectación térmica del suelo es capaz de replicar este fenómeno con un aceptable grado de ajuste, ya que durante la validación el coeficiente de determinación se mantuvo superior a 0.9. También se concluye que las suposiciones hechas durante la fase de diseño de este modelo numérico fueron adecuadas.

Trabajo a futuro

Como trabajo a futuro se propone:

- Ampliar la investigación bibliográfica para conocer los avances que se dan en el tema y aplicarlos a las necesidades del lugar donde se desea instalar el sistema EAHE.
- Reconsiderar las suposiciones hechas en el diseño de los distintos modelos numéricos para poder obtener resultados más realistas.
- Trabajar en un módulo de las condiciones hidráulicas de trabajo para integrarlo al simulador principal a fin de conocer la caída de presión y proponer un equipo impulsor.
- Instalar sistemas EAHE con distintas configuraciones y tomar mediciones bajo distintas condiciones de trabajo para aumentar la base de datos disponible para la validación.
- Investigar sobre el funcionamiento óptimo de EAHE con base a estudios paramétricos.
- Estudiar otras fuentes como sumidero de calor para presentar alternativas de aplicación cuando no se cuenten con las condiciones óptimas de instalación.

Bibliografía

1. Stober, I., & Bucher, K. (2013). History of geothermal energy use. In Geothermal Energy (pp. 15-24). Springer, Berlin, Heidelberg.
2. Huttrer, G. W. (2020, April). Geothermal power generation in the world 2015-2020 update report. In Proceedings world geothermal congress (Vol. 1).
3. Lund, J. W., & Toth, A. N. (2021). Direct utilization of geothermal energy 2020 worldwide review. Geothermics, 90, 101915.
4. Peretti, C., Zarrella, A., De Carli, M., & Zecchin, R. (2013). The design and environmental evaluation of earth-to-air heat exchangers (EAHE). A literature review. Renewable and Sustainable Energy Reviews, 28, 107-116.
5. Sakhri, N., Menni, Y., & Ameur, H. (2020). Effect of the pipe material and burying depth on the thermal efficiency of earth-to-air heat exchangers. Case Studies in Chemical and Environmental Engineering, 2, 100013.
6. Rosa, N., Soares, N., Costa, J. J., Santos, P., & Gervásio, H. (2020). Assessment of an earth-air heat exchanger (EAHE) system for residential buildings in warm-summer Mediterranean climate. Sustainable Energy Technologies and Assessments, 38, 100649.
7. Zajch, A., Gough, W. A., & Yoon, G. (2020). Influence of daily temperature behavior on earth-air heat exchangers: A case study from Aichi, Japan. City and Environment Interactions, 8, 100054.
8. Cuny, M., Lin, J., Siroux, M., & Fond, C. (2020). Influence of rainfall events on the energy performance of an earth-air heat exchanger embedded in a multilayered soil. Renewable Energy, 147, 2664-2675.
9. Amanowicz, Ł. (2018). Influence of geometrical parameters on the flow characteristics of multi-pipe earth-to-air heat exchangers–experimental and CFD investigations. Applied energy, 226, 849-861.
10. Xamán, J., Hernández-Pérez, I., Arce, J., Álvarez, G., Ramírez-Dávila, L., & Noh-Pat, F. (2014). Numerical study of earth-to-air heat exchanger: The effect of thermal insulation. Energy and buildings, 85, 356-361.
11. Domingues, A. M. B., Nóbrega, E. S. B., Ramalho, J. V. A., Brum, R. S., & Quadros, R. S. (2021). Parameter analysis of Earth-air heat exchangers over multi-layered soils in South Brazil. Geothermics, 93, 102074.
12. Li, H., Ni, L., Yao, Y., & Sun, C. (2019). Experimental investigation on the cooling performance of an Earth to Air Heat Exchanger (EAHE) equipped with an irrigation system to adjust soil moisture. Energy and Buildings, 196, 280-292.
13. Hou, G., Taherian, H., Song, Y., Jiang, W., & Chen, D. (2022). A systematic review on optimal analysis of horizontal heat exchangers in ground source heat pump systems. Renewable and Sustainable Energy Reviews, 154, 111830.
14. Tasdelen, F., & Dagtekin, I. (2022). A numerical study on heating performance of horizontal and vertical earth-air heat exchangers with equal pipe lengths. Thermal Science, 26(4 Part A), 2929-2939.
15. Liu, Z., Yu, Z. J., Yang, T., Li, S., El Mankibi, M., Roccamena, L., ... & Zhang, G. (2019). Experimental investigation of a vertical earth-to-air heat exchanger system. Energy Conversion and Management, 183, 241-251.

16. Darius, D., Misaran, M. S., Rahman, M. M., Ismail, M. A., & Amaludin, A. (2017, July). Working parameters affecting earth-air heat exchanger (EAHE) system performance for passive cooling: A review. In IOP Conference Series: Materials Science and Engineering (Vol. 217, No. 1, p. 012021). IOP Publishing.
17. DiPippo, R. (2022). Pathé geothermal power plant, Hidalgo, Mexico: A comprehensive retrospective assessment of the first plant of its kind in the Americas. Geothermics, 98, 102285.
18. Gutiérrez-Negrín, L. C., Canchola Félix, I., Romo-Jones, J. M., & Quijano-León, J. L. (2020). Geothermal energy in Mexico: update and perspectives. In Proceedings world geothermal congress.
19. Noman, S., Tirumalachetty, H., & Athikesavan, M. M. (2022). A comprehensive review on experimental, numerical and optimization analysis of EAHE and GSHP systems. Environmental Science and Pollution Research, 29(45), 67559-67603.
20. Xamán, J., Hernández-López, I., Alvarado-Juárez, R., Hernández-Pérez, I., Álvarez, G., & Chávez, Y. (2015). Pseudo transient numerical study of an earth-to-air heat exchanger for different climates of México. Energy and Buildings, 99, 273-283.
21. Rodríguez-Vázquez, M., Xamán, J., Chávez, Y., Hernández-Pérez, I., & Simá, E. (2020). Thermal potential of a geothermal earth-to-air heat exchanger in six climatic conditions of México. Mechanics & Industry, 21(3), 308.
22. Ramírez-Dávila, L., Xamán, J., Arce, J., Álvarez, G., & Hernández-Pérez, I. (2014). Numerical study of earth-to-air heat exchanger for three different climates. Energy and buildings, 76, 238-248.
23. Rodríguez-Vázquez, M., Hernández-Pérez, I., Xamán, J., Chávez, Y., & Noh-Pat, F. (2018). Computational fluid dynamics for thermal evaluation of earth-to-air heat exchanger for different climates of Mexico. In CFD Techniques and Thermo-Mechanics Applications (pp. 33-51). Springer, Cham.
24. Becerra, G., Picazo, M., Aguilar, J. O., Xamán, J., Osorio, E., Hernandez, J., & Ledesma-Alonso, R. (2022). Experimental study of a geothermal earth-to-air heat exchanger in Chetumal, Quintana Roo, Mexico. Energy Efficiency, 15(4), 1-13.
25. Maytorena, V. M., Hinojosa, J. F., Moreno, S., & Buentello-Montoya, D. A. (2023). Thermal performance analysis of a passive hybrid earth-to-air heat exchanger for cooling rooms at Mexican desert climate. Case Studies in Thermal Engineering, 41, 102590.
26. Díaz-Hernández, H. P., Macias-Melo, E. V., Aguilar-Castro, K. M., Hernández-Pérez, I., Xamán, J., Serrano-Arellano, J., & López-Manrique, L. M. (2020). Experimental study of an earth to air heat exchanger (EAHE) for warm humid climatic conditions. Geothermics, 84, 101741.
27. Tereshchenko, I. E., & Filonov, A. E. (2001). Air temperature fluctuations in Guadalajara, Mexico, from 1926 to 1994 in relation to urban growth. International Journal of Climatology: A Journal of the Royal Meteorological Society, 21(4), 483-494.
28. Burke, M., González, F., Baylis, P., Heft-Neal, S., Baysan, C., Basu, S., & Hsiang, S. (2018). Higher temperatures increase suicide rates in the United States and Mexico. Nature climate change, 8(8), 723-729.
29. Thornton, P. K., Ericksen, P. J., Herrero, M., & Challinor, A. J. (2014). Climate variability and vulnerability to climate change: a review. Global change biology, 20(11), 3313-3328..

30. Zhao, Y., Li, R., Ji, C., Huan, C., & Zhang, B. (2019). Parametric study and design of an earth-air heat exchanger using model experiment for memorial heating and cooling. Applied thermal engineering, 148, 838-845.
31. Bisoniya, T. S. (2015). Design of earth–air heat exchanger system. Geothermal Energy, 3, 1-10.
32. Benhammou, M., & Draoui, B. (2015). Parametric study on thermal performance of earth-to-air heat exchanger used for cooling of buildings. Renewable and Sustainable Energy Reviews, 44, 348-355.
33. Pérez-Lombard, L., Ortiz, J., & Pout, C. (2008). A review on buildings energy consumption information. Energy and buildings, 40(3), 394-398.
34. Hollmuller, P., & Lachal, B. (2001). Cooling and preheating with buried pipe systems: monitoring, simulation and economic aspects. Energy and buildings, 33(5), 509-518.
35. Lee, K. H., & Strand, R. K. (2006, August). Implementation of an earth tube system into EnergyPlus program. In Proceedings of the SimBuild 2006 Conference, Boston MA, USA.
36. Kanaris, A. G., Mouza, A. A., & Paras, S. V. (2006). Flow and heat transfer prediction in a corrugated plate heat exchanger using a CFD code. Chemical Engineering & Technology: Industrial Chemistry-Plant Equipment-Process Engineering-Biotechnology, 29(8), 923-930.
37. Wang, Y., Dong, Q., & Liu, M. (2007). Characteristics of fluid flow and heat transfer in shellside of heat exchangers with longitudinal flow of shellside fluid with different supporting structures. In Challenges of Power Engineering and Environment: Proceedings of the International Conference on Power Engineering (Vol. 1, pp. 474-479).
38. Muehleisen, R. T. (2012). Simple design tools for earth-air heat exchangers. Proceedings of SimBuild, 5(1), 723-730.
39. De Paepe, M., & Janssens, A. (2003). Thermo-hydraulic design of earth-air heat exchangers. Energy and buildings, 35(4), 389-397.
40. Kusiak, A., Li, M., & Tang, F. (2010). Modeling and optimization of HVAC energy consumption. Applied Energy, 87(10), 3092-3102.
41. Balaras, C. A., Droutsa, K., Dascalaki, E., & Kontoyiannidis, S. (2005). Heating energy consumption and resulting environmental impact of European apartment buildings. Energy and buildings, 37(5), 429-442.
42. De Assis, E. S., & Frota, A. B. (1999). Urban bioclimatic design strategies for a tropical city. Atmospheric Environment, 33(24-25), 4135-4142.
43. Eicker, U., & Vorschulze, C. (2009). Potential of geothermal heat exchangers for office building climatisation. Renewable Energy, 34(4), 1126-1133.
44. Rodrigues, M. K., da Silva Brum, R., Vaz, J., Rocha, L. A. O., dos Santos, E. D., & Isoldi, L. A. (2015). Numerical investigation about the improvement of the thermal potential of an Earth-Air Heat Exchanger (EAHE) employing the Constructal Design method. Renewable Energy, 80, 538-551.
45. Yu, W., Chen, X., Ma, Q., Gao, W., & Wei, X. (2022). Modeling and assessing earth-air heat exchanger using the parametric performance design method. Energy Sources, Part A: Recovery, Utilization, and Environmental Effects, 44(3), 7873-7894.
46. WONG LOYA, J. A., & Andaverde, J. A. (1843). Simulation of subsoil conditions for ground heat exchanger for application of heating and cooling buildings. In Proceedings of the International Conference on Applied Energy (Vol. 1853).

47. Molina-Rodea, R., & Wong-Loya, J. A. (2021). A new model to predict subsoil-thermal profiles based on seasonal rain conditions and soil properties. Geothermics, 97, 102261.
48. Molina-Rodea. R., & Wong-Loya. J.A. (2020). Application of distinct configurations of vertical earth to air heat exchangers for the warm weather population of Temixco, Morelos (Mexico). In Proceedings world geothermal congress.
49.
50. Molina-Rodea, R., Saucedo-Velazquez, J., Gomez-Franco, W., & Wong-Loya, J. A. " U" Type Earth Heat Exchanger Proposal to Operate a Half-Effect Absorption Cooling System, Harnessing an Abandoned Well in the Geothermal Field “La Primavera”, Jalisco, Mexico.
51. Saucedo-Velázquez, J., Gutiérrez-Urueta, G., Wong-Loya, J. A., Molina-Rodea, R., & Rivera Gómez Franco, W. (2022). Cooling Potential for Single and Advanced Absorption Cooling Systems in a Geothermal Field in Mexico. Processes, 10(3), 583.
52. Molina-Rodea, R., Wong-Loya, J. A., & Valades-Pelayo, P. J. (2020). A new simulator to determine thermal disturbance and recovery processes during wellbore drilling: Experimental validation with a scaled-down wellbore prototype. Computers & Geosciences, 135, 104359.
53. Tedeschi, L. O. (2006). Assessment of the adequacy of mathematical models. Agricultural systems, 89(2-3), 225-247.
54. Amanowicz, Ł., & Wojtkowiak, J. (2018). Validation of CFD model for simulation of multi-pipe earth-to-air heat exchangers (EAHEs) flow performance. Thermal Science and Engineering Progress, 5, 44-49.
55. Bisoniya, T. S., Kumar, A., & Baredar, P. (2015). Energy metrics of earth–air heat exchanger system for hot and dry climatic conditions of India. Energy and Buildings, 86, 214-221.
56. Wang, X., Bjerg, B. S., & Zhang, G. (2018). Design-oriented modelling on cooling performance of the earth-air heat exchanger for livestock housing. Computers and Electronics in Agriculture, 152, 51-58.
57. Bisoniya, T. S., Kumar, A., & Baredar, P. (2014). Parametric analysis of Earth-air heat exchanger system based on CFD modelling. Int J Power Renew Energy Syst, 1, 36-46.
58. Andaverde, J. A., Wong-Loya, J. A., Vargas-Tabares, Y., & Robles, M. (2019). A practical method for determining the rheology of drilling fluid. Journal of Petroleum Science and Engineering, 180, 150-158.
59. Hernández-Magallanes, J. A., Ibarra-Bahena, J., Rivera, W., Romero, R. J., Gómez-Arias, E., Dehesa-Carrasco, U., ... & Kozhiparambil Chandran, S. (2019). Thermodynamic analysis of a half-effect absorption cooling system powered by a low-enthalpy geothermal source. Applied Sciences, 9(6), 1220.

Fin